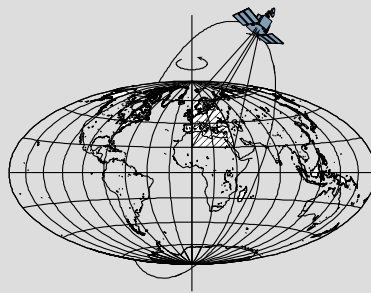


# **Satellite Altimetry and Hydrologic Modeling of Poorly-Gauged Tropical Watershed**

by

**Yohanes Budi Sulistioadi**



Report No. 505

Geodetic Science

The Ohio State University  
Columbus, Ohio 43210

November 2013

# **SATELLITE ALTIMETRY AND HYDROLOGIC MODELING OF POORLY-GAUGED TROPICAL WATERSHED**

By

Yohanes Budi Sulistioadi

Report No. 505  
Geodetic Science  
The Ohio State University  
Columbus, Ohio 43210  
November 2013

Copyright by  
Yohanes Budi Sulistioadi  
2013

## Preface

This report was prepared for and submitted to the Graduate School of the Ohio State University as a dissertation for partial fulfillment of the requirements for the Doctor of Philosophy (PhD) degree.

This research was carried out under supervision of Professor C.K. Shum, Division of Geodetic Science, School of Earth Sciences, The Ohio State University. Hidayat at Hydrology and Quantitative Water Management Department of Wageningen University and Limnology Research Agency of Indonesian Institute of Sciences (LIPI) are especially acknowledged for providing *in-situ* discharge, rating curve and precipitation data for the Upper Mahakam Sub-watershed study region.

This research is primarily supported by the Fulbright PhD Presidential Scholarship administered by American Indonesian Exchange Foundation (AMINEF) and the Institute for International Education (IIE). In addition, this study is partially funded by grants from NASA's Ocean Surface Topography Science Team project (Univ. of Colorado, 154-5322), NASA's Geodetic Imaging project (NNX12AQ07G), NASA's Application Science Program under the SERVIR project (NNX12AM85G), and The Ohio State University's Climate, Water, and Carbon (<http://cwc.osu.edu/>) program.



## Abstract

Fresh water resources are critical for daily human consumption. Therefore, a continuous monitoring effort over their quantity and quality is instrumental. One important model for water quantity monitoring is the rainfall-runoff model, which represents the response of a watershed to the variability of precipitation, thus estimating the discharge of a channel (Bedient and Huber, 2002, Beven, 2012). Remote sensing and satellite geodetic observations are capable to provide critical hydrological parameters, which can be used to support hydrologic modeling. For the case of satellite radar altimetry, limited temporal resolutions (*e.g.*, satellite revisit period) prohibit the use of this method for a short (<weekly) interval monitoring of water level or discharge. On the other hand, the current satellite radar altimeter footprints limit the water level measurement for rivers wider than 1 km (Birkett, 1998, Birkett *et al.*, 2002). Some studies indeed reported successful retrieval of water level for small-size rivers as narrow as 80 m (Kuo and Kao, 2011, Michailovsky *et al.*, 2012); however, the processing of current satellite altimetry signals for small water bodies to retrieve accurate water levels, remains challenging.

To address this scientific challenge, this study poses two main objectives: (1) to monitor small (40–200 m width) and medium-sized (200–800 m width) rivers and lakes using satellite altimetry through identification and choice of the over-water radar waveforms corresponding to the appropriately waveform-retracked water level; and (2) to develop a rainfall-runoff hydrological model to represent the response of mesoscale watershed to the variability of precipitation. Both studies address the humid tropics of Southeast Asia, specifically in Indonesia, where similar studies do not yet exist. This study uses the Level 2 radar altimeter measurements generated by European Space Agency's (ESA's) Envisat (Environmental Satellite) mission.

The first study proves that satellite altimetry provides a good alternative or the only means in some regions to measure the water level of medium-sized river (200–800 m width) and small lake (extent <1000 km<sup>2</sup>) in Southeast Asia humid tropic with reasonable accuracy. In addition, the procedure to choose retracked Envisat altimetry water level heights via identification or selection of over water waveform shapes is reliable; therefore this study concluded that the use of waveform shape selection procedure should be a standard measure in determining qualified range measurements especially over small rivers and lakes. This study also found that Ice-1 is not necessarily the best retracker as reported by previous studies, among the four standard waveform retracking algorithms for Envisat altimetry observing hydrologic bodies.

The second study modeled the response of the poorly-gauged watershed in the Southeast Asia's humid tropic through the application of Hydrologic Engineering Center – Hydrologic Modeling System (HEC-HMS). The performance evaluation of HEC-HMS discharge estimation confirms a good match between the simulated discharges with the observed ones. As the result of precipitation data analysis, this study found that Tropical Rainfall Measuring Mission (TRMM) Multi-satellite Precipitation Analysis (TMPA) is the preferred input forcing for the model, given the thorough evaluation of its relationship with field-measured precipitation data prior to its use as primary climatic forcing. This

research also proposes a novel approach to process the TRMM precipitation estimation spatially through Thiessen polygon and area average hybrid method, which model the spatial distribution of TRMM data to match the spatial location of field meteorological stations.

Through a simultaneous validation that compares the water level anomaly transformed from HEC-HMS simulated discharge and satellite altimetry measurement, this study found that satellite altimetry measures water level anomaly closer to the true water level anomaly than the water level anomaly converted from HEC-HMS simulated discharge.

Some critical recommendations for future studies include the use of waveform shape selection procedure in the satellite altimetry based water level measurement of small and medium-sized rivers and small lakes, as well as the exploration to implement data assimilation between satellite altimetry and the hydrologic model for better discharge and water level estimations.

## Table of Contents

Preface.....	i
Abstract .....	ii
Table of Contents .....	iv
1. Introduction .....	1
1.1. Fresh Water Resources.....	1
1.2. Hydrology of the Humid Tropics .....	3
1.3. Satellite Radar Altimetry.....	4
1.4. Motivation and Contribution of this Study .....	9
2. Theoretical Background .....	11
2.1. Satellite Radar Altimetry.....	11
2.1.1. Historical Review.....	11
2.1.2. Satellite Altimetry Measurement .....	12
2.1.3. Error Corrections .....	14
2.1.4. Waveform Retracking.....	17
2.1.5. Non-Ocean Surface Waveform Retracking.....	23
2.2. Hydrological Analysis and Modeling .....	30
2.2.1. Hydrological Cycle and Watershed Concepts .....	30
2.2.2. Rainfall-runoff Process .....	31
2.2.3. Runoff Volume Estimation .....	33
2.2.4. Unit Hydrograph .....	38
2.2.5. Flow Routing .....	40
2.2.6. Watershed Hydrologic Modeling.....	42
3. Satellite Radar Altimetry for Small Water Bodies in the Tropics.....	44
3.1. Introduction.....	44
3.1.1. Monitoring Rivers and Lakes in Humid Tropics .....	44
3.1.2. Remote Sensing and Satellite Altimetry .....	44
3.1.3. Satellite Altimetry Waveform Retracking Algorithms for Inland Waters..	44
3.1.4. Motivation and Contribution of This Study.....	44
3.2. Study Area.....	45
3.2.1. Mahakam River and Lakes in East Kalimantan.....	45
3.2.2. Lake Matano and Lake Towuti in South Sulawesi .....	47
3.3. Methodology .....	48
3.3.1. Envisat Radar Altimeter.....	48
3.3.2. The Role of Remote Sensing and Geospatial Datasets .....	50
3.3.3. Waveform Shape Analysis.....	51
3.3.4. Outlier Removal.....	52
3.3.5. Validation and Performance Evaluation .....	52
3.3.6. Data Processing Workflow .....	54
3.4. Results and Discussions .....	55
3.4.1. Water Level of Mahakam and Karangmumus Rivers.....	55
3.4.2. Water Level of Lake Semayang, Lake Matano and Lake Towuti .....	71
3.5. Conclusions and Recommendations .....	82

4. Hydrologic Modeling of Upper Mahakam Sub-Watershed .....	84
4.1. Introduction .....	84
4.2. Study Area .....	86
4.3. Precipitation Data Analysis .....	86
4.4. HEC-HMS Model Preparation .....	94
4.4.1. Terrain Analysis and Basin Characterization .....	94
4.4.2. Hydrological Parameter Estimation .....	98
4.4.3. Setting up the HEC-HMS Model .....	103
4.4.4. Model Calibration and Optimization .....	104
4.5. Results and Discussion .....	108
4.5.1. Validation of the Model .....	108
4.5.2. Final Simulation and the Flood Events .....	110
4.6. Conclusions and Recommendations .....	116
5. Integrating Satellite Altimetry and Hydrologic Model .....	118
5.1. Introduction .....	118
5.2. Simultaneous Validation of Satellite Altimetry and Hydrologic Model .....	119
5.3. Conclusions and Recommendations .....	121
6. Conclusions and Future Studies .....	122
6.1. Conclusions .....	122
6.2. Future Studies .....	122
Bibliography .....	124

# 1. Introduction

## 1.1. Fresh Water Resources

The “blue marble” planet called Earth is 70% covered by water in various forms and only the remaining 30% of the whole surface area is dry land. Fresh water, which includes ice sheets, glaciers, groundwater, permafrost, river and lake, holds only about 2.5% of the Earth’s surface water, compared saline water in the ocean, which accounts for almost 97.5%. Out of this proportion, only 0.26% of the fresh water can be found in rivers and lakes (Shiklomanov, 1998). On the other hand, rivers and lakes are among the most influential sources of water for daily human consumption. With the great and increasing human population, the numbers of people who rely on the fresh water, the impact of land use change, accelerated urban development and the change of global climate to hydrological regime of most watershed, there is no doubt that the monitoring of water resources is a crucial issue to date. Water quantity monitoring and water quality assurance require a reliable system to ensure continuous availability and good quality of fresh water from rivers and lakes.

Water level (also called *stage*) and discharge are essential parameters in monitoring the quantity of fresh water resources. The best way to monitor such rivers and lakes is through *in-situ* measurement by installing instruments to measure the water level and velocity of the river flows to infer the amount of water flow through the monitoring station at a time (Hersch, 2009). The discharge is expressed by volume per specific period (e.g. m<sup>3</sup>/s, cfs). A tremendous number of small to medium-sized rivers (defined as 40-200 m width with 10-100 m<sup>3</sup>/s and 200-800 m width and 100-1000 m<sup>3</sup>/s average discharge, respectively, according to Meybeck *et al.* (1996)) around the world are poorly gauged for various reasons (Alsdorf and Lettenmaier, 2003). In contrast, despite the installation and operation of in-situ measurement, such permanent gauging is often considered costly and less important while the need for continuous hydrological monitoring of small rivers is increasing. Therefore, it is a scientific and social challenge to provide reliable water level and discharge information given the absence of continuously operating in-situ measurement efforts.

Hydrology, the branch of science that deals with the water cycle on Earth, is growing vastly in order to support the needs of fresh water monitoring through various innovations. One important approach is hydrologic modeling, which has been developed for the past 100 years for various descriptive and predictive purposes. With the complexities of processes involved in the water cycle for each catchment, it is immensely difficult if not impossible to generate one universal model that can be applied anywhere. Therefore, in the effort of developing a reliable hydrologic model, the scientist needs to define the scale, heterogeneity, temporal and spatial discretization and many other aspects carefully (Rosbjerg and Madsen, 2005). Beyond the complexities noted above, the purpose of model development may lead to correct answers to questions about the parameters to be defined and inputs to be fed into the model.

Specifically, Rosbjerg and Madsen (2005) classified hydrologic models based on the outputs produced as defined in the purpose of model development, into the following categories:

- (1) River and reservoir models. This model describes how the water flows and routes through various infrastructures along the river, which makes it suitable for studying flood wave propagation, as well as the impact of infrastructures built in the river.
- (2) Rainfall-runoff models or catchment/watershed models. This model calculates the variation of runoff caused by variation of precipitation inputs.
- (3) The distributed models take into account the spatial variation of the variables and carefully define the runoff process, runoff transformation up to the dynamic of streamflow as the result of the whole process.
- (4) Groundwater models. This model deals with subsurface part of the water cycle, which includes abstraction of groundwater and various movement of groundwater up to the point where the flow merges with surface runoff.
- (5) Design and management models. With the advances of statistical science, this hydrologic model assesses the uncertainty of the estimate and predicts the response of the watershed to changes in land-use management and other model forcing.

According to Bedient and Huber (2002), one of the foremost models for water quantity monitoring is the rainfall-runoff model, inspired by the fact that rainfall is distributed into evaporation, infiltration, detention or depression storage, overland flow and by the nature of water it accumulates and flows with gravity to end up within streamflow. Important factors to be included in this model are topographical information, drainage network, land use and proportion of impervious surface, soil infiltration capability, channel characteristics and watershed physical properties. As a result, discharge could be estimated as the watershed responses to the precipitation that has occurred in the area (Beven, 2012).

Further down along the river, the flow of the water can be modeled with a hydraulic model, which describes its movement as a function of time within the watershed. Based on the equation of continuity, a hydraulic model computes the dynamic of water flow in the river and floodplain, as well as identifying when the volume of transported water exceeds the bank full level, in which case a flood would occur. Further, based on accurate topographic information, the spread of inundation from flooding events could be identified from this model; therefore it could also be called flood inundation modeling. Similar to the development of a hydrologic model, hydraulic modeling is also becoming significant with the improvement of computation capability. Initial cross-sectional area averaged one-dimensional models have been evolved into multidimensional models (2D and 3D) that consider lateral, longitudinal, and vertical hydrodynamics in the river channels. On the other hand, hydraulic models are prone to uncertainties from various interdependent factors such as design flow, terrain, hydraulic model and mapping techniques. Therefore, an integrated model that includes hydrologic and hydraulic models, complete with uncertainty analysis framework is recommended (Merwade *et al.*, 2008).

Hydrologic and hydraulic modeling approaches help a variety of users to understand the river system and the watershed they are dealing with, enabling them to make very important decisions and provide guidance for better water resources management. A common problem with all kinds of hydrologic and hydraulic modeling is that the models involve so many factors and most of the time those factors can only be

estimated. Errors and uncertainty stemming from estimation of these variables/factors may then produce misleading results or even correct results with somehow erroneous processes. Therefore, calibration and validation of a model are necessary before a hydrologist may declare one model to be operational (Duan, 2003). Calibration and validation of a model are usually carried out using split-sample data with the highest confidence level, which is used for calibration and validation separately. In terms of hydrologic models, the dataset required for validation is mainly the discharge of the watershed being modeled, and specifically for this study, the validation process is considered to be performance validation (Biondi *et al.*, 2012).

Space geodetic and remote sensing from space has proven to be one viable source of observation to complement or replace field measured data, which is lacking for many parts of the world, in efforts to develop reliable watershed hydrologic and hydraulic modeling. Copious research has demonstrated the capability of remotely-sensed data to provide continuous estimation of a number of hydrological variables (Tang *et al.*, 2009). For instance, remotely-sensed data could also perform side-to-side estimation of hydrology variables (*e.g.* discharge), given the accuracy of the geodetic observations from space (Siddique-E-Akbor *et al.*, 2011). However, exclusive use of remotely-sensed and geodetic data to develop hydrologic model is continuously developing. To support this initiative, there should be integration and complementary calibration of the model using remote sensing data and *in-situ* measurement to obtain the best and most reliable model to represent the behavior of watersheds and river systems in response to climatological changes.

## **1.2. Hydrology of the Humid Tropics**

Humid tropics are defined as the region of the Earth that is mostly covered with tropical rainforests (*i.e.* forest dominated by broadleaf evergreen trees). These forests include the Amazon, most of Central Asia, the Caribbean, Central Africa, coastal West Africa, Eastern Madagascar, southwest India, Bangladesh and most of Southeast Asia (Fosberg *et al.*, 1961). This region presents unique climate relative to other climate zones, which could be described as less variation in weather features compared with those in high latitudes, but the tropical weather and climate vary greatly in time scales (*e.g.* from diurnal to decadal) and its spatial distribution (Manton and Bonnell, 1993). In terms of the temperature ranges, the humid tropics region never gets below 18°C for the coldest month. From rainfall record and wet-month point of view, humid tropics region almost always receive monthly rainfall in excess of 100 mm, which is also known as a wet-month threshold and is part of the definition of humid tropics. In addition, the number of thunderstorm days exceeds 30 in a year in most of the Southeast Asia region (Chang, 1993).

The hydrological regime of the Asian humid tropics is greatly influenced by changes in land use, urbanization, soil and water conservation measures, and diversion of surface and groundwater discharges. There are three river regimes in the Asian humid tropics as described by Chang (1993), which are: (1) typhoon-prone, including northern Philippines, Hainan, Taiwan and coastal region of Vietnam; (2) equatorial, which includes southern Philippines, Indonesia, Malaysia and Sri Lanka, (3) tropical, with

distinct and prolonged dry season that covers continental Southeast Asia and the coast of India and Bangladesh. This study focuses on the equatorial region of humid tropics, in particular Indonesia, where the dry season is particularly short while the rivers transport large volumes of water. Thunderstorms and disturbances due to monsoon atmospheric circulation usually happen in short duration and produce flash floods in the small basins. The runoff typically exceeds 1000 mm, and at some peak moments could reach 2500 mm in part of Borneo Island and eastern Sulawesi. Despite the above description, some mid-size rivers show complex behaviors in response to intense storms with slow-increasing flooding that remains for weeks, and slowly decreases thereafter. Still, the headwaters of this river show typical flash-flood response on high intensity rainfall. In terms of soil erosion, Asia's humid tropics carry the highest erosion rate compared to any other continent (El-Swaify, 1982). The evidence of this enormous erosion rate could be visibly investigated from the amount of sediment loads in most rivers. Erosion and sedimentation cause aggregation of river channels, increasing flood hazards, clogged irrigation diversions and the effect on water quality for industry and domestic use. The complexity of Asia's humid tropics increases by changes in land use, (*e.g.* conversion of forest into other land use), which alters the balance hydrological cycle through the increase of erosion and surface runoff.

In addition to the complex phenomenon and variation in hydrological regimes mentioned above, humid tropical Asia has a truly large population. Water has been a very significant resource for daily life and to support agricultural products. On the other hand, destructive natural disasters have consistently caused losses of human life and property. Therefore, research in hydrology of medium sized basins in the equatorial region of Asian humid tropics is deemed urgent for supporting human life, as well as important to increase the level of understanding to the hydrological behavior of this region.

### **1.3. Satellite Radar Altimetry**

Satellite radar altimetry was first envisioned in NASA's Williamstown conference and with the first satellite mission, GEOS-3, launched and operated globally in 1975. It is a satellite-mounted radar-ranging system which continuously operating along its orbit (Fu and Cazenave, 2001). The main function of satellite altimetry is to measure the vertical distance between the antenna phase center of satellite-mounted radar sensor and the Earth's surface. As with any radar system, the radar transmitter beams microwave pulses to Earth's surface, and the radar echo is then recorded by the onboard receiver with the round trip travel time measured using a precise time-keeping device, the Ultra Stable Oscillator (USO). Range is then derived from the round trip time and the speed of light, along with other corrections to calculate the precise range from the satellite to the Earth's surface. The initial purpose of satellite altimetry system included the determination of marine geoid, large-scale ocean circulation, and mesoscale oceanic variability (Shum *et al.*, 1993), but it has also been expanded into global sea-level research, and studies of the cryosphere, geophysics, and hydrology. Considering the highly quantitative characteristics of this instrument and significant error sources along the radar signal path, the use of this measurement system requires a comprehensive knowledge of these error sources or corrections, including the precise determination of



the satellite orbit, the physics of propagation of microwave signals through the atmosphere, the instrument corrections, and the geophysical corrections (Rapley *et al.*, 1990).

Initially, satellite altimetry missions were introduced to support studies of oceanographic phenomena (Brown and Cheney, 1983) even though at a later stage scientists found a way to study large inland water bodies (Fu and Cazenave, 2001). The use of satellite altimetry for monitoring of inland water level is potentially difficult due to several problems such as wide along-track ground resolution and the media and geophysical corrections that were developed for open ocean applications; therefore they sometimes do not exist for inland waters or continents. The most important problem is the radar echoes from surrounding topography (ESA, 2012), or the so-called tracker biases. Various studies have been carried out in the last couple decades to utilize early satellite altimetry missions for inland water hydrology studies. Wingham and Rapley (1987) studied Seasat altimeter returns over land and inland water as well as sea ice, to understand their characteristics and defined strategies to process narrow-peaked altimeter returns. In the other study, Rapley *et al.* (1987) exclusively determined the characteristics of the Seasat radar waveforms and their correlation with properties of the Earth's surface. Rapley *et al.* (1987) found that the surface elevations of large lakes, lakes and rivers smaller than altimeter footprint are all possible with a precision of 1 m or better, contingent upon the ability to compute adequately accurate satellite orbit ephemeris to infer the water surface height above a defined reference ellipsoid using the measured altimeter range. Koblinsky *et al.* (1993) utilized Geosat altimeter measurement to measure water level variations over the Amazon River basin by both automatic procedure and manual selection of radar returns with specular waveform shapes. This study found that the use of satellite altimeter is one promising approach for measuring river levels from space and provide estimated accuracy of ~10 cm. It is important to note that standard deviation of the difference and the Root-Mean-Square Error (RMSE) are used interchangeably by various researchers, while both terms refer to similar magnitude. This finding was confirmed by other study by Morris and Gill (1994a), which also processed Geosat altimeter data to reveal the water level variation of Great Lakes and found similar accuracy. Further, Morris and Gill (1994b) evaluated the initial cycles of TOPEX/Poseidon altimeter measurement over the Great Lakes and found even higher accuracy of ~3 cm, especially because tidal effects are minimal. In a global approach, Birkett *et al.* (1995) developed a new Global Lakes Database based on satellite radar altimetry. Still dealing with large lakes—a water body which is even called a “sea”—Cazenave *et al.* (1997) studied the water level of Caspian Sea through an analysis of TOPEX/Poseidon altimeter data and found that the “sea” level was continuing to rise during 1993-1995 and suddenly fell to a considerable amount thereafter. More recently, Birkett (1998) found that large wetlands and a river with >1 km width can be successfully tracked by TOPEX/Poseidon satellite that carries NASA Radar Altimeter (NRA) on board, and produced reliable water level estimates with accuracy as low as ~11 cm. Alsdorf *et al.* (2001) integrated interferometric processing of JERS-1 SAR data and TOPEX/Poseidon radar altimetry to measure water surface heights of an Amazon lake and found an agreement from both measurements in terms of the rate of water level rise.

The dynamic of the Black Sea was also studied through processing of TOPEX/Poseidon and ERS-1 radar altimeter data (Korotaev *et al.*, 2001), which revealed the water level estimated accuracy of ~3 cm. In a more comprehensive study, Birkett *et al.* (2002) concluded that the minimum river width attainable for satellite radar altimetry observation of water level is ~1 km. Further, this study found the mean accuracy of 1.1 m with the best results being 0.4-0.6 m, in particular for the Amazon Basin. Moving along to Africa, Mercier *et al.* (2002) studied 12 major African lakes through a 7-year long water level time series as derived from TOPEX/Poseidon and found the accuracy of <10 cm for the estimation of water level on large lakes. Small lakes, however, gave lower accuracy of 30–50 cm. This study also revealed consistent water storage change along with precipitation dynamic over the study area.

During the last decade, the number of studies related to the use of satellite altimetry for inland water dynamic increased significantly. Various study sites were investigated, while various methods were also tested and verified. The Plata Basin, the second largest basin in South America, was studied for its water level dynamic, and the results revealed a spatial and temporal signature of climate variability in this area (Maheu *et al.*, 2003). Still using TOPEX/Poseidon altimeter data, Kouraev *et al.* (2004) estimated the discharge of Ob' River (with a few kilometers width) in the Arctic during the various hydrological phases and found that TOPEX/Poseidon altimeter data could be used to estimate river level with reasonable accuracy. Coe and Birkett (2004) studied Lake Chad in Africa using TOPEX/Poseidon radar altimetry and indicated that the river discharge upstream of the lake could be determined; therefore the lake and marsh height could be predicted in advance. Frappart *et al.* (2005), combined satellite altimetry observation of water level with microwave remote sensing (Synthetic Aperture Radar) derived inundation patterns to determine water volume variation in order to describe inundation dynamic of river floodplains. Hwang *et al.* (2005) studied the dynamics of inland lakes in China through 10-year TOPEX/Poseidon altimetry data and various dynamics of different lakes in the China's inland waters. In addition, it is noteworthy that the dynamics of China's inland lakes correlate closely with precipitation and El Nino Southern Oscillation (ENSO). At the other end of Asian continent, Cretaux *et al.* (2005) studied the dynamic of Big Aral Sea near Kyrgyzstan and Uzbekistan using TOPEX/Poseidon radar altimetry. This study found that combination of satellite altimetry with other parameters of the water budget presents a remarkable result of the water cycle temporal changes in the arid or semiarid regions, even for the regions with poor ground monitoring network. Move along to Southeast Asia, Frappart *et al.* (2006) analyzed satellite altimetry data from ERS-2, Envisat and TOPEX/Poseidon to estimate water level of Mekong river basin during the 8-year period (1996-2004). This study found a clear inter-annual signal from the derived water level from satellite altimetry. It is confirmed by optical satellite imageries, as well as total water volume changes as inferred from gravity mission satellite GRACE. Zhang *et al.* (2006) also studied Dongting Lake in China, and found the TOPEX/Poseidon altimeter data useful for dense and continuous monitoring of the temporal variations in water dynamic in moderate to large lakes. To conclude some intermediate results from various studies, Berry *et al.* (2005) summarized that lake height data can be obtained through retracking of multi-mission altimeter data, given the surface

area of those lakes exceed 500 km<sup>2</sup>. In similar comprehensive studies, Calmant and Seyler (2006) and Cretaux and Birkett (2006) concluded that satellite altimetry data have been successfully complemented hydrological measurements such as time series of stages, discharges, river altitude profiles as well as lake level variability, given the satellite ground track passes through the rivers or lakes. Both studies also agreed that the accuracy of satellite altimetry derived hydrological measurements varies from a few centimeters down to several decimeters, depends on the physical condition of the study area. It is also worth noting that satellite altimetry needs specific and complicated processing such as waveform retracking, media, instrument and geophysical corrections.

In a more recent study, Zakharova *et al.* (2007) analyzed the water level dynamic of Euphrates-Tigris Rivers at the Arabian Gulf and found that multiple satellite missions with altimeter on board (TOPEX/Poseidon, Geosat Follow On or GFO and Envisat) could monitor the water level of large rivers in this area. In addition, the temporal evolution of the backscatter coefficient could also help the detection of water in the marshes and reservoirs as well as for mapping the flooded areas. On the other side of the world, Chu *et al.* (2007) studied four natural lakes: the Poyang, Dongting, Tai, and Chao, within the Yangtze River basin in China, using Envisat Geophysical Data Record (GDR) with simple editing criteria and considering appropriate geophysical corrections. This study revealed that the lakes' water level follows the Yangtze River. This relationship contributes to floods and other disasters in the middle and lower reaches of the Yangtze River. Medina *et al.* (2008) studied the dynamic of Lake Izabal in Guatemala, Central America using Envisat GDR combined with in-situ measurements and found a good agreement between those two data sets with estimated accuracy of 9 cm. In addition, this study also revealed that the water level shows seasonal signal forced by rainy and dry climate seasons in the region while a connection was also found between higher or lower extreme values in the lake level with rainfall anomalies influenced by global climate forces such as El Nino Southern Oscillation and the Tropical North Atlantic anomaly. Moving back to Africa, Munyaneza *et al.* (2009) studied the water level of Lake Kivu in Central Africa using Envisat radar altimetry through a relationship of the elevation-surface area characteristics and found the estimated accuracy of ~30 cm. In China, Cai and Ji (2009) studied Poyang Lake using Envisat RA-2 and suggested that derived water surface heights from the altimeter data have a good accuracy.

In the area with severe data scarcity such as Afghanistan, Envisat radar altimetry was used along with active remote sensing satellite of Advanced Land Observing Satellite (ALOS) Phased Array type L-Band Synthetic Aperture Radar (PALSAR) Interferometric Synthetic Aperture Radar (InSAR) to detect the changes of Helmand River wetland water level (Lu *et al.*, 2009). This study revealed that integrating these satellite observations can provide spatial and temporal measurements of water level where in-situ measurements are absent. Some experiments to apply satellite altimetry to estimate water level of the small rivers were undertaken by Kuo and Kao (2011), who retrieved surface heights of Bajhang River in Taiwan from Jason-2 20-Hz radar altimeter waveform using several retracking techniques such as offset center of gravity (OCOG, also known as Ice-1), threshold, modified threshold and ice retrackers. This study found that a river with a minimum width of ~100 meters still can be observed through Jason-2

radar altimetry with threshold retracking methods and reasonable accuracy. On the other side of the world, Michailovsky *et al.* (2012) processed Envisat radar altimetry for Zambezi River in Africa with less than 80 meters width. Using detailed mask from optical remote sensing system (*i.e.* Landsat), this study estimates water level with estimated accuracy as low as 32 cm when compared to available *in-situ* measurements. The results from studies mentioned above confirmed that processing altimetry data to monitor small bodies of water requires a distinguished approach and less research were completed in this field.

Study about inland waters that makes use of satellite radar altimetry is growing significantly. Many studies offer improvement in the waveform retracking techniques or integration with other remote sensing system to answer hydrological questions. Guo *et al.* (2009) offers so-called improved threshold retracker (ITR) to retrack waveforms over Hulun Lake in China. The retracker developed by Guo *et al.* (2009) considers the stochastic feature of the waveform and results in accurate estimation of lake levels. Improvement of the waveform retracking algorithm for estimation of water levels in small water bodies was also used for estimating water level of Gorki reservoir in Russia with 10–15 cm accuracy (Troitskaya *et al.*, 2012). This study offered an adaptive retracking method, which based on the analysis of the shape of reflected telemetric impulses and the application of threshold retracking algorithm. Tseng *et al.* (2013) introduced a classification algorithm to identify the anomalous waveforms and then use an empirical retracking gate correction to mitigate lake ice contamination. This algorithm improved the accuracy of Ice-1, Ocean and threshold retracker as they were applied to estimate water levels of Lake Qinghai in China.

A number of interesting studies tried to integrate and complement satellite radar altimetry measurements to enhance the reliability of the hydrologic models. This trend is obviously essential to improve the monitoring of un-gauged or poorly gauged watersheds. Getirana *et al.* (2009) developed high accuracy relationships between water levels observed by satellite altimetry and water discharge computed by hydrological model for northern Amazon basin. In Southeast Asia, Birkinshaw *et al.* (2010) estimate the discharge at a downstream site in Mekong River using statistical methods and found that the model that includes satellite altimetry data produced estimated discharge with higher accuracy. To support flood monitoring in Bangladesh, Siddique-E-Akbor *et al.* (2011) compared the water level estimates from one-dimensional hydraulic model with satellite altimetry observation, and found that satellite altimetry presents disagreement with hydraulic models especially for the small and medium-sized basins that are mountainous and flashy. In other studies, satellite altimetry was used to calibrate hydrological models developed based on other satellite observations in a study area where no *in-situ* data available. In Amazon Basin, Getirana *et al.*, (2010) developed a large-basin model of Negro Basin and validated it with both *in-situ* gauge data and complimentary satellite altimetry dataset. Moving along to the African continent, Velpuri *et al.*, (2012) developed a water balance model for Lake Turkana in East Africa based on digital elevation dataset, satellite-based rainfall estimates, runoff and evaporation. A composite of TOPEX/Poseidon, Jason-1 and Envisat satellite altimetry data, were then used to calibrate and validate the model, resulting in good agreement between the model and

calibration data, as well as the capability for capturing patterns and seasonal variations of the Lake Turkana. In a different setup and geographic region, *i.e.* large river in North America, Sun *et al.*, (2012) developed coupled hydrologic and hydraulic models to describe the relation between streamflow and water stage of Upper Mississippi Basin and calibrated them with TOPEX-Poseidon satellite radar altimetry. This study revealed that the contribution of satellite altimetry data uncertainty to the overall model performance is minimum.

#### **1.4. Motivation and Contribution of this Study**

To conclude this chapter, it is worth mentioning that fresh water resources are critically valuable for human life; therefore, an operational method must be highly accurate but remain simple to build and operate, in order to monitor fresh water quantity and quality continuously. The advance of computing systems has led to rapid development and advances in hydrologic and hydraulic modeling, even as the necessity to address the response to the changing climate has grown vastly. However, these models critically need a set of data such as:

- (1) Reliable inputs or model forcing (*e.g.* precipitation, temperature and other meteorological data)
- (2) Physical properties of watershed and river channels (*e.g.* basin and sub-basins geometry, channel cross sections and floodplain profile)
- (3) Calibrated parameters (*e.g.* derived hydrological parameters from soil and land use types, Manning's roughness coefficient, subsurface flow coefficients)

In addition, not all hydrological and climatological regions have the same level of accuracy of input data for hydrologic and hydraulic models. Asia's humid tropics are one region where reliable scientific and operational data are very hard to find.

Remote sensing and satellite geodetic observations have been supporting hydrology studies to overcome the "lack of data" situations and successfully complement or fulfill the needs of *input* data, indirectly providing information to calculate some parameters or used for calibration and validation in the framework of hydrologic modeling. However, various limitations of remotely-sensed and geodetic data have hampered the advancement of hydrology studies; for example, the current radar altimeters footprints limit the measurement into only rivers with ~1 km width (Birkett, 1998, Birkett *et al.*, 2002). Even some studies present successful retrieval of water level of small-sized rivers down to ~80 – 100 m width (*e.g.* Kuo and Kao, 2011, Michailovsky *et al.*, 2012), the processing of current satellite altimetry signals for small water bodies still remains challenging. In less than a decade, NASA's Surface Water and Ocean Topography (SWOT) Mission will orbit the Earth carrying Ka-band radar interferometry to measure surface water levels with the ability to monitor smaller rivers down to 100 m wide with up to 10 cm accuracy (Biancamaria *et al.*, 2010). Still, there are a lot of important rivers with width less than 100 m threshold. A number of initiatives to develop global rivers' and lakes' water level database exist to date, but none of them count small to medium-sized rivers and lakes in the humid tropics. On the other hand, the fresh water sources in this region are critically vital either in terms of their function as daily water sources or their impacts upon natural disaster such as floods.

**Table 1.1** List of Global River and Lakes Database based on Satellite Altimetry

Provider	Service Name	URL
US Department of Agriculture	USDA Global Reservoir and Lake Elevation Database	<a href="http://www.pecad.fas.usda.gov/cropexplorer/global_reservoir/">http://www.pecad.fas.usda.gov/cropexplorer/global_reservoir/</a>
French Space Agency	CNES Hydrology by Altimetry	<a href="http://www.legos.obs-mip.fr/soa/hydrologie/hydroweb/">http://www.legos.obs-mip.fr/soa/hydrologie/hydroweb/</a>
European Space Agency	River and Lake Dataset	<a href="http://tethys.eaprs.cse.dmu.ac.uk/RiverLake/shared/main">http://tethys.eaprs.cse.dmu.ac.uk/RiverLake/shared/main</a>

As outlined by previous studies listed above, satellite altimetry measurement of water levels and hydrologic modeling are the future of indirect and affordable combination in monitoring inland water bodies from space. Therefore, this research addresses the span of the following **research questions**:

1. What is the minimum width of a river and the extent of a lake that current satellite altimetry can still measure? Can geospatial information and waveform shape selection procedure help the existing waveform retracking algorithm to observe small water bodies?
2. How can a reliable hydrologic model be built to apply to an area in Southeast Asia's humid tropics with limited data availability (*e.g.* by optimizing all possible inputs from satellite observations and available ancillary data)? Is a rainfall-runoff based hydrologic model applicable for long-term discharge estimation in this area?

The research questions above will be addressed through hypotheses-based experiments that include (1) application of standard waveform retracking algorithms as provided in Envisat radar altimetry Geophysical Data Record (GDR) dataset on small and medium sized rivers, which characterized by 40–200 m and 200–800 m main channel width, respectively (Meybeck *et al.*, 1996), and small lakes in Southeast Asia's humid tropics, assuming that every single high-sampling rate observation (*e.g.* 18 Hz Envisat radar altimeter) represents valid water level observation, (2) development of event-based hydrologic model to represent the response of medium-sized watershed to the variability of rainfall and other parameters, assuming all unknown parameters could be carefully estimated based on theoretical and empirical methods and field experience. Therefore, the main objective of this study is to monitor the small and medium-sized river and lakes through satellite altimetry and develop continuous estimation of discharge from rainfall-runoff based hydrologic model in the same region. The hypothesis is that satellite altimetry provides high accuracy measurements of water level fluctuation, which shall be complementary to the estimated discharge from the hydrologic model or the altimeter data could be assimilated into the model.

## 2. Theoretical Background

### 2.1. Satellite Radar Altimetry

#### 2.1.1. Historical Review

Williamstown Symposium in 1969 mentioned the pioneering recommendation to build a satellite altimetry system for the first time (McGoogan, 1975). The symposium summarized a detailed design for a satellite radar altimetry mission and requested the National Aeronautics and Space Administration (NASA), primarily the Electronic Research Center to build and commission the proposed satellite mission with the principal mission objective of measuring the shape of the Earth (Kaula, 1970). Among the minimum recommended characteristics in the proposed satellite altimetry missions were: 1 m accuracy, 10 seconds measurement interval, 1 year lifetime, circular orbit, not sun or moon-commensurate and preferably high orbital inclination. All these characteristics matched closely with the subsequent series of developed and launched altimeter technologies, such as that existed in Skylab (1973), GEOS-3 (1975-1978) and Seasat (1978) (Townsend, 1980). With advanced instruments and a higher precision orbit satellite, radar altimetry kicked off its mission to support various studies in Geodesy, Oceanography, Geophysics, Glaciology and Continental Hydrology (Benveniste, 2011). The next generation of satellite radar altimeter missions includes the US Navy Geosat mission launched in 1985 (Kilgus, 1988), the European Space Agency (ESA) ERS-1 mission in 1991, its predecessor missions ERS-2 (1995) and Envisat (2002), as well as joint NASA and CNES mission of the first dual-frequency radar altimeter, TOPEX/Poseidon, which is launched in 1992. With minimum publication, the Russian mission GEOIK operated between 1984 and 1996 with a 9.5 GHz radar altimeter and a set of other spaceborne geodetic instruments onboard of the satellite. The Geosat follow-on mission was launched in 1998 to continue the Geosat. TOPEX/Poseidon mission is the start of a series of accurate radar altimeter missions dedicated for the primary scientific objectives to the monitoring of global sea level and study of large-scale general ocean circulation. In particular, TOPEX/Poseidon is the first satellite altimetry mission with radial orbit accuracy at the level of under 5 cm RMS, a dual-frequency altimeter system which removes the first order ionosphere delay, and a downward looking radiometer to measure the integrated water vapor column along the altimeter radar path (Benveniste, 2011). The development of satellite radar altimetry missions during the last decade includes Jason-1, Envisat (Roca *et al.*, 1999) and Jason-2, which is the predecessor of Jason-1, launched in 2001, 2002 and 2008, respectively. The more recent radar altimeter missions include CryoSat-2 (launched in 2010) carrying an altimeter instrument which operates in three modes: the Low Resolution Mode (LRM or same as pulse-limited conventional nadir altimeters), the Synthetic Aperture Radar (SAR) and the SAR Interferometry (SARIn) modes. The most recent launch of altimetry satellites is the Chinese HaiYang-2A ocean observation satellite in 2011 (Jiang *et al.*, 2012) and the CNES and Indian Space Agency mission, AltiKa (single frequency radar altimeter at Ka-band or 35 GHz) on board of SARAL (Satellite with ARGOS and ALtiKa) in February 2013 as a joint mission by the French and Indian Space Agencies (Vincent *et al.*, 2000). NASA and CNES are currently developing the two dimensional observation systems on

the Surface Water Ocean Topography (SWOT), which will provide a high resolution sea or water surface height and slope measurements and is capable of measuring sub-mesoscale ocean variability, and river storage change and discharge. SWOT will be able to measure sea surface heights on a 2 x 2 km grid with accuracy better than 0.5 cm and terrestrial water heights of lakes and river as narrow as 100 m with accuracy of 10 cm and a slope accuracy of 1 cm/1 km (Fu *et al.*, 2012).

**Table 2.1** Satellite Radar and Laser Altimetry Missions

Mission/Sensor	Operation Period	Accuracy	Inclination	Altitude	Repeat Period
Skylab	1973 - 1974	> 100 cm		435 km	N/A
GEOS-3	Apr 1975 – Dec 1978	60 cm	115°	840 km	N/A
Seasat	Jul 1978 – Oct 1978	10 cm	108°	800 km	3, 17 days
Geosat GM & ERM	Mar 1985 – Jan 1990	4 cm	108°	800 km	23, 17 days
ERS-1	Jul 1991 – Jun1995	4 cm	98.5°	785 km	3, 35, 168 days
TOPEX/Poseidon	Aug 1992 – Dec 2005	2 cm	66°	1336 km	9.9 days
ERS-2	Apr 1995 – Jun 2003	3 cm	98.5°	785 km	35 days
Geosat Follow-On	May 1998 – Sep 2008	3.5 cm	108°	800 km	17 days
Jason-1	Dec 2001 - 2013	1.5 cm	66°	1336 km	9.9 days
Envisat	Mar 2002 - 2012	2 cm	98.5°	785 km	35 days
ICESat-1	Jan 2003 – Aug 2010	1.6 cm	94°	600 km	8.9, 91 days
Jason-2	June 2008 - Present	2.5 cm	66°	1336 km	9.9 days
Cryosat-2	Apr 2010 - Present	1.2 cm	92°	717 km	30 days
HY-2A	Aug 2011 - Present	N/A	99.3°	963.6 km	14 days
SARAL/AltiKa	Feb 2013 - Present	N/A	98.5°	800 km	35 days
Sentinel-3 2-satellite constellation	Planned 2013	N/A	98.6°	814 km	27 days
Jason-3	Planned 2014	N/A	66°	1336 km	9.9 days
ICESat-2	Planned 2016	N/A	94°	600 km	91 days
Jason-CS	Planned 2017	N/A	66°	1336 km	9.9 days
SWOT	Planned 2019	N/A	70-80°	800-1000 km	15-25 days

### 2.1.2. Satellite Altimetry Measurement

A satellite altimeter consists of a radar signal transmitter, a receiver and an ultra-stable oscillator (USO) or clock on board (Stewart, 1985). As shown in the Figure 2.1 and its nature as a ranging system, the satellite altimeter transmits microwave pulses to measure the travel time between microwave pulse emission and echo reception; then estimates the range (*i.e.* distance between the antenna and the Earth's surface) (McGoogan, 1975; Rees, 1990). Therefore, the main observable in the system is a time series of the received power distribution of returned pulses.



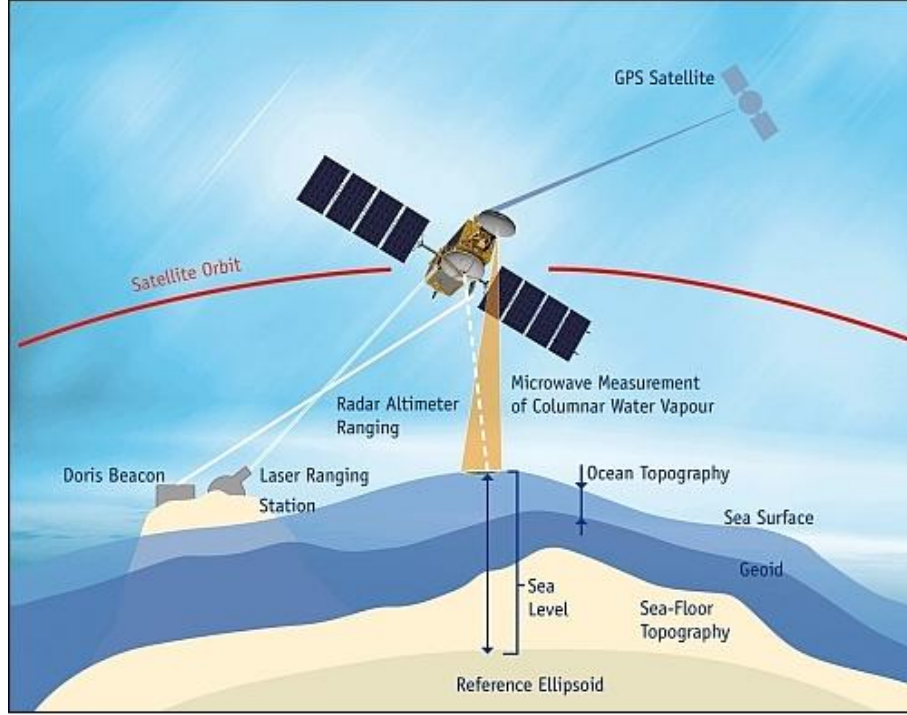


**Figure 2.1** Concept of satellite radar altimeter measurement  
(Courtesy of EUMETSAT & ESA)

The distance  $a$  from the satellite to the mean sea level is calculated based on the travel time of the radar signal's round trip as follows (Shum *et al.*, 1995):

$$a = \frac{c\Delta t}{2} - \sum_j \Delta a_j \quad (2.1)$$

Where  $c$  is the speed of light in vacuum ( $3 \times 10^8$  m/s),  $\Delta t$  is the one-way travel time,  $\Delta a_j$ ,  $j = 1, \dots$  are corrections for various components. The corrections are categorized into propagation corrections (*e.g.* dry and wet troposphere, ionospheric electrons), instrument corrections (*e.g.* tracker bias, Doppler shift, oscillator drift, etc.), surface corrections (*e.g.* inverse barometer and electromagnetic bias) and geophysical corrections (*e.g.* orbit, various tides, and tidal loading). If  $b$  is the actual ellipsoidal height of the measured surface and  $h$  is the satellite altitude with respect to the same ellipsoid, Equation (2.1) can be modified to represent the actual ellipsoidal height of the surface measured as follows.

$$b = h - a = h - \frac{c\Delta t}{2} + \sum_j \Delta a_j \quad (2.2)$$

To be consistent with the explanation of corrections below, the geometrical relationships between the satellite radar altimetry with the Earth surface to be monitored are illustrated in Figure 2.2 and can be expressed as follows (Seeber, 2003):

$$h = N + H + \Delta H + a + d \quad \text{With} \quad b = N + H + \Delta H \quad (2.3)$$

With

$h$	=	ellipsoidal height of satellite
$N$	=	geoidal height
$H$	=	sea surface topography
$\Delta H$	=	instantaneous tidal effects
$a$	=	altimeter measurements
$d$	=	orbit discrepancy

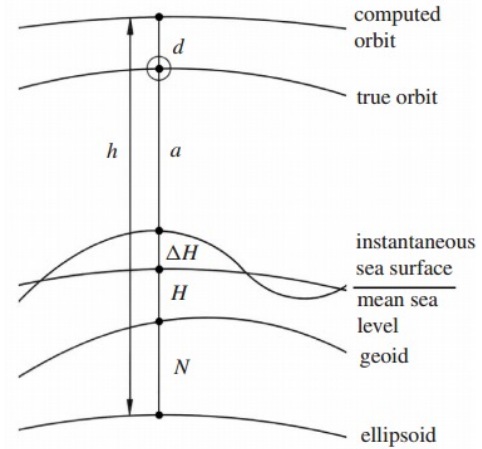


**Figure 2.2** Geometrical relationships in satellite altimetry (excerpt from Seeber 2003)

### 2.1.3. Error Corrections

The altimeter range measurement described above is subject to various sources of errors; therefore a set of corrections needs to be applied as described below.

**Table 2.2** Corrections involved for satellite radar altimetry measurement (Chelton *et al.*, 2001 and ESA, 2013a)

Propagation Corrections	Instrument Corrections
<ul style="list-style-type: none"> <li>• Dry troposphere</li> <li>• Wet troposphere</li> <li>• Ionosphere</li> </ul>	<ul style="list-style-type: none"> <li>• Tracker Bias</li> <li>• Waveform Sampler Gain Calibration Biases</li> <li>• Antenna Gain Pattern</li> <li>• Automatic Gain Control Attenuation</li> <li>• Doppler Shift</li> <li>• Range Acceleration</li> <li>• Oscillator Drift</li> <li>• Pointing Angle/Sea State</li> </ul>
Geophysical Corrections	
<ul style="list-style-type: none"> <li>• Solid earth tide</li> <li>• Pole tide</li> <li>• Geocentric Ocean Tide Correction (consists of Ocean Tide and Tidal Loading)</li> </ul>	
Surface Corrections	
<ul style="list-style-type: none"> <li>• Electromagnetic Bias</li> <li>• Inverse Barometer</li> </ul>	

#### (1) Propagation Corrections

This correction is essentially required, considering that the radar pulses travel for hundreds up to thousands of kilometers before they reach the Earth's surface and pass through the Earth's atmosphere that reduces their travel velocity. Dry gases, water vapor and free electrons are three main components of the atmosphere that obstruct radar pulse travel (Chelton *et al.*, 2001). The atmospheric corrections include ionospheric delay, dry tropospheric delay and wet tropospheric delay. Further, Chelton *et al.* (2001) stated that

the ionospheric refraction depends on the existence of free electrons along the line of the radar signal transmission and reception. In addition, this effect also depends on the frequency of the radar signals. Tropospheric refraction is not related to the radar frequency and categorized into the dry and wet tropospheric corrections. The dry tropospheric refraction, which mainly driven by the sea-level pressure (in mbar), is currently the largest correction compared to all atmospheric adjustments (Chelton *et al*, 2001). Since the measurement of the sea-level pressure is scarce, this correction is usually modeled through a global analysis such as the European Center for Medium-range Weather Forecast (ECMWF). The wet tropospheric correction is mainly calculated through the vertically integrated water vapor presence (in g/cm<sup>2</sup>). In addition, these effects can be modeled with measurement at two frequencies, such as implemented in TOPEX/Poseidon and Jason-1/-2 (Seeber, 2003).

## (2) Surface Corrections

The returned waveform shape received by the altimeter is not necessarily representing the actual sea surface height distribution within the altimeter footprint; rather, it is defining the distribution of the specular reflectors. This difference is called the electromagnetic (EM) bias, which subjects to correction such as the one developed by Hevizi *et al* (1993) and Rodriguez and Martin (1994a). Aside from this bias, the difference between the mean and the median of the scattering surface also caused a bias that is called skewness bias. These two biases (EM and skewness) comprise the total sea-state bias. Gaspar and Florens (1998), Vandemark *et al.* (2002); Hausman and Zlotnicki (2010) provided extended discussion on the methods in estimating these biases.

The variation of the sea surface height is also due to atmospheric pressure variation, which is known as atmospheric loading (Wunsch and Stammer, 1997, McCarthy and Petit, 2004). The inverted barometer correction compensates this variation in the process of satellite altimetry measurements (ESA, 2013b).

## (3) Geophysical Corrections

The state of sea surface depends on a number of geophysical phenomena that directly affect the accuracy of range measurements through satellite altimetry. The one with the largest magnitude is the ocean tide, which is driven by the attraction of the Sun and Moon. The magnitude of this variation varies from 15–20 cm to 1 m in the middle of an ocean (ESA, 2013a). This variation can be eliminated through a global ocean tide that comprised of eight major components with accuracy as high as 2.6 cm to date (LeProvost, 2001). Solid earth tide, which is generated by the movement of the Earth's crust, is the second largest contributor to the sea surface variation with the magnitude around 50 cm (ESA, 2013a). Tidal loading is the third geophysical effect that is generated by self-gravitation due to tides acting on Earth's surface. Similar to the preceding two geophysical corrections, the effect of tidal loading is removable through a global model. The last and the least geophysical factor affecting satellite altimetry measurement is the pole tide due to the centrifugal effect of polar motion (McCarthy and Petit, 2004). This effect also can be modeled once the Earth's Love numbers and a time series of perturbation of the Earth's rotation axis are known (Wahr, 1985). In addition to these four

geophysical effects, the high-frequency wind also needs to be corrected through available ocean models, for instance the one developed specifically to address wind effects (Witter and Chelton, 1991).

**Table 2.3** Typical magnitude of total atmospheric corrections and sea-state bias as applied to Topex/Poseidon range estimates at different latitudes (after Chelton *et al.*, 2001)

Range Corrections	Total (cm)	Method of Calculation
<b>Dry Tropospheric Corrections</b> <ul style="list-style-type: none"> <li>Latitude 30°N to 30°s</li> <li>Latitude 30 to 60</li> </ul>	226 226	The wet tropospheric correction is $\Delta R_{dry}(cm) \approx 0.223P_0$ where $P_0$ is sea-level pressure in mbar with uncertainty of less than 5 mbar in operational weather analysis.
<b>Wet Tropospheric Corrections</b> <ul style="list-style-type: none"> <li>Latitude 30°N to 30°s</li> <li>Latitude 30 to 60</li> </ul>	24 10	The dry tropospheric correction is $\Delta R_{vap}(cm) \approx 6.4V$ where $V$ is the vertically integrated water vapor in $g/cm^2$ with uncertainty of 0.15 $g/cm^2$ in estimates of $V$ from a three-frequency microwave radiometer.
<b>Ionospheric Refractions</b> <ul style="list-style-type: none"> <li>Latitude 30°N to 30°s</li> <li>Latitude 30 to 60</li> </ul>	12 6	The ionospheric range correction for $K_u$ -band radar frequency of 13.6 GHz is $\Delta R_{ion}(cm) \approx 0.22E$ where $E$ is the vertically integrated electron contents in Total Electron Content Unit ( $TECU \equiv 10^6 electrons/cm^2$ ).
<b>Sea-state Bias</b> <ul style="list-style-type: none"> <li>Latitude 30°N to 30°s</li> <li>Latitude 30 to 60</li> </ul>	4 6	The sea-state bias correction is $\Delta R_{ssb}(cm) \approx 0.02H_{1/3}$ where $H_{1/3}$ is significant wave height in cm. The estimated uncertainty assumes an uncertainty of 1% of $H_{1/3}$ in sea-state bias correction and a typical wave height of $H_{1/3} = 2m$ .

#### (4) Instrument Corrections

Besides the external errors described above, the satellite altimeter also subject to a number of errors originated by the instrument operational settings as extensively explained in Chelton *et al.* (2001) and briefly summarized here:

- (1) Doppler shift is a slight difference in the returned frequency as compared to the transmitted frequency, due to a displacement of either the satellite or the target on the Earth surface. This error is commonly corrected through the implementation of Doppler Slope Correction, as regularly carried out for Envisat Radar Altimeter (Blarel and Legresy, 2012)
- (2) Acceleration error is caused by the vertical acceleration of the satellite relative to the Earth's surface and overlooked by the standard  $\alpha - \beta$  tracker. This error is compensated by the algorithms such as the inverse filtering applied for TOPEX (Rodriguez and Martin, 1994b) or the proposed twice-filtering algorithm (Xu and Liu, 2007).
- (3) Oscillation drift error is due to slight drift in the oscillator frequency on board of the satellite. This error should be compensated by adding the range difference as calculated from the Ultra Stable Oscillator correction as provided by the reference atomic clock in the ground stations, such as those of Envisat and ERS (*e.g.* ESA, 2013c).

- (4) Pointing angle contributes most of overall magnitude in the instrumental error. This error is caused by the maneuver of the platform that hinders the altimeter from fixed pointing normally to the Earth's surface (Wingham, 1988). This error is corrected through various embedded algorithms that regularly implemented during the scientific processing of the altimeter data by the ground stations. Various methods have been introduced to reduce the errors due to satellite pointing angle, including the early work of Brown (1977), Wingham (1988) until the recent development proposed by Amarouche *et al.* (2004) that combine the second order model of altimeter waveform and a 4-parameter maximum likelihood estimator (MLE4).

Considering all corrections above and referring to notations in Figure 2.2, the relationship between the corrected distance between the sea (or any other water bodies) surface ( $a_c$ ) and the instantaneous sea surface height (SSH) ( $b$ ) can be inferred through the following (Shum *et al.*, 1995 and ESA, 2011).

$$a_c = a + \Delta a_{wt} + \Delta a_{dt} + \Delta a_{iono} + \Delta a_{ssb} + \Delta a_{instr} \quad (2.4)$$

The instantaneous sea surface height (SSH), which is the height of the sea surface relative to the reference ellipsoid, is then expressed as:

$$SSH = h - a_c \quad (2.5)$$

Since the sea level anomaly (SLA), is the main variable of interest in satellite altimetry observation, the relationship with the geophysical corrections is given as (ESA, 2011):

$$SLA = SSH - (N + H) - \varepsilon - \Delta a_{otide} - \Delta a_{etide} - \Delta a_{ptide} - \Delta a_{tload} - \Delta a_{ib} \quad (2.6)$$

where

$a_c$	: Corrected range	$SSH$	: Sea Surface Height
$a$	: Measured range	$SLA$	: Sea Level Anomaly
$N + H$	: Mean Sea Surface	$\varepsilon$	: Measurement bias
$\Delta a_{wt}$	: Wet tropospheric correction	$\Delta a_{otide}$	: Ocean tide correction
$\Delta a_{dt}$	: Dry tropospheric correction	$\Delta a_{etide}$	: Earth tide correction
$\Delta a_{iono}$	: Ionospheric correction	$\Delta a_{ptide}$	: Pole tide correction
$\Delta a_{ssb}$	: Sea surface bias correction	$\Delta a_{tload}$	: Tidal loading correction
$\Delta a_{instr}$	: Instrument corrections	$\Delta a_{ib}$	: Inverted barometer correction

#### 2.1.4. Waveform Retracking

Satellite altimeter transmits the microwave radar pulses to the Earth's surface, which correspondingly reflect these pulses back to the altimeter. The returned radar pulses, also known as *echoes*, are recorded in a range of *gates* or bins, the so called the *waveform*, which essentially represents the magnitude of the echoes relative to time. The waveform has a straight leading edge that indicates the behavior of the returned radar

pulses after initial contacts with the Earth's surface (Ridley and Partington, 1988). Over calm water surfaces (Figure 2.3, left panel), the leading edge of the waveform suddenly rises as soon as the radar signal hits calm water. The magnitude of this rising echo is much greater compared to the rising leading edge of the radar pulses over rough water (Figure 2.3, right panel).

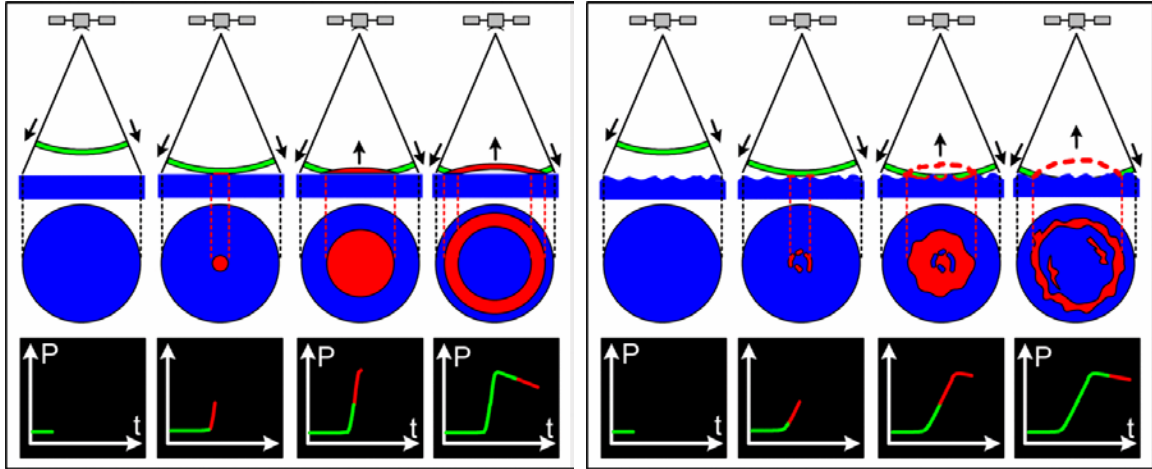


**Figure 2.3** Waveform variation over time on calm (left panel) and rough (right panel) ocean water surface (courtesy of CNES)

The waveform is the basis for the whole process of range measurement conducted by satellite altimetry. Beside the time difference that records the round trip travel time of the radar signal, the slope of the leading edge facilitates the calculation of the Significant Wave Height (SWH) that is influential for Oceanographic applications while the backscatter coefficient, along with the shape of the waveform indicate the characteristics of the Earth's surface (Ridley and Partington, 1988).

The pulse and shape of the waveform provides additional information about the Earth's surface. According to Brown (1977), echo waveforms that represent ocean surfaces possess shapes that can be differentiated from other surfaces on Earth. Over a calm ocean surface, there is a sudden hike in the waveform when the leading edge of the radar signal hits the ocean surface while over a rough ocean surface the peak develops gradually. These characteristics then allow scientists to analyze and estimate ocean wave height from this parameter. Regarding the non-ocean water bodies, Rapley *et al.* (1987) comprehensively reported the radar return of SEASAT altimetry over various non-ocean surfaces and confirmed this hypothesis. Over the large lakes, which are assumed to have similar characteristics with calm oceans, the radar return pattern (waveform) shows similar with those of the ocean (see Figure 2.4), with an addition of narrow-peaked waveforms. The waveform becomes irregular or complex (*e.g.* contains several peaks) when the altimeter signals are interfered with by land surface (*e.g.* Birkett, 1998, Berry *et al.*, 2005).

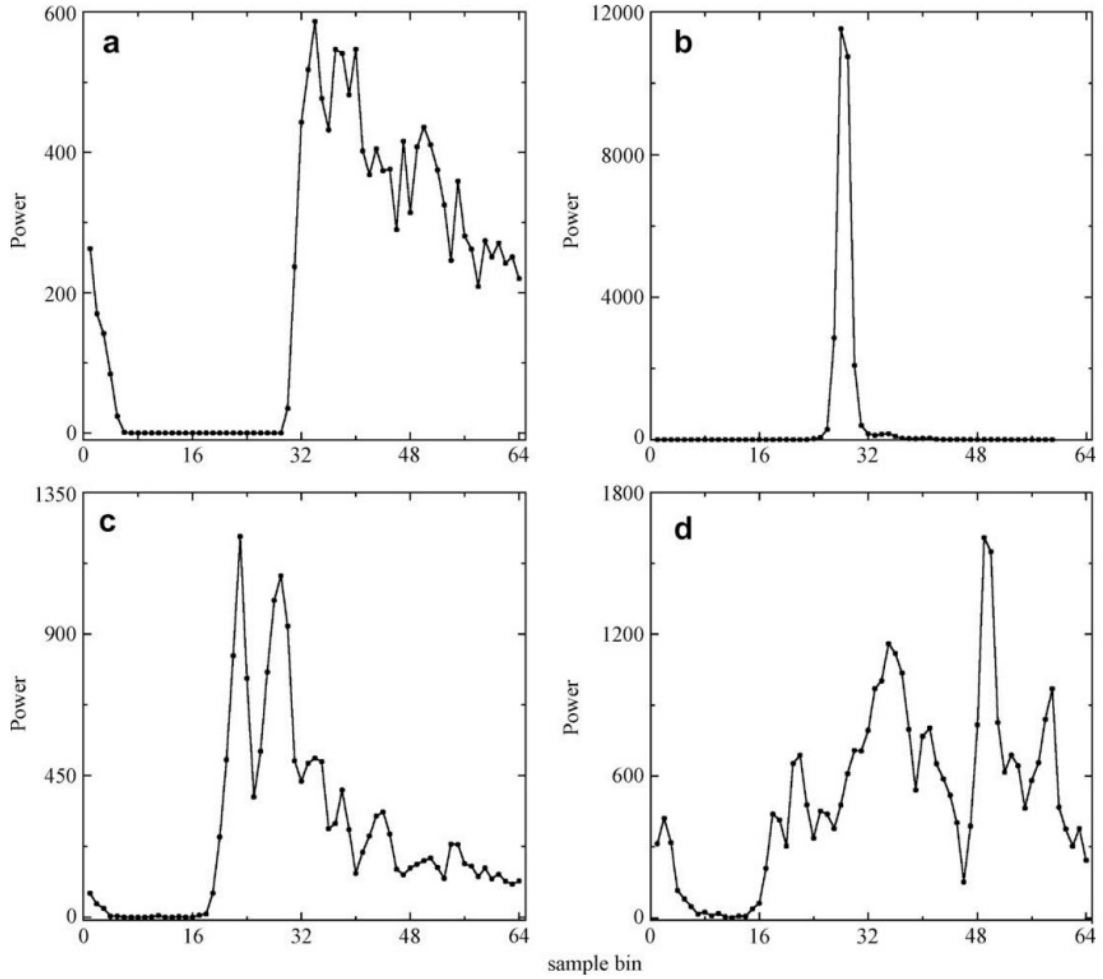


**Figure 2.4** Examples of returned pulse waveform for (a) ocean (b) ice (c) multi peak waveform and (d) complex waveform (excerpt from Bao *et al.*, 2009)

The waveform of the returned radar pulses represents a time series of the mean returned power and can be separated into three main parts (Rodriguez and Chapman, 1989) as illustrated in Figure 2.5:

- The thermal noise, which represents a flat power level prior to any interaction between the radar pulses and the Earth’s surface.
- The trailing edge, which represents dropped return power as the radar pulses depart from the Earth surface.
- The leading edge, which comprises the essential part of the waveform and represents the peak return power as reflected by the Earth surface. The leading edge also could infer the distance between the satellite altimeter and the observed Earth surface.

An onboard “tracking” of the returned radar signal initially determines the range between the satellite altimeter and the Earth’s surface by keeping the leading edge at the center of the waveform sample gates (Brenner *et al.*, 1990). A uniform range interval, of which the returned radar signal is averaged, is called the “gate”. Since the tracking algorithm aims at keeping the leading edge at a specific and constant nominal gate (*i.e.*

gate/bin 32.5, also known as the track point) and specific amplitude, this method is also called “gate tracking algorithm” (Jensen, 1999). As illustrated in the right panel of Figure 2.5 below, the thermal noise, automatic gain control, and the early, middle and late tracking gates of TOPEX altimeter system are labeled as N, AGC,  $E_n$ ,  $M_n$  and  $L_n$ , respectively. The gate value may differ from one satellite mission to another.

The bottom part of the right panel of Figure 2.5 shows a division of the container of the returned radar signals into 64 bins or gates. The automatic gain control (AGC) gate range is the instrumental part in the onboard tracking since it defines the frame to adjust the center of waveform’s leading edge to fit the tracking gate at bin 32.5 (Jensen, 1999).

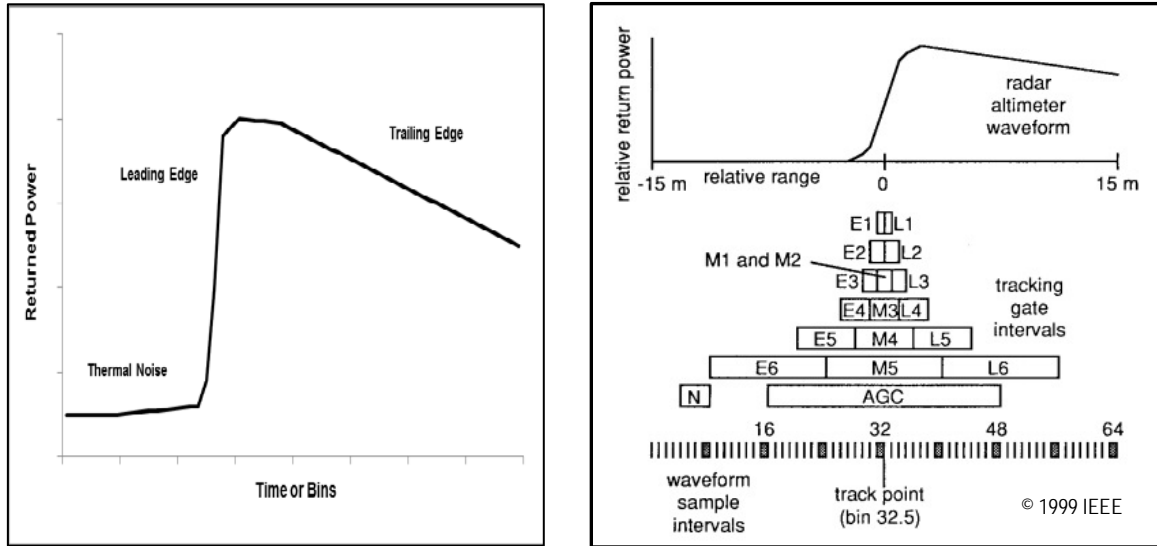


**Figure 2.5** Schematic diagram of an average return waveform (left) and definitions of tracking gates for TOPEX altimeter (right, excerpt from Jensen, 1999)

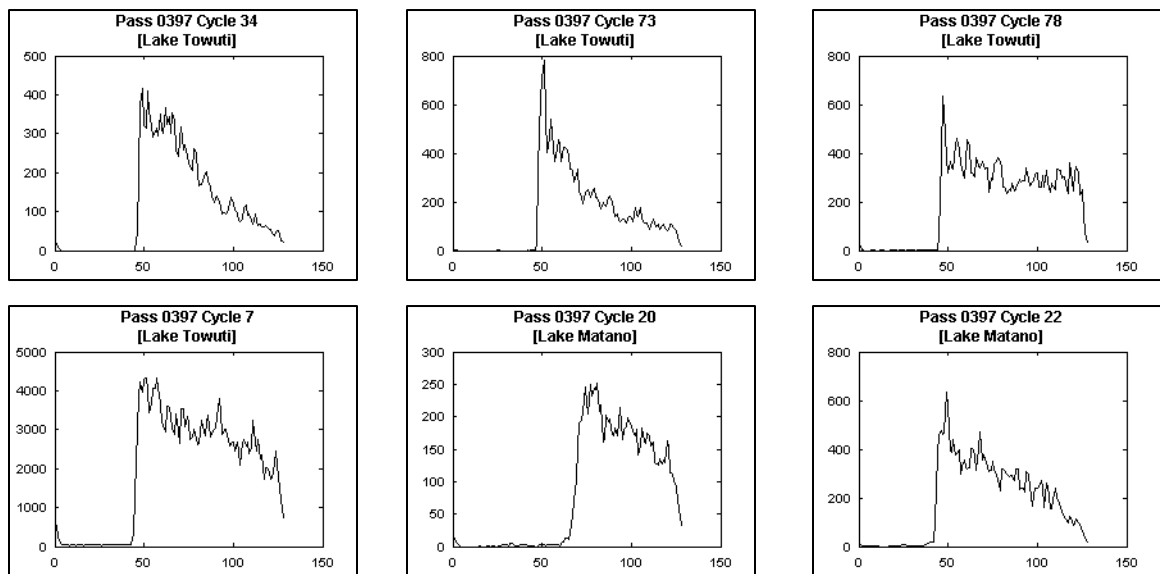


**Figure 2.6** Some examples of real waveform pattern over tropical lakes



Quantitatively, the time series of the mean returned power of the radar signals at an instantaneous time  $W(t)$  can be inferred by the flat surface impulse response  $P_{FS}(t)$ , the probability density function (PDF) of the radar observed surface elevation  $q_s(z)$  and the radar altimeter power point target response  $p_r(t)$ , through the following convolution (Brown 1977, Hayne 1980, Rodriguez 1988):

$$W(t) = P_{FS}(t) \otimes q_s(z) \otimes p_r(t) \quad (2.7)$$

The flat surface impulse response  $P_{FS}(t)$ , is defined through the following relationship, which considering the Earth's curvature and assuming Gaussian distribution of the antenna gain (Rodriguez, 1988).

$$\begin{aligned} P_{FS}(t) &= A \exp(-\alpha t) I_0(\beta t^{1/2}) U(t) \\ \alpha &= \frac{\ln 4}{\sin^2(\theta/2)} \frac{c}{h} \frac{1}{1 + h/R} \cos(2\xi) \\ \beta &= \frac{\ln 4}{\sin^2(\theta/2)} \left[ \frac{c}{h} \frac{1}{1 + h/R} \right]^{1/2} \sin(2\xi) \end{aligned} \quad (2.8)$$

with

$A$	: Scaling constant	$R$	: Radius of the Earth
$I_0$	: Modified Bessel function of the second kind	$\theta$	: Antenna half-power beamwidth
$U(t)$	: Unit step function	$c$	: Speed of light
$h$	: Altimeter height above the mean ocean surface	$\xi$	: Off-nadir pointing angle

The scaling constant (A) actually can be defined through the knowledge of several radar constants, as given in the following equation (Hayne, 1980):

$$A = \frac{G_0^2 \lambda^2 c \sigma^\circ(0)}{4(4\pi)^2 L_p h^3} \exp\left(-\frac{4}{\gamma} \sin^2 \xi\right) \quad (2.9)$$

with

$\lambda$	: radar wavelength	$G_0$	: Radar antenna boresight gain
$\sigma^\circ(0)$	: surface backscattering cross section at nadir	$L_p$	: Two-way signal propagation loss

The Modified Bessel function of the second kind  $I_0(\beta t^{1/2})$  could be estimated by  $\exp(\beta^2 t/4)$  with negligible error (Rodriguez, 1988), so  $P_{FS}(t)$  can be simplified into:

$$P_{FS}(t) = A \exp[-(\alpha - \beta^2 t/4)t] U(t) \quad (2.10)$$

The point target response (PTR) for linear and ideal radar signals is given as follows (Ulaby *et al.*, 1981, Rodriguez, 1988)

$$p_\tau(t) \sim \frac{\sin^2[(at/2)(T - |t|)]}{(at/2)^2} \quad -T \leq t \leq T \quad (2.11)$$

with

$2T$  : Radar pulse length       $a$  : Constant related to the radar bandwidth

The specular point PDF in spatial domain  $q_s(z)$  is formulated as (Rodriguez, 1988):

$$q_s(z) = \frac{1}{(2\pi)^{1/2}\sigma} \exp\left(-\frac{\eta^2}{2}\right) \left[1 + \frac{\lambda}{6}(\eta^3 - 3\eta)\right] \quad (2.12)$$

$$\eta = \frac{z - z_T}{\sigma}$$

with

$\sigma$  : Ocean surface standard deviation       $z$  : Height above mean ocean surface ( $z = 0$ )  
 $\lambda$  : Ocean surface skewness       $z_T$  : Tracker bias, which represents the altimeter height estimation error

When necessary, the specular point PDF  $q_s(z)$  presented in equation 2.12 can also be expressed in time domain  $q_s(t)$ , by changing of variables (Rodriguez, 1988):

$$t = -2z/c \quad (2.13)$$

Some of the actual sea state parameters such as the significant wave height (SWH), altimeter height and the skewness of the sea surface can be estimated through an inverse solution of the specular point PDF. Rodriguez and Chapman (1989) offered the de-convolution method to define those parameters from PDF through a least square approach. Noting  $W(t)$  as  $y$ , equation (2.7) can be expressed as matrix relationship:

$$y = Mx \quad \text{where} \quad y = W(t) \quad M = P_{FS}(t) \otimes p_\tau(t) \quad \text{and} \quad x = q_s(z) \quad (2.14)$$

The regular least-square algorithm to inversely calculate  $x$  is as follow:

$$x = (M^T M)^{-1} M^T y \quad (2.15)$$

Due to its sensitivity to noise, an additional algorithm is needed to “smooth” this deconvolved function (Rodriguez and Chapman, 1989). This is obtained by introducing a constraint that involves the second derivative (Twomey, 1963), so that the above least square algorithm becomes:

$$x = (M^T M + \gamma B)^{-1} M^T y \quad (2.16)$$

With  $\gamma$  is a variable parameter and B is the second derivative operator as follows:

$$B = \begin{bmatrix} 1 & -2 & 1 & 0 & 0 & . & . & . \\ -2 & 5 & -4 & 1 & 0 & . & . & . \\ 1 & -4 & 6 & -4 & 1 & 0 & . & . \\ 0 & 1 & -4 & 6 & -4 & 1 & 0 & . \\ . & . & . & . & . & . & . & . \end{bmatrix} \quad (2.17)$$

Further details on the waveform gate tracking are revisited by Jensen (1999), along with the proposition of its extension. It is known that the waveform gate tracking algorithm was built with the assumption that the behavior of the returned radar signals always follow those open ocean backscatter characteristics. However, the onboard waveform gate tracking may overlook the change of range and backscatter due to change of Earth's surface especially on the undulating surface, hence misses the leading edge of the waveform (Martin *et al.*, 1983), which is known as “loss of lock or loss of track” (Scott *et al.*, 1994), therefore, introduces errors in the range estimation. To overcome this situation, an additional tracking effort called “retracking” is introduced, which minimizes this erroneous estimation by fitting the actual waveform into a model of averaged waveform and then re-measure the distance between the leading edge and the center of range window, convert the result and add back to the estimated range (Martin *et al.*, 1983; Ridley and Partington, 1988; Bamber, 1994). This procedure is regularly carried out after the data are telemetered to the ground station, which separates it from the regular “tracking”.

#### 2.1.5. Non-Ocean Surface Waveform Retracker

Considering the different characteristics of the non-ocean surfaces, a number of waveform retracking methods were developed to address those differences. Among the retracker developed for this purpose are volume scattering retracker (Davis, 1993), NASA  $\beta$  – retracker (Zwally, 1996), surface / threshold retracker (Davis, 1997), Offset Center of Gravity (OCOG) (Wingham *et al.*, 1986; Bamber, 1994), also known as Ice-1, Ice-2 (Legresy and Remy, 1997) and Sea Ice retracker (Laxon, 1994). In this section, the first three retracker are described briefly, while the latter four retracker are described in detail since they are applied in this research.

##### (1) Surface/Volume Scattering Retracker

Subsurface and surface volume scattering evidently influence the altimeter return waveforms from the ice sheets, and it is deemed necessary to account this effect to improve the accuracy of cryosphere topographic analysis (Ridley and Partington, 1988). In the same study, Ridley and Partington (1988) developed a model that based on the Rayleigh backscatter to describe the volume scattered in addition to the surface scattered altimeter waveforms. A later development by Davis (1993) then proposed a combined surface and volume-scattering model that makes use of the thermal noise, gate number and the maximum amplitude of the waveform.

## (2) NASA $\beta$ – Retracker Version 4

In a comprehensive study on the Seasat-1 over the Antarctic and Greenland, Martin *et al.* (1983) proposed the so-called  $\beta$  – retracker that consists of 5 parameters functions to fit single-ramp waveforms and 9 parameters to fit double-ramp waveforms.

The list of parameters and the schematic diagrams are described below.

- $\beta_1$  : The thermal noise (or DC level) of the waveform
- $\beta_2$  : Waveform amplitude
- $\beta_3$  : Mid-point of the leading edge which marks the correct time delay
- $\beta_4$  : Slope of the leading edge which is related to SWH
- $\beta_5$  : Slope of the trailing edge which is related to the scattering at the footprint

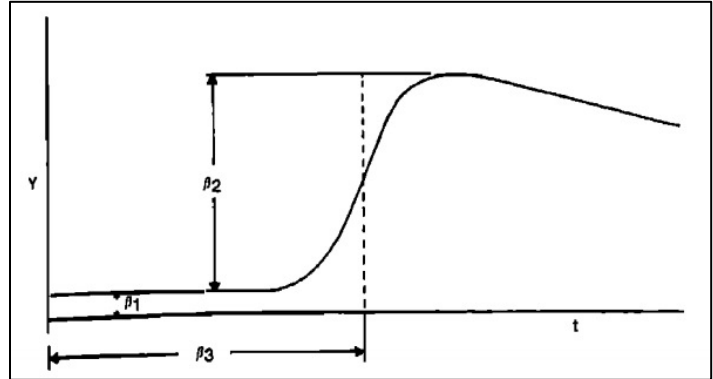


**Figure 2.7** Five parameters in NASA  $\beta$ - retracker (excerpt from Martin *et al.*, 1983)

- $\beta_5$  : Waveform amplitude of the second ramp
- $\beta_6$  : Mid-point of the leading edge which marks the correct time delay for the second ramp
- $\beta_7$  : Slope of the leading edge which is related to SWH for the second ramp
- $\beta_8$  : Slope of the trailing edge for the second ramp
- $\beta_9$  : Slope of the trailing edge for the first ramp

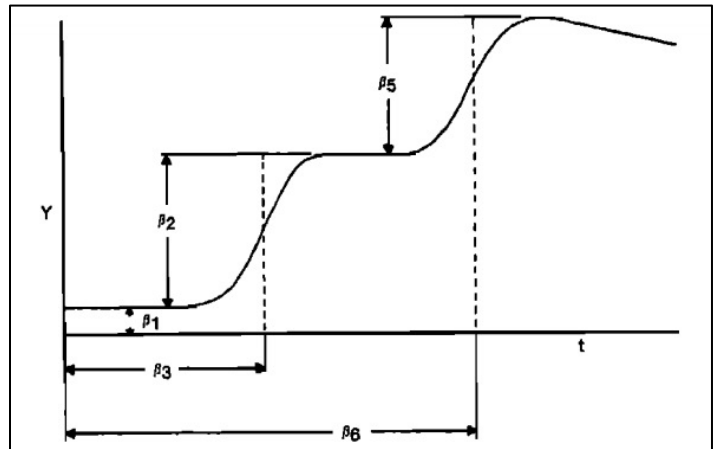


**Figure 2.8** Nine parameters in NASA  $\beta$ - retracker (excerpt from Martin *et al.*, 1983)

## (3) Threshold Retracker

The development of threshold retracker algorithm was initially aims at studying ice sheet elevation change. The basic threshold retracker considers a certain percentage value of the maximum waveform amplitude to define the threshold level, which introduces some bias due to the variable thermal noise level prior to the interaction between the radar signal and the Earth's surface (Davis, 1997). This algorithm addressed such problem by computing and removing the thermal noise and considering only the

amplitude of the returned radar signal thereafter. The recommended threshold levels for general ice-sheet elevation change studies, combinations of surface and volume scattering and domination of surface scattering are 10%, 20% and 50%, respectively (Davis, 1997).

(4) Offset Center of Gravity (OCOG) or Ice-1 Retracker

This algorithm, first proposed by Wingham *et al.* (1986), was specifically developed to study the ice sheet topography using ERS-1 altimetry data and the complex pattern of the returned radar signals due to speckle noise generated by varying ice-sheet topographic surfaces (Wingham *et al.*, 1986, Bamber, 1994).

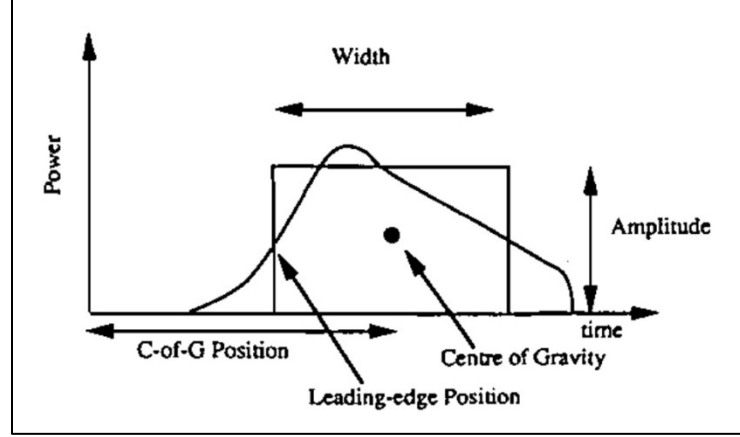


**Figure 2.9** Schematic diagram of OCOG algorithm components (Bamber, 1994)

A detailed waveform analysis is tedious and requires prior information on the topographic surfaces. Therefore, this algorithm assumes a flat, homogeneous and diffuse surface with normal distribution of small slopes and introduces the following equations to calculate the center of gravity (COG), amplitude and width of an imaginary box (see Figure 2.9) that contains all waveform samples (Wingham *et al.*, 1986; Bamber, 1994).

$$\text{Centre of gravity (COG)} = \frac{\sum_{n=1+aln}^{n=64-aln} n y^2(n)}{\sum_{n=1+aln}^{n=64-aln} y^2(n)} \quad (2.18)$$

$$\text{Amplitude} = \sqrt{\frac{\sum_{n=1+aln}^{n=64-aln} y^4(n)}{\sum_{n=1+aln}^{n=64-aln} y^2(n)}} \quad (2.19)$$

$$\text{Width} = \left( \sum_{n=1+aln}^{n=64-aln} y^2(n) \right)^2 / \sum_{n=1+aln}^{n=64-aln} y^4(n) \quad (2.20)$$

Here  $y$  is the value of sample at the  $n^{th}$  bin and  $aln$  is the number of aliased bins at the beginning and end of the waveform. The adjusted leading edge position (LEP) is then:

$$LEP = COG - \frac{Width}{2} \quad (2.21)$$

The ocean center of gravity (OCOG) is a simple but robust retracker, which requires only the statistics of the waveform samples and does not require any model; hence it is later called model-free retracker. In addition, the OCOG retracker builds the basic algorithm towards Ice-1 retracker that becomes standard waveform retracking for Envisat RA-2 altimeter (Resti, 1999). It is well suited to surfaces with rapid changes, for instance the continental ice, but its use for accurate range retrieval is limited due to its formulation that is not related to any physical properties of the scattering surfaces.

#### (5) Ice-2 Retracker

To understand the cryosphere dynamic, Ice-2 retracker was developed based on the principle of fitting the waveform shape using the Brown (1977) model in order to optimize ocean-like Ku-and S-band radar signal returns from the continental ice-sheet. Brown (1977) inferred the returned power waveform as a convolution of flat sea impulse response  $P_{FS}(t)$ , probability density function (pdf) of the radar observed surface elevation  $q_s(t)$  and the radar altimeter point-target response  $p_\tau(t)$ .

$$W(t) = P_{FS}(t) \otimes q_s(t) \otimes p_\tau(t) \quad (2.22)$$

Considering that variable features on the Earth's surface such as snow, ice sheet, sand or vegetation could interference the default scattering pattern as assumed by the original ocean retracking algorithm, Legresy and Remy (1997) introduces a scattering distribution ( $f_{scat}$ ), which describes the vertical profile of the reflecting surfaces. Therefore, the convolution relationship becomes:

$$W(t) = P_{FS}(t) \otimes q_s(t) \otimes f_{scat} \otimes p_\tau(t) \quad (2.23)$$

With  $t_0$  is the time of the impact and  $s$  is the root-mean-square (rms) of the surface roughness, the impulse response shape  $P_{FS}(t)$ , the point distribution function (assuming Gaussian distribution)  $q_s(t)$  and the scattering distribution  $f_{scat}(t)$  are given by:

$$\begin{aligned} P_{FS}(t) &= 0 & \text{for} & & (t < t_0) \\ &= e^{-\delta(t-t_0)} & \text{for} & & (t \geq t_0) \end{aligned} \quad (2.24)$$

$$q_s(t) = \frac{1}{s\sqrt{\pi}} e^{-\left(\frac{t-t_0}{s}\right)^2} \quad (2.25)$$

$$\begin{aligned}
f_{scat}(t) &= 0 & (t < t_0) \\
&= \sigma_s & (t = t_0) \\
&= \sigma_v e^{-2k_e c(t-t_0)} & (t_g > t > t_0) \\
&= \sigma_g & (t = t_g) \\
&= 0 & (t > t_g)
\end{aligned} \tag{2.26}$$

The power point target response  $P_t(t)$  is converted from the antenna pattern function  $P_t(\Omega)$  and finally the gamma is given subsequently as:

$$P_t(\Omega) = e^{-\alpha\Omega^2} \quad P_t(t) = 0 \quad \text{for} \quad (t < t_0) \tag{2.27}$$

$$P_t(t) = e^{-(\alpha\theta^2 + (g_0 + \beta\theta^2) * \gamma * (t-t_0))} \quad \text{for} \quad (t \geq t_0)$$

$$\gamma = \frac{(1 + 2Hc_{topo})}{(1 + H/R)} \tag{2.28}$$

where

- |            |  |            |                                |
|------------|--|------------|--------------------------------|
| $c$        | : the speed of light within the medium | $k_e$      | : the extinction coefficient   |
| $\sigma_s$ | : surface scattering                   | $\sigma_g$ | : ground scattering            |
| $\sigma_v$ | : volume scattering                    | $R$        | : the Earth's radius           |
| $\Omega$   | : the incidence angle on the target    | $\theta$   | : the surface topography slope |
| $c_{topo}$ | : the surface curvature                |            | or the antenna mispointing     |
| $H$        | : satellite altitude                   |            |                                |

The satellite orbit and antenna size determine  $g_0$ ,  $\alpha$  and  $\beta$ . For Envisat, these parameters are computed as follow:

$$\begin{aligned}
g_0 &= 4.23 \cdot 10^6 s^{-1} & \text{For Ku band} \\
&= 0.22 \cdot 10^6 s^{-1} & \text{For S band}
\end{aligned} \tag{2.29}$$

$$\begin{aligned}
\alpha &= 10899 rad^{-2} \quad 3.32 deg^{-2} & \text{For Ku band} \\
&= 591 rad^{-2} \quad 0.18 deg^{-2} & \text{For S band}
\end{aligned} \tag{2.30}$$

$$\begin{aligned}
\beta &= 4.497 \cdot 10^{-6} s^{-1} rad^{-2} \quad 1.37 \cdot 10^7 s^{-1} deg^{-2} & \text{For Ku band} \\
&= 1.44 \cdot 10^{-8} s^{-1} rad^{-2} \quad 4.40 \cdot 10^4 s^{-1} deg^{-2} & \text{For S band}
\end{aligned} \tag{2.31}$$

#### (6) Sea-Ice Retracker

Laxon (1994) introduced the Sea-Ice retracker to produce sea ice elevation products out of ERS-1 radar altimetry. As the first step, this algorithm parameterize the altimeter waveform shape to characterize the power and shapes of the radar returns, by

dividing the waveform shape into three “broad sea-ice gates” noted as  $SIG_{T0}$ ,  $SIG_{T1}$  and  $SIG_{T2}$  (see Figure 2.9) and defining the peak backscatter value  $SIG_{PK}$ .

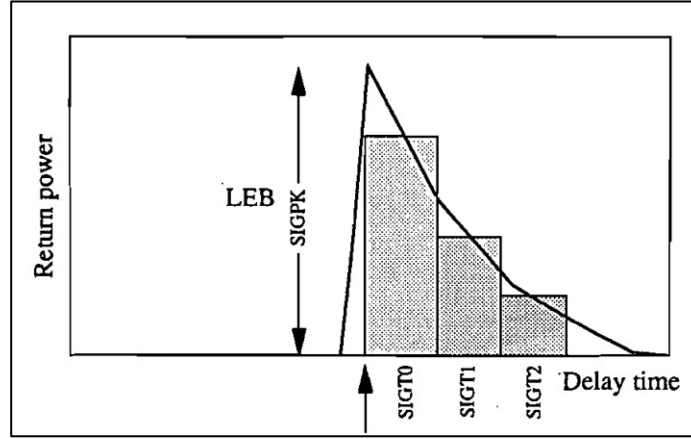


**Figure 2.10** Schematic diagram of partitioned sea ice gates (Laxon, 1994)

The peak backscatter value ( $SIG_{PK}$ ) and the broad gates ( $SIG_{T0}$ ,  $SIG_{T1}$ ,  $SIG_{T2}$ ) can then be computed as follow (Laxon, 1994):

$$SIG_{PK} = 10\log_{10}[PEAK] + gain \quad (2.32)$$

$$SIG_{T0} = 10\log_{10} \left[ \frac{1}{SW} \sum_{i=LEB}^{LEB+SW-1} P'(i) \right] + gain \quad (2.33)$$

$$SIG_{T1} = 10\log_{10} \left[ \frac{1}{SW} \sum_{i=LEB+SW}^{LEB+2SW-1} P'(i) \right] + gain \quad (2.34)$$

$$SIG_{T2} = 10\log_{10} \left[ \frac{1}{SW} \sum_{i=LEB+2SW}^{LEB+3SW-1} P'(i) \right] + gain \quad (2.35)$$

where

$PEAK$  : maximum count value occurring in the waveform

$P'(i)$  : count values in waveform corrected for antenna and individual range bin gain

$SW$  : number of samples to be included in each ‘broad’ gate

$gain$  : normalizing value to convert  $SIG_{PEAK}$  into effective backscattering coefficient

$LEB$  : integer bin closest to the 0.75  $PEAK$  threshold on the leading edge



In addition to the calculation of the peak backscatter value and the broad sea-ice gates detailed above, three thresholds ( $T_{LOW}, T_{MED}, T_{HI}$ ) are calculated as a fixed fraction of the waveform peak value and plugged in as a factor to compute the leading edge ( $LE_{WID}$ ) and the leading edge difference ( $LE_{DIFF}$ ) through the gate-to-meter ( $g2m$ ) constant (Laxon, 1994).

$$LE_{WID} = T_{HI} - T_{LOW} \times g2m \quad LE_{DIFF} = [(T_{HI} + T_{LOW})/2 - T_{MED}] \times g2m \quad (2.36)$$

Two additional parameters are needed to accomplish the classification of sea ice, *i.e.*  $SIG_{TD}$  that represents the acceleration of power drop in the return radar signals with incidence angle and  $SIG_{TR}$  that represents the difference of the trailing edge from an exponential decay. These two parameters are defined as follow:

$$SIG_{TD} = SIG_{T1} - SIG_{T2} \quad SIG_{TR} = \frac{(SIG_{T0} - SIG_{T2})}{2} - SIG_{T1} \quad (2.37)$$

The next step upon the determination of waveform parameters described above is classifying sea ice type using the mean and standard deviations of  $SIG_{PK}$ ,  $SIG_{TD}$ ,  $SIG_{TR}$ ,  $LE_{WID}$  and  $LE_{DIFF}$  parameters.

Finally, retracking correction ( $\Delta R$ ) is defined through simple threshold algorithm with the maximum count value ( $PEAK$ ) and retracking fraction  $SI_{RT}$ , which equals 0.5.

$$\Delta R = PEAK \times SI_{RT} \quad R' = R + \Delta R \quad (2.38)$$

## 2.2. Hydrological Analysis and Modeling

### 2.2.1. Hydrological Cycle and Watershed Concepts

The hydrological or water cycle is a comprehensive circulation of water in various forms (gas, liquid or solid) throughout the atmosphere and land. According to Figure 2.10; the components in the water cycle could be described as follows (NWS, 2013): (1) evaporation transforms the water stored in the ocean, lake, river, and any other exposed surface into water vapor, (2) transpiration carries out a similar task, the only difference is that it is transforming water from the exposed surface of vegetation (*i.e.* leaves), while (3) sublimation transforms water from its solid form as ice directly into its gas phase. (4) The condensation process transfers the water vapor back into the liquid phase in the form of water droplets after a cooling process in the atmosphere, followed by (5) transportation process, which brings gaseous water through the atmosphere. Precipitation (6) is the falling of water droplets down to the land surface in the form of water, snow, hail and other forms. Another process is (7) deposition, which directly transforms water in the gaseous phase into the solid phase in the form of ice. Once the precipitation touches down the Earth, some of them flow into (8) infiltration that carries the water into the porous layer below the land surface. Some of the infiltration process goes far down into the base rock, which is known as percolation. Some of the groundwater fills up the aquifers while some other forms the (9) groundwater flow and sent is back to the river or ocean. Excess water flow above ground forms (9) surface water flow, which is called runoff. Vegetation takes another part in the cycle through (10) plant uptake, which sucks the water back up to the vegetation for its nutritional needs.

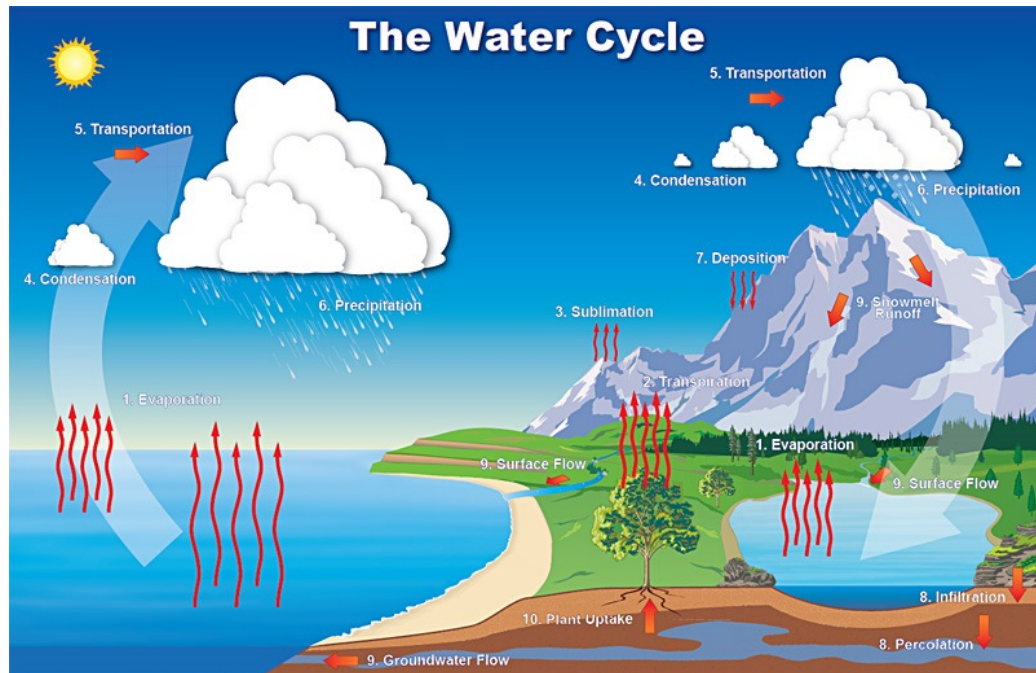


**Figure 2.11** Simplified Hydrological Cycle (NWS, 2013)

A watershed is an area that receives precipitation and passes it through a sequence of processes that discharge the accumulation of the water into a main channel that ends at an outlet (Bedient and Huber, 2002; Davie, 2003). A topographic divide that separates watersheds is called a watershed boundary and developed from an imaginary line that connects the highest point between two or more watersheds. This line separates the flow or accumulation of precipitation into different main channels and outlets (Chow *et al.*, 1998; Mays, 2012). Watersheds vary from those of micro-size (catchment), mesoscale (watershed) and macro-size (basin). Although there is no clear definition across these names and their categorization, a number of classification systems have been proposed toward a uniform definition of hydrological unit of analysis (*e.g.* Eyles, 1971; Lotspeich, 1980; Khan *et al.*, 2001). A watershed is an ideal unit for various hydrology studies, since the portions of a watershed simultaneously respond to changes of the climatic forcing, and therefore compose a cumulative behavior of an integrated physical landform.

### 2.2.2. Rainfall-runoff Process

Rainfall-runoff is an influential process as part of the whole hydrological cycle over the land surface since it regulates the surface runoff that is of primary interest of the hydrologist, as well as the main source of flooding that affects the human's life. In a very simplified language, rainfall-runoff presents a sequence of processes that begins with precipitation over the land surface. Infiltration and baseflow come afterwards and present the dynamic of the water under the land; while surface runoff presents the movement of the excess water over the land once the soil is saturated and infiltrates no more water. Horton (1933 in Beven, 2004) presented a theory that assumes the excess water are collected in the depression storage due to topographic variation and collectively move in a shallow sheet over the land. The surface runoff then accumulates and discharges into the small channels, merges with other channels in the main channel and form the streamflow.

Precipitation presents the falling of the water droplets on the Earth's surface in the various forms such as water, snow and some other forms (*e.g.* Chow *et al.*, 1998). The precipitation is quantified through its depth over an area within a certain period and usually recorded regularly by a meteorological station. It is an interesting fact that precipitation varies over time and space; therefore a number of methods are developed to model the spatial distribution of precipitation over a unit of analysis. The simplest model makes use of arithmetic mean to calculate the average of precipitation presented by separated stations. Thiessen (1911 in Kopec, 1963) introduced a method to create unique polygons that separated the influence of one stations from another. The isohyet method involves lines connecting places with equal precipitation rate (*i.e.* isohyet) and a linear interpolation to represent gradual changes between the meteorological stations, while the hypsometric method takes the elevation difference into account when calculating the weighted average of the precipitation rates (Davie, 2003).

Evapotranspiration is simply a cumulative value of evaporation and transpiration. Both evaporation and transpiration are quantified in the unit of depth over an area within a certain period. Evaporation and evapotranspiration can be measured by simple devices such as the evaporation pan and lysimeter, or complex instruments such as Eddy

correlation and Bowen ratio, even a Light Detection and Ranging (LIDAR) remote sensing system (Abtew and Melesse, 2013). However, considering that evaporation and evapotranspiration vary significantly with time and space as well as the complexities of setting up the above equipment, the evaporation and evapotranspiration are often estimated by the knowledge of other parameters such as temperature, solar radiation, wind speed, humidity and air pressure. Among the methods developed to estimate evapotranspiration, the Priestley-Taylor method is popular due to its minimum input requirements, while the Penman-Monteith is mostly preferred complex method due to its similarity with the physical evapotranspiration estimation (Abtew and Melesse, 2013).

Infiltration describes the vertical and horizontal movement of water below the land surface; therefore it highly depends on the physical properties of the soil, which mainly represented by the proportion of water, air and pores within the soil structure (Horton, 1933 in Beven, 2004). The actual measure of the infiltration amount (expressed as the “infiltration capacity”) is related exponentially to the period of observation (Horton, 1939 in Beven, 2004):

$$f(t) = f_c + (f_0 - f_c)e^{-K_f t} \quad (2.39)$$

where

$$\begin{array}{ll} f(t) & : \text{Infiltration capacity at time } t \\ f_c & : \text{Minimum constant infiltration capacity} \\ f_0 & : \text{Infiltration capacity at time } t = 0 \end{array} \quad \begin{array}{ll} K_f & : \text{Constant of decay} \\ t & : \text{Time period (hr)} \end{array}$$

Another fundamental development in the field of infiltration is presented by Green and Ampt (1911, in Chow *et al.* 1988), which is an alternative to quantify the infiltration through a set of required parameters, *i.e.* hydraulic conductivity, porosity and the wetting front soil suction head, which particularly can be estimated by the effective saturation rate. In addition, Phillips (1957) carried on Horton (1939) work and realized such theory into an equation with less restrictive condition (Chow *et al.* 1988).

Infiltration drowns the water deeper until it stops at the saturated zone. This is the zone where no more infiltration occurred due to the absence of space for the water to move downward. The saturated zone is separated from the unsaturated zone by a water table. Depending on the slope of the water table, the water at the unsaturated zone may still move downward along with the slope of the water table and discharge to the main channel, which is known as the subsurface flow (*e.g.* Mays, 2012). Further below the water table, the water also moves downward along the slope and comprises the groundwater flow, which eventually discharges to the main channel. The subsurface and groundwater flow contribute and ensure the continuity of the flow in the main channel, in the absence of precipitation, which is called base flow (Bedient and Huber, 2002).

The response of a watershed to the precipitation is comprehensively expressed in a hydrograph, which presents the time-series of the accumulated channel flow that include surface runoff/streamflow, subsurface and groundwater flow and precipitation over the channel on a specific location of the watershed (Chow *et al.*, 1988; Bedient and Huber, 2002). A “normal depletion curve” can be estimated by an exponential relation as

given in the equation below, and then the curve can be used to analyze the hydrograph and separate the base flow from overall hydrograph (Horton, 1933 in Beven, 2004).

$$q_t = q_0 e^{-kt} \quad \text{with} \quad (2.40)$$

$q_t$ : Discharge at time $t$	$k$ : Recession constant
$q_0$ : Specified initial discharge	$t$ : Period (hr)

Direct runoff holds the largest portion out of the overall flow quantified in the hydrograph after the subtraction of baseflow. It comprises of the surface runoff generated by excess precipitation, which refers to the amount of precipitated water subtracted by the infiltration, evaporation and surface depression storage. The difference between the total precipitation and the excess precipitation is abstraction or loss (Chow *et al.*, 1988). Determination of the direct runoff and quantification of the abstraction are the keys in the rainfall-runoff analysis in order to study the response of a watershed to the dynamic of precipitation. The simplest approach to determine direct runoff is through the  $\Phi$ -Index, which is a constant rate of abstraction and the number of rainfall intervals (N) that keep adjusted until the direct runoff and excess precipitation depth are equal (Mays, 2012).

Another essential method in the determination of direct runoff from the excess precipitation is the time-area curve, which assumes the overall hydrograph is generated solely by translation of direct runoff to the main outlet with consistent speed (Bedient and Huber, 2002). This method then imaginarily divide the watershed into sections with similar “runoff travel time” to the main outlet. In the rainfall event, the closest section will contribute its runoff to the main outlet, followed by those with larger “runoff travel time”. This sequence then develops a chronological unit hydrograph that is useful to estimate the flow magnitude. Clark Unit Hydrograph is actually using the time-area curve as one of its parameter.

### 2.2.3. Runoff Volume Estimation

A number of methods were developed for predicting the runoff volume from the amount of precipitation. The US Department of Agriculture (USDA) Soil Conservation Service (SCS), now Natural Resources Conservation Service (NRCS), in 1956 developed a method that estimates direct runoff and runoff volume through a curve number that presents the characteristics of a landform in terms of infiltration and surface runoff generation (USDA NRCS, 2004). This method is widely applied to studies in the US and worldwide over various hydrological scales and characteristics, mainly because it is well established, simple yet reliable and requires only one parameter that readily developed from commonly available dataset (Ponce and Hawkins, 1996).

The SCS Curve Number method was developed with focus to estimate the abstraction (which includes interception, surface storage and infiltration) from rainfall, by neglecting the evaporation and transpiration processes (Misra and Singh, 2003). Therefore it relates the direct runoff ( $Q$ ) only as a function of total rainfall ( $P$ ), initial abstraction ( $I_a$ ) and the potential maximum retention ( $S$ ) (all terms are expressed in a measure of *depth* in inch) through the following equations (USDA NRCS, 2004):

$$Q = \frac{(P - I_a)^2}{P - I_a + S} \quad \text{With } I_a = 0.2S, \text{ therefore} \quad Q = \frac{(P - 0.2S)^2}{P + 0.8S} \quad (2.41)$$

Therefore, the equations for computing depth of excess rainfall or direct runoff from a storm and for estimating the potential maximum retention from the curve number are:

$$P_e = \frac{(P - 0.2S)^2}{P + 0.8S} \quad S = \frac{100}{CN} - 10 \quad (2.42)$$

CN is a runoff curve number (dimensionless number ranges from 0 to 100) that is a function of land cover, hydrology soil group, antecedent soil moisture, treatment and hydrology condition of the land and other factors affecting runoff and retention in a watershed (USDA NRCS, 1986). Curve number for water bodies, urban and impervious surfaces without or with very limited infiltration capacity gets close to 100 while areas with high permeability the curve numbers are lower and may be close to zero. Curve numbers have been tabulated by USDA Soil Conservation Service based on soil type and land use. The following tables' presents the hydrology soil groups with their minimum infiltration rate and the curve numbers for various land uses (USDA NRCS, 2004, 1986).

**Table 2.4** Hydrology Soil Groups for curve number analysis (USDA NRCS, 2004)

Soil Group	Physical Characteristics	Min. Infiltration Rate (in/hr)
Group A	Deep sand, deep loess, aggregated silts	0.30 - 0.45
Group B	Shallow loess, sandy loam	0.15 - 0.30
Group C	Clay loams, shallow sandy loam, soils low in organic content and soil usually high in clay	0.00 - 0.05
Group D	Soil that swell significantly when wet, heavy plastic clays and certain saline soils	0.00

**Table 2.5**      **Runoff curve number for urban areas (USDA NRCS, 1986)**

Land Use Description	Average % Impervious Area <sup>1</sup>	Curve Numbers for Hydro. Soil Group			
		A	B	C	D
Fully developed urban areas (vegetation established)					
Lawns, open spaces, parks, golf courses, cemeteries, etc. <sup>2</sup>					
Good condition: grass cover 75% or more of the area		68	79	86	89
Fair condition: grass cover 50-75% of the area		49	69	79	84
Poor condition: grass cover 50% or less of the area		39	61	74	80
Impervious areas					
Paved parking lots, roofs, driveways, etc.		98	98	98	98
Streets and roads					
Paved; curbs and storm sewer excluding right of way		98	98	98	98
Paved; open ditches (including right of way)		83	89	92	93
Gravel (including right of way)		76	85	89	91
Dirt (including right of way)		72	82	87	89
Western desert urban areas					
Natural desert landscape (pervious areas only) <sup>3</sup>		63	77	85	88
Artificial desert landscape (impervious weed barrier, desert shrub with 1-2 in sand or gravel mulch and basin borders		96	96	96	96
Urban districts					
Commercial and business	85	89	92	94	95
Industrial	72	81	88	91	93
Residential districts by average lot size					
1/8 acre or less (townhouses)	65	77	85	90	92
1/4 acre	38	61	75	83	87
1/3 acre	30	57	72	81	86
1/2 acre	25	54	70	80	85
1 acre	20	51	68	79	84
2 acre	12	46	65	77	82
Developing Urban Areas					
Newly graded areas					
Pervious areas only, no vegetation <sup>5</sup>		77	86	91	94
Idle lands (CN's are determined using cover types)					

<sup>1</sup> The average percent impervious area shown was used to develop the composite CN's. Other assumptions are: (1) impervious areas are directly connected to the drainage system, (2) impervious areas have a CN of 98 and (3) pervious areas are considered equivalent to open space in good hydrology condition. CN's for other combinations may be computed

<sup>2</sup> CN's shown are equivalent to those of pasture. Composite CN's may be computed for other combinations of cover type

<sup>3</sup> Composite CN's for natural desert landscaping should be computed through graphical approach based on the impervious area percentage (CN = 98) and the pervious area CN. The pervious area CN's are assumed equivalent to desert shrub in poor hydrology condition

<sup>4</sup> Composite CN's for design of temporary measures during grading and construction should be computed using graphical approach based on the degree of development (impervious area %) and the CN's for the newly graded pervious areas

**Table 2.6** Runoff CN for arid and semi-arid rangeland (USDA NRCS, 1986)

Land Use Description	Hydrologic Condition <sup>1</sup>	Curve Numbers for Hydro Soil Group			
		A	B	C	D
Arid and Semi-arid Rangelands					
Herbaceous-mixture of grass, weeds and low-growing brush, with brush the minor element	Poor		80	87	93
	Fair		71	81	89
	Good		62	74	85
Oak-aspen-mountain brush mixture of oak brush, aspen, mountain mahogany, bitter brush, maple and other brush	Poor		66	74	79
	Fair		48	57	63
	Good		30	41	48
Pinyon-juniper - pinyon, juniper, or both; grass understory	Poor		75	85	89
	Fair		58	73	80
	Good		41	61	71
Sagebrush with grass understory	Poor		67	80	85
	Fair		51	63	70
	Good		41	47	55
Desert shrub – major plants include salthbush, greasewood, creosotebush, blackbrush, bursage, palo verde, mesquite and cactus	Poor	63	77	85	88
	Fair	55	72	81	86
	Good	49	68	79	84

<sup>1</sup> Poor: <30% ground cover (litter, grass and brush understory), Fair: 30% - 70% ground cover, Good: >70% ground cover

**Table 2.7** Runoff curve number for other agricultural lands (USDA NRCS, 1986)

Land Use Description	Hydrologic Condition	Curve Numbers for Hydro Soil Group			
Other Agricultural Lands		A	B	C	D
Pasture, grassland or range – continuous forage for grazing <sup>1</sup>	Poor	68	79	86	89
	Fair	49	69	79	84
	Good	39	61	74	80
Meadow – continuous grass, protected from grazing & generally mowed for hay	---	30	58	71	78
Brush – brush-weed-grass mixture with brush the major element <sup>2</sup>	Poor	48	67	77	83
	Fair	35	56	70	77
	Good	30 <sup>3</sup>	48	65	73
Woods – grass combination (orchard or tree farm) <sup>4</sup>	Poor	57	73	82	86
	Fair	43	65	76	82
	Good	32	58	72	79
Woods <sup>5</sup>	Poor	45	66	77	83
	Fair	36	60	73	79
	Good	30	55	70	77
Farmsteads – buildings, lanes, driveways and surrounding lots	---	59	74	82	86

<sup>1</sup> Poor: <50% ground cover or heavily graze with no mulch  
Fair: 50% - 75% ground cover and heavily grazed  
Good: >75% ground cover and lightly/occasionally grazed

<sup>3</sup> Actual CN is <30, use 30 instead for runoff computation

<sup>4</sup> CN's shown were computed for areas with 50% woods and 50% grass (pasture) cover. Combination allowed

<sup>2</sup> Poor: <50% ground cover  
Fair: 50% - 75% ground cover  
Good: >75% ground cover

<sup>5</sup> Poor: forest litter, small trees and brush are destroyed  
Fair: Woods grazed but not burned, some forest litters  
Good: No grazing on woods, litter and brush cover the soil



**Table 2.8**      Runoff curve number for cultivated agricultural lands  
(USDA NRCS, 1986)

Land Use Description	Treatment of Practice	Hydrologic Condition	Curve Numbers for Hydro Soil Group			
			A	B	C	D
Agricultural Lands						
Fallow	Bare Soil	---	77	86	91	94
	Crop residue cover (CR)	Poor	76	85	90	93
Row crops		Good	74	83	88	90
	Straight row (SR)	Poor	72	81	88	91
		Good	67	78	85	89
	SR + CR	Poor	71	80	87	90
		Good	64	75	82	85
	Contoured (C)	Poor	70	79	84	88
		Good	65	75	82	86
	C + CR	Poor	69	78	83	87
		Good	64	74	81	85
	Contoured & Terraced (C&T)	Poor	66	74	80	82
		Good	62	71	78	81
	C&T + CR	Poor	65	73	79	81
Good		61	70	77	80	
Small grain	SR	Poor	65	76	84	88
		Good	63	75	83	87
	SR + CR	Poor	64	75	83	86
		Good	60	72	80	84
	C	Poor	63	74	82	85
		Good	61	73	81	84
	C + CR	Poor	62	73	81	84
		Good	60	72	80	83
	C & T	Poor	61	72	79	82
		Good	59	70	78	81
	C&T + CR	Poor	60	71	78	81
		Good	58	69	77	80
Close-seeded or broadcast legumes or rotation meadow	SR	Poor	66	77	85	89
		Good	58	72	81	85
	C	Poor	64	75	83	85
		Good	55	69	78	83
	C&T	Poor	63	73	80	83
		Good	51	67	76	80

<sup>1</sup> Crop residue cover applies only if residue on at least 5% of the surface throughout the year

<sup>2</sup> Hydraulic condition is based on combination factors that affect infiltration and runoff, including (a) density and canopy of vegetative areas, (b) amount of year-round cover, (c) amount of grass or clos-seeded legumes, (d) percent of residue cover on the land surface (good  $\geq$  20%) and (e) degree of surface roughness

Poor: factors impair infiltration and tend to increase runoff

Good: factors encourage average and better than average infiltration and tend to decrease runoff

#### 2.2.4. Unit Hydrograph

Sherman (1932 in Elliott and Sherman, 1940) for the first time introduced the “unit-graph”, which later known as the unit hydrograph, as the hydrograph produced by a 1-inch (or one unit of other system) rainfall excess distributed evenly over the entire hydrological unit. This concept is widely used to date; however, the use of unit hydrograph is subject to the following assumptions that should be considered prior to its application to certain study areas (Chow *et al.*, 1988): (1) the excess rainfall produces hydrograph with the same duration, which means the rainfall intensity is neglected, (2) the excess rainfall is uniform in terms of spatial and temporal distribution, (3) the magnitude of direct runoff expressed in the hydrograph is linearly proportional to the excess rainfall, (4) the duration of the direct runoff is constant.

Unit hydrograph for gauged watershed can be derived from an actual hydrograph through a deconvolution, *i.e.* reverse process of the following discrete time convolution of direct runoff  $Q_n$  from rainfall  $P_m$  and unit hydrograph  $U_{n-m+1}$  (Chow *et al.*, 1988).

$$Q_n = \sum_{m=1}^{n \leq M} P_m U_{n-m+1} \quad (2.43)$$

In practice, the unit hydrograph for gauged watershed is developed based on a time series of observed direct runoff and rainfall, while the deconvolution of the matrix forms that can be completed either by linear regression or linear programming to minimize the error between the actual and estimated direct runoff.

For a non-gauged watershed, a synthetic unit hydrograph can be developed either based on the (1) hydrograph geometry (*e.g.* Snyder Unit Hydrograph), (2) dimensionless unit hydrograph (*e.g.* SCS Unit Hydrograph) or (3) time-area relationship of the storage (*e.g.* Clark Unit Hydrograph). The first two methods are discussed in detail in most hydrology textbooks (*e.g.* Chow *et al.*, 1988; Bedient and Huber, 2002) while the Clark Unit Hydrograph is described here since it is the direct runoff method used in this study. Clark’s method involves instrumental physical factors in determining the shape of its unit hydrograph, *i.e.* the shape of the watershed and the storage of rainfall excess, in which not explicitly considered in other unit hydrograph methods (Sabol, 1988).

In order to describe the abstraction of excess rainfall over a watershed, Clark Unit Hydrograph method introduces the hydrograph representation of translation flow, *i.e.* the downward flow of water due to gravity and attenuation flow, *i.e.* the combination of frictional forces and resistance to the downward flow due to channel storage effect (Straub *et al.*, 2000). Translation flow is based on the continuity equation (2.50a), which then relates the storage through a linear reservoir model (2.50b) (HEC, 2000):

$$dS/dt = I_t - O_t \quad (2.44)$$

$$S_t = RO_t \quad (2.45)$$

where

$dS/dt$	: Rate of storage change at time $t$	$S_t$	: Storage at time $t$
$I_t$	: Average inflow to storage at time $t$	$O_t$	: Outflow at time $t$
		$R$	: Storage coefficient

Equations 2.50a and 2.50b can be combined and solved by a simple infinite difference approximation to determine the outflow at time  $t$  (e.g. Chow *et al*, 1988):

$$O_t = c_A I_t + c_B O_{t-1} \quad \text{with coefficients} \quad c_A = \frac{\Delta t}{R + 0.5\Delta t} \quad c_B = 1 - c_A \quad (2.46)$$

The average outflow at period  $t$  is then given by a simple averaging:

$$\overline{O}_t = \frac{O_{t-1} + O_t}{2} \quad (2.47)$$

The translation can be illustrated by a time-area curve that represents the proportion of area within the watershed that contributes to runoff over time and limited by the time of concentration ( $t_c$ ) (HEC, 2000).

$$\begin{aligned} \frac{A}{A_c} &= 1.414 \left( \frac{t}{t_c} \right)^{1.5} & \text{for} & \quad 0 \leq \frac{t}{t_c} \leq 0.5 \\ \frac{A}{A_c} &= 1 - 1.414 \left( 1 - \frac{t}{t_c} \right)^{1.5} & \text{for} & \quad 0.5 \leq \frac{t}{t_c} \leq 1.0 \end{aligned} \quad (2.48)$$

Here,  $A$  is the contributing area at time  $t$ ,  $A_c$  is the total watershed area and  $t_c$  is the time of concentration of the watershed area.

The implementation of Clark Unit Hydrograph in developing the unit hydrograph for rainfall-runoff modeling (e.g. HEC-HMS) needs two parameters, *i.e.* the watershed storage coefficient ( $R$ ) that indicates the temporary storage of excess precipitation and can be estimated through calibration once the gauged precipitation and discharge is available and time of concentration ( $T_c$ ), which can be estimated through the same approach as applied in the SCS Curve Number Unit Hydrograph method.

$$t_c = t_{channel} + t_{sheet} + t_{shallow} \quad (2.49)$$

$t_{channel}$  is the sum of travel time in the channel segments,  $t_{sheet}$  is the sum of travel time in the sheet flow (*i.e.* flow over the land surface before reaching a channel) segments, and  $t_{shallow}$  is the sum of travel time in the shallow flow (*i.e.* concentrated sheet flow after 100 m) segments. These three terms can be estimated as follows (HEC, 2000):

$$t_{channel} = \frac{L}{V} \quad V = \frac{CR^{2/3}S^{1/2}}{n} \quad (2.50)$$

where

$C$ : Conversion constant (1.49 for US)	$n$ : Manning's roughness coefficient
$R$ : Hydraulic radius of the cross section	$L$ : Channel length
$S$ : Slope of the energy grade ~ bed slope	

$$t_{sheet} = \frac{0.007(NL)^{0.8}}{(P_2)^{0.5}S^{0.4}} \quad t_{shallow} = \frac{L}{V} \quad V = \begin{cases} 16.1345\sqrt{S} & \text{unpaved surface} \\ 20.3282\sqrt{S} & \text{paved surface} \end{cases} \quad (2.51)$$

where

$P_2$  : 2-yr 24-hr rainfall depth (inch)       $S$  : Slope of hydraulic grade line ~ bed slope  
 $N$  : Overland flow roughness coefficient       $L$  : Flow length

### 2.2.5. Flow Routing

Flow routing is a model that determines the flow dynamic over different channel sections. This model is essential, considering the different characteristics of each channel section and the dynamic of input flow from each channel before they conveyed to the main channel. The most preferred method for flow routing is the Muskingum method (Chow *et al.*, 1988). This method quantifies the dynamic of the channel's sections based on measures of weighted average of inflow and outflow, assuming that the storage is linearly correlated (McCarthy, 1939; Nash, 1959).

The Muskingum routing model is based on the simple finite difference approximation of the continuity equation (McCarthy, 1939).

$$\left(\frac{I_{t-1} + I_t}{2}\right) - \left(\frac{O_{t-1} + O_t}{2}\right) = \left(\frac{S_{t-1} + S_t}{\Delta t}\right) \quad (2.52)$$

where

$I_t$  : Inflow to the channel at time  $t$        $S_t$  : Storage in the channel at time  $t$   
 $O_t$  : Outflow from the channel at time  $t$

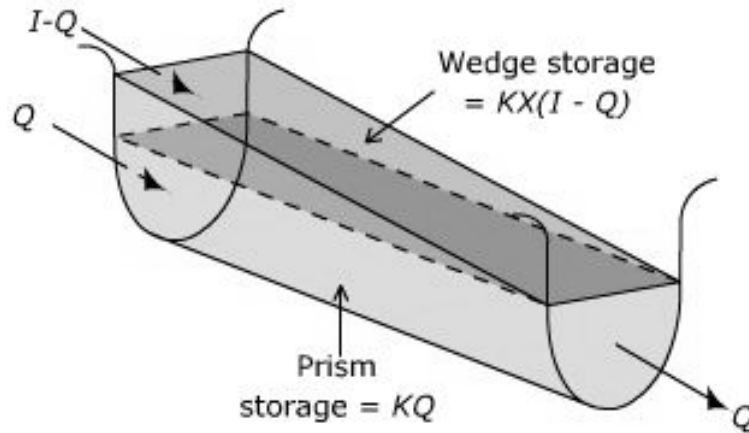


**Figure 2.12** Schematic of prism and wedge storage in Muskingum routing method  
 (Source: College of Engineering and Technology, Old Dominion Univ.)

The Muskingum routing model introduces the “wedge” storage, *i.e.* the flow difference originated by the floodwave rising or falling (the first term in the following equation), and “prism” storage, *i.e.* the volume of water along the channel with constant

slope (the second term in the following equation), which comprises the total storage ( $S$ ) as given in the following equations (McCarthy, 1939; Sturm, 2001; Chaudry, 2008).

$$S = KQ + KX(I - Q) \qquad S = K[XI + (I - X)Q] \qquad (2.53)$$

Where  $K$  is proportionality coefficients and  $X$  is a weighting factor ranges from 0 to 0.5. The routing equation for the Muskingum method is then given as:

$$Q_{j+1} = C_1 I_{j+1} + C_2 I_j + C_3 Q_j \qquad C_1 = \frac{\Delta t - 2KX}{2K(1 - X) + \Delta t} \qquad (2.54)$$

With Muskingum coefficients ( $C_i$ )  $\rightarrow$

$$C_2 = \frac{\Delta t + 2KX}{2K(1 - X) + \Delta t}$$

$$C_3 = \frac{2KX(1 - X) - \Delta t}{2K(1 - X) + \Delta t}$$

Cunge (1969) expanded the linear storage routing principle in Muskingum routing method toward a kinematic wave routing model, considering that the coefficients involved in the Muskingum routing method (*i.e.*  $K$  and  $X$ ) are not physically determined. First, the storage discharge at ( $x = i + 1$ ) and ( $t = j + 1$ ) can be estimated through the modification of Equation 2.59 with the same coefficients.

$$Q_{i+1}^{j+1} = C_1 Q_i^{j+1} + C_2 Q_i^j + C_3 Q_{i+1}^j \qquad (2.55)$$

The two coefficients ( $K$  and  $X$ ) are then considered as coefficients of storage in time unit and relative influence of inflow to storage, respectively, which are estimated as follow:

$$K = \frac{\Delta x}{c_k} = \frac{\Delta x}{dQ/dA} \qquad (2.56)$$

$$X = \frac{1}{2} \left( 1 - \frac{Q}{B c_k S_0 \Delta x} \right) \qquad (2.57)$$

where

$c_k$  : Celerity of Q and B

$\Delta x$  : Channel length

$Q$  : Discharge

$B$  : Water surface width

$A$  : Cross-sectional area

$S_0$  : Total storage

The Muskingum-Cunge routing method is actually the most preferred method for hydrological routing over a watershed due to its two-fold advantages, *i.e.* its capability to present the entire hydrograph at any cross sections with known parameters instead of calculating the final results for the entire channel length and its flexibility to compute the flow at any given time and space interval, *e.g.* compared to the kinematic wave method. However, this method tends to produce erroneous result in areas with backwater effect that propagate flow upstream and those with complex flow dynamics (Chow *et al.*, 1988).

### 2.2.6. Watershed Hydrologic Modeling

Considering the hydrological cycle as a complex process, there may be no model perfectly capable to represent every detail of its phases. However, advances in computation allow for simultaneous execution of commands and computation algorithms. Most hydrologic models developed to quantify watershed behavior over the dynamic of the model forcing (*e.g.* precipitation and physical properties of the watershed) hold a set of assumptions that may or may not be true over the condition of a watershed (Beven, 2012). In addition, the unlimited variation of purposes behind the development of a hydrologic model complicates the choice of the right model to be applied in a specific study area.

**Table 2.9** Categorization of models for hydrology analysis and engineering (Ford and Hamilton, 1966)

Category	Description	
	<b>Event Model</b>	<b>Continuous Model</b>
<b>Event or continuous</b> This distinction applies primarily to models of watershed-runoff processes	An event model simulates a single storm. The duration of the storm may range from a few hours to a few days.	A continuous model simulates a longer period, prediction watershed response both during and between precipitation events
	<b>Lumped Model</b>	<b>Distributed Model</b>
<b>Lumped or distributed</b> HEC-HMS modules are primarily lumped models	Lumped model neglect spatial variations in developing the processes	Distributed model involve spatial variations in developing the processes
	<b>Empirical Model</b>	<b>Conceptual Model</b>
<b>Empirical or conceptual</b> HEC-HMS contains both empirical ( <i>e.g.</i> Snyder UH) and conceptual ( <i>e.g.</i> kinematic wave runoff model)	Conceptual model is built upon a base of knowledge of the pertinent physical, chemical and biological processes that act on the input to produce output.	Empirical model is built upon observation of input and output, without seeking to represent explicitly the process of conversion.
	<b>Deterministic Model</b>	<b>Stochastic Model</b>
<b>Deterministic or stochastic</b> All HEC-HMS modules are deterministic	Deterministic model considers all input, parameters and processes are free of random variation and known with certainty	Stochastic model describes the random variation and incorporates the description in the prediction of output
	<b>Measured-parameter</b>	<b>Fitted-parameter</b>
<b>Measured or fitted parameter</b> HEC-HMS includes both measured and fitted parameter	Measured-parameter model determines its parameters from system properties, either directly or indirectly	Fitted-parameter model includes parameters that cannot be measured

HEC-HMS is the US Army Corps of Engineers' Hydrologic Modeling System program developed by the Hydrologic Engineering Center (HEC). This program simulates precipitation-runoff and routing process in a dendritic watershed system, either natural or controlled. HEC-HMS is the successor to and replacement of HEC's HEC-1 program with a number of improvements and extension of functions such as distributed

modeling and continuous simulation (HEC, 2000). Precipitation-runoff processes had been covered in great details in the previous section; therefore, the coming section exclusively presents the way HEC-HMS represents the runoff process. The following table describes the major categorization of hydrologic models along with those offered by the Hydrologic Engineering Center – Hydrologic Modeling System (HEC-HMS), which is used in this study.

HEC-HMS divides rainfall-runoff processes into four sequential phases, *i.e.* (1) runoff volume computation, (2) direct runoff (overland flow and interflow) estimation, (3) base flow estimation and (4) channel flow modeling. Various modules are available to facilitate the computation of each phase. However, this study applies Soil Conservation Service Curve Number (SCS-CN) module for runoff volume computation, Clark unit hydrograph module for direct runoff estimation, exponential recession module for base flow estimation and standard Muskingum-Cunge for channel flow modeling. Details on these modules have been covered previously in Section 2.2.

### 3. Satellite Radar Altimetry for Small Water Bodies in the Tropics

#### 3.1. Introduction

##### 3.1.1. Monitoring Rivers and Lakes in Humid Tropics

A tremendous number of small (40-200 m width) and medium-sized (200-800 m width) rivers and lakes around the world are poorly gauged for various reasons (Alsdorf and Lettenmaier, 2003). With no doubt, this situation also happens in humid tropics, if not even worse, considering the economic development still holds the highest priority compared to environmental monitoring and prevention of natural disaster. In addition, Southeast Asia's humid tropic has very large population, and fresh water supplied by the river and lake systems is evidently critical to support daily life and agricultural production (Chang, 1993).

##### 3.1.2. Remote Sensing and Satellite Altimetry

With the absence of field gauges to measure the river or lake water level, indirect measurement or estimation is an alternative to provide near real-time water storage and its dynamics. Remote sensing from space is capable to estimate various hydrological parameters to complement field measured data continuously (Tang *et al.*, 2009). In addition to the optical/infrared remote sensing technique, the use of satellite geodetic observations such as satellite radar altimetry has evidently grown during the last couple decades, which is favorable especially considering its high accuracy on the determination of geocentric water surface changes (*e.g.* Birkett, 1998, 2002).

##### 3.1.3. Satellite Altimetry Waveform Retracking Algorithms for Inland Waters

The early development on the use of satellite altimetry to retrieve water level of the river makes uses of waveform shape to match the *specular* characteristics, which exclusively belongs to the signals returned by the river (Koblinsky *et al.*, 1993). The ocean center of gravity (OCOG) or Ice-1 (Wingham *et al.*, 1986) is a simple but robust retracker, which requires only the statistics of the waveform samples and does not require any model; hence it is later called model-free retracker (Bamber, 1994). This algorithm, which later called as Ice-1, was still carried out as one standard retracker for Envisat Radar Altimeter sensor until Envisat decommissioned in June 2012 and evidently the best available retracker for medium to large-sized rivers (Frappart *et al.*, 2006). Some notable recent developments of inland water retracking methods include threshold retracker (Davis, 1997) and its improvements (*e.g.* Lee, 2008, Bao *et al.*, 2009), sub-waveform analysis (*e.g.* Hwang *et al.*, 2006 and Fenoglio-Marc *et al.*, 2009) and sub-waveform filtering and track offset correction (Tseng *et al.*, 2012).

##### 3.1.4. Motivation and Contribution of This Study

After all, there is no "one size fits all" method for satellite altimetry waveform retracking available up to now, especially those devoted to measuring near-real time water level of small (40–200 m width) and medium-sized (200–800 m width) rivers and lakes. This led to the integration of geospatial information, remote sensing and satellite



geodetic approaches to monitor important water bodies and therefore, one of the motivations of this study. This study contributes to the application of satellite altimetry for hydrology studies, especially those which are using a combination of multi-satellite missions, geospatial information, field measurements and ancillary data/information.

In this study, standard waveform retracking procedures (*i.e.* Ocean, Ice-1, Ice-2 and SeaIce for Envisat radar altimetry system) are applied to observe water level of one small and one medium-sized rivers and three lakes with different characteristics in the humid tropics. The results are then evaluated to assess their reliability and accuracy.

### 3.2. Study Area

This study takes place in Mahakam and Karangmumus Rivers (one tributary downstream of Mahakam River) and Lake Semayang in East Kalimantan, Lake Matano and Lake Towuti in South Sulawesi, Indonesia. The study areas represent typical humid tropics in Asia with different geomorphology, climate and anthropogenic settings.

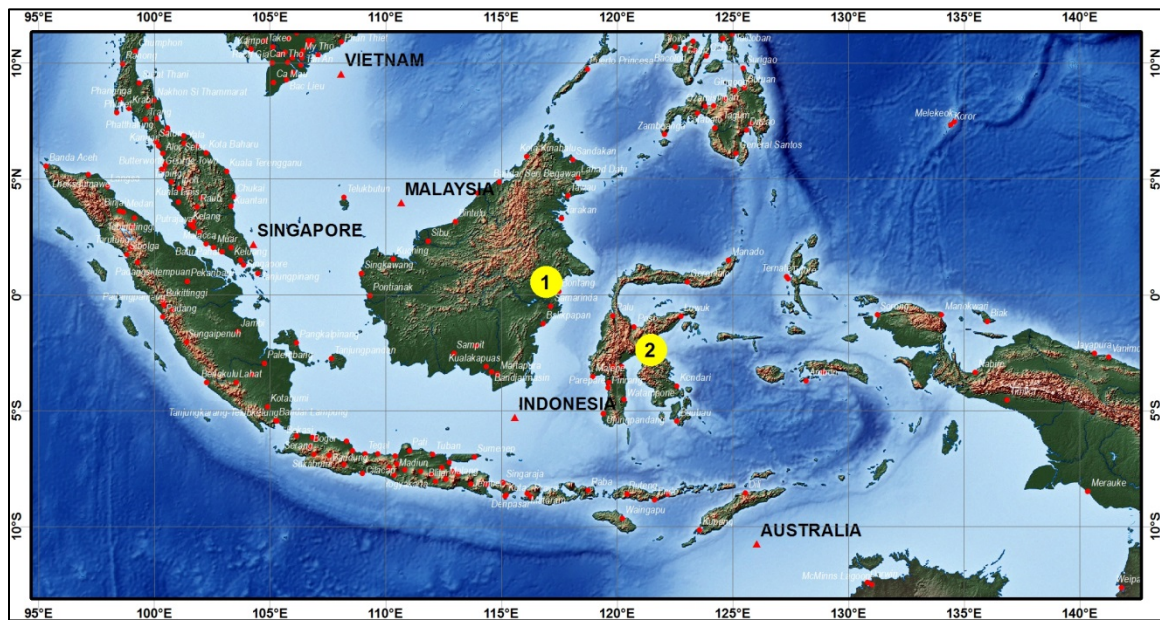


**Figure 3.1** Study area: (1) Mahakam and Karangmumus River and Lake Semayang in East Kalimantan and (2) Lake Matano and Lake Towuti in South Sulawesi

#### 3.2.1. Mahakam River and Lakes in East Kalimantan

Mahakam Watershed is located between  $113^{\circ} 40'$  to  $117^{\circ} 30'$  E longitude and  $1^{\circ} 00'$  S to  $1^{\circ} 45'$  N latitude. Mahakam is its main river that stretches a length of  $\sim 920$  km and drains an area of  $77,095 \text{ km}^2$ , which declares this river as the second longest river both in Borneo Island and the Republic of Indonesia. The upper part and the middle part of this basin are scarcely inhabited ( $5 \text{ people/km}^2$  and  $7 \text{ people/km}^2$ , respectively) while the downstream part is inhabited heavily with  $138 \text{ people/km}^2$  (Estiaty *et al.*, 2007). Figure 3.2 presents the configuration of the Mahakam Basin, which similar to the other river systems in Borneo Island. The river rises in the mountainous forest ranges with

dramatic elevation drops in the first hundreds of kilometers, which led to the formation of rolling hills and steep slopes in the upstream part of this basin. Then forms up the Middle Mahakam Lake and Wetlands starting from the fifth hundreds of its length and transforming into the Mahakam Delta estuary in its last hundred kilometers (MacKinnon *et al.*, 1996). In addition, climatic setting for this basin also varies with a similar pattern, *i.e.* highest (2400-3000 mm/year), modest (2000-2400 mm/year) and lowest (1800-2000 mm/year) precipitation rate occurs in the upper sub-basin, middle wetlands and lower sub-basin, respectively. In terms of the channel physical characteristics and the land use, the upstream part of Mahakam River presents narrow channel width of 40-100 m with depth varies from 5 to 10 m and slope greater than 2%, with forest and small patches of subsidence agricultural farms dominate the land use. The middle part presents channel width of 100-300 m, 10-24 m depth and 0.5-2% slope, with extensive lowland and agricultural areas spread out everywhere along with country-style residential areas and vast distribution of lakes and swampy shrubs. The lower part and the Mahakam Delta present wide channel of 500-850 m width, 10-24 m depth and 0-0.5% slope while with regard to land use, the lower sub-basin is a typical developed area with lots of residential areas, very scarce forest patches and heavily inhabited land (Estiaty *et al.*, 2007).

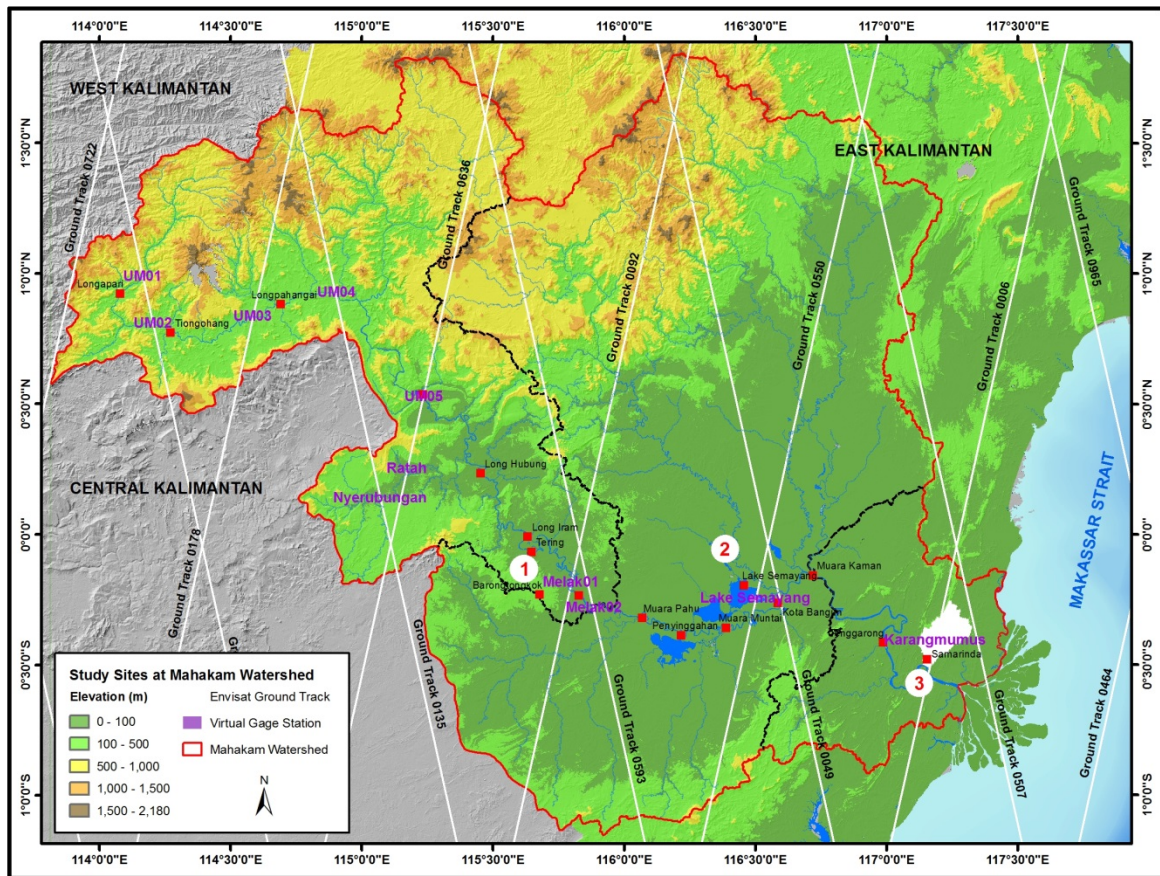


**Figure 3.2** Study area in Mahakam Watershed, *i.e.* (1) Town of Melak, (2) Lake Semayang and (3) Karangmumus Sub-Watershed, along with the virtual gage stations and corresponding Envisat theoretical ground tracks

The geomorphology, terrain configuration and climatic settings described above leads to the division of three main sub-basins with distinguished characteristics, *i.e.* (1) the Upper Mahakam sub-basin, which dominated by steep slopes and rolling hills, short river reaches, hence possesses higher erosion risk, more responsive with extreme precipitation, and therefore, prone to flash floods, (2) the Middle Mahakam Lakes and Wetlands, which acts as retention zone, and (3) the Lower Mahakam sub-basin and Mahakam Delta, which transfers the overflow from the retention zone and regulates the backwater flow as it is generated by the tides from the ocean through the estuary. These main sub-basins are presented in the map above, separated by black dashed lines.

### 3.2.2. Lake Matano and Lake Towuti in South Sulawesi

Lake Matano is located between 121° 12' to 121° 29' E longitude and 2° 34' to 2° 23' N latitude. Despite its small extent, this lake counts as the seventh deepest lake of the world (Herdendorf, 1982). With its maximum depth of 595 m and mean water surface elevation measured at only 392 m, Lake Matano represents a cryptodepression which essentially means its bed is dropped below the mean sea level (Hehanussa and Haryani, 1999). Originated by tectonic process since 2–3 million years ago, this lake is included as one of the oldest lakes of the world and hosts endemic faunas that provide remarkable examples of ecological diversification and speciation (Cristescu *et al.*, 2010). In terms of its geomorphology, the basins in the surrounding of Lake Matano formed by the hardness of the rocks and the softness of uplift tectonic fault that forms very limited number of alluvial plain. Regarding the bed topography, Lake Matano has two flat depressions separated by a saddle. Lake Matano drains through the Petea River into Lake Mahalona, still in the same Malili Lakes complex (Vaillant *et al.*, 1997).

Lake Towuti is recognized as the largest tectonic lake in Indonesia (Russel and Bijaksana, 2012). Located at the downstream end of the Malili Lakes Complex, this lake covers an extent of 562 km<sup>2</sup> with 206 m depth, and similar to Lake Matano, also carries locally endemic fauna due to its nature as one of the ancient lakes. Previous research in Malili Lakes Complex indicates the accumulation of rainfall during the monsoon between November and March each year, and the dry period during April until October each year (Renggono, 2011).

There are only 5–6 rivers discharge continuously into Lake Matano; however, the collective discharge of the Malili Lakes catchment system (*i.e.* consists of Lake Matano, Lake Mahalona and Lake Towuti and their corresponding catchment) is enough to run the 165-250 Megawatts Larona hydropower that supply nickel industry of PT Vale Indonesia in this area (Haryani and Hehanussa, 1999).



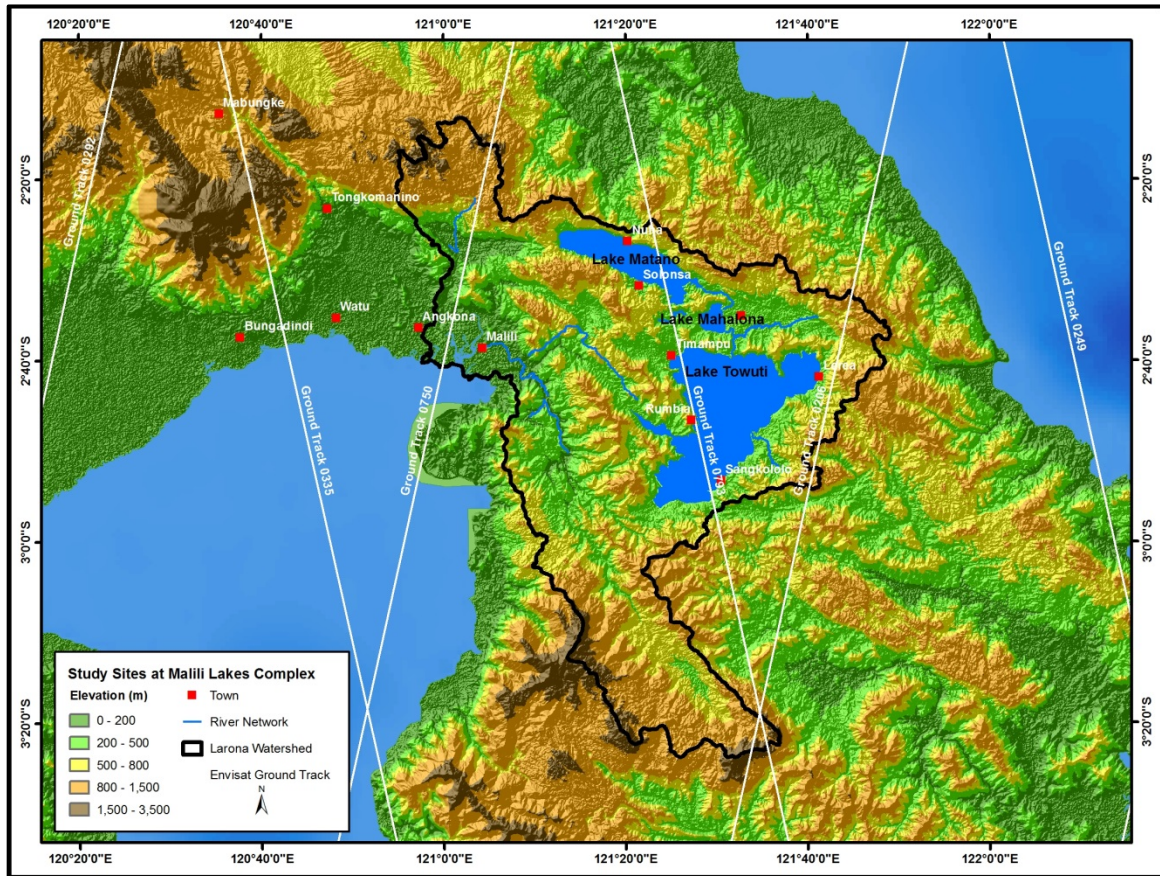


**Figure 3.3** Study area in Lake Matano and Lake Towuti with corresponding Envisat pass

### 3.3. Methodology

### 3.3.1. Envisat Radar Altimeter

This study utilizes satellite radar altimeter measurements provided by ESA's Envisat RA-2. RA-2 is a shortened name of Radar Altimeter 2, which is a continuation of ERS radar altimeter system (RA). RA-2 is mounted at the Envisat, a sun synchronous and near-polar orbiting Earth observation satellite operates at the inclination of  $\sim 98.5^\circ$  with cross-track interval of about 80 km at the Equator. Just like other nadir or pulse-limited radar altimeter instruments, the RA-2 determines the two-way delay of radar echo from the Earth's surface to a very high precision of less than a nanosecond. In addition, it also measures the power and shape of the reflected radar pulses. The RA-2 telemetry provides averaged 18 range measurements per second (*i.e.* 18 Hz) which corresponds to an along-track sampling interval of  $\sim 350$  m (ESA, 2011). As the nature of Level-2 Envisat radar altimetry product, the averaged 18 Hz waveforms are arranged into 128 gates with 3.125 ns time resolution and default tracking gate at #46 (ESA, 2007).

This study uses the Envisat RA2/MWR SGDR product that contains the final (Level-2) Geophysical Data Record (RA2\_GDR) and Microwave Sensor Data Record (MWR\_L2) offline data, which contain the most precise instrument calibrations and orbit

solutions. The GDR and MWR Level-2 products mainly contain parameters for time tagging, geo-location, output from retracers (range, wind speed, significant wave height, etc.) at 1 Hz, plus some 18Hz parameters such as range and orbital altitude. In addition, the RA2/MWR SGDR also contains the 18 Hz waveforms to use in the waveform shape selection procedure. The dataset covers the period of July 2002 to October 2010, corresponding to cycle 6 to 93 (ESA, 2007). To prove the current assumption on the Ice-1 as the best retracking algorithm for inland waters (Frappart *et al.*, 2006), this study compares the water level anomaly obtained from water surface elevation measured by the Ocean, Ice-1, Ice-2 and Sea Ice retracers with the water level anomaly obtained from the *in-situ* gage measurement. Water level anomaly represents the fluctuation of water level relative to its mean level during the period of observation. It is obtained by removing the mean of the water surface elevation measured by altimeter and *in-situ* gage.

The physiographic settings of the study areas along with the layout of Envisat RA-2 theoretical ground track are shown in Figure 3.2 and Figure 3.3. In more detail, the configuration of the Envisat pass according to Archiving, Validation and Interpretation of Satellite Oceanographic Data (AVISO) provided Google Earth (GE) .kmz file and actual RA-2 orbit, cycle and observation period for each study sites are listed as follows.

**Table 3.1** Envisat RA-2 pass, cycles and observation period for each study sites

Site Name	Longitude	Latitude	Pass # (GE)	Pass # (ESA)	River/Lake Width*	In-Situ Data	(Cycle) Period and Remarks
<b>Mahakam Watershed</b>							
UM01	114°10'00" E	0°59'20" N	0679	340	48 m	No	(6-93) 2002-2010
UM02	114°12'21" E	0°48'34" N	0679	340	53 m	No	(6-93) 2002-2010
UM03	114°35'10" E	0°50'02" N	0178	89	54 m	No	(6-93) 2002-2010
UM04	114°54'00" E	0°55'41" N	0135	68	61 m	No	(6-93) 2002-2010
UM05	115°14'10" E	0°31'42" N	0636	318	177 m	No	(6-93) 2002-2010
Melak01	115°53'20" E	0°17'08" S	0092	46	247 m	Yes	(6-93) 2002-2010**
Melak02	115°47'58" E	0°11'03" S	0593	297	294 m	Yes	(6-93) 2002-2010**
Nyerubungan	115°04'26" E	0°08'29" N	0135	68	35 m	No	(6-93) 2002-2010
Ratah	115°10'26" E	0°15'03" N	0636	318	55 m	No	(6-93) 2002-2010
Semayang	116°30'13" E	0°14'46" S	0550	275	2,388 m	Yes	(6-93) 2002-2010**
Kotabangun	116°35'24" E	0°13'26" S	0049	25	240 m	Yes	(6-93) 2002-2010**
Karangmumus	117°11'20" E	0°24'21" S	0006	3	8-45 m	Yes	(6-93) 2002-2010**
<b>Larona Watershed</b>							
Matano/Towuti	121°23'57" E	2°30'10" S	0793	397	8,159 m	Yes	(6-93) 2002-2010**

\* River/lake width is measured according to the crossing Envisat ground track, as explained in the following section

\*\* Envisat-observed water level for these sites are validated with in-situ water level measurements

Geophysical corrections (*i.e.* inverse barometer, sea state bias, ocean tide, polar tide, Earth tide), propagation corrections (ionospheric correction, wet tropospheric correction, dry tropospheric correction) and instrument error corrections (*i.e.* Doppler correction, time delay due to flight and time delay due to ground corrections and antenna center of gravity) are applied as it is described as the standard procedure to obtain Level-2 products (ESA, 2011).

### 3.3.2. The Role of Remote Sensing and Geospatial Datasets

Optical remote sensing and geospatial data processing play an important role in this study, especially in the determination of physical characteristics and spatial boundary of water bodies to observe by satellite geodetic techniques. For instance, measurements of the river and lake width are carried out through visual interpretation of (1) remote sensing image, *i.e.* through dark-blue color reflected by the water bodies in the red-green-blue combination of band #5-4-3 on Landsat-5 and Landsat-7, or band #6-5-4 on Landsat-8, or (2) medium-scale (1:50,000) topographic maps from government.

Standard optical remote sensing data processing techniques include geometric correction, development and contrast of pseudo-natural color composite (*e.g.* red-green-blue color composite using bands 5, 4 and 3 for Landsat 5 and 7 and bands 6, 5 and 4 for recently launched Landsat 8) were applied to obtain imagery with precise position with good contrast between land and water.

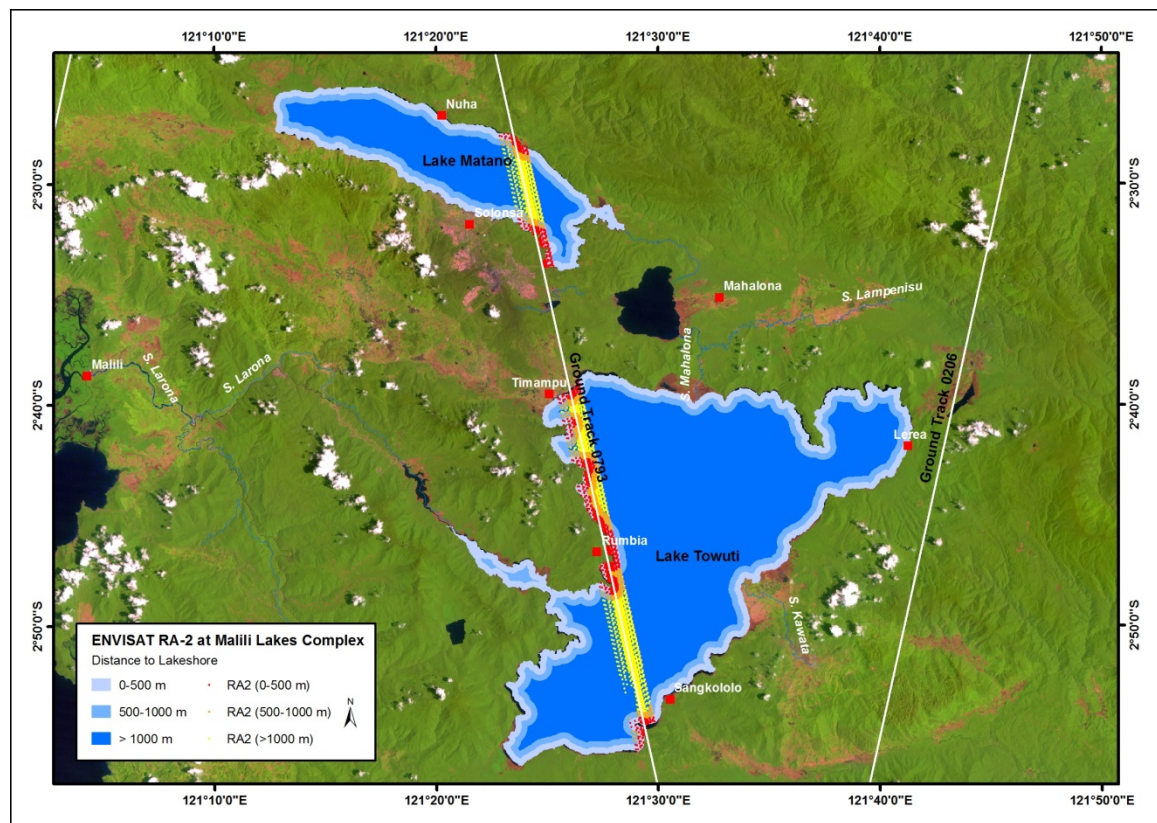


**Figure 3.4** Envisat RA-2 actual ground tracks categorized based on the distance to the shores (0-500, 500-1000 and >1000 m) of Malili Lakes Complex in South Sulawesi. Background: Landsat-5 pseudo-natural color of October 1997

Once the lake boundaries are identified, a buffer with different distances (*i.e.* 500 m and 1000 m for lakes) are generated and included in the spatial processing so that the altimeter measurements can be analyzed based on the distance between its projected



ground track to the lakeshores. As for the river, a 5-meter buffer is created to reduce the contamination of land surface to the analyzed waveforms.

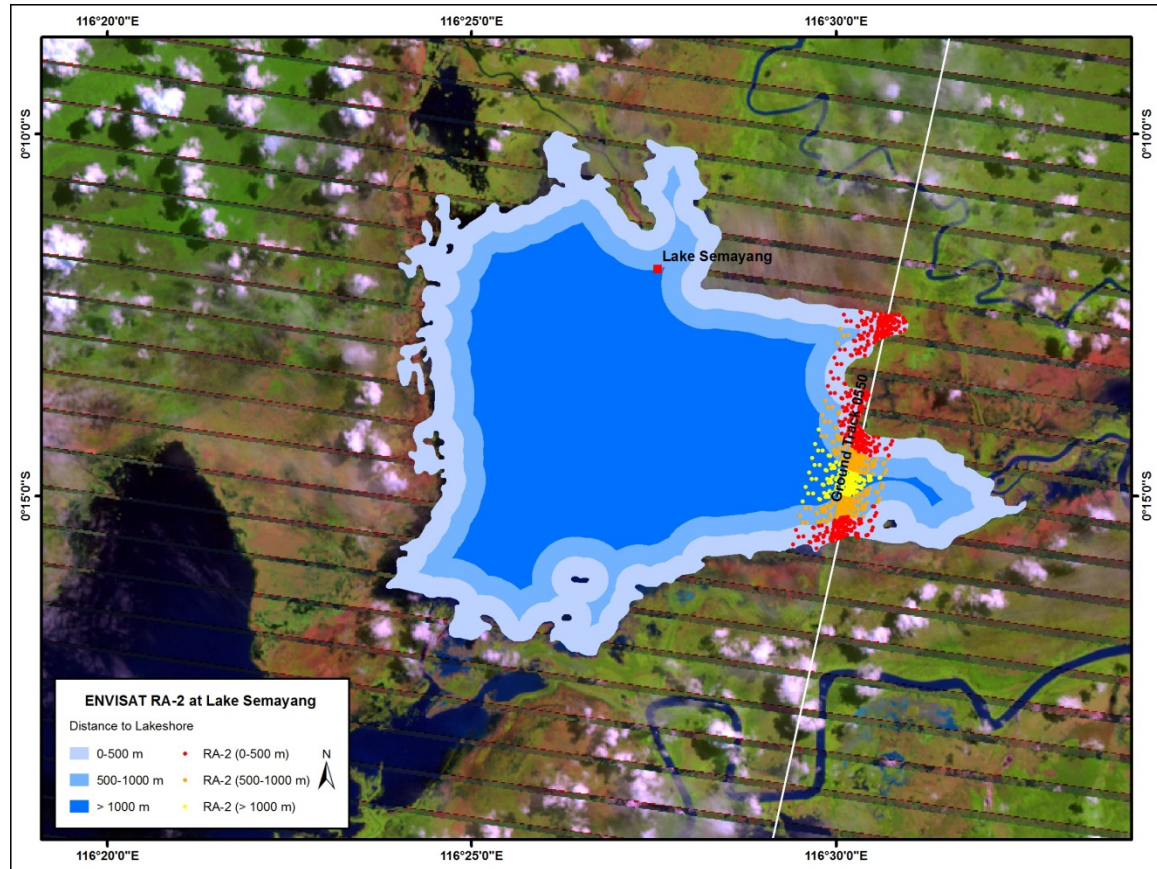


**Figure 3.5** Envisat RA-2 actual ground tracks categorized based on the distance to the shores (0-500, 500-100 and >1000 m) of Lake Semayang in East Kalimantan. Background: Landsat-7 pseudo-natural color of July 2008

### 3.3.3. Waveform Shape Analysis

The diameter of pulse-limited footprint of the Envisat RA-2 over a smooth surface is about 1.7 km (Rees 1990, ESA 2007). Therefore, it is necessary to analyze the waveform shapes as the radar pulse reflected by the water surface might be influenced by other surface along with different distance from projected radar footprint to the land surface. For the lakes, 1-km distance to the lake shore should be enough consider that the radius of the Envisat footprint (half of its diameter) is about 850 m. In the case of small and medium-sized rivers (19-300 m width), this becomes very challenging, and the waveform produced by the processed radar pulse reflection might be unpredictable.

Considering the fact that inland water surface is smoother than the ocean (Birkett, 1998), the (quasi) specular shape is declared as the standard waveform shapes for radar pulse returns that reflected by inland water bodies, in contrast to the ocean-reflected diffuse shape (Koblinsky, 1993). Additional shapes of Envisat RA-2 returned radar pulse over inland water are quasi-Brown, flat patch, and complex (Berry *et al.*, 2005), which

generally represent a transition from land to water, an intermediate surface, and a mixture between water and vegetation, respectively (Dabo-Niang *et al.*, 2007). In this study, the (quasi) specular, quasi-Brown and flat-patch shapes are considered as qualified waveform to perform reliable range measurement while the complex and other non-classified shapes are considered as non-qualified waveform and therefore, discarded from further process. Some categorized waveform examples from this study are presented below.

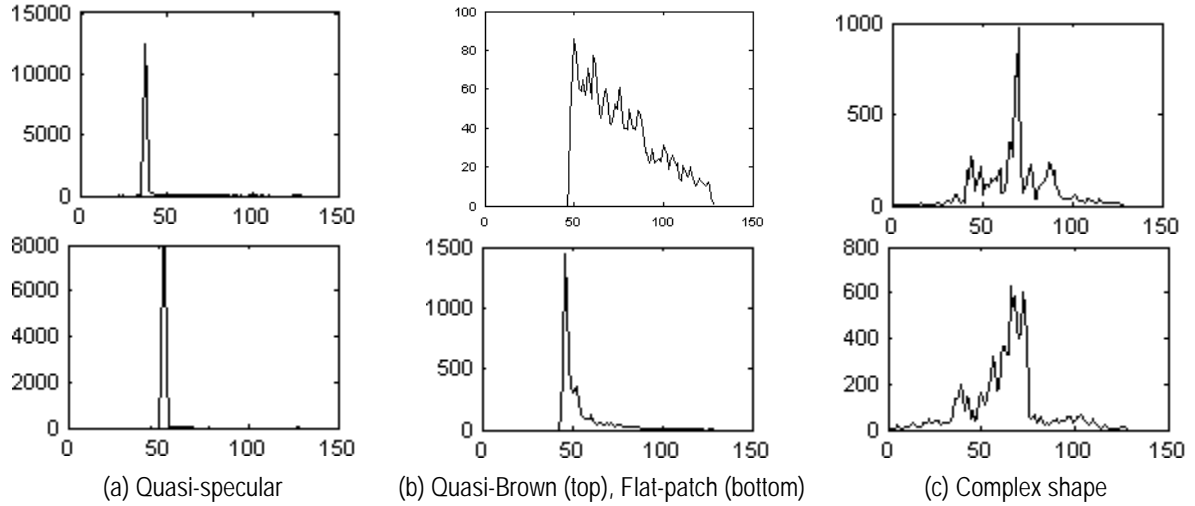


**Figure 3.6** General categories of waveform shapes. Notice the level of returned power represented by y-axis, specular waveform tends to increase sharp

### 3.3.4. Outlier Removal

Even after the exclusion of non-qualified waveform shapes, some observations are outlying from the most value range. In order to obtain the dataset with minimum influences from outliers, the mild outliers were excluded after the definition of the inter-quartile-range (IQR) for each data array (Kenney and Keeping, 1947; Panik, 2012):

$$\begin{aligned} \text{IQR} &= Q_{0.75} - Q_{0.25} & \text{Therefore,} & & WSE_{min} &= Q_{0.25} - 1.5(\text{IQR}) & (3.1) \\ & & & & WSE_{max} &= Q_{0.75} + 1.5(\text{IQR}) \end{aligned}$$

Consequently, any measurements below the  $WSE_{min}$  and above the  $WSE_{max}$  threshold were not involved in the further processing. WSE represents the water surface elevation as measured by Envisat radar altimetry.

### 3.3.5. Validation and Performance Evaluation

Validation and statistical evaluation performance of satellite altimetry water level measurements are carried out for some of the virtual stations where *in-situ* measurements are available by standard deviation of the difference (SDD), root-mean-square error (RMSE) and the coefficient of correlation ( $r$ ).



Standard deviation of the difference (SDD) shows how much the observation varies from their mean. Here the observation values are the *difference* between Envisat altimetry and *in-situ* measured water level anomaly, which is calculated as follow.

$$SDD = \sqrt{\sum_{i=1}^n \frac{(z_i - \bar{z}_i)^2}{n}} \quad \text{where:} \quad (3.2)$$

$z_i$  is the difference between Envisat altimetry and *in-situ* water level anomaly

$\bar{z}_i$  is the mean of the difference between Envisat altimetry and *in-situ* water level anomaly

The RMSE is a measure on how well estimation performs over the “truth” value and calculated following the standard statistical notation (*e.g.* Nagler, 2004 and Li, 2010).

$$RMSE = \sqrt{\sum_{i=1}^n \frac{(x_i - y_i)^2}{n}} \quad \text{where:} \quad (3.3)$$

$x_i$  is the Envisat water level anomaly

$y_i$  is the *in-situ* measured water level anomaly

The correlation coefficient is the standard measure of association for continuous type of data (Whittaker and Robinson, 1967; deSa, 2007); therefore, it is used to measure the association between satellite altimetry and *in-situ* water level measurements as described in the following equation.

$$r = \frac{S_{xy}}{S_x S_y} \quad \text{with} \quad S_{xy} = \sum_{i=1}^n \frac{(x_i - \bar{x})(y_i - \bar{y})}{(n - 1)} \quad (3.4)$$

With  $S_x$  and  $S_y$  are variances for each measurement and  $n$  is the number of observations,  $r$  value falls within the interval  $[-1, 1]$ , where coefficient of 0 indicates no correlation between two measurements, +1 indicates total correlation in the same direction and -1 indicates total correlation in the opposite direction.

Indonesia’s Ministry of Public Works provided the datasets used for validation of water level of Mahakam River at Melak and Kotabangun stations, Lake Semayang at Kotabangun (2002-2004) and Karangmumus River (2008-2010) while PT Vale Indonesia provides validation data for Lake Matano and Lake Towuti (2002-2012).

### 3.3.6. Data Processing Workflow

To provide a comprehensive understanding on the data processing sequences in this study, the following flowchart shows each data processing step and their relationship.

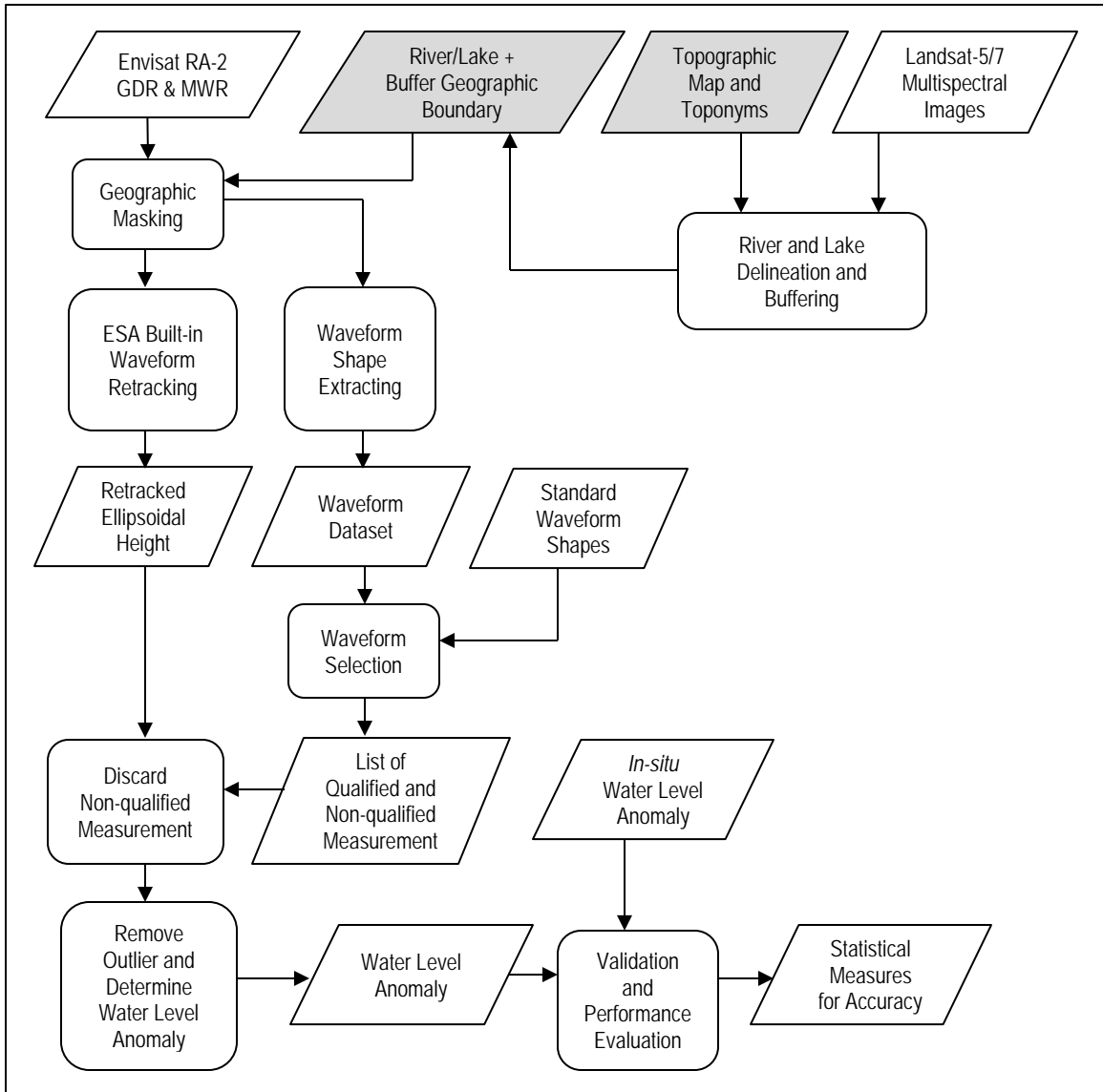


**Figure 3.7** The workflow of data processing for measurement of water level anomaly through satellite altimetry and its performance evaluation

### 3.4. Results and Discussions

#### 3.4.1. Water Level of Mahakam and Karangmumus Rivers

##### (1) Mahakam River and its middle sub-basin tributaries

The waveforms resulted from processed returned radar pulses were carefully selected, and only those matching with the standard waveform shape of water surface were processed (*e.g.* waveforms with complex shape or no obvious peak were discarded). A set of waveforms from the uppermost virtual station (UM01) is displayed below.

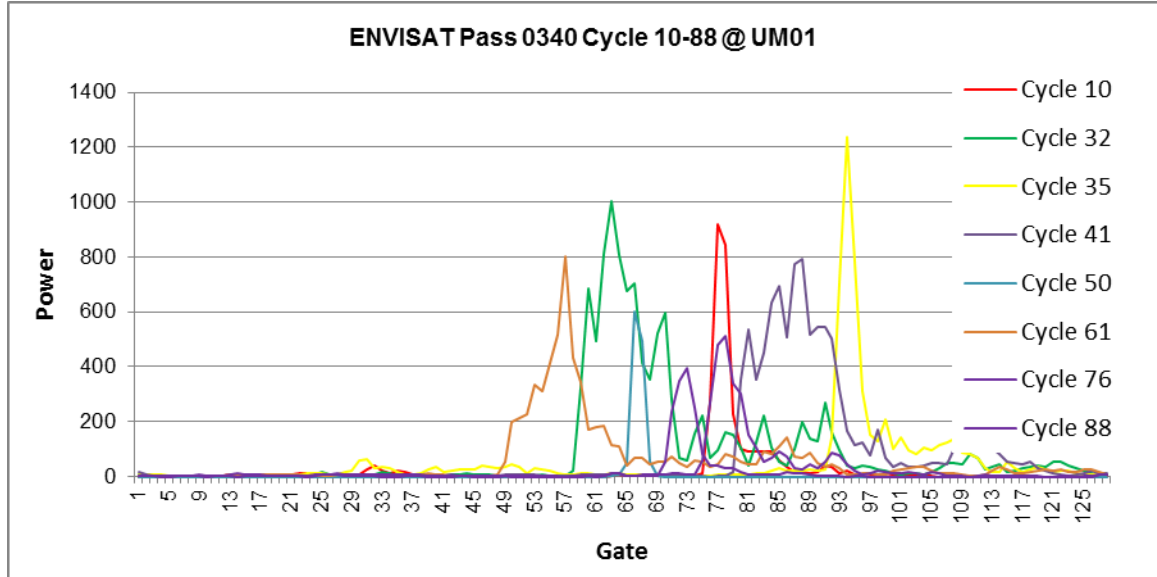


**Figure 3.8** The waveforms of Envisat RA-2 measurements over virtual station UM01. The river width is 48 m

From Figure 3.8 it can be seen that there is one measurement that has a waveform with no obvious peak (cycle 76); therefore, that measurement was excluded from the analysis. The same procedure was carried out for all other virtual stations (*i.e.* where Envisat ground tracks pass the river), which are UM02 to UM05, Melak01, Melak 02, Ratah, Nyerubungan and Kotabangun (see Table 3.2).

As described in Table 3.2 below, most of the radar pulse returns produce qualified and useful waveforms that reflect water level trend at all virtual stations, regardless the width of the river. One particular virtual station, *i.e.* UM03, even indicates the water level fluctuation as indicated by 46 qualified measurement and longer period of coverage, despite the narrow width of the channel (*i.e.* 54 m). Unfortunately, there is no *in-situ* gage water level data available for validation of this extracted water level.

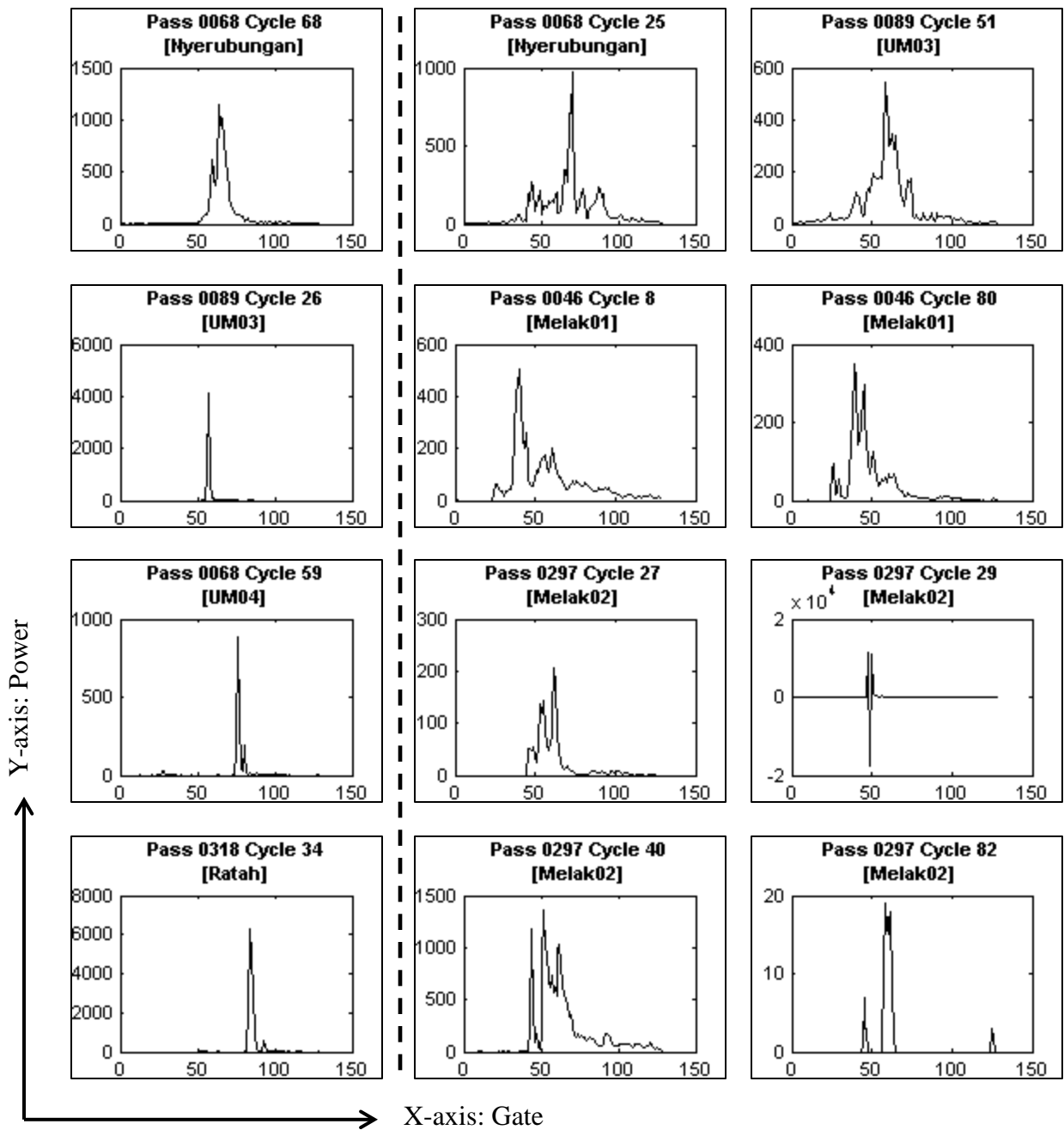


**Figure 3.9** Example of qualified (left panels) and non-qualified waveforms (middle and right panels) of Envisat RA-2 measurements over all virtual stations at Mahakam River (river width varies between 48 to 289 m)

**Table 3.2** The number of qualified and non-qualified altimeter measurements and outliers for all virtual stations at Mahakam River

Virtual Station Name	Cycles Covered	No. of Missing Cycles*	Measurements within water body (#)	Qualified Measurement (#)	Qualified (%)	Non-qualified Measurement (#)	Non-qualified (%)	No. of outlier (#)	River width (m)
UM01	10 – 88	79	8	7	87.5	1	12.5	N/A	48 m
UM02	16 – 85	63	21	16	76.2	5	23.8	N/A	53 m
UM03	9 – 93	34	51	46	90.2	5	9.8	N/A	54 m
UM04	19 – 86	78	9	8	88.9	1	11.1	N/A	61 m
UM05	12 – 93	73	14	14	100.0	0	0.0	N/A	177 m
Melak01	7 - 93	8	225	220	97.8	5	2.2	8	247 m
Melak02	7 – 93	11	148	134	90.5	14	9.5	0	294 m
Nyerubungan	9 – 84	80	13	10	83.3	2	16.7	N/A	35 m
Ratah	8 – 79	66	22	13	61.9	8	38.1	N/A	55 m
Kotabangun	6 – 93	17	71	68	95.8	3	4.2	2	240 m

\* Missing cycles are altimetry cycles without measurement within the water bodies' boundary

After all, this finding becomes the second successful satellite radar altimetry exploitation toward very small water bodies (*e.g.* 80 m width or less) after Michailovsky *et al.*, (2012), who extracted 13 useful water level measurements from a river with 40 m width, also without validation. By the time of this write up, no other studies indicated successful exploitation of the river with 100 m width or less, except Kuo and Kao (2011), who revealed the water level of Bajhang River in Taiwan with less than 100 m width with remarkable accuracy.

Successful retrieval of qualified satellite radar altimetry measurement is very much supported by detailed geographic masking, which carefully excludes all altimetry measurements with projected nadir position outside of the water bodies.

Once the range measurements that carry non-qualified waveforms excluded, water surface elevation at different virtual stations in Mahakam River and its middle sub-basin tributaries already retracked using the Ocean, Ice-1, Ice-2 and Sea Ice waveform retrackers on the GDR were then selected. The outliers are then defined and excluded from the water surface elevation dataset and subsequently the water level anomalies are calculated by removing the mean. The results of water level anomaly observations for each virtual station are presented in the following set of figures. The temporal coverage differs from one virtual station to another due to the availability of the qualified measurements, which confirms the temporal resolution problem in using satellite altimetry for monitoring inland waters.

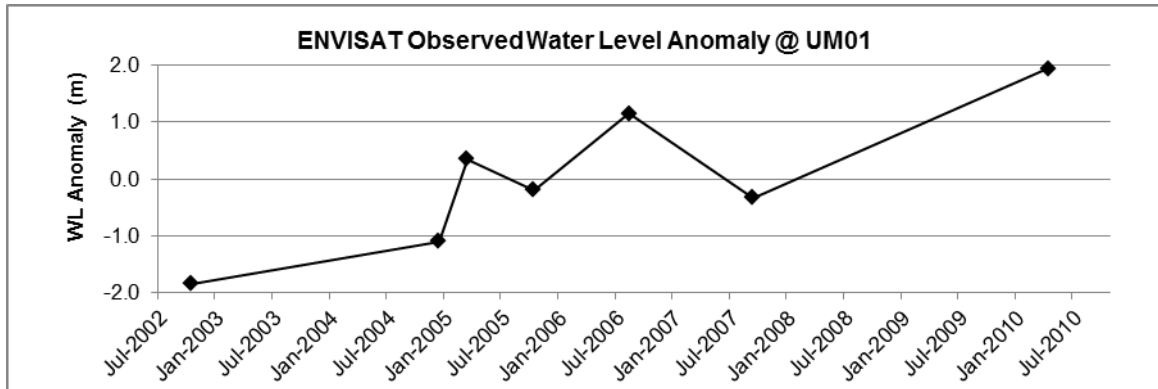


**Figure 3.10** Water level anomaly at virtual station UM01 (river width 48 m) as measured by Envisat RA-2 and processed by Ice-1 retracker

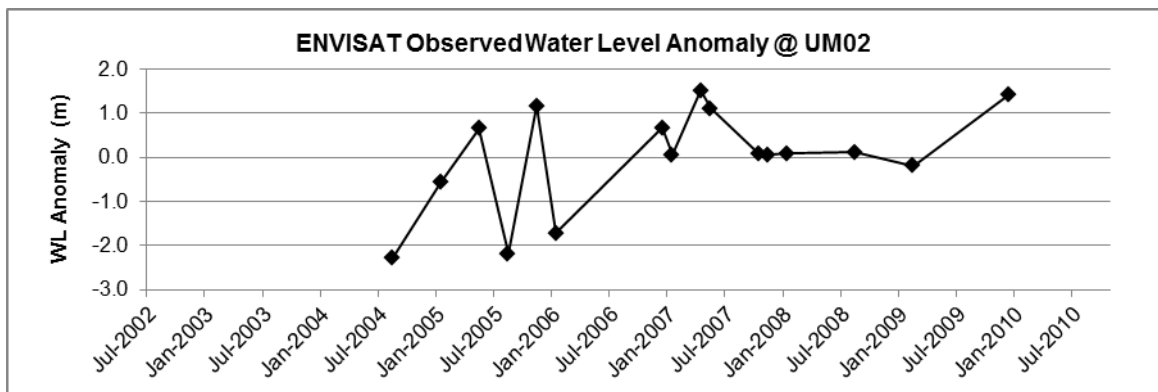


**Figure 3.11** Water level anomaly at virtual station UM02 (river width 53 m) as measured by Envisat RA-2 and processed by Ice-1 retracker

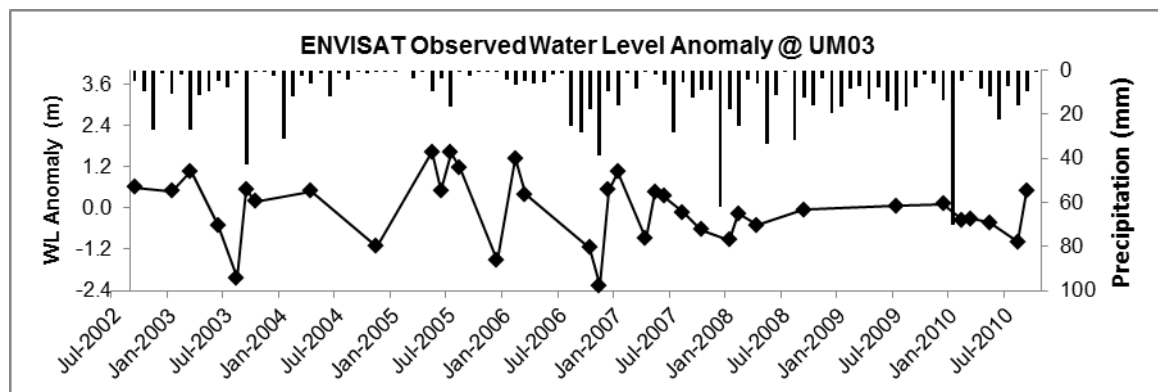


**Figure 3.12** Water level anomaly at virtual station UM03 (river width 54 m) as measured by Envisat RA-2 and processed by Ice-1 retracker. The second y-axis represents the TRMM estimated precipitation

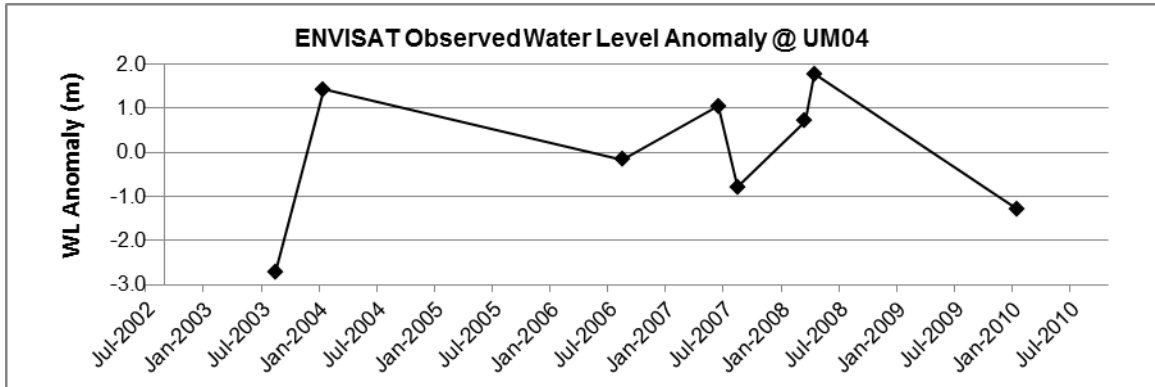


**Figure 3.13** Water level anomaly at virtual station UM04 (river width 61 m) as measured by Envisat RA-2 and processed by Ice-1 retracker

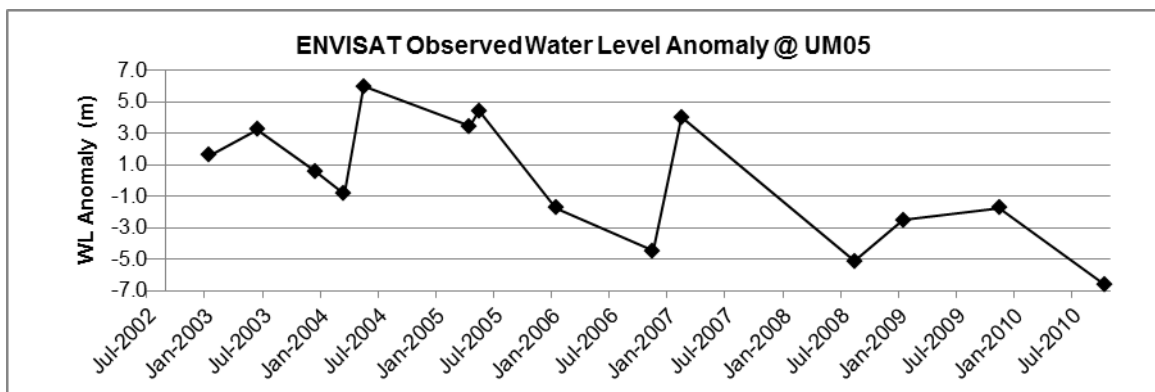


**Figure 3.14** Water level anomaly at virtual station UM05 (river width 177 m) as measured by Envisat RA-2 and processed by Ice-1 retracker

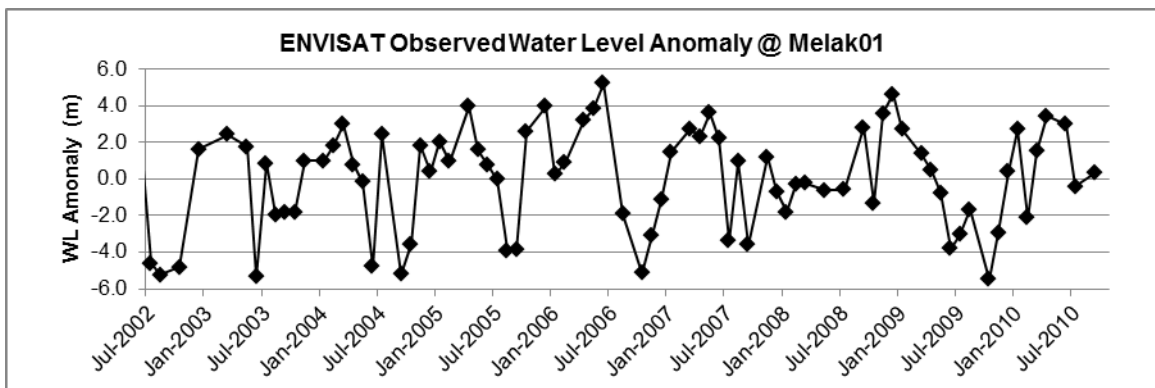


**Figure 3.15** Water level anomaly at virtual station Melak01 (river width 247 m) as measured by Envisat RA-2 and processed by Ice-1 retracker

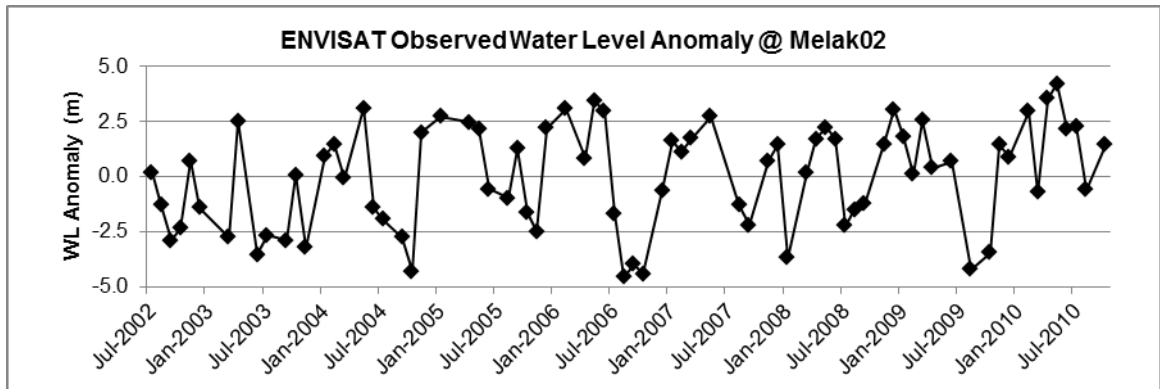


**Figure 3.16** Water level anomaly at virtual station Melak02 (river width 294 m) as measured by Envisat RA-2 and processed by Ice-1 retracker

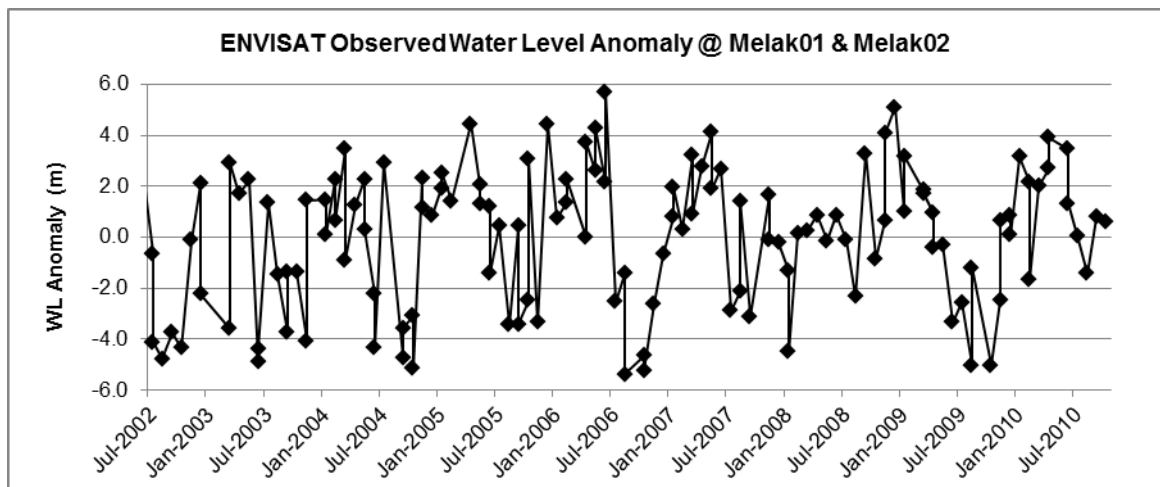


**Figure 3.17** Overall water level anomaly at Melak Town retracked by Ice-1 algorithm over virtual station Melak01 and Melak02

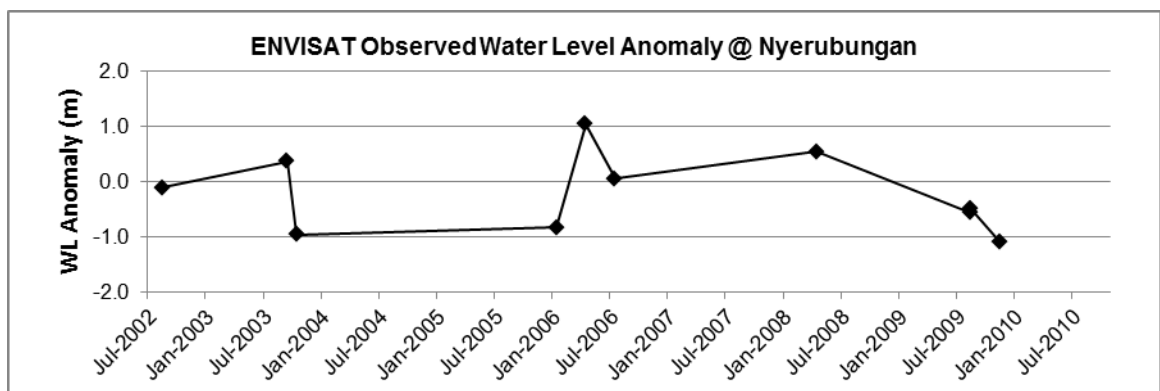


**Figure 3.18** Water level anomaly at virtual station Nyerubungan (river width 35 m) as measured by Envisat RA-2 and processed by Ice-1 retracker



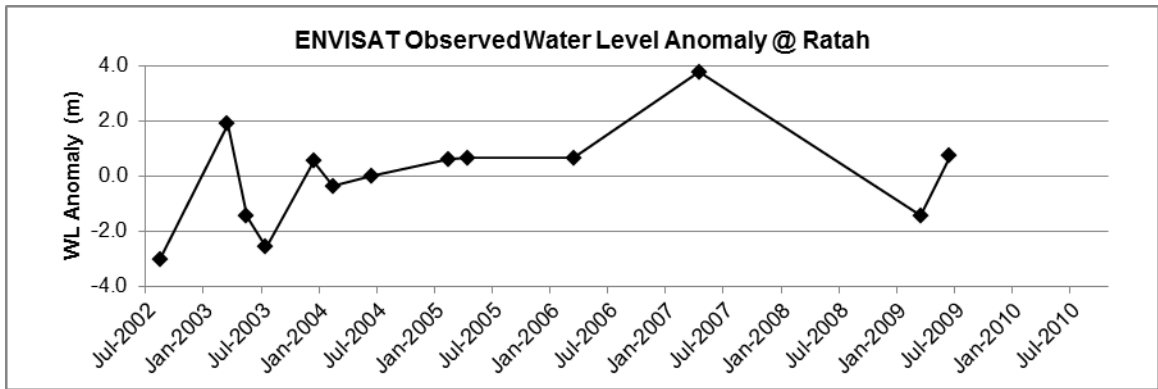


**Figure 3.19** Water level anomaly at virtual station Ratah (river width 55 m) as measured by Envisat RA-2 and processed by Ice-1 retracker

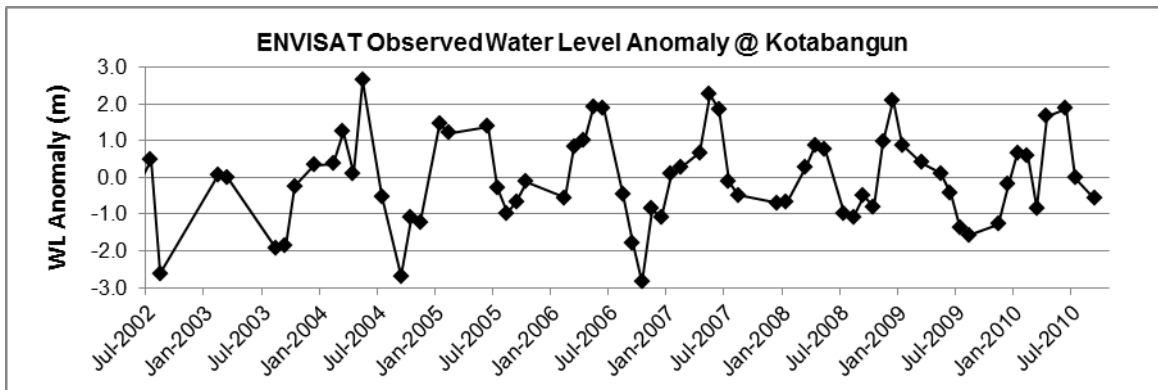


**Figure 3.20** Water level anomaly at virtual station Kotabangun (river width 240 m) as measured by Envisat RA-2 and processed by Ice-1 retracker

From Figure 3.10 until Figure 3.20, it is clear that river width limits the ability of Envisat RA-2 satellite radar altimeter to measure water level, especially considering its spatial and temporal resolution, *i.e.*  $\sim 1.7$  km projected pulse-limited footprint diameter and 35 days revisit period. While 1 km seems a favorable width to expect typical altimetry radar returns from the water surface (Birkett, 1998, Birkett *et al.*, 2002), this study reveals that medium size rivers as narrow as 240 m can still be monitored and validated satisfactorily, given the water surface boundary is identified accurately through medium-resolution optical imageries with a ground resolution of  $\sim 30$  m, such as Landsat. In addition, satellite altimeter measurement over a virtual station with river width of 54 m (Figure 3.12) shows a good temporal coverage between the study periods (2002-2010). Nevertheless, it is hard to conclude that the water level anomaly follows the precipitation pattern. With the absence of validation dataset for this particular virtual station, alternative validation is needed to support previous studies that found that through careful treatment, satellite radar altimetry can still measure the water level of the river with width less than 100 m (Kuo and Kao, 2011, Michailovsky *et al.*, 2012).

To evaluate the performance of satellite altimetry observations at Melak and Kotabangun virtual stations, the water level anomaly inferred by the Ocean, Ice-1, Ice-2 and Sea Ice satellite altimetry retracers was validated with available *in-situ* stage measurements through the assessment using statistics including the standard deviation of the difference, root-mean-square error (RMSE) and correlation coefficient.

With regard to virtual stations at Melak (*i.e.* Melak01 and Melak02), these virtual stations are combined since they are only separated by 14–40 km distance and there is no drastic change in terrain and configuration of the channel. The Ministry of Public Works' gage station is actually installed right in the middle between these two virtual stations as depicted in the map following the plot for water level anomaly. Having two different satellite tracks nearby in fact increases the spatial and temporal sampling intensity for this particular location. The combined water level anomaly from both virtual stations is plotted along with the water level anomaly observed by the gage station.

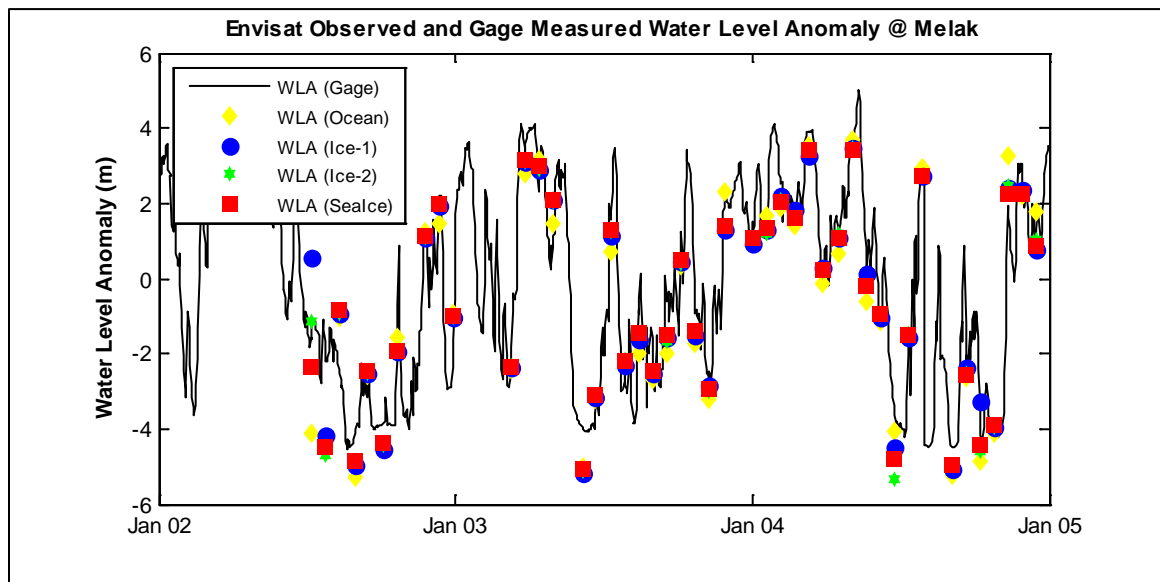
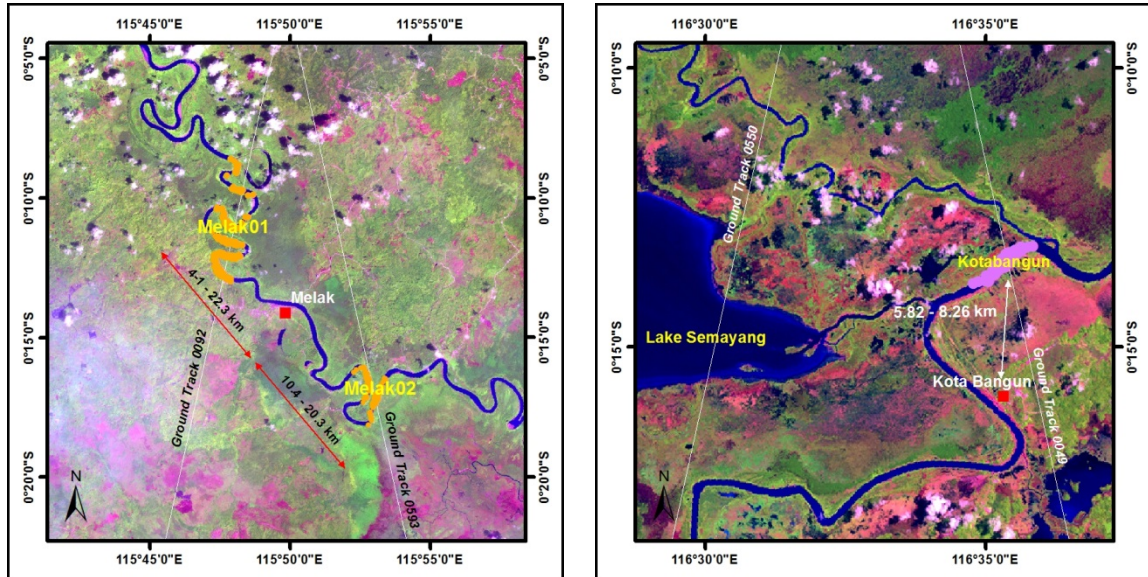


**Figure 3.21** Water level anomaly at Melak as observed by two Envisat passes and retracked by four retracers; compared with in-situ water level anomaly

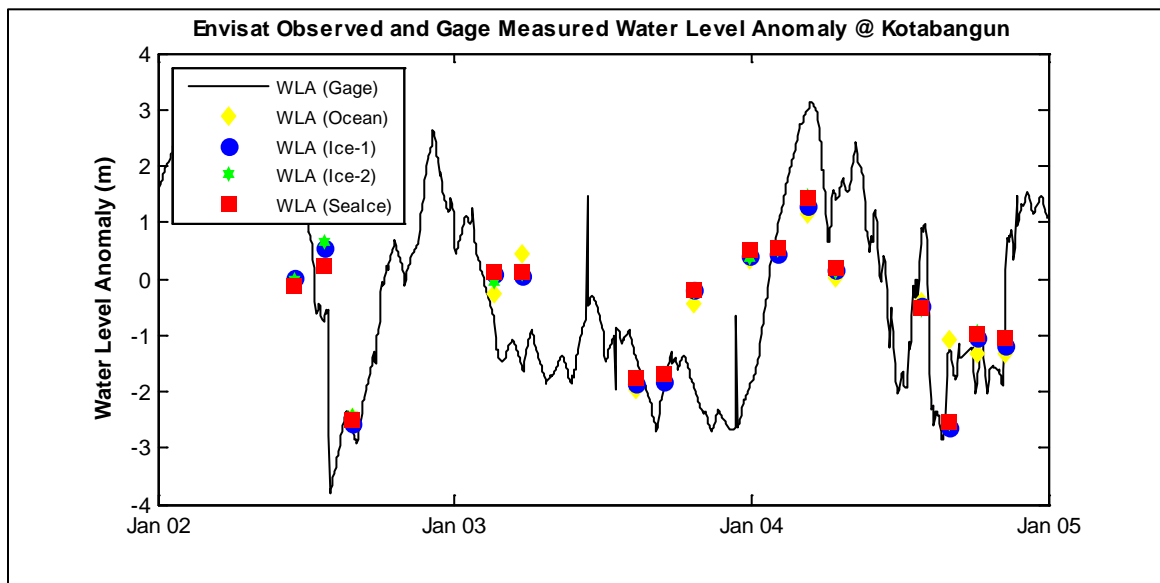
Figure 3.22 (left panel) indicates dynamic channel morphology in this area. The channel is heavily meandering just before and along the virtual station Melak01, which then changes into 13 km straight channel along the heavily populated Melak Town before it is back into lightly meandering channel. In addition, topographic map and digital elevation model shows no drastic changes neither in channel slope, nor the terrain.

Figure 3.22 (right panel) shows there is only one virtual station at Kotabangun, in addition, the Ministry of Public Works' gage station is located from 5.82 to 8.26 km upstream relative to Envisat footprints. Assuming there is no drastic change in the terrain and configuration of the channel, this virtual station is validated by the *in-situ* measurement during 2002 to 2004. The situation in this virtual station is different with the previous validation site, where there is only one Envisat pass, hence less altimetry

measurements can be expected. The same figure shows the interconnection between the main channel (Mahakam River, south on the map), Lake Semayang and its outlet (Semayang River), and one of the tributary (Belayan River, north of the virtual station on the map). Each of this component influences each other in a complex hydraulic flow characteristics.



**Figure 3.22** Location of Envisat virtual stations and in-situ water level gage stations at Melak Town (left) and Kotabangun Town (right)



**Figure 3.23** Water level anomaly at Kotabangun as observed by Envisat pass #25 compared with in-situ water level measurement

**Table 3.3** Performance evaluation of Envisat RA-2 radar altimetry measurements over validated virtual stations at Mahakam River

Virtual station	River width (m)	Cycles covered	Validated measurements	Number of pass	Re-tracker	St. Dev (m)	Correlation coefficient	RMSE (m)
Melak	247	7 – 33	46	2	Ocean	0.820	0.955	0.885
					Ice-1	0.710	0.962	0.720
					Ice-2	0.691	0.966	0.724
					Sealce	0.649	0.970	0.685
Kotabangun	240	6 – 32	17	1	Ocean	1.400	0.652	1.360
					Ice-1	1.332	0.692	1.302
					Ice-2	1.322	0.697	1.287
					Sealce	1.325	0.695	1.290

From the results of performance evaluation above, it is obvious that Envisat radar altimeter measurement over the combined virtual stations at Melak Town outperforms the same measurement carried out over virtual station near Kotabangun Town as indicated by higher correlation coefficient and lower root-mean-square (RMS) Error. These improved results are assumingly due the presence of two satellite tracks that located conveniently close to the *in-situ* gage station that was being used for validation.

With regard to the retracking algorithm inter-comparison, there is no single best retracker among the four retrackers implemented in this study due to the variable result of the performance evaluation. Indeed the Sea Ice retracker performed slightly better than the Ice-1 retracker (*e.g.* lower RMSE) and both retrackers are better than the rest in their implementation in Melak virtual stations. However, for Kotabangun virtual stations, Ice-2 performed just slightly better than the Sea Ice as confirmed by its statistical measures. The Ocean retracker algorithm showed poorest performance among others, as reflected by the results of evaluation over Melak and Kotabangun virtual stations.

It is interesting to investigate the fluctuation range of the water level anomaly retracked by each individual retrackers for each the virtual stations (*i.e.* Melak and Kotabangun). From Figure 3.21 and 3.23, it is obvious that the water level anomaly at Kotabangun has less range than those measured at Melak, which indicates that Mahakam River profile fluctuates more upstream than downstream.

To facilitate visual investigation, the correlation between the satellite altimetry observed and gage-measured are presented in the scatter plots between each retracking algorithm and the gage-measured water level anomaly. In addition, the correlation also calculated and presented in the same plots.

From Figure 3.24 and 3.25 it is obvious that Ocean and Ice-1 retrackers inferred water level anomaly with lowest correlation with the gage-measured water level anomaly.

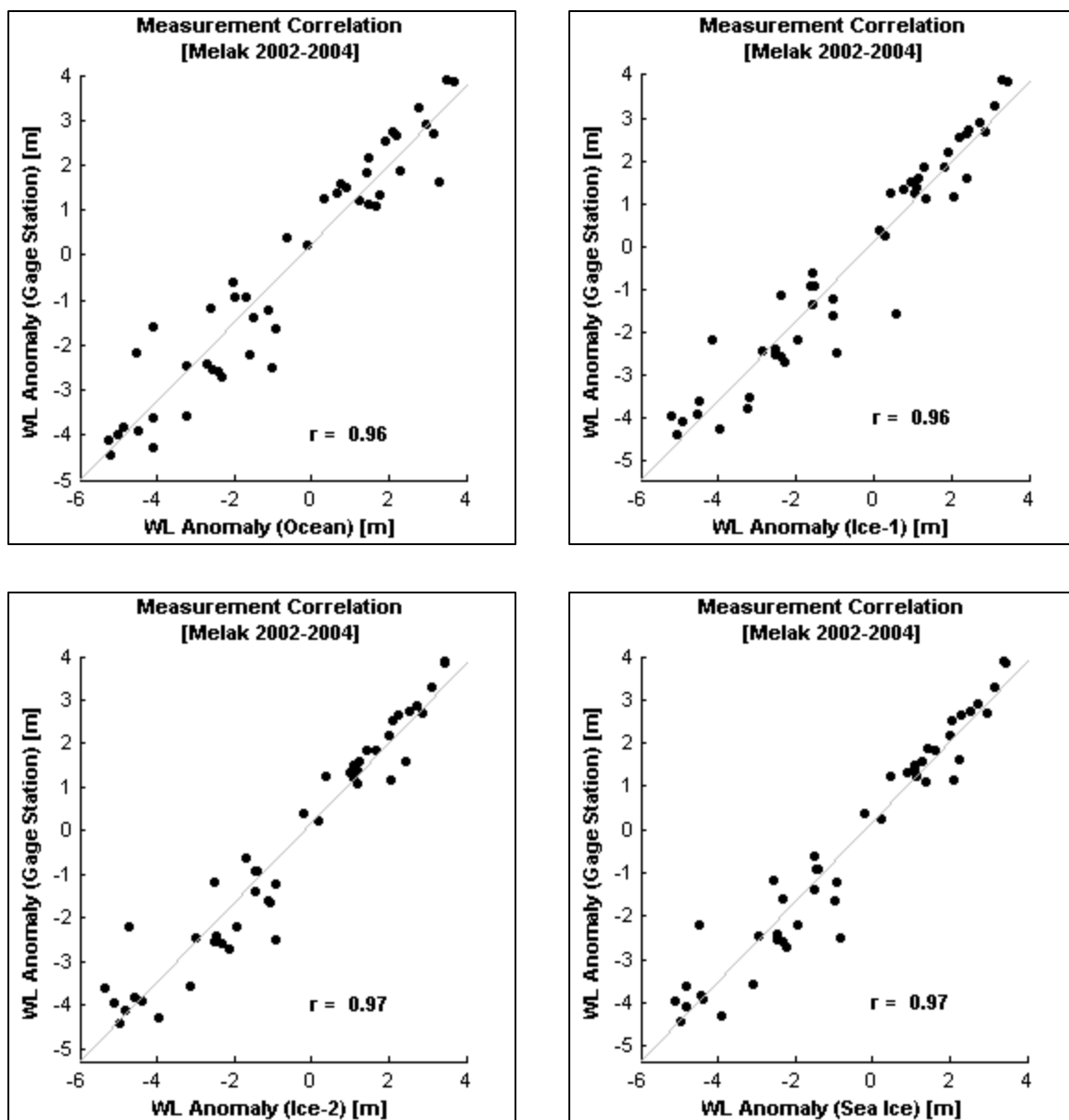


**Figure 3.24** Correlation between water level anomaly measured by Envisat altimeter and processed with Ocean (top left), Ice-1 (top right), Ice-2 (bottom left) and Sea Ice (bottom right) retracers and in-situ water level measurement over Melak Town

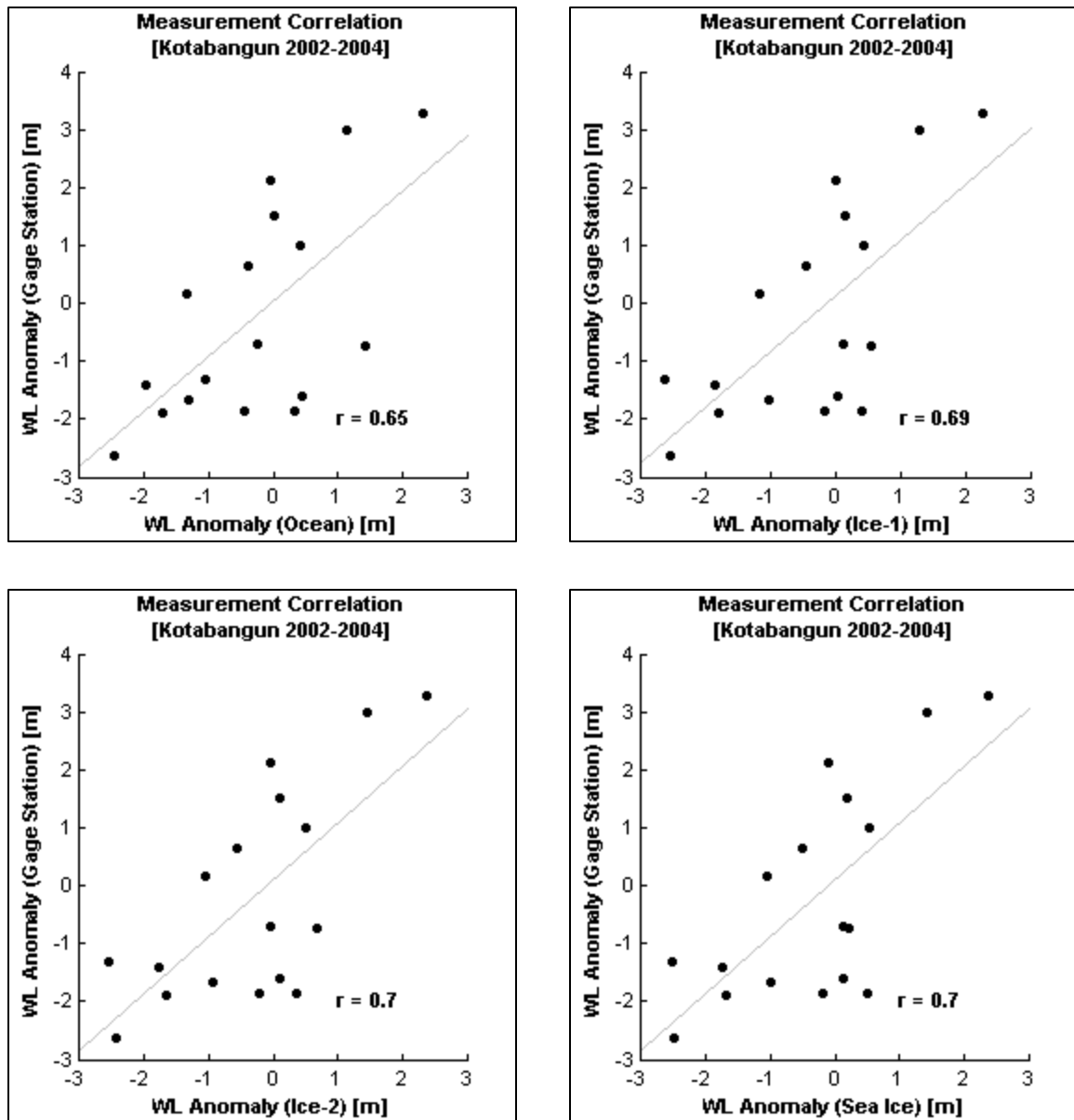


**Figure 3.25** Correlation between water level anomaly measured by Envisat altimeter and processed with Ocean (top left), Ice-1 (top right), Ice-2 (bottom left) and Sea Ice (bottom right) retracers and in-situ water level measurement over Kotabangun Town

With the coefficient of correlation **up to 0.97**, the satellite radar altimetry presents very convenient alternative for monitoring of the medium-sized river (200-800 m width), even for poorly-gauged basin such as the Mahakam Watershed. Referring to other studies, the magnitude of root-mean-square error (RMSE) reflected in this study, *i.e.* 0.69, is just about the average of RMSE obtained from other studies deal with medium sized rivers (200-800 m width).

**Table 3.4** Summary of studies on satellite radar altimetry for water level over river

Reference	Location	River Width	Satellite / Sensor	Reported Error (m)
Koblinsky <i>et al</i> (1983)	Amazon Basin	N/A	Geosat	STDE: 0.31-1.68 m
Birkett, <i>et al</i> (1998, 2002)	Amazon Basin	1.5 km	TOPEX / Poseidon	RMSE: 0.60 m
Kouraev <i>et al</i> (2004)	Ob' River	3 km	TOPEX / Poseidon	%: 8 %
Frappart <i>et al</i> (2006)	Mekong River	450 m	Envisat	RMSE: 0.23 m
			TOPEX / Poseidon	RMSE: 0.15 m
Zakharova <i>et al</i> (2007)	Euphrat-Tigris River	N/A	T/P, GFO, Envisat	N/A
Kuo and Kao (2011)	Bajhang River	100 m	Jason-2	STDE: 0.31 m
Michailovsky <i>et al</i> (2012)	Zambezi River	80 m	Envisat	RMSE: 0.72 m
Sulistioadi (2013)	Mahakam River	279 m	Envisat	RMSE: 0.69 m

\* STDE (Standard Deviation of Error), % (% difference), RMSE (Root Mean Square Error)

It is important to note however, that this study did not adjust the magnitude of the satellite altimetry range measurements in any way. Beside a careful spatial selection of the range measurements with the projected nadir footprint center within the water body and the removal of outliers, the only intervention applied to the dataset was the selection of the range measurements based on its waveform shape to strictly follow the standard waveform shape for inland water body as described in the previous studies (Koblinsky *et al*, 1983; Birkett, 1988; Berry *et al*, 2005; Dabo-Niang *et al*, 2007). Therefore, there must be ample room for improvement to increase the accuracy of the satellite altimetry measurement of river water level, especially for this study area.

For the case of Kotabangun area, further investigation is proposed considering the complexities of hydraulic flow in this area, due to the effects of backwater flow and mixing of outflow from the lake outlets and Belayan River. As previously studied by Hidayat *et al.* (2012), vast areas in the middle Mahakam Lake and Wetland becomes inundated during high flows, as reflected in the synthetic aperture radar image. In addition, the influence of ocean tides is striking up to this part of Mahakam Watershed, even the distance to the estuary is quite far, *i.e.* ~300 km, hence creating backwater effects that influence the water level profile (Hidayat *et al.* 2011a).

## (2) Karangmumus River

Karangmumus River is a very narrow channel (3 to 45 m width), which is very important for the residents of Samarinda City in East Kalimantan. Due to poor land cover and its short distance to the ocean, this sub-watershed often experiences gradually increasing and steady high discharge during heavy rainfall. This small channel is also affected by ocean tide that intrudes through the Mahakam Delta. These factors led to the occurrence of slow-paced flood that inundated most of the residential areas two to three times a year. The northeast-southwest river orientation makes it difficult to find the crossing Envisat ground tracks. However, high resolution IKONOS image (1 m ground resolution) allows detailed selection of the altimeter ground tracks that fall within its narrow channel.



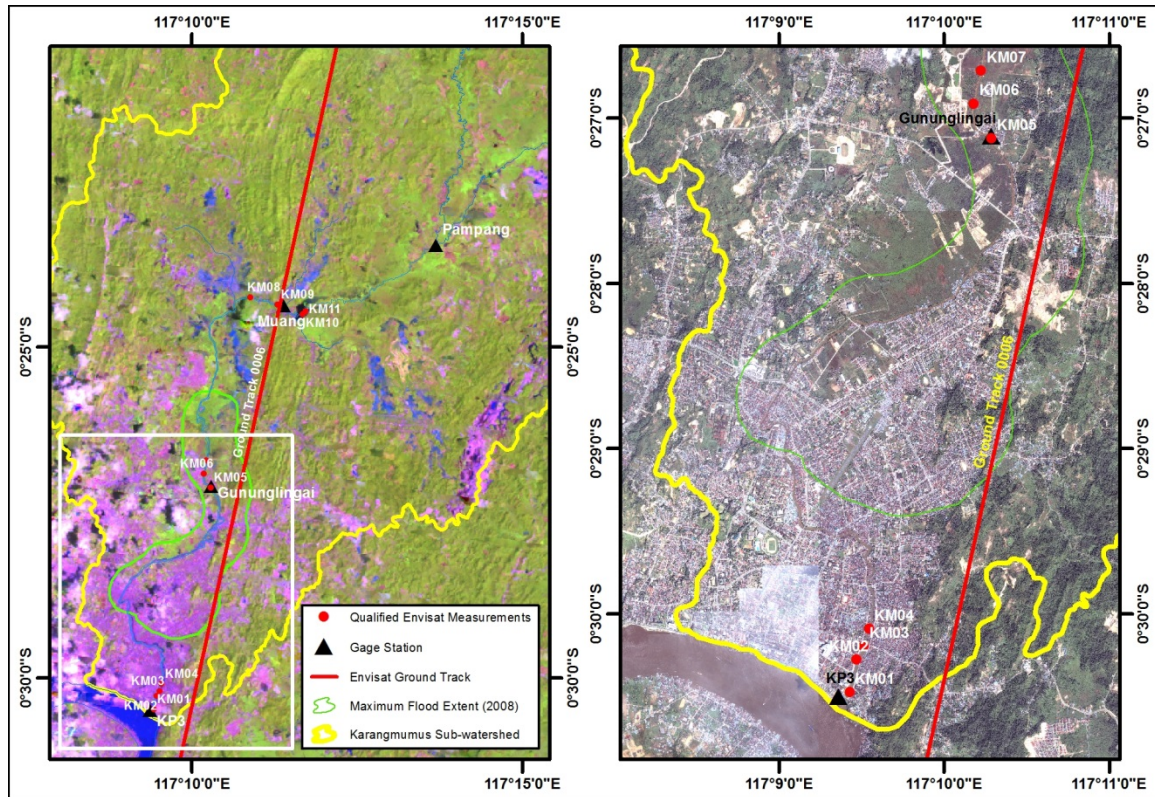


**Figure 3.26** Overview of Karangmumus Sub-watershed and Envisat ground track with background of Landsat-7 image of January 2007 (left) and IKONOS of February 2002 (right, in the extent of white box of the left image)

**Table 3.5** Qualified Envisat RA-2 range measurements for Karangmumus River

Cycle	Date	ENV_ID	Longitude	Latitude	Water Surface Elevation (m)*	Remarks
8	07/23/2002	KM08	117.181540	-0.404124	59.63	
9	08/27/2002	KM10	117.194581	-0.408362	55.18	Located in Benanga Reservoir
13	01/13/2003	KM11	117.195384	-0.407573	62.64	Located in Benanga Reservoir
23	12/30/2003	KM01	117.157190	-0.507934	57.77	
23	12/30/2003	KM02	117.157910	-0.504634	57.38	
28	06/22/2004	KM09	117.188367	-0.405981	63.33	Closest point to field gage (47 m)
37	05/03/2005	KM06	117.169721	-0.448573	59.59	
37	05/03/2005	KM07	117.170441	-0.445263	59.57	
39	07/12/2005	KM03	117.158610	-0.503317	57.42	
42	10/25/2005	KM05	117.171486	-0.452076	63.81	
49	06/27/2006	KM04	117.159139	-0.501533	58.76	

\* Water surface elevation is the measured through ICE-1 waveform retracking

After careful examination, 11 qualified individual Envisat RA-2 measurements (e.g. those with waveform shapes that closely match the shape of common waveform as



generated by radar pulse return from the water body) were selected and processed to estimate water level anomaly. All measurement points are separated by some distances, although a few measurements are clustered separately. The results of waveform evaluation and the spatial distribution of the measurement points within each cluster are as follow.

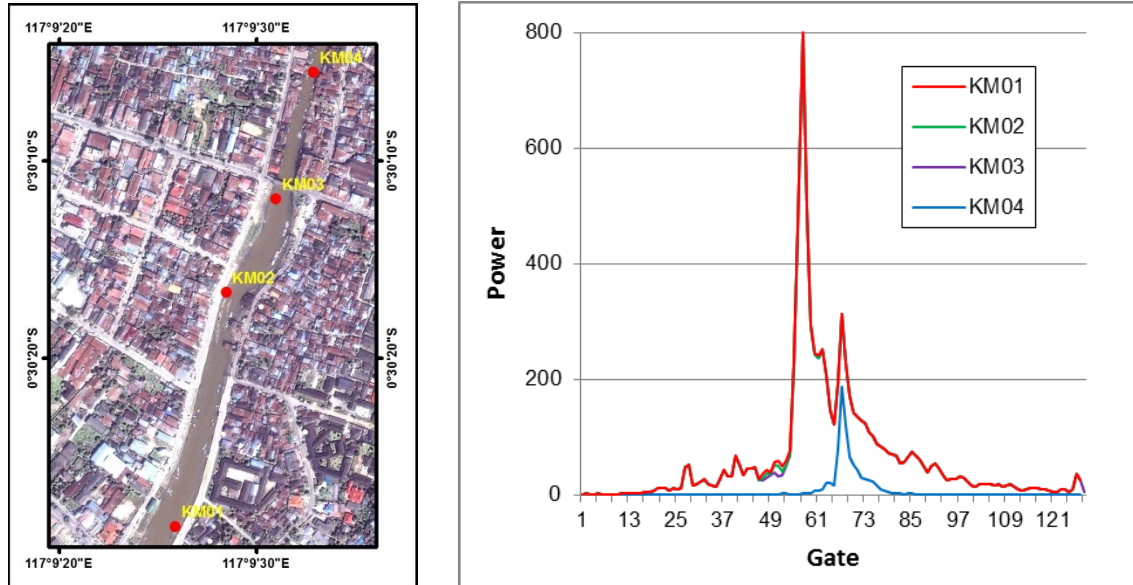


**Figure 3.27** Distribution and Envisat RA-2 waveform shape of downstream of Karangmumus River (width ~22-45 m)

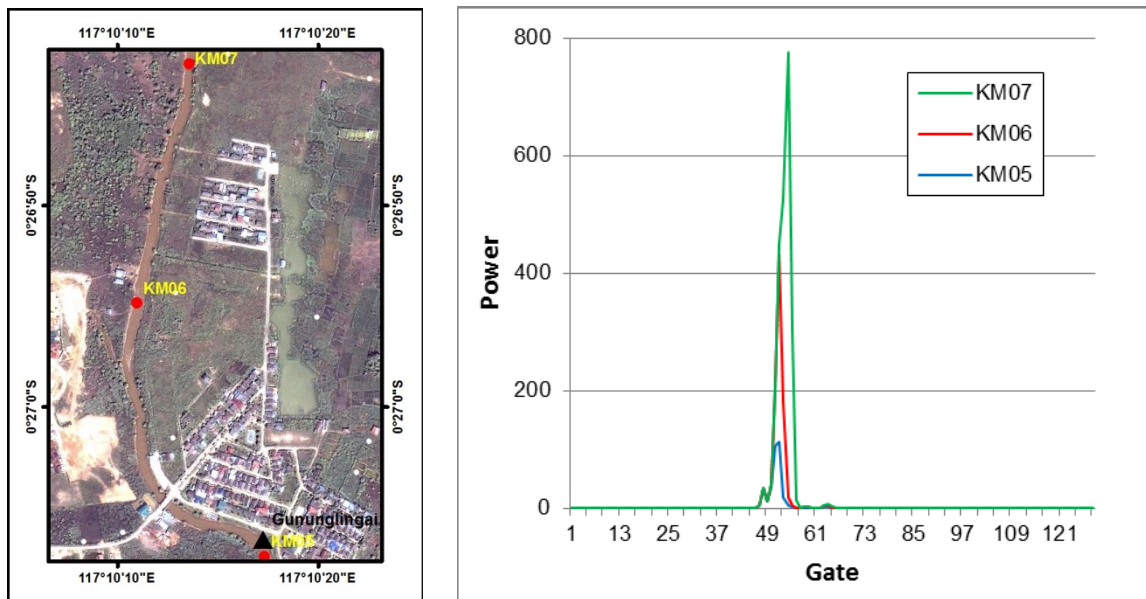


**Figure 3.28** Distribution and Envisat RA-2 waveform shape of middle part of Karangmumus River (width ~8-17 m)

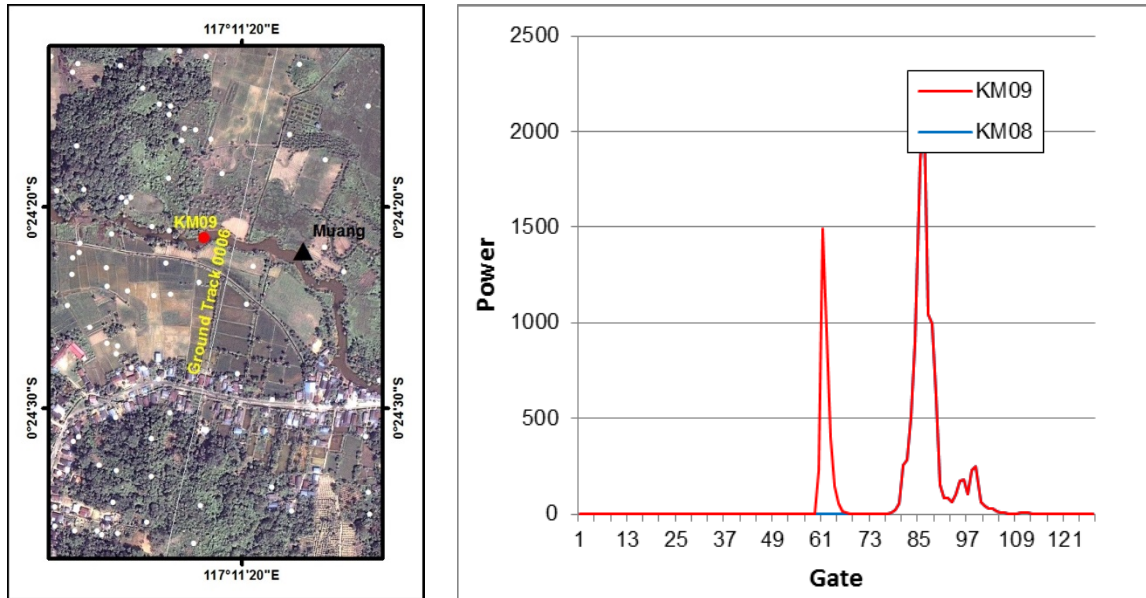


**Figure 3.29** Distribution and Envisat RA-2 waveform shape of upstream part of Karangmumus River (width ~3-12 m)

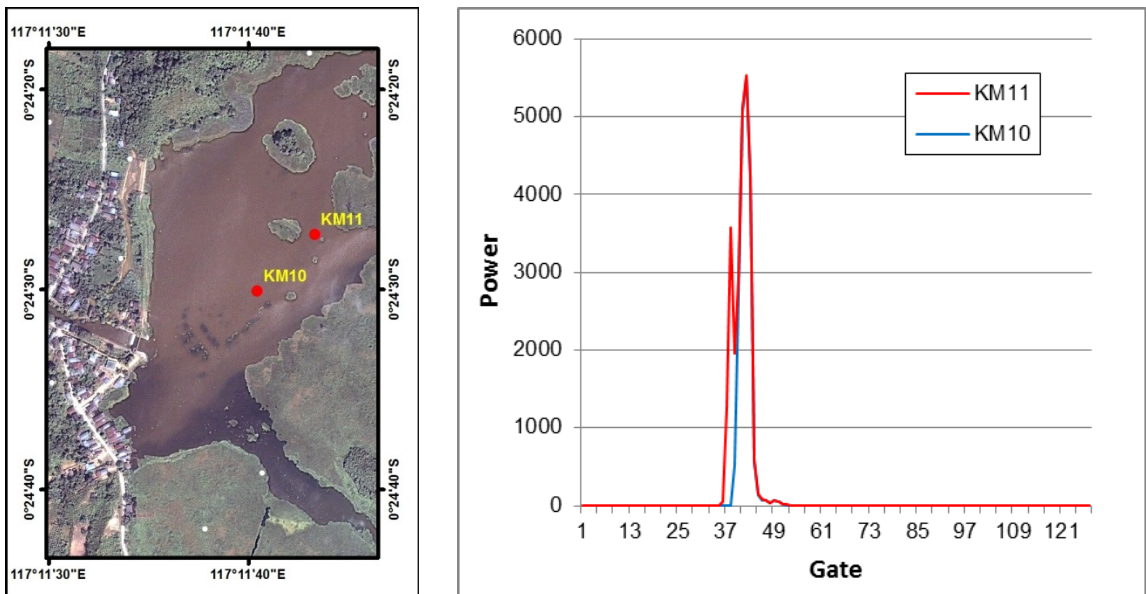


**Figure 3.30** Distribution and Envisat RA-2 waveform shape of Benanga Reservoir in upstream part of Karangmumus River (width ~300 m)

Given the limitation on its spatial and temporal resolution, the satellite altimetry measurement still indicates the inter-annual water level fluctuation of the Karangmumus River during 2004 to 2006, as compared to the magnitude of precipitation. Due to unknown relationship with the vertical datum, only water surface anomaly is presented. In addition, the in-situ measurement record from the nearest available gage stations (*i.e.*

Pampang, Muang, Gununglingai, and the outlet of the Karangmumus River) are available only during 2008–2010 so that the performance of satellite altimetry measurements over this very small river cannot be evaluated. It is interesting to note however, that the low-level period does not always occur in the same month or even season. From the altimeter observation, the high water level was occurred on June–July 2004 and November 2005–January 2006 while the low water level was experienced in January 2004, July 2005 and July 2006. This trend seems linearly related with the rainfall occurrence as plotted along in Figure 3.31, and shows lags between the rainfall and the water level peak.

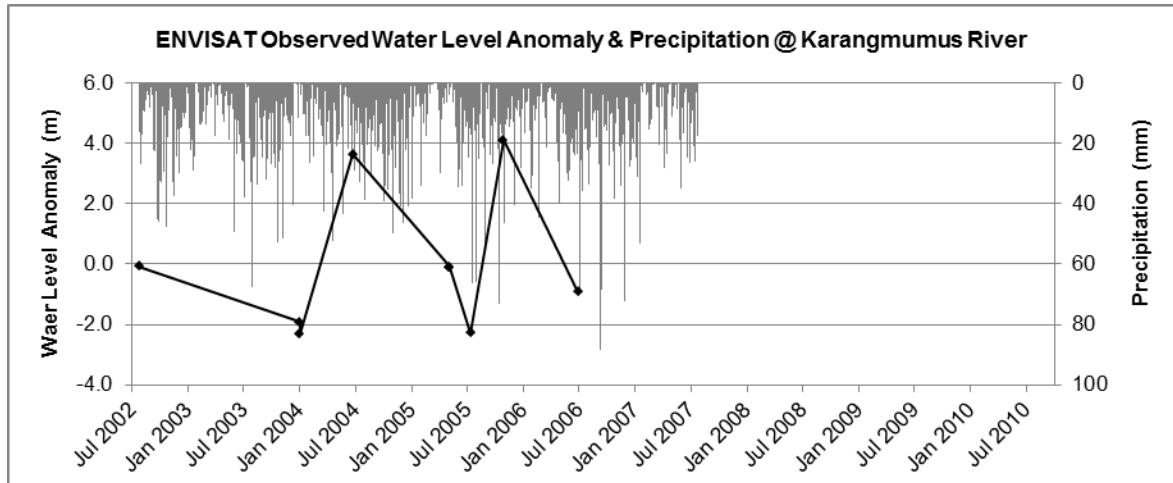


**Figure 3.31** Water level anomaly of Karangmumus River from Envisat RA-2

Due to very limited points of measurement, it seems not viable to monitor water level of this class of river (width <40 m) through satellite altimetry technique. Spatial (*e.g.* the size of radar footprint) and temporal (*e.g.* satellite revisit period) resolution are the most problematic issues to do such effort. This result is similar with the measurement over the tributaries and upstream Mahakam River as presented in the previous section.

#### 3.4.2. Water Level of Lake Semayang, Lake Matano and Lake Towuti

Inland water has been known to produce different, sometimes irregular waveform shapes and pattern compared to the ocean with respect to their response to radar pulse signal transmitted by satellite based active sensor. The response of much smaller water bodies in the form of small to medium-sized rivers had been discussed in the previous section. In this section, the waveform patterns of lakes with minimum width of about 2 kilometers are explored. With identical procedure, three lakes with completely different geomorphology and physical characteristics are studied for their response to satellite altimetry measurement. Some examples of distinguished waveform shapes from Lake Semayang, Lake Matano and Lake Towuti at different buffer distances from the lakeshore are presented below.

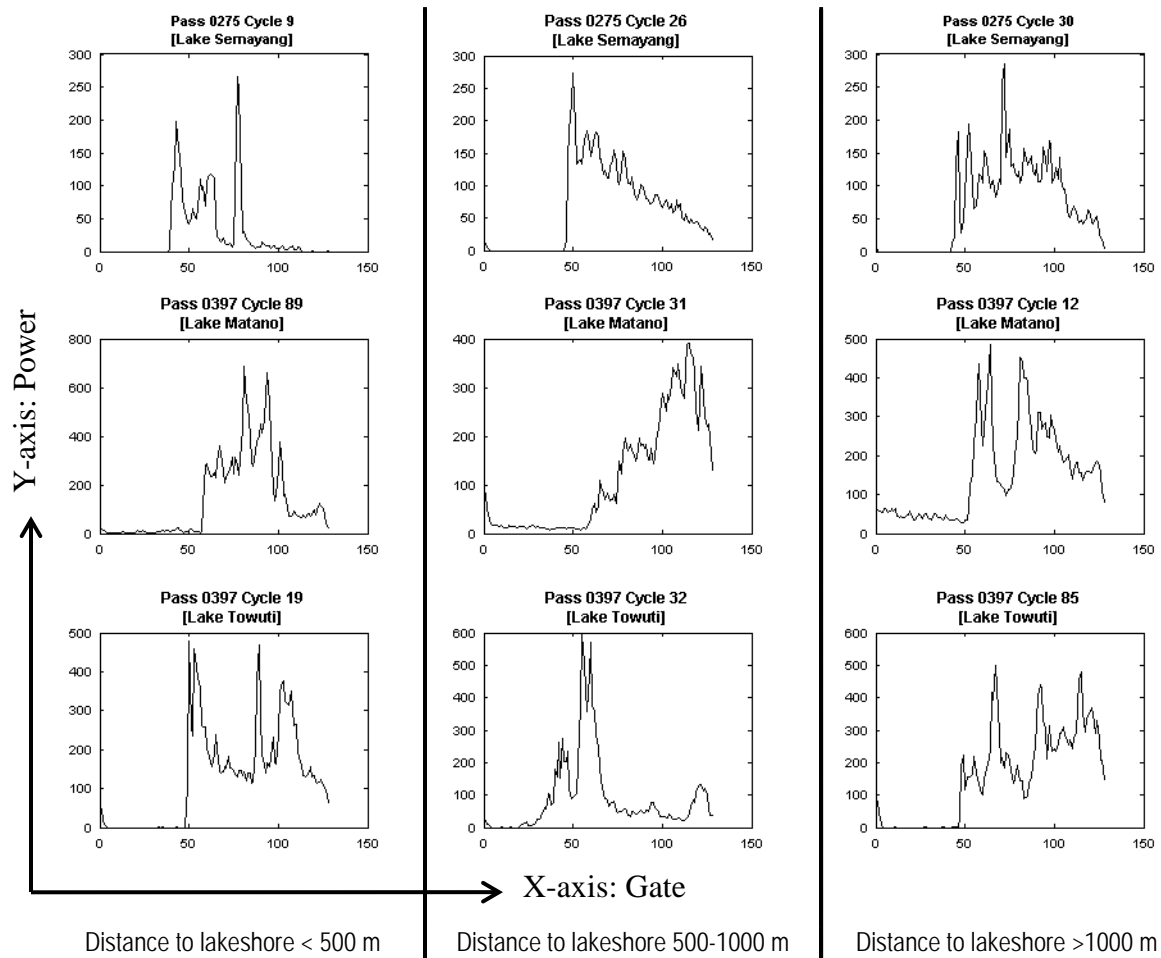


**Figure 3.32** Distinguished waveform shapes as reflected by Lake Semayang, Lake Matano and Lake Towuti at different buffer distances to the lakeshore

Clearly, the waveform shapes resulted from satellite altimetry measurement over the lakes are more variable compare to those over the small to medium-sized rivers. From Figure 3.32, one can see the typical ocean-like, multi and low peaks, gradually rising and many other kinds of irregular patterns. Considering the dynamic of the surface of the lake and river, this is understandable, since lake has much larger extent and much more influenced by wind that may develop wave with some height. With the absence of verified categorization of waveforms shapes especially those occur on inland waters, other than Dabo-Niang *et al.* (2007), further study on this field might worth to consider in the future.

The next assessment is the selection of qualified waveforms and the outliers to indicate which altimetry measurements processed further. The summary on the waveform qualification is presented in the following table.

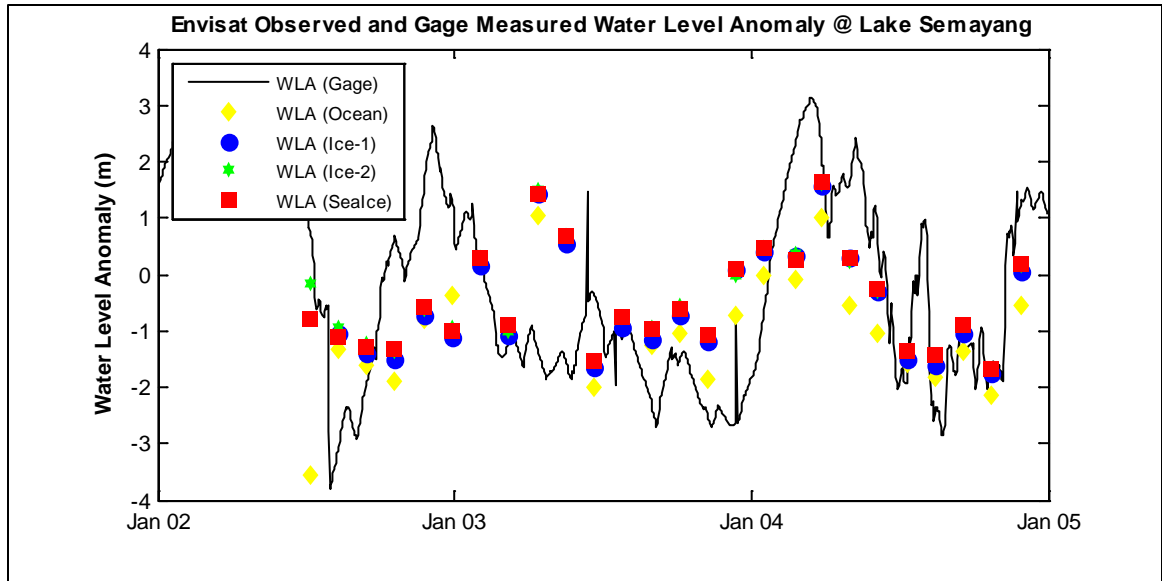
**Table 3.6** The number of qualified and non-qualified altimeter measurements and outliers over Lake Semayang, Lake Matano and Lake Towuti

Location	Lake width (m)	Cycles Covered	Distance to Lakeshore (m)	Measurements within water body (#)	Qualified Measurement (#)	Qualified (%)	Non-qualified Measurement (#)	Non-qualified (%)	No. of outlier
Lake Semayang	2,388 m	10 – 88	< 500 m	466	438	94.0	28	6.0	9
			500 m – 1 km	257	243	94.6	14	5.4	4
			> 1000 m	157	156	99.4	1	0.6	2
Lake Matano	8,159 m	8 – 79	< 500 m	453	416	91.8	37	8.2	68
			500 m – 1 km	253	215	85.0	38	15.0	27
			> 1000 m	989	805	81.4	184	18.6	115
Lake Towuti	28,818 m	8 – 79	< 500 m	1314	786	59.8	528	40.2	79
			500 m – 1 km	1328	764	57.5	564	42.5	64
			> 1000 m	2450	1353	54.3	1137	45.7	156

Similar to the result of satellite altimetry measurements to the small to medium-sized river in the previous section, most of the radar pulse returns produced qualified waveforms that were used to compute water level anomaly at these three lakes. On the other hand, the waveforms from Lake Matano and Lake Towuti present more variable shapes compare to Lake Semayang. It is also noticed that separation of distance to the lakeshore seems does not significantly affect the number of qualified waveforms. For instance, from Table 3.6 one can see the percentage of qualified waveforms for the lake surface with distance more than 1 km in Lake Matano and Lake Towuti is lower than those closer to the lakeshore. However, an opposite situation is shown by the waveforms from Lake Semayang. This complex result calls for further investigation in the field of satellite altimetry application for small and medium lakes in the tropics, given the fact that the land cover does not necessarily influence the shapes of the returned altimeter waveform. One possible cause of is the lake surface roughness, which is caused by the range of crest and trough of the wave, which is mainly driven by the wind.

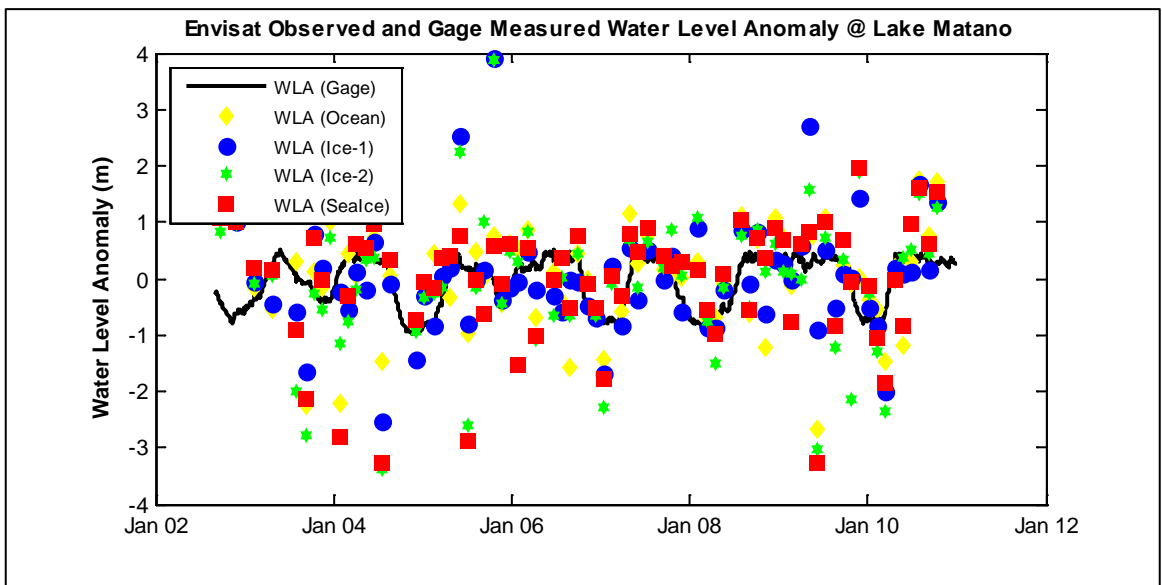
Upon the completion of waveform sorting, the range measurements as performed by Ocean, Ice-1, Ice-2 and Sea Ice retracers were processed and evaluated against observed water level from *in-situ* gage station. For Lake Semayang, the gage station used for validation is the same with the one used to validate the Mahakam River's water level, *i.e.* Kotabangun gage station dated 2002–2004. For Lake Matano, the gage station is located right at the outlet of the lake, which is operated to monitor the supply of PT Vale Indonesia's hydro power operation.

Figure 3.33 below shows the water level anomaly measured by satellite altimetry at Lake Semayang, which follows the inter-annual fluctuation of water level measured in Kotabangun gage station, although the water level anomaly is not close enough to the *in-situ* measured water level anomaly. It has been discussed in the previous section however, that complex hydraulic flow characteristics of this area may play a major role in the discrepancies of water profile in different locations.



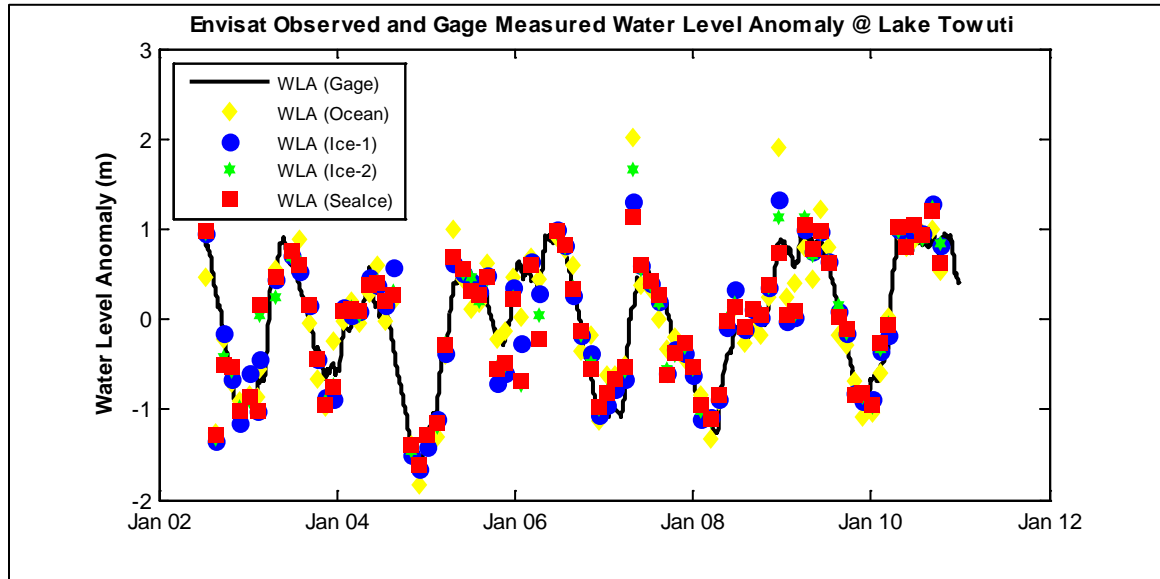
**Figure 3.33** Water level anomaly at Lake Semayang as measured by Envisat RA-2 and processed by all retracker, compared with in-situ measurement

Figure 3.34 below shows that satellite altimetry measurements over Lake Matano follows the water level anomaly observed by *in-situ* gage station; even the overall fluctuation rate is much lower compared to those in Lake Semayang.



**Figure 3.34** Water level anomaly at Lake Matano as measured by Envisat RA-2 and processed by all retracker, compared with in-situ measurement

On the other hand, it is also obvious that the Envisat radar altimetry measurements present considerable noises, especially those inferred by the Ocean retracker. Figure 3.35 below shows the satellite altimetry derived and *in-situ* gaged water level anomaly at Lake Towuti and indicates the best match among the three lakes studied. In this location, the satellite altimetry derived water level anomaly seems closely follow the water level anomaly measured in the field.



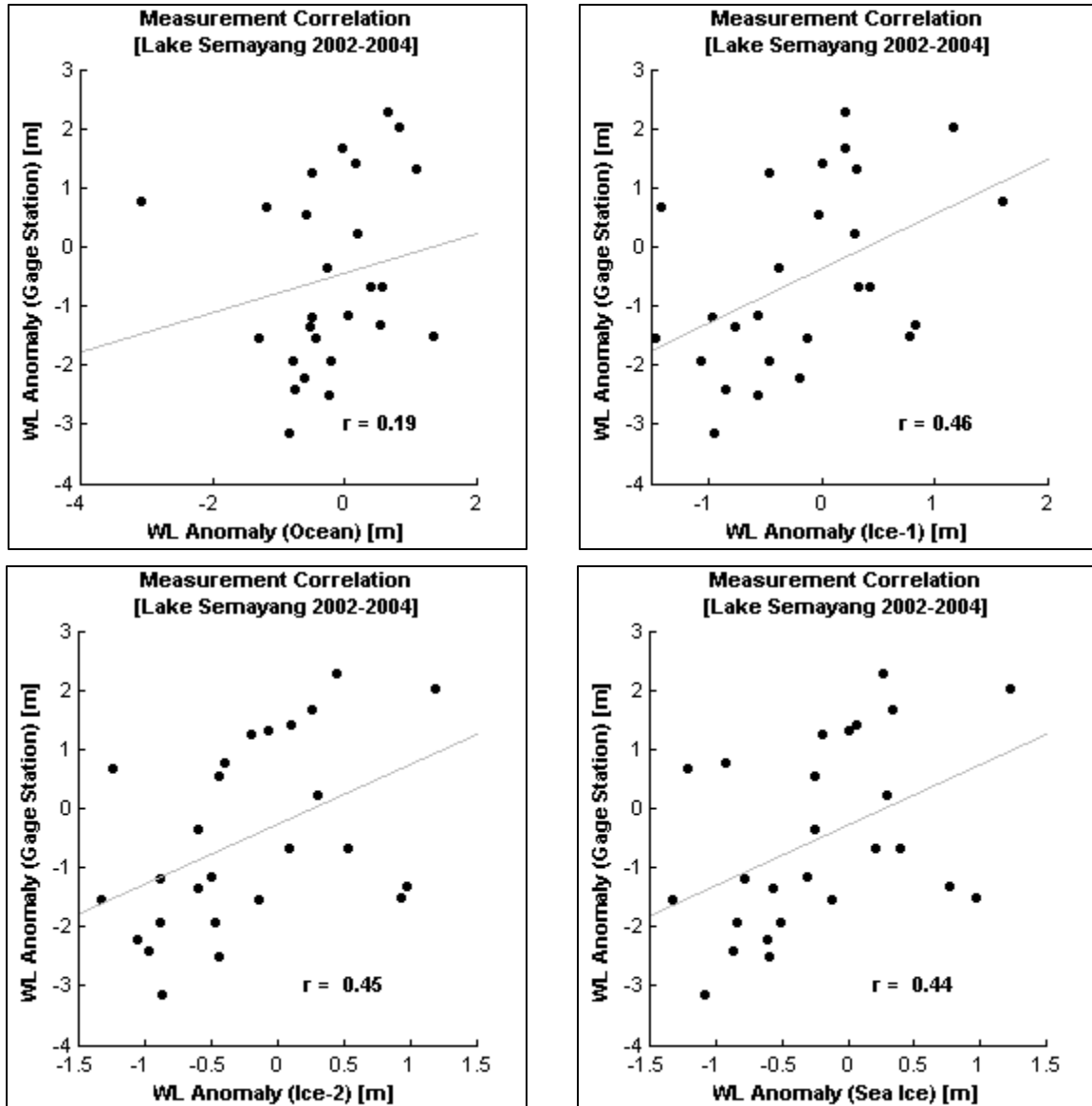
**Figure 3.35** Water level anomaly at Lake Towuti as measured by Envisat RA-2 and processed by all retracker, compared with *in-situ* measurement

Physically, the three lakes being studied possess very different characteristics. Lake Semayang is naturally a very shallow alluvial lake, which lies in a very low elevation (*e.g.* less than 20 m above sea level) and functions as an instrumental temporary storage in the retarding basin complex of Middle Mahakam Lake and Wetlands (Estiaty *et al.*, 2007). Along with other two major lakes, hundreds of small lakes and vast floodplain of the Middle Mahakam Lake and Wetlands complex, Lake Semayang regulates complicated flow including flashy discharge in the magnitude of 2,000-3,000 m<sup>3</sup>/s, which is originated from the hilly and mountainous upper Mahakam sub-basins with maximum annual precipitation of 4,000 mm, medium-paced flow from Mahakam River tributaries and the backwater effects coming from the Makassar Strait through the Mahakam Delta. As the result, the water level profile of Lake Semayang is very dynamic and somehow not fully controlled by the precipitation inputs.

Lake Matano is a very gentle and ultra-deep lake, which regulates a maximum annual precipitation of 2,800 mm into very low mean discharge of 133 m<sup>3</sup>/s at its outlet. Other research indicates that nearly half of the water within the catchment upstream of Lake Matano circulates through groundwater interaction, which explains why this particular lake outflows less discharge compared to its inflow (Hehanussa, 2006). As the result, the water level profile fluctuates very gently and ranges in the magnitude of 1.2 m.

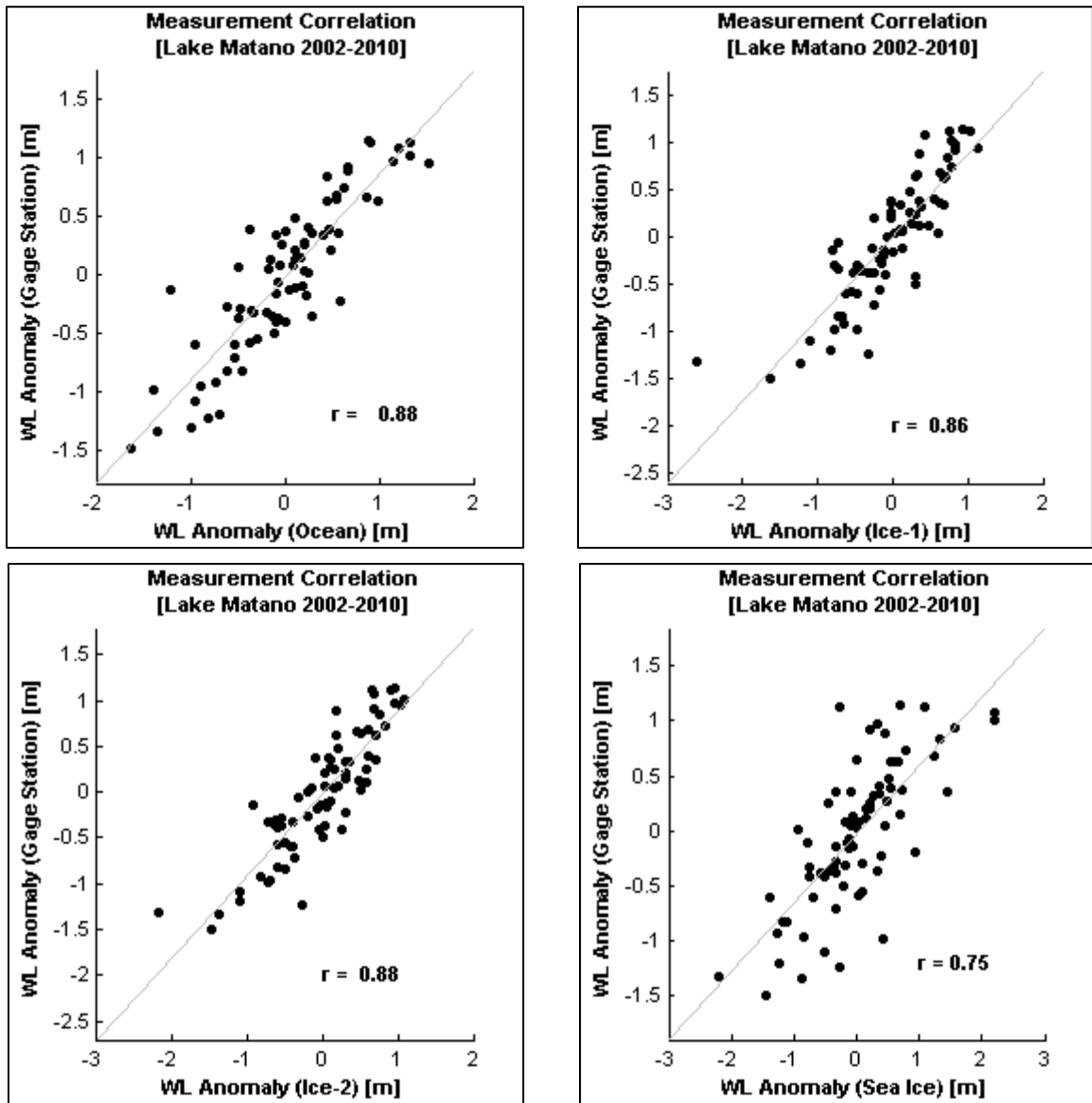
Lake Towuti is the largest lake among all lakes in Malili Lakes Complex but possesses less depth compared to the Lake Matano. Considering its surface area, this lake is influenced by wind that comprises the Lake Breeze, which blocks the cloud propagation and pushes the precipitating cloud over the lakeshore (Renggono, N.D). The water level profile of this lake also fluctuates gently in the ranges of 1.4 m.

Figure 3.36, 3.37 and 3.38 illustrate the correlation between the Envisat radar altimeter measurements as processed by Ocean, Ice-1, Ice-2 and Sea Ice retrackerers with the gage measured water level anomaly for Lake Semayang, Lake Matano and Lake Towuti, respectively.



**Figure 3.36** Correlation between water level anomaly at Lake Semayang as measured by Envisat RA-2 altimeter and processed with Ocean (top left), Ice-1 (top right), Ice-2 (bottom left) and Sea Ice (bottom right) retrackerers





**Figure 3.37** Correlation between water level anomaly at Lake Matano as measured by Envisat RA-2 altimeter and processed with Ocean (top left), Ice-1 (top right), Ice-2 (bottom left) and Sea Ice (bottom right) retrackers

In terms of performance, Envisat radar altimetry measurements over Lake Towuti outperform those on Lake Matano and Lake Semayang, considering the lower RMS error obtained by the best retracker for each lakes (0.27 for Lake Towuti compared to 0.33 for Lake Matano and 0.45 for Lake Semayang, see Table 3.7 below). This fact is further confirmed by the scatterplots of the correlation between the altimetry measured and gage measured water level anomaly in Figure 3.36, 3.37 and 3.38, which shows higher correlation between altimetry and gage measured water level anomaly over Lake Towuti and Lake Matano, compared to more scattered measurements over Lake Semayang.

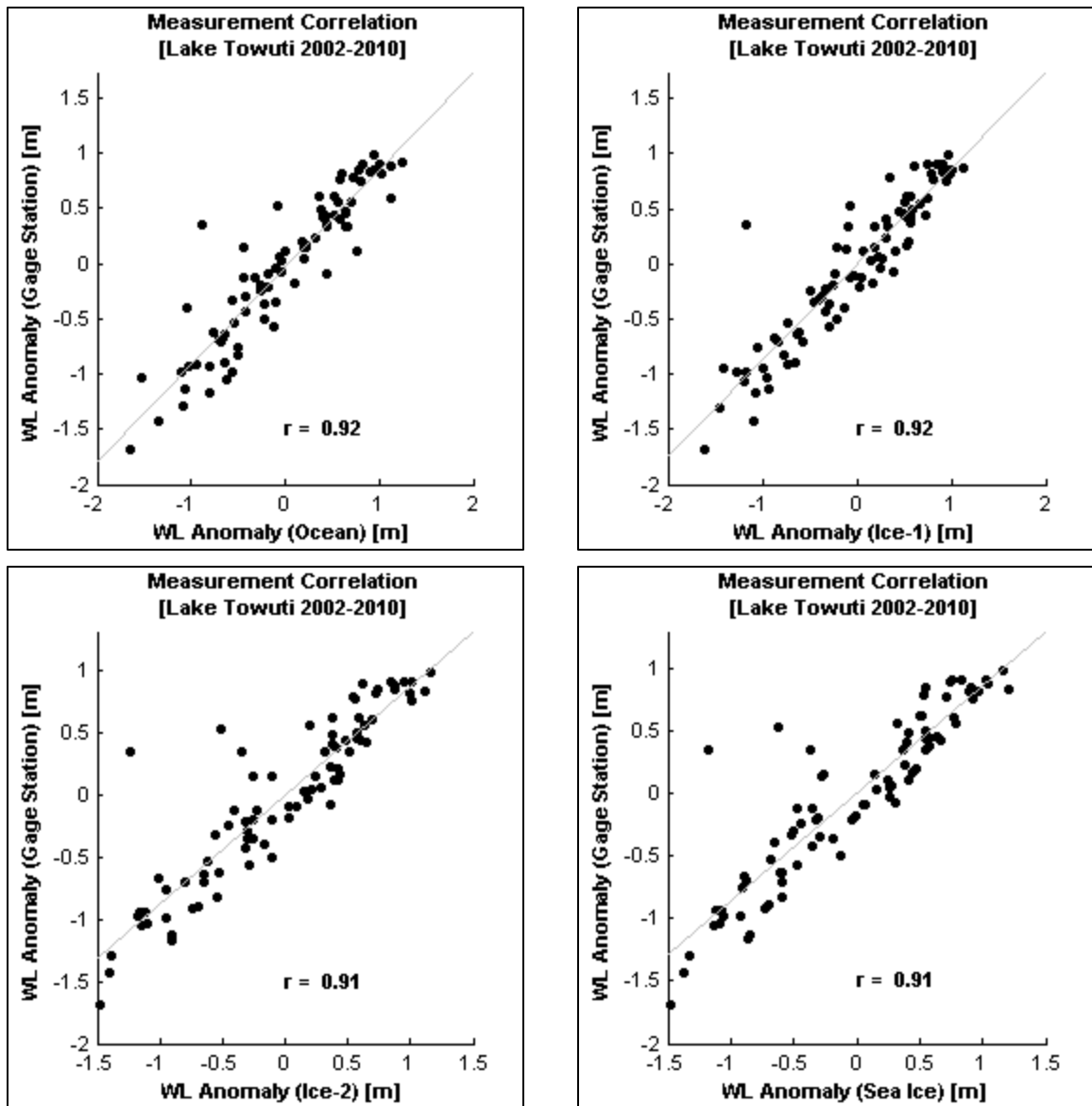


**Figure 3.38** Correlation between water level anomaly at Lake Towuti as measured by Envisat RA-2 altimeter and processed with Ocean (top left), Ice-1 (top right), Ice-2 (bottom left) and Sea Ice (bottom right) retracers

The result of performance evaluation shows that the initial assumption regarding the effect of distance from lakeshore to the accuracy of satellite altimetry measurement is in-consistent. The measurement of water level anomaly over Lake Semayang indicates higher RMS error and lower correlation coefficient relative to the *in-situ* gaged water level anomaly with the increase of distance from the altimeter footprint to the lakeshore. On the other hand, inverse relationship is shown by the measurement of water level anomaly over Lake Matano and Lake Towuti, which indicates lower RMS error and higher correlation coefficient relative to the *in-situ* gaged water level anomaly with the

increase of distance from the altimeter footprint to the lakeshore. Some statistical measures resulted from the performance evaluation over different distance to the lakeshore are illustrated in the following charts. Considering the complicated results from splitting the altimeter measurements by the distance from the lakeshore, this study does not recommend such classification of samples based on the distance to the lakeshore. A complete list of statistical measures resulted from the performance evaluation over different distance to the lakeshore are illustrated the subsequent table.

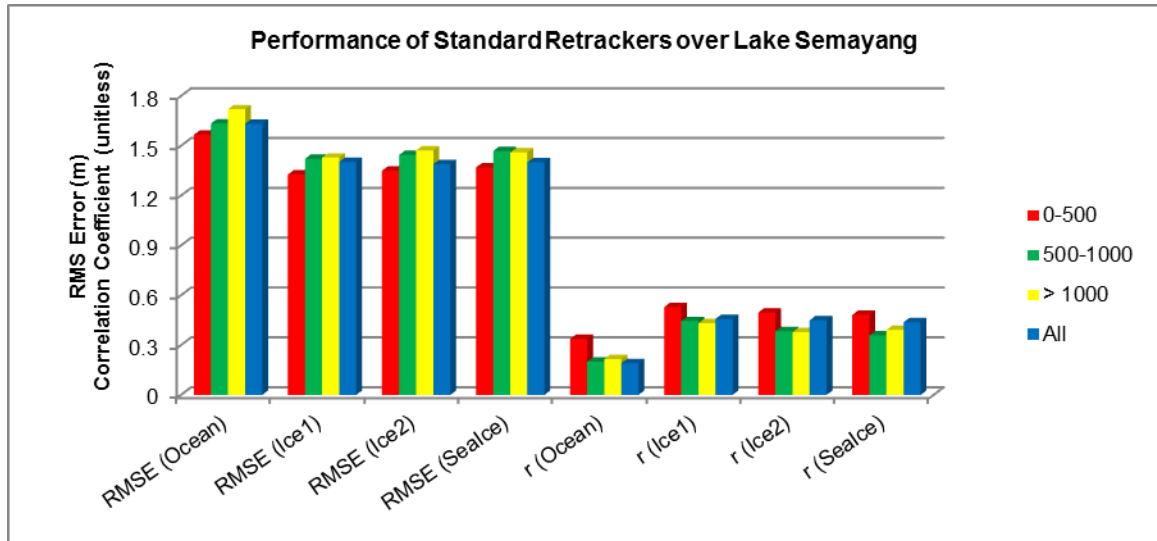


**Figure 3.39** The performance of Envisat RA-2 radar altimetry measurements over Lake Semayang, classified by the distance to the lakeshore

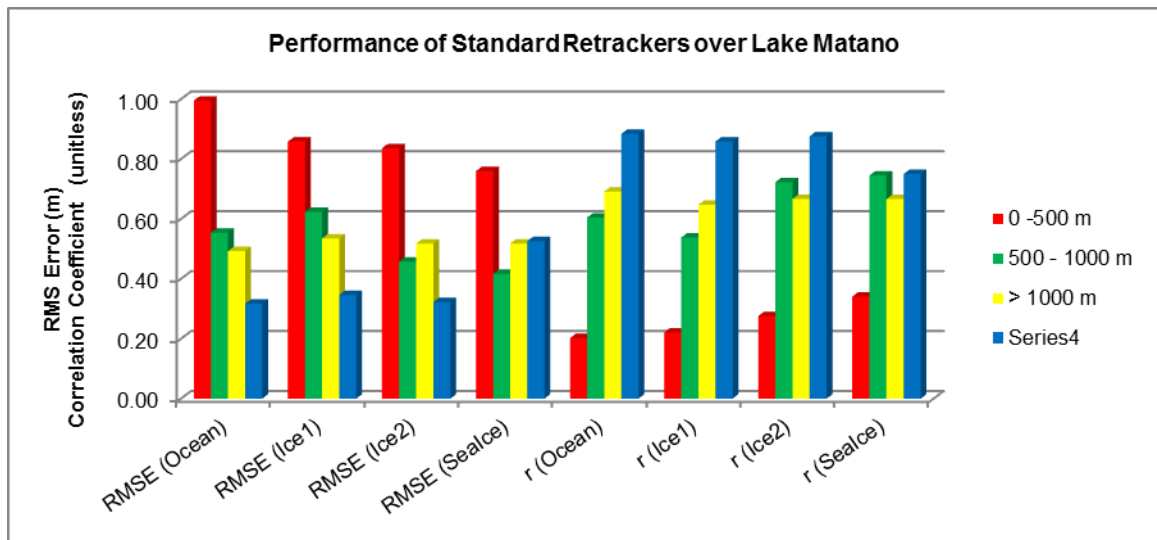


**Figure 3.40** The performance of Envisat RA-2 radar altimetry measurements over Lake Matano, classified by the distance to the lakeshore

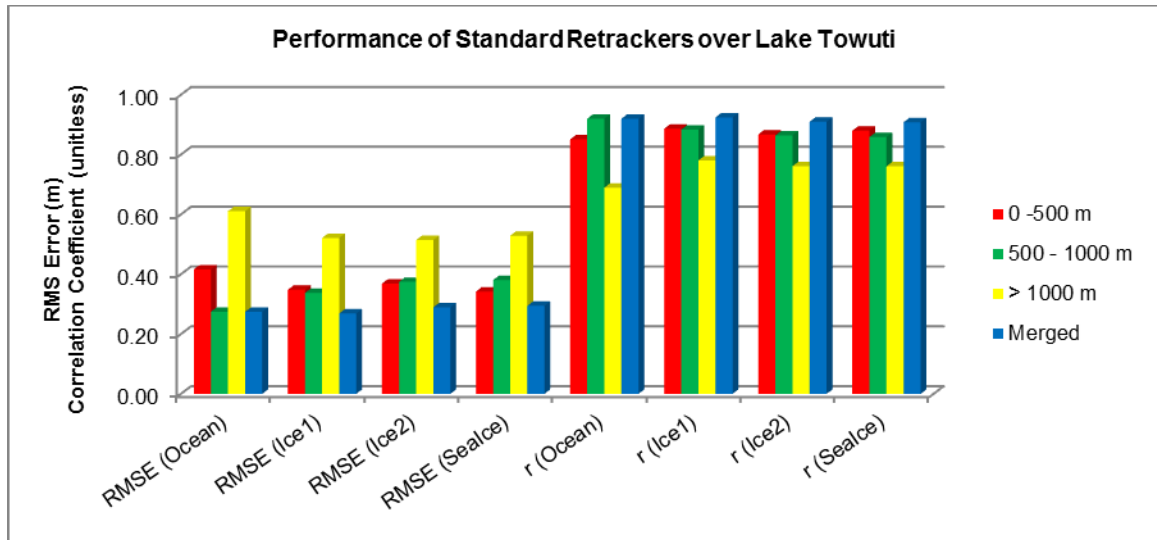


**Figure 3.41** The performance of Envisat RA-2 radar altimetry measurements over Lake Towuti, classified by the distance to the lakeshore

**Table 3.7** Performance evaluation of Envisat RA-2 radar altimetry measurements over Lake Semayang

Virtual station	Lake width (m)	Cycles covered	Validated meas.	Re-tracker	St. Dev (m)	Correlation coefficient	RMSE (m)	No / % of Outliers
Lake Semayang	2,388	7 - 32						
0 – 500 m			26	Ocean	1.576	0.337	1.566	9/438
				Ice-1	1.349	0.529	1.327	2.05%
				Ice-2	1.363	0.496	1.350	
				Sealce	1.381	0.482	1.369	
500 – 1000 m			26	Ocean	1.666	0.200	1.634	4/243
				Ice-1	1.448	0.445	1.421	1.65%
				Ice-2	1.472	0.383	1.444	
				Sealce	1.497	0.359	1.469	
> 1000 m			24	Ocean	1.734	0.216	1.720	2/156
				Ice-1	1.448	0.432	1.429	1.28%
				Ice-2	1.485	0.378	1.472	
				Sealce	1.476	0.391	1.460	
Merged			26	Ocean	1.641	0.191	1.633	15/837
				Ice-1	1.385	0.457	1.403	1.79%
				Ice-2	1.391	0.449	1.389	
				Sealce	1.399	0.438	1.400	

**Table 3.8** Performance evaluation of Envisat RA-2 radar altimetry measurements over Lake Lake Matano and Lake Towuti

Virtual station	Lake width (m)	Cycles covered	Validated meas.	Re-tracker	St. Dev (m)	Correlation coefficient	RMSE (m)	No / % of Outliers
Lake Matano								
0 – 500 m	8,159	8 – 79	75	Ocean	1.001	0.202	0.995	68/416
				Ice-1	0.861	0.221	0.858	16.35%
				Ice-2	0.841	0.276	0.836	
				Sealce	0.765	0.341	0.760	
500 – 1000 m			71	Ocean	0.558	0.605	0.554	27/215
				Ice-1	0.628	0.538	0.624	12.56%
				Ice-2	0.460	0.723	0.458	
				Sealce	0.419	0.745	0.417	
> 1000 m			73	Ocean	0.496	0.692	0.493	115/805
				Ice-1	0.538	0.647	0.535	14.29%
				Ice-2	0.521	0.667	0.517	
				Sealce	0.521	0.666	0.518	
Merged			75	Ocean	0.318	0.884	0.317	210/1436
				Ice-1	0.348	0.858	0.346	14.62%
				Ice-2	0.324	0.876	0.322	
				Sealce	0.529	0.750	0.526	
Lake Towuti								
0 – 500 m	28,818	8 – 79	75	Ocean	0.418	0.851	0.416	79/786
				Ice-1	0.350	0.886	0.348	10.05%
				Ice-2	0.371	0.867	0.369	
				Sealce	0.344	0.880	0.342	
500 – 1000 m			71	Ocean	0.268	0.920	0.275	64/764
				Ice-1	0.336	0.884	0.337	8.38%
				Ice-2	0.373	0.864	0.375	
				Sealce	0.379	0.859	0.380	
> 1000 m			73	Ocean	0.614	0.689	0.611	156/2490
				Ice-1	0.521	0.780	0.521	6.27%
				Ice-2	0.512	0.761	0.514	
				Sealce	0.529	0.761	0.529	
Merged			75	Ocean	0.274	0.920	0.274	299/4040
				Ice-1	0.270	0.924	0.269	7.40%
				Ice-2	0.291	0.910	0.289	
				Sealce	0.296	0.908	0.294	

Inter-comparison between the available retracker (*i.e.* Ocean, Ice-1, Ice-2 and Sea Ice) cannot suggest any single retracker to infer water level of the small lakes, since Ice-2 performed best for Lake Semayang and Lake Matano, but Ice-1 retracker performed best for Lake Towuti. A conclusion that could be drawn from this part of research is that

Ice-1 is not necessarily the best retracker to measure water level anomaly over small to medium lakes in Southeast Asia humid tropics.

Compared to other studies, the best RMS error obtained from measurements of water level anomaly in this study, *i.e.* 0.29 m at Lake Towuti, is close to the lowest one among the *small* lakes being studied throughout the world. Table 3.8 below clearly states that satellite altimetry measurements over the small lakes give the RMS error magnitude in the range of 0.30 to 0.50 m, as compared to large lakes that produce RMS error as low as 3 cm. Lake Matano is in fact the smallest among all lakes listed in Table 3.8.

**Table 3.9** Summary of studies on satellite radar altimetry for water level over lakes

Reference	Location	Lake Extent	Satellite / Sensor	Reported Error
Morris and Gill (1994a)	Superior, Ontario	Large	Geosat	RMSE: 0.09 m
	Michigan, Huron	Large	Geosat	RMSE: 0.11 m
	Erie		Geosat	RMSE: 0.13 m
	Lake St Clair		Geosat	RMSE: 0.17 m
Morris and Gill (1994b)	Great Lakes		Topex / Poseidon	RMSE: 0.03 m
Korotaev <i>et al</i> (2001)	Black Sea	436,402 km <sup>2</sup>	T/P, ERS-1	RMSE: 0.03 m
Mercier <i>et al</i> (2002)	Victoria, Tanganyika	131-390 x 10 <sup>3</sup>	TOPEX / Poseidon	RMSE: 0.10 m
	Malawi and Turkana			
	Rukwa and Kyoga	75-80 x 10 <sup>3</sup>	TOPEX / Poseidon	RMSE: 0.50 m
Coe and Birkett (2004)	Lake Chad	2.5 x 10 <sup>6</sup> km <sup>2</sup>	TOPEX / Poseidon	RMSE: 0.21 m
Zhang <i>et al</i> (2006)	Dongting Lake	2,623 km <sup>2</sup>	TOPEX / Poseidon	RMSE: 0.08 m
Medina <i>et al</i> (2008)	Lake Izabal	717 km <sup>2</sup>	Envisat	RMSE: 0.09 m
Munyaneza <i>et al</i> (2009)	Lake Kivu	2,400 km <sup>2</sup>	Envisat	RMSE: 0.30 m
Cai and Ji (2009)	Poyang Lake	20,290 km <sup>2</sup>	Envisat	Mean Error: 0.31 m
Guo <i>et al</i> (2009)	Hulun Lake	2,339 km <sup>2</sup>	TOPEX / Poseidon	RMSE: 0.13 m
Troitskaya <i>et al</i> (2012)	Gorki Reservoir	1,358 km <sup>2</sup>	T/P, Jason-1	RMSE: 0.15 m
Tseng <i>et al</i> (2013)	Qinghai Lake	4,186 km <sup>2</sup>	Envisat	RMSE: 0.06 m
Sulistioadi (2013)	Lake Semayang	6 - 113 km <sup>2</sup>	Envisat	RMSE: 1.39 m
	Lake Matano	164 km <sup>2</sup>	Envisat	RMSE: 0.32 m
	Lake Towuti	562 km <sup>2</sup>	Envisat	RMSE: 0.29 m

\* STDE (Standard Deviation of Error), % (% difference), RMSE (Root Mean Square Error)

### 3.5. Conclusions and Recommendations

From the results and obstacles of the sequence of experiments conducted and described above, the following conclusions are presented.

- (1) Satellite altimetry had been proven as a reliable tool to monitor the hydrology of medium-sized (200–800 m width) rivers in the Southeast Asia's humid tropics, as indicated by the high correlation between the water level measured by satellite altimetry and the validation dataset measured on the ground, *i.e.*  $r = 0.97$ . Even the results vary in terms of the performance; water level anomaly inferred by Envisat radar altimetry through standard waveform retracking method has been validated and therefore, capable to represent the fluctuations of water level of medium rivers

- (2) This study found that small rivers (40–200 m width) are potentially observable through satellite altimetry, as indicated by reasonably good altimetry-derived water level anomaly recovered for a river with 54 m width, given the water surface boundary is identified carefully through medium-resolution optical imageries (*e.g.* Landsat with 30 m ground resolution). Even this measurement was not validated due to absence of *in-situ* gage station, its relationship with precipitation and sufficiently good temporal coverage provide good indicators of the satellite altimetry reliability for small rivers. It is important to note however, that this situation might be different from one region to another; therefore a specific approach should be developed for each region, as part of the development of permanent monitoring effort of those regions.
- (3) In contrast with the common assumption as summarized by Frappart *et al.* (2006), Ice-1 is not necessarily the best retracker for monitoring small water bodies, especially for the Southeast Asia humid tropics area. It is obvious though, that the Ocean retracker performs worst as it is compared to other retrackers. Ice-1, Ice-2 and Sea Ice alternately produced the best results in various locations of this study.
- (4) The RMS errors of satellite altimetry measurement of Lake Matano and Lake Towuti relative to validation measurement, *i.e.* 0.33 m and 0.27 m, respectively, are about the average of *small* lakes being studied throughout the world. It is worth noting that the extent of Lake Matano, which has been investigated in this study, is the smallest water bodies among any other studies of satellite altimetry measurement of water level involving lakes and reservoirs.

On the other hand, by learning from obstacles and problems encountered during the experiment, the following recommendation is proposed to advance future studies.

- (1) The radar pulse returned by inland water surface varies in their waveform shapes. Therefore, the selection of the range measurements based on its waveform shape to strictly follow the standard waveform shape for inland water body (Koblinsky 1983, Birkett 1988, Berry *et al.*, 2005, Dabo-Niang *et al.*, 2007) is proposed for future studies involving small (40-200 m width) to medium rivers (200-800 m width), as well as small lake (*e.g.* those with extent less than 1000 km<sup>2</sup>).
- (2) Over lakes, classification of distance from the satellite altimetry measurements to the lakeshore is not recommended since it did not suggest significant difference in the number of qualified altimetry measurement.

## **4. Hydrologic Modeling of Upper Mahakam Sub-Watershed**

### **4.1. Introduction**

#### **4.1.1. Hydrologic Monitoring of Tropical Watershed**

Humid tropics are the regions with tropical rainforests as their main land cover (Fosberg *et al.*, 1961); however, anthropogenic factors such as increased development of commercial agricultural, various mineral mining and expansion of residential areas are constantly reducing the portions of the rainforest or are converting it to other land cover over time. The changes in landscape evidently affect the hydrological capability of the watershed to regulate the water cycle and result in a number of natural disasters such as flood and drought in many different locations. The Upper Mahakam Sub-Watershed is no exception. In the past, with lower population density and with considerable portions of forest cover, this sub-watershed used to be very stable in regulating the hydrological regime in previous decades. There were times of high water events, but it did not lead to massive destruction and long period of inundation. More recently, this sub-watershed experiences more frequent flash floods and slow-paced flood inundation as a consequence of more intensive development and the extraction of natural resource in the area. The following table describes the occurrence of floods in the last decade over this sub-watershed, as summarized by various news media.

With the absence of active monitoring of the hydrological variable and flood warnings, the hydrologic models provide an alternative to help understanding the behavior of a watershed in response to the rainfall events, especially those of the magnitudes that lead to flooding (Beven, 2012). Very limited hydrological studies were carried out in the Upper Mahakam Sub-watershed, apparently since this area is less populated than its downstream sub-basins.

#### **4.1.2. Motivation and Contribution of This Study**

This study is therefore conducted with a focus on the upstream part of a critical watershed in the humid tropics along with limited data from the study area. This study also contributes to the knowledge of hydrological responses of upstream sub-watershed systems in the humid tropics. Practically, an event based rainfall-runoff model is developed with the condition of insufficient input data and observed discharge that is very useful in calibrating and validating such a model. Most model inputs and parameters are derived from satellite observations whenever possible so that the model requires less geospatial data from local agencies.



**Table 4.1** Reported floods in the last decade in Upper Mahakam Sub-watershed (Sulistioadi, 2013)

Date	Sub-districts Impacted	Description of the Event
May 2005	Unknown	About 3,500 houses were damaged due to flooding from Mahakam River that lasted a couple of weeks
July 2006	17 sub-districts*	About 40,000 people were evacuated from their residence due to 6 days flooding from Mahakam River that damaged their houses and destroyed their agricultural farms
May 2007	19 sub-districts	A heavy storm event that started on April 29, 2006 led to flood that lasted for 6 weeks and caused 1 death. The water level was reported to rise up to 3 meters beyond its average.
February 2008	Long Bagun Sub-district	A full week of rainstorm led to the rise of the Boh River (one tributary of the main Mahakam River) water level but limited only to 1 district
September 2008	4 sub-districts	Long Hubung sub-district experienced a level rise of water up to 2 m, as well as Long Iram and Tering sub-districts
December 2008	Melak Sub-district	A flash flood hit the capital of this district, that was characterized by a rise of water level up to 1.5 m overnight
May 2009	Damai Sub-district	1-2 m of water level rise at residency area due to overflow of Nyuatan and Kedang Pahu Rivers
December 2009	Tering and Long Iram Sub-districts	A flood occurred in these two sub-districts for relatively short period of time (a couple days)
April 2010	10 sub-districts	Most of the downstream residential areas around Muara Lawa Sub-district were inundated for a couple days
January 2012	Melak, Muara Lawa and Resak Sub-districts	A flood occurred in these sub-districts for a couple days
November 2012	10 sub-districts	A flood occurred in Laham, Long Hubung, Long Iram, Tering, Mook Manaar Bulatn and a couple other sub-districts
April 2013	Tering Sub-district	Hundreds of houses and farms were inundated due to flooding that hit this sub-district
May 2013	4 sub-districts	Flash flood hit Long Bagun and Datah Bilang Sub-districts, which located in the upstream part of the sub-watershed, as well as Tering and Long Iram in the middle part of the sub-watershed

\* Upper Mahakam Sub-watershed comprises most of the area of Kutai Barat District that comprises of 21 sub-districts

The US Army Hydrologic Engineering Center's Hydrologic Modeling System (HEC-HMS) is chosen as the platform for this model, due to its capability to integrate geospatial data inputs and it is also known that this model provides the most reliable predictions on the discharge (Horritt and Bates, 2002). The results of the developed model in the form of continuous discharge estimations are then calibrated and validated by a short periods of field measurements.

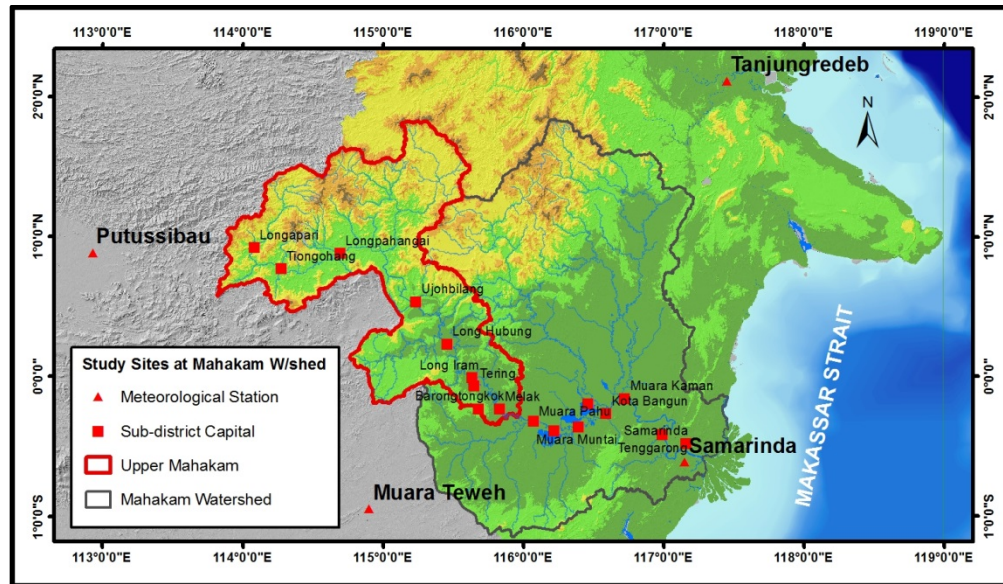


**Figure 4.1** Study area and locations of class-1 meteorological stations operated by the national meteorology, climatology and geophysics agency

## 4.2. Study Area

This study is carried out in the Upper Mahakam Sub-watershed, which is a part of the Mahakam Watershed in East Kalimantan, Indonesia. Located at  $113^{\circ} 50' 8'' - 116^{\circ} 1' 16''$  E Longitude and  $0^{\circ} 22' 38''$  S to  $1^{\circ} 48' 31''$  N Latitude, this medium-sized catchment is scarcely inhabited and mostly consists of mountainous, hilly and rugged terrain, which leads to the occurrence of flash flooding during heavy storms. The mean annual precipitation in this area ranges from 2400 to 3000 mm/year, while the main channel width is about 40-100 m, with depth varying from 5-10 m and with a slope greater than 2% (Estiaty *et al.*, 2007). With major soil types that are prone to erosion risk, *i.e.* red-yellow *pod sols*, this sub-watershed presents a very good example of a flash flood-prone catchment, with significant impacts on the downstream sub-basins, therefore justifying the urgency of monitoring its hydrological response to precipitation.

## 4.3. Precipitation Data Analysis

Precipitation is the most important forcing in the rainfall-runoff watershed model (Beven, 2012); therefore, a specific effort was dedicated to determine the best available precipitation input for this model. Figure 4.1 shows the study area along with active meteorological stations at some distance. Regarding the meteorological data availability, the only official publicly available *in-situ* precipitation data for a long period (*e.g.* 10 years from 2001-2010) for this area is the accumulated monthly precipitation. On the other hand, the HEC-HMS hydrologic model needs at least daily precipitation rate to support all of its modeling methods. Therefore, satellite-based precipitation estimates are chosen as the solution for this lack of input forcing data.

The Tropical Rainfall Measuring Mission (TRMM) is a joint US-Japan satellite mission to monitor tropical and subtropical precipitation. The rainfall measuring instruments on the TRMM satellite include the Precipitation Radar (PR), electronically

scanning radar operating at 13.8 GHz; TRMM Microwave Image (TMI), nine-channel passive microwave radiometer; and Visible and Infrared Scanner (VIRS), and five-channel visible/infrared radiometer (Huffman *et al.*, 2007).

The estimation process includes modeling many atmospheric processes and is comprehensively called the TRMM Multi-Satellite Precipitation Analysis (TMPA) with different sequences of algorithms for each final product. The 3B42 algorithm produces TRMM-adjusted merged-infrared (IR) precipitation rates (in mm/hr) and root-mean-square (RMS) precipitation-error estimates. The final Daily TRMM and Others Rainfall Estimate (3B42), which shortened as TRMM\_3B42\_daily version 7 precipitation grid consists of precipitation (in mm/hr) and RMS precipitation-error estimates with 3-hour temporal resolution and 0.25° by 0.25° spatial resolution. The spatial coverage extends from 50° S to 50° N latitude. The daily accumulated rainfall product is derived from this 3-hourly product and used by this study.

Since the TRMM\_3B42\_daily data is delivered as a Network Common Data Format (NETCDF) and provided as world coverage in each time stamps, it is necessary to appropriately import and mask this global dataset into a familiar tabular format and have them exclude all data outside the study area. The ArcGIS Model Builder was used for this purpose and was able to successfully import and export the data into text files.

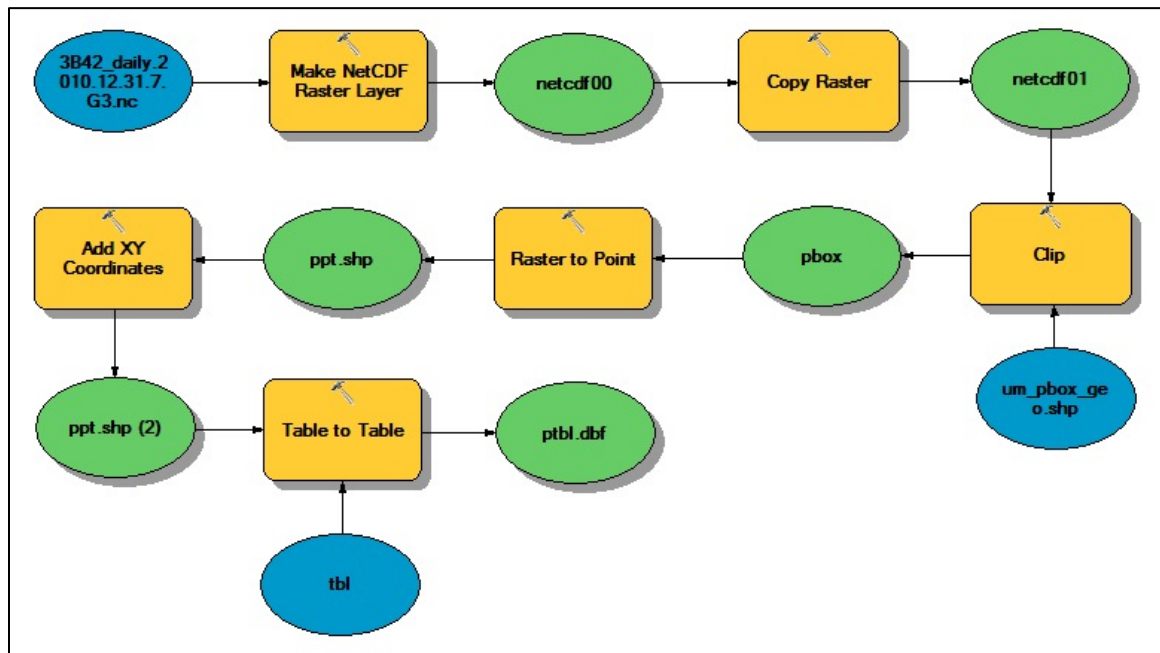


**Figure 4.2** Steps for retrieving and masking TRMM estimated precipitation in NetCDF data format and exporting to tabular format as done through ArcGIS Model Builder

There are three main methods to spatially process the precipitation, *i.e.* arithmetic mean, Thiessen polygon and isohyet map (Chow *et al.*, 1988). Thiessen polygon is a set of polygons bounded by lines dividing an area into equidistance from one meteorological

station to the other surrounding stations (Brassel and Reif, 1979), while isohyet is a line connecting the areas with the equal precipitation depth (*e.g.* USDA-NRCS, 1993).

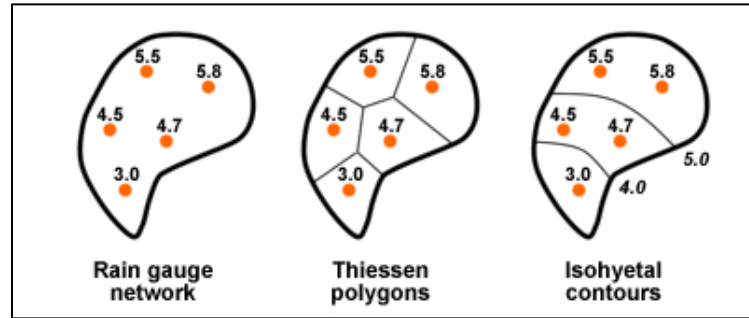


**Figure 4.3** Meteorological Station Network Analysis (Source: The COMET Program)

The HEC-HMS model used in this study requires discrete precipitation time series from separated meteorological station, therefore a novel approach in the spatial post-processing of TRMM data, which is called the Thiessen polygon and area average hybrid approach is proposed. This proposed approach assumes the Thiessen polygon as the most suitable distribution method of rainfall but due to the nature of gridded TRMM data along with its higher spatial resolution compared to the geographic location of the meteorological stations, rainfall estimates within each Thiessen polygon are arithmetically averaged. Hence the final products are “virtual meteorological station” precipitation estimates that are bounded by the Thiessen polygon boundary within the study area. The logical framework of this approach is illustrated in the following flowchart, followed by the resulting map.

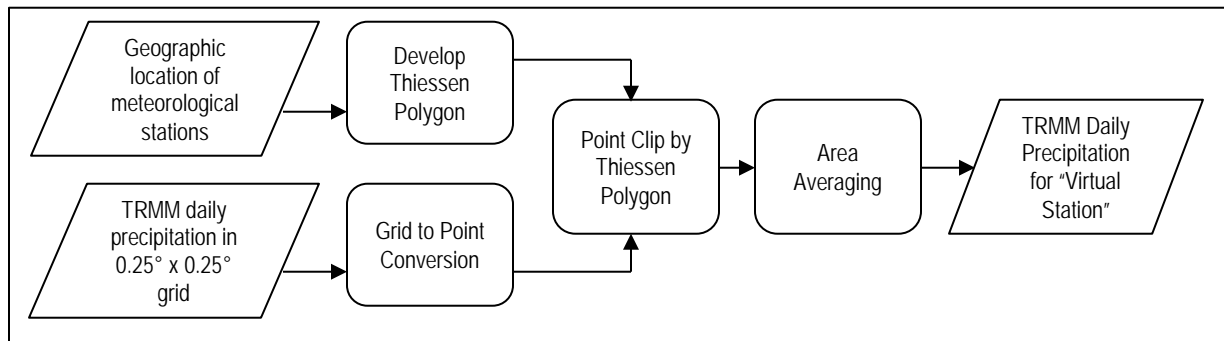


**Figure 4.4** Operational steps of Thiessen polygon and area average hybrid approach

The Thiessen polygon and area average hybrid approach was implemented for 8-year period from 2002 to 2010. Afterward, the estimated precipitation for each virtual gage stations were averaged to mimic the real meteorological station, then being evaluated for its performance by visual inspection through scatter-plots and statistical measures such as coefficient of correlation and RMS Error.



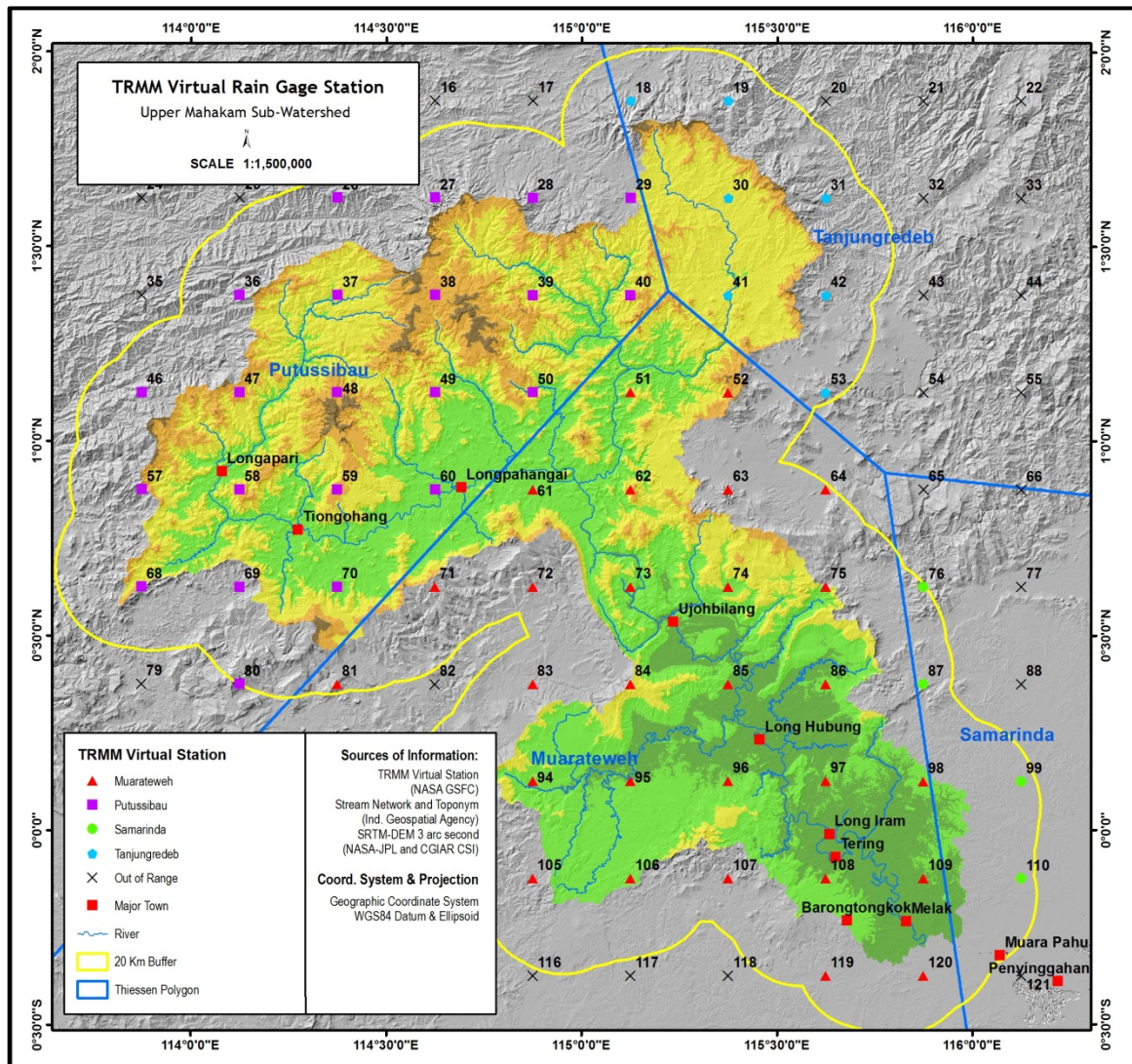


**Figure 4.5** The distribution of virtual gage stations after the Thiessen polygon and area average hybrid approach spatial processing

The following plot shows the accumulated monthly precipitation depth as processed from the 8-year rainfall estimates from TRMM\_3B42\_daily version 7. The TRMM estimated precipitations are compared side by side to the average monthly precipitation for each meteorological station, which has been inferred from various statistical reports provided by local agencies.

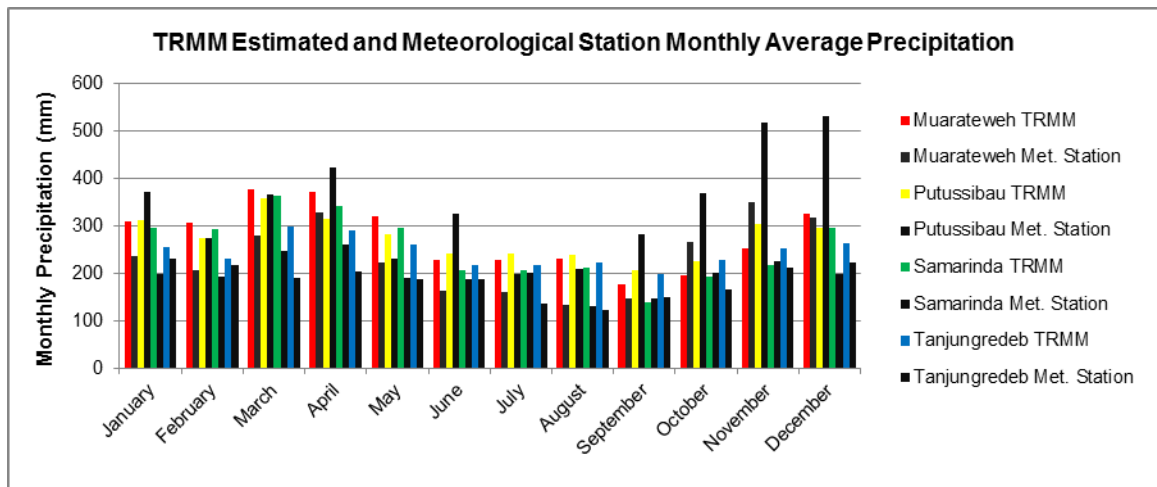


**Figure 4.6** TRMM estimated and meteorological station monthly average precipitation from 2002 to 2010

Due to the fact that only monthly rainfall accumulation data are officially available, a relationship between the TRMM estimation and each meteorological station is then built upon the accumulative monthly precipitation data and applied to the daily estimation by assuming that the relationship remains the same. For detailed investigation, the following figures show the monthly average precipitation for both measurements.

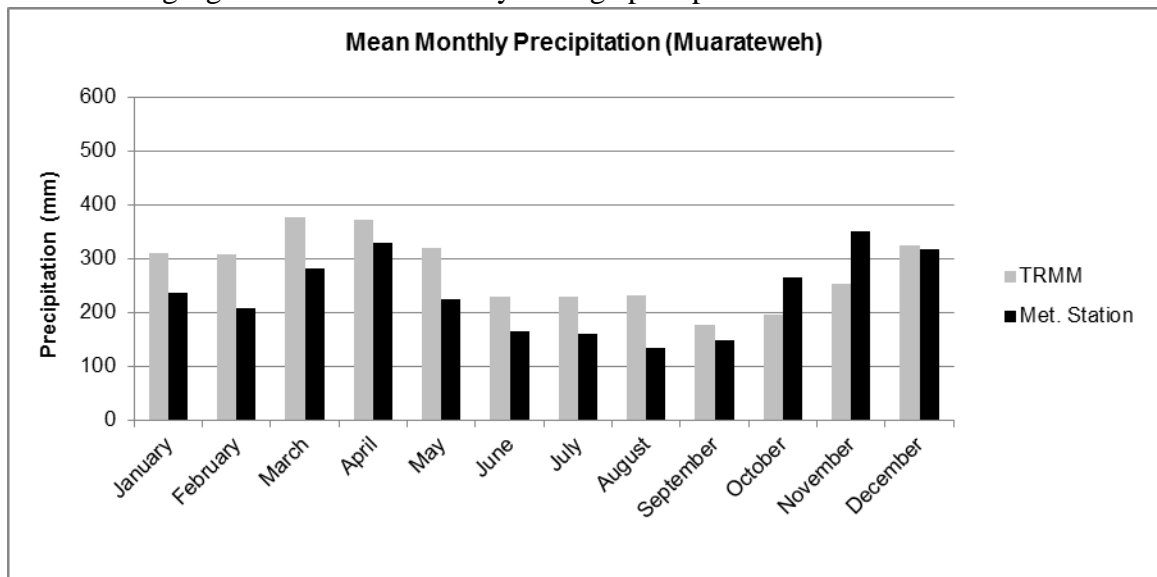


**Figure 4.7** TRMM estimated and meteorological station monthly average precipitation at Muarateweh from 2002 to 2010

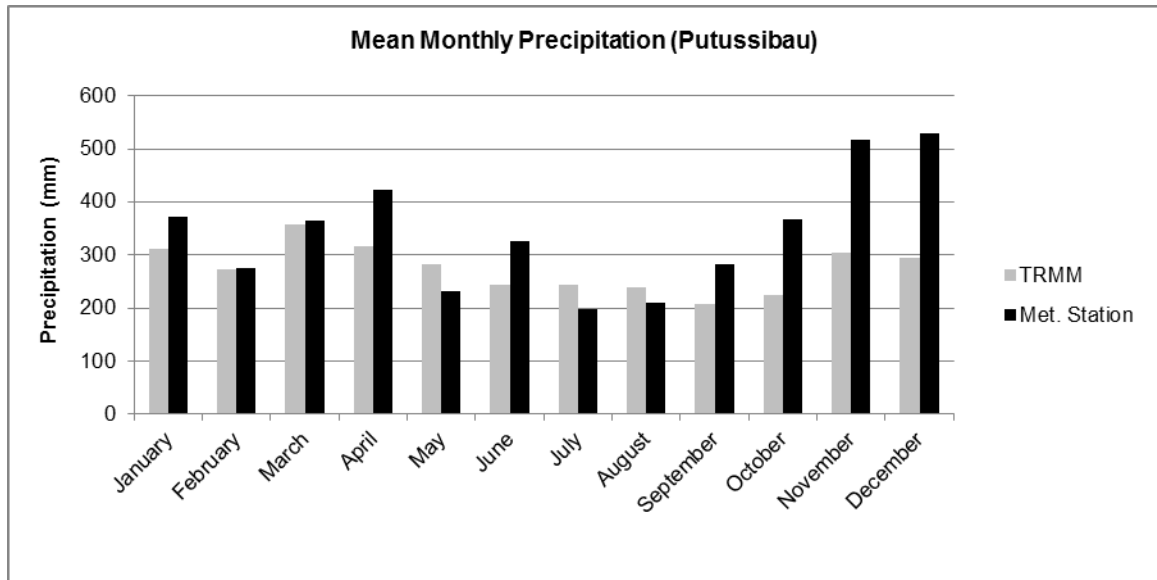


**Figure 4.8** TRMM estimated and meteorological station monthly average precipitation at Putussibau from 2002 to 2010

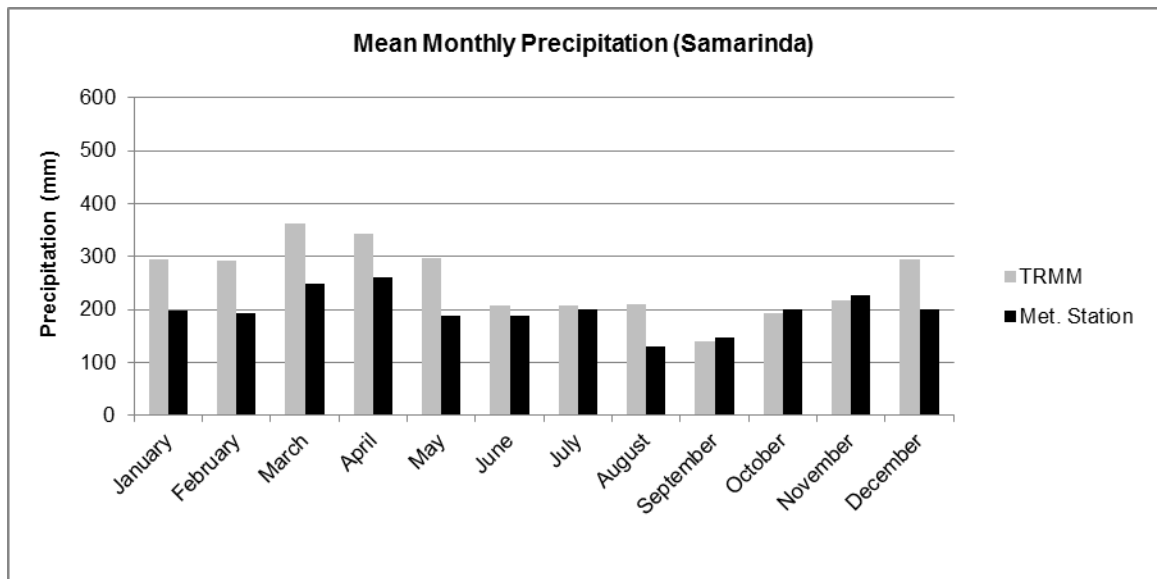


**Figure 4.9** TRMM estimated and meteorological station monthly average precipitation at Samarinda from 2002 to 2010

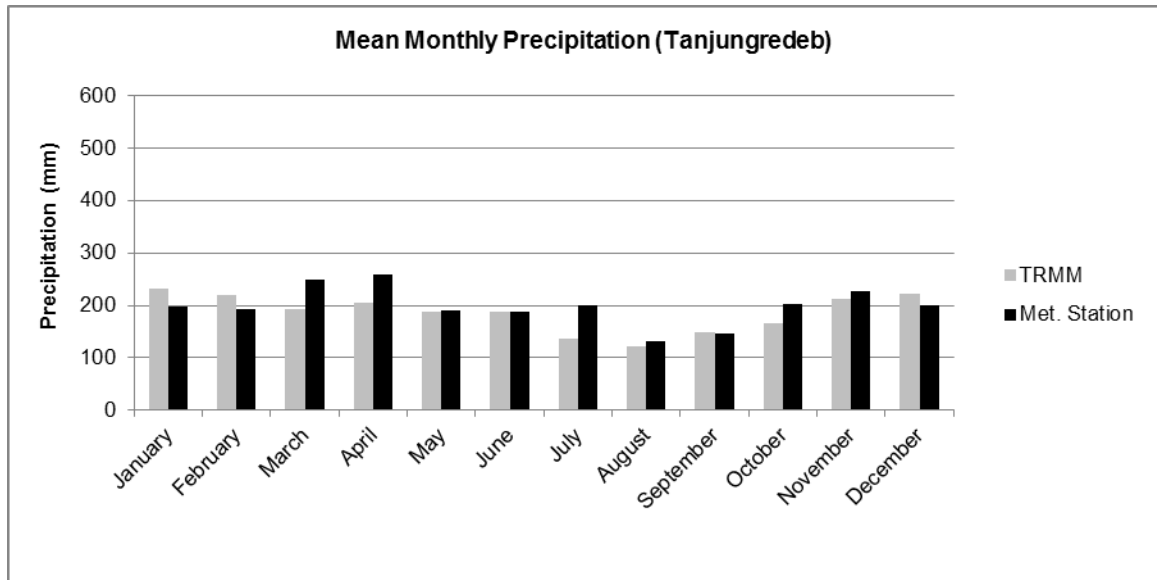


**Figure 4.10** TRMM estimated and meteorological station monthly average precipitation at Tanjungredeb from 2002 to 2010

From Figure 4.7 to Figure 4.10, it is clear that Putussibau area receives the most precipitation throughout the year, followed in order of higher to lower precipitation by Muarateweh, Samarinda and Tanjungredeb as the driest. In addition, it seems that most of the TRMM estimated accumulated monthly precipitations are overestimated with a few exceptions. The opposite situation exists in the estimation for Putussibau station, which seems underestimated, especially on the months with more precipitation such as November and December. To quantify these differences, statistical measures were conducted along with plotting the scatter-plots for the whole dataset. The results of this statistical evaluation are presented in Table 4.2, while a set of correction factors are then introduced to offset the TRMM estimation to match the validation data.

**Table 4.2** Statistical measures on the performance of TRMM daily precipitation over the average monthly precipitation for all meteorological stations

Statistics	Muarateweh	Putussibau	Samarinda	Tanjungredeb
RMS Error (mm)	75.78	113.545	74.71	65.64
Correlation Coefficient	0.57	0.50	0.67	0.58
Correction Factor	0.85	1.24	0.78	0.76

The correlation between TRMM estimates and those measured by the meteorological station precipitation is not that strong, but the TRMM data is still used as the model forcing, considering no better sources of precipitation data available.



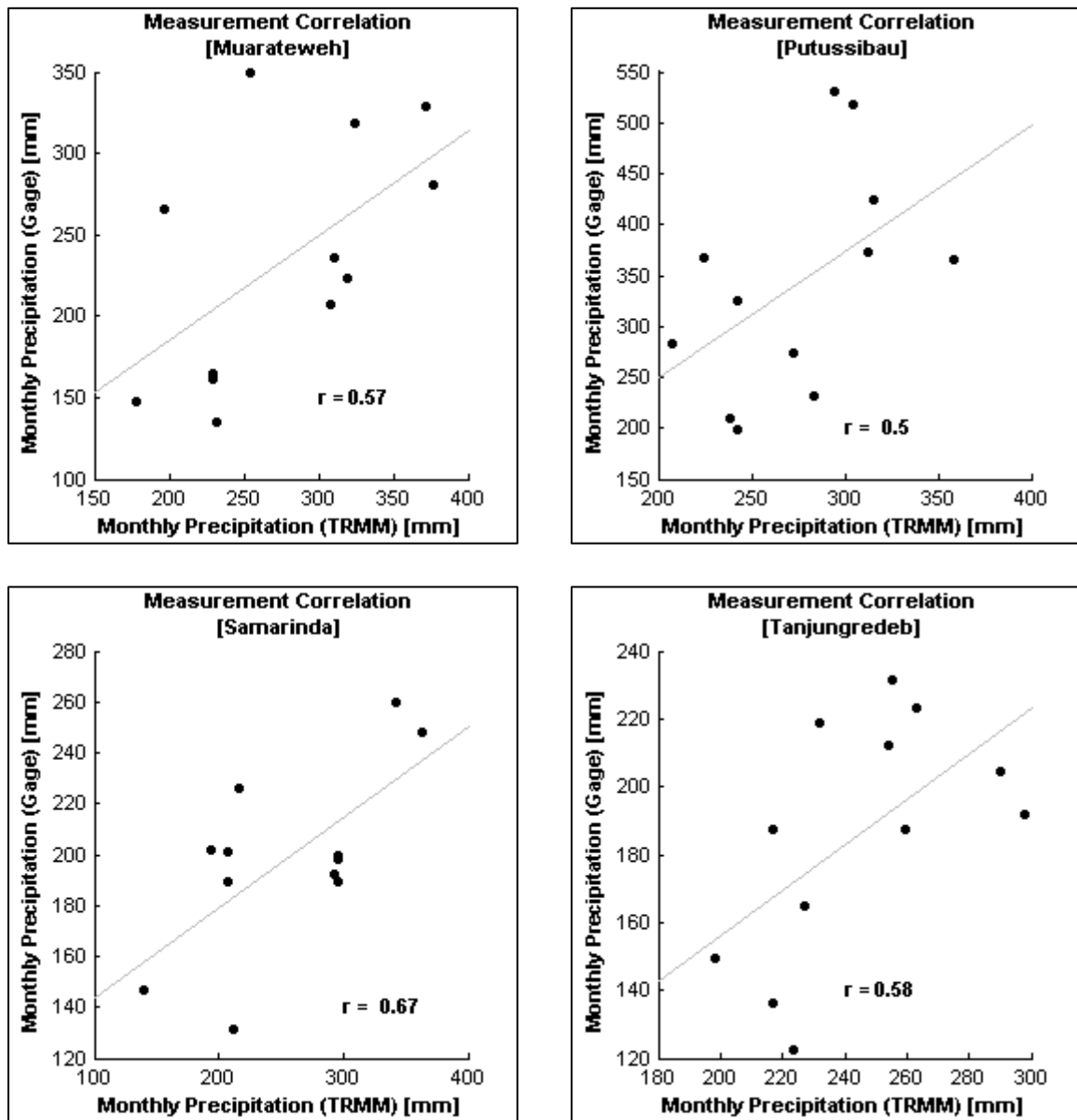


**Figure 4.11** Scatterplots of relationship between TRMM estimated and meteorological station monthly average precipitation at Muarateweh (top left), Putussibau (top right) Samarinda (bottom left) and Tanjungredeb (bottom right)

#### 4.4. HEC-HMS Model Preparation

##### 4.4.1. Terrain Analysis and Basin Characterization

This study uses the HEC Hydrologic Modeling System (HEC-HMS) as the main model to estimate discharge from precipitation along with other factors. Since the basin characteristics, input parameters and channel network involved in the hydrological simulation are all geographically referenced and geometrically measured, a specific tool is needed to manage and transform the spatial datasets before they are fed into the hydrological simulation system of HEC-HMS. To assist the preparation process prior to running the hydrologic model in the HEC-HMS module, the HEC Geospatial Hydrologic Modeling System (HEC-GeoHMS) extension for ArcGIS was used, so that all geospatial data can be preprocessed properly and supply the main HEC-HMS model.

The determination of basin physical characteristics is the first and very important step needed to build a reliable hydrologic model. A terrain model is used as an input to derive additional datasets that collectively describe the drainage pattern of the watershed and allows for stream and sub-basin delineation. Those datasets are comprised of grid datasets of flow direction and accumulation, stream network, stream segmentation and watershed divides. In addition, the terrain processing results vector layers of watershed divides and modeled streams. The last vector dataset is aggregated watersheds, which is primarily built to improve the performance of watershed delineation (HEC, 2010).

This study uses a terrain model developed from the Shuttle Radar Topographic Mission (SRTM), which provides a detailed terrain with 90 m ground resolution over the study area. The Shuttle Radar Topographic Mission (SRTM) was collaboration between the NASA Jet Propulsion Laboratory (JPL) and the National Geospatial-Intelligence Agency (NGA) that used a radar interferometer to generate a globally consistent digital elevation model (DEM) for latitudes lower than 60° (van Zyl, 2001). The SRTM carried two single-pass interferometers, *i.e.* the US C-band system and the German/Italian X-band system X-SAR. The absolute position of the baseline in space was measured by the GPS receivers with an accuracy of about 1 m. This small error contributes directly to the DEM height error. Other sources of error are the measurement of the baseline length and angle in space, which was measured by an inertial navigation unit. It was developed through an across-track Synthetic Aperture Radar (SAR) interferometer approach that made use of two antennas with different tasks, *i.e.* the primary antenna transmits pulses, while both antennas (primary and secondary) receive the radar echoes (Rabus *et al.*, 2003). After processing a series of returned radar pulses, the Earth's surface elevation is inferred based on the range measurement and the position of the space shuttle, with a set of corrections. Nevertheless, the SRTM also carries a set of errors described as follows. The absolute geo-location error refers to the positional error of the SRTM image relative to a precisely known landmark on the Earth, while the absolute height error refers to the difference between the SRTM estimated elevations with other sources of topographic data and finally the relative height error refers to the estimated difference between two points in a 1-degree grid (Rodriguez *et al.*, 2006). The Southeast Asia humid tropic is part of the Eurasia plate; therefore, it also generally suffers from 6.2 m absolute height error and 8.8 m geo-location error as presented in Table 4.3. These errors might contribute to the terrain processing phase of the hydrologic model preparation in various ways.

**Table 4.3** Various errors of the Shuttle Radar Topographic Mission (SRTM) in meters (Rodriguez *et al.*, 2006)

Error Type	Africa	Australia	Eurasia	Islands	N America	S America
Absolute Geo-location Error	11.9	7.2	8.8	9.0	12.6	9.0
Absolute Height Error	5.6	6.0	6.2	8.0	9.0	6.2
Relative Height Error	9.8	4.7	8.7	6.2	7.0	5.5

In the HEC-GeoHMS framework, the terrain data is processed and analyzed using the eight-pour point approach, which uses the steepest slope to define the direction that water flows from one cell grid to one of eight neighbors, hence determining the flow paths. Once the flow path for each cell grid is determined the computation continues with defining the accumulation of the flow, followed by the definition of the theoretical stream network. With certain limitations, the sub-basins are delineated based on the theoretical stream, flow direction and accumulation and additional boundary conditions set by the analyst. The sequence of terrain analysis in the Arc Hydro Tools, which works identically with the HEC-GeoHMS environment, is described as follow (Djokic, 2008).

There are four key elements that define the flow pattern for an arbitrary terrain. They are (1) sinks (depressions, pits), which are the area where water flows in but does not flow out, (2) known streams, which represent observed drainage patterns (*e.g.* it is expected that the drainage pattern generated by the DEM matches the real-world drainage pattern), (3) known lakes, which represent sinks if the lakes do not have any outlets, or if the lakes flow out to a main stream, (4) known drainage area boundaries, which represent physical boundaries for any hydrological events in the watershed (Djokic, 2008).

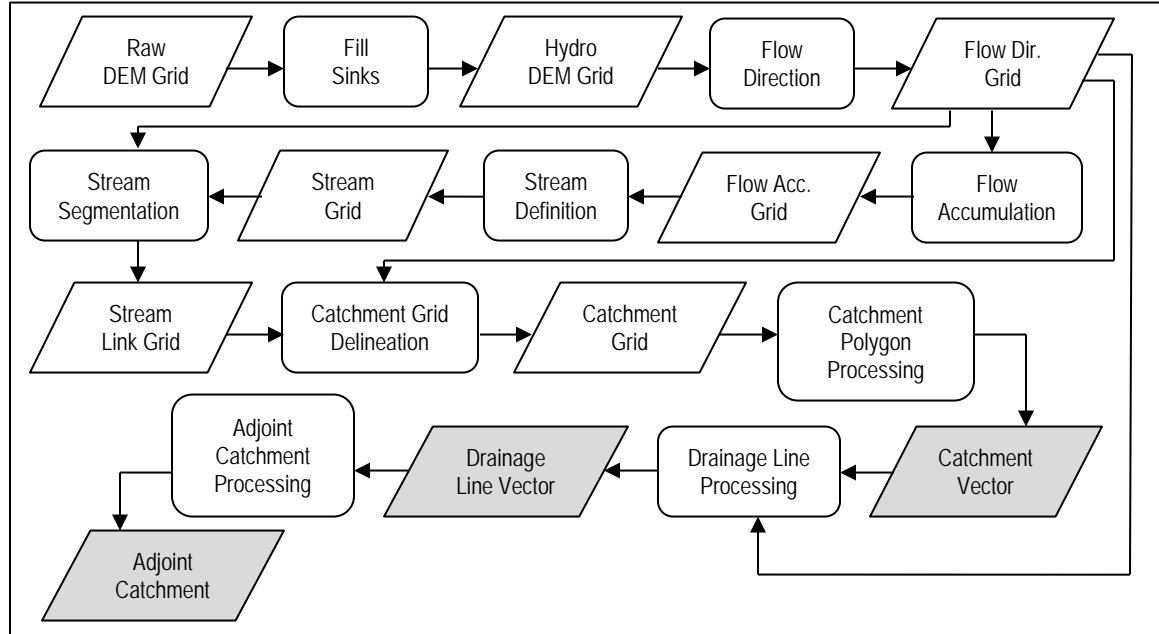


**Figure 4.12** Workflow of terrain analysis on dendritic watershed, rounded rectangle represents process, the parallelogram represents grid dataset and the shaded parallelogram represents vector dataset

In this study, several experiments were tried to mimic the real world watershed situation, for instance by (1) adding a DEM reconditioning process based on the known stream network in the vector dataset, (2) using a known watershed boundary, which had been built prior to the terrain analysis, or even (3) replacing the generated stream grid with a gridded known stream network, but only one of them (#2) was successful in improving the generated watershed divides and artificial stream network. It took about 27 trials before it was determined that neither the generated stream grid nor the delineated catchment can be altered at all. In addition, the terrain analysis is a provided set of process that is not intended to mimic the real watershed configuration for the sake of computational purpose. During the terrain analysis for this study, it is also found that neither Arc Hydro Tools nor HEC-GeoHMS are able to “force” the theoretical stream flow network to follow the real stream network, especially very flat areas such as those in the middle part of Upper Mahakam Sub-watershed. In the following figure (Figure 4.13c), the theoretical stream channel is described as a simple straight line while the real channel is meandering heavily, which cannot be followed by intervention within the sequence of terrain analysis in either Arc Hydro Tools or HEC-GeoHMS. It turns out that the alteration of the sub-basins finally could only be done once the theoretical stream and watershed divide are completed and the results had been transferred into a HEC-GeoHMS project preparation.

The SRTM-derived Digital Elevation Model carries a number of artifacts. One of them is presented at the bottom right of Figure 4.13, which shows grey area for no-data areas. To overcome this problem, the areas were masked and re-interpolated with some height points interpreted from other sources, such as topographic maps, or lower resolution elevation model, *e.g.* Global 30 Arc Second Elevation Data Set (GTOPO30) provided by USGS, then added back to its position (Endreny *et al.*, 2000).

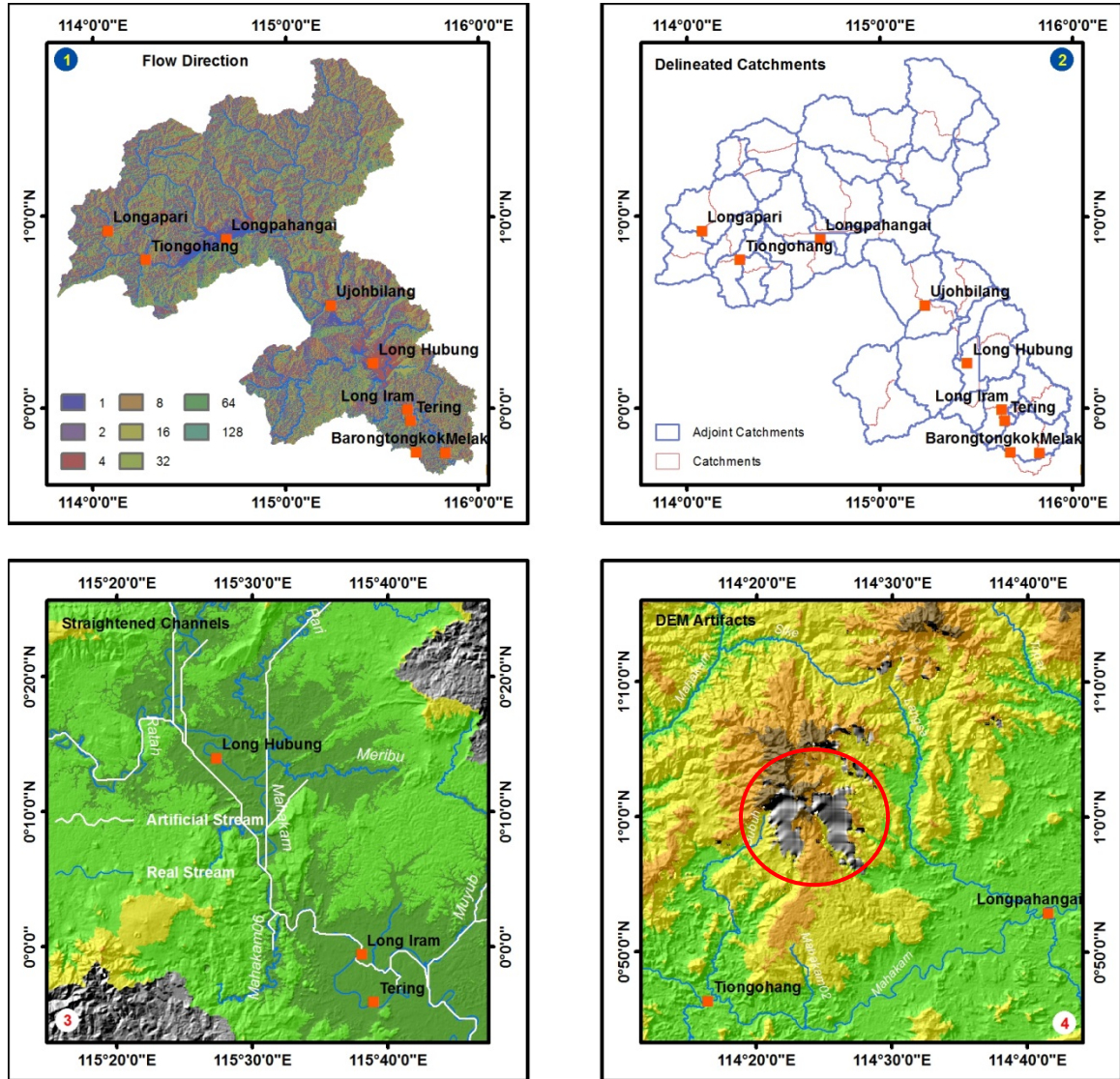


**Figure 4.13** Intermediate product of terrain analysis, *i.e.* (1) flow direction grid, final product of terrain analysis (2) catchment and adjoint catchment, and problems encountered during terrain analysis (3) straightened channels, (4) DEM artifacts that contains no data

Following the completion of terrain analysis with satisfactory catchment division, the HEC-GeoHMS project was generated with the inputs from previous steps. The project setup includes determination of the main outlet, which was predefined to be Melak Town, where the *in-situ* discharge data are partially available, as well as defining the final boundary of the watershed to be modeled. Basin and sub-basins modification includes merging and splitting basins wherever the configuration does not match the existing stream network map. Here the detailed adjustment on the catchment division was carried out, since those could not be completed previously in the terrain analysis process.

**Table 4.4** Physical characteristics of the stream and basin data layer (HEC, 2010)

Data Layer	Physical Characteristics	Attribute Name
Stream	Length	RivLen
	Upstream elevation	ElevUP
	Downstream elevation	ElevDS
	Slope	Slp
Sub-basin	Area	Area
Centroid	Centroid location	Elevation
	Centroid elevation	
Longest Flow Path	Location of the longest flow path	LongestFL
	Longest flow length	
	Upstream elevation	
	Downstream elevation	
	Slope between endpoints	
Centroidal Flow Path	Location of the centroidal flow path	CentroidalFL
	Centroidal length	

#### 4.4.2. Hydrological Parameter Estimation

Once the physical characteristics of the streams, basin and sub-basins are defined, the hydrological parameters to be used in hydrologic modeling can be determined. The first step was to define the modeling methods to be carried out in the HEC-HMS, since that information will be contained in the model file generated by HEC-GeoHMS, and exported to HEC-HMS for simulation process. The following table describes all available models to use in order to simulate the rainfall-runoff process in a watershed.

**Table 4.5** Available components of precipitation-runoff-routing simulation model in HEC-HMS (HEC, 2000)

HEC-HMS Component	Functions
Precipitation-specification options	Describes an observed precipitation event, a frequency-based hypothetical precipitation event or an event
Loss model	Estimates the volume of runoff, given the precipitation and properties of the watershed
Direct runoff model	Accounts for overland flow, storage and energy loss as water runs off a watershed and into the stream channels
Hydrologic routing model	Accounts for storage and energy flux as water moves through stream channels
Man-made structures model	Accounts for naturally confluences and bifurcations
Water-control measures model	Accounts for diversions and storage facilities
Distributed runoff model	Use distributed precipitation data, such as those available from weather radar
Continuous soil moisture accounting model	Simulates long-term response of a watershed to wetting and drying
Automatic calibration	Estimates certain model parameters and initial conditions, given observations of hydro-meteorological conditions
Link to database mgt system	Allows data storage, retrieval and connectivity with other analysis tools

**Table 4.6** HEC-HMS Processes and Methods Used for the Simulation

HEC-HMS Process	Method Used
Precipitation-specification	A novel approach called the Thiessen polygon and area average hybrid is used to accommodate limited spatial resolution of the TRMM precipitation estimation and match with Gage Weights meteorological model available in HEC-HMS
Runoff volume model	SCS Curve Number method is used, considering the compatibility with the available geospatial datasets of soil type and land cover in the study area, as well as the model characteristic that focus all computations in each sub-basins, with composite curve number that can be generated through spatial analysis of the soil type and land cover map
Direct runoff model	Clark Unit Hydrograph method is used, considering that the storage coefficient (R), the only unknown parameter can be estimated through calibration process
Hydrologic routing model	Muskingum-Cunge method is used, considering that this model is based on mostly physical parameters and allows estimation. In addition, the model is the most suitable for channel with slope $< 0.0004$ , which is the case of the lowland area in the sub-watershed
Baseflow model	The exponential recession model is used, considering this model had been evaluated for small to medium-size basin (e.g. 30 to 16,000 km <sup>2</sup> )

In order to run the simulation to model the response of Upper Mahakam Sub-watershed to the rainfall while still considering the limitation of the input datasets, the characteristics of the precipitation input, the period and interval of discharge calibration dataset, this study applies the following combination of methods listed above.

Choosing the right methods in a hydrologic model is not an easy task. However, experiences both from the study location, or those inferred from other studies are the most helpful factors in making the decision. For the case of the direct runoff method, unit hydrograph theory combined with standard infiltration methods is sufficient to handle the conversion of an input rainfall into a hydrograph for both small and large watersheds (Bedient and Huber, 2002).

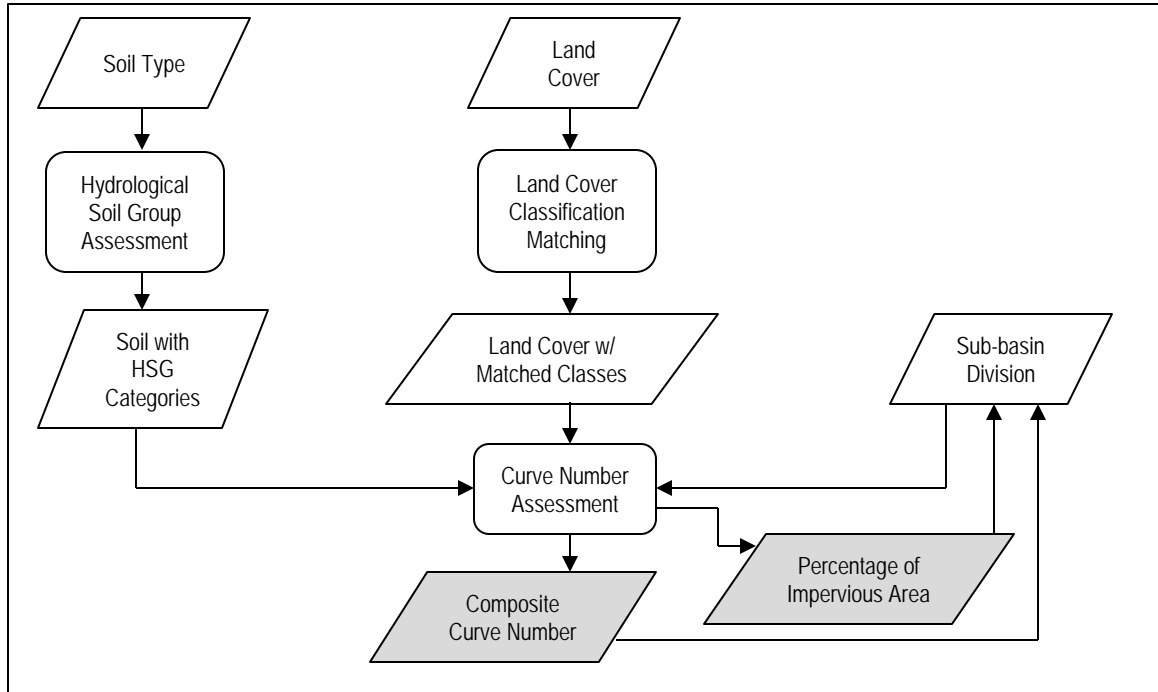


**Figure 4.14** Workflow of Curve Number (CN) determination through analysis of various geospatial datasets, shaded components represent computed value that added back as the attribute table into the sub-basin division map

Defining model parameters is the next step in the preparation of a hydrologic model using HEC-HMS in this study. Since this study uses SCS Curve Number method as its runoff volume computation method, the initial parameters to be defined are the curve numbers (CN) of each sub-basin. This is obtained through spatial analysis that involves sub-basin division, soil type and land cover maps, along with some attribute table modifications in order to calculate the actual curve number and initial abstraction.

Challenges arose due to the differences of land cover and soil type classification systems in Indonesia, which are different from those used to build the Hydrological Soil Group (HSG) and Curve Number (CN) determination table. To overcome this, a specific study was conducted to assess the physical properties of the soil types listed in the soil type map from the local agency to match the physical properties as listed in Table 2.5. A similar approach was also carried out for land cover classification to match the standard land cover classification listed in Table 2.6 to Table 2.9. The following table describes the soil orders, the physical properties and assigned hydrology soil group.

Regarding the Clark Unit Hydrograph method, initial estimates for storage coefficient (R) value for each sub-basin are assigned following Kuok *et al.* (2010).

$$R = 0.0535A - 1.4093 \quad \text{with } A = \text{watershed area in km}^2 \quad (4.1)$$



**Table 4.7** Great groups, physical properties and hydro-soil groups (USDA, 1996)

Order	Sub-Order	Great Group	Remarks	HSG
<b>Inceptisols</b> 1. Soils that show a moderate amount of development: they have more development than an Entisol, but not enough to qualify as an Alfisol, Mollisol, Vertisol, or other order. 2. Often have a cambic subhorizon, formed by removal of carbonates, formation of mottles, limited movement of silicate clays and iron and aluminum (hydr)oxides, or other processes	<b>Aquepts</b> Have an aquic moisture regime	<b>Tropepts</b> Have an iso temperature regime	Texture varies from loamy to clayey The natural drainage is poor or very poor	D
<b>Inceptisols</b> 1. Soils that show a moderate amount of development: they have more development than an Entisol, but not enough to qualify as an Alfisol, Mollisol, Vertisol, or other order. 2. Often have a cambic subhorizon, formed by removal of carbonates, formation of mottles, limited movement of silicate clays and iron and aluminum (hydr)oxides, or other processes	<b>Tropepts</b> Have an isomesic or warmer iso temperature regime	<b>Dystropepts</b> Have base saturation < 50 % in all subhorizons between 25 and 100 cm <b>Eutropepts</b> Have base saturation <sup>3</sup> 50 % in all subhorizons between 25 and 100 cm	Generic Inceptisols texture: Loamy or finer	B B
<b>Ultisols</b> Ultisols are mineral soils that have an argillic or kandic horizon and base saturation < 35 % at a prescribed depth in the argillic horizon, which depth depends on color, depth to lithic contact, or the presence of a fragipan. Alternately, if it has a fragipan with clay coatings ? 1 mm thick and base saturation <35 %, it may also be classified as an Ultisol. Formerly required to have a mesic or warmer temperature regime	<b>Udults</b> Have a udic moisture regime	<b>Kandiudults</b> Have low activity clays and < 20 % decrease in clay in the upper 150 cm	Clay	D
<b>Alfisols</b> Alfisols are mineral soils that have a pedogenic accumulation of clay in the B horizon and base saturation <sup>3</sup> 35% and that have sufficient water during the growing season to support the growth of plants or have a fragipan that has clay films <sup>3</sup> 1mm in thickness	<b>Udalfs</b> Occur in a udic moisture regime	<b>Paleudalfs</b> Well-developed argillic	Finer than loamy fine sand	A

The Muskingum-Cunge method requires the geometry of each channel to input to the model in order to carry out the hydrological routing simulation. There were no field measurements for all 70 sub-basin outlets throughout Upper Mahakam Sub-watershed. Thus the river width was measured through remote sensing and GIS approach, while the other parameters were estimated through field experiences of the author. The bottom width of the channel and the side slope are estimated based on the result of surface width inferred from Landsat image, while the Manning's roughness coefficient was assessed based on the land cover in the surrounding of the channel, following the Manning's  $n$  classification (HEC, 2000). The Muskingum-Cunge shape for all channels was assumed to be trapezoidal. The time of concentration ( $t_c$ ) for each sub-basin was estimated based on 2-year rainfall amount, slopes, flow distance of precipitation excess on the land surface for sheet flow, shallow concentrated flow and channel flow. Additional input parameters such as Manning's roughness coefficient, channel cross-sectional area and wetted perimeter were then assessed based on the data collected above.

One very important process, which is the definition of meteorological model were also completed to ease the process later once the model is transferred into HEC-HMS. It is better to define the meteorological model before exporting to HEC-HMS to avoid manual entry of the precipitation gage weights for each sub-basin. Upon the completion of all above parameter estimation processes, the basin model was ready to be exported to the HEC-HMS interface in the format of a basin file that contains sub-basin division along with its physical characteristics and all derived parameters.

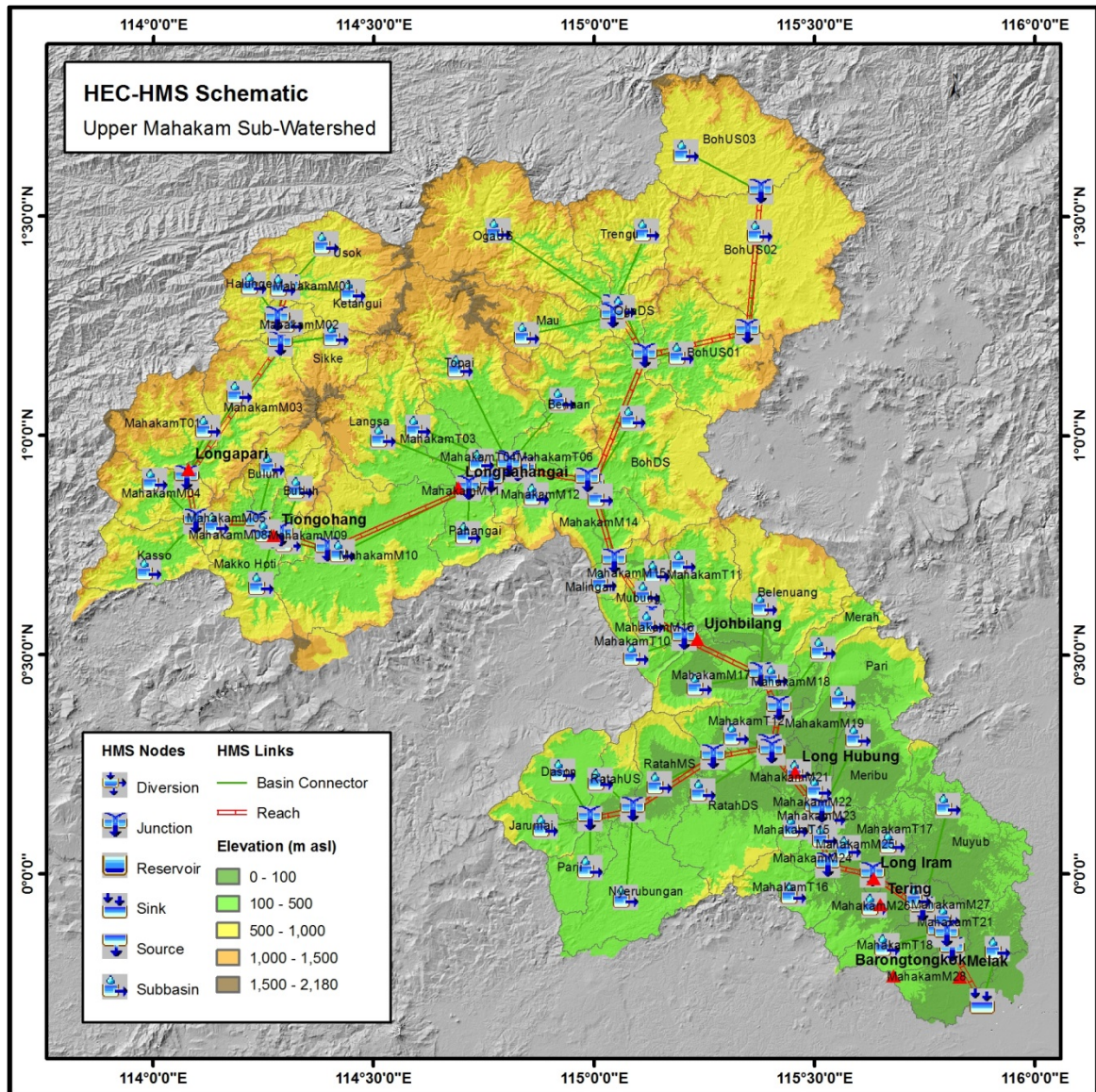


**Figure 4.15** The HEC-HMS elements schematic of Upper Mahakam Sub-watershed

#### 4.4.3. Setting up the HEC-HMS Model

The parameterization of basin and meteorological models have been completed and stored in a project file while the basin is processed in the HEC-GeoHMS environment. The last one to define is the control specification, which is one of the main components in a project. This model control when the simulation starts and stops, and what time interval is used in the simulation. Considering that the methods used to estimate the discharge are mostly event-based, the period of simulation is set up not to exceed one year per simulation. To define the starting simulation cycle, a few of short-period discharge records from other studies were thoroughly examined and it was found that the period of lowest discharge and precipitation are around July until September each

year. Considering that the simulation needs initialization period of a couple weeks, the simulation period is set up to start at August and ends at the end July of each year. In addition, the forcing data interval, *i.e.* precipitation, is daily. The discharge datasets used for calibration and validation are separated at 3-hour intervals, therefore the interval of the simulation for the calibration and validation periods follow such 3-hr intervals. However the interval for the simulation for the whole period is kept as one day to minimize the computation cost, since the total period for each simulation is one year.

**Table 4.8** Summary of the time window for the period of calibration, validation and 8-year final simulation period

Start Date	End Date	Interval	Period	Remarks
01 January 2003	31 December 2003	1 day	First Trial	Rejected. Precipitation input was based on NCDC NOAA, underestimated to 30%
08 January 2009	20 February 2009	3 hr	Calibration	Discharge inferred from H-ADCP
22 March 2008	13 July 2008	3 hr	Validation	Discharge inferred from H-ADCP
01 August 2002	31 July 2010	1 day	Final Simulation	The first 6 weeks of each water year are invalid. The model is not converged yet (See Figure 4.16 for example)

Following the definition of control specification, the time series data that include daily precipitation for all virtual meteorological stations during 2002-2010, 3-hour discharge during the calibration and validation periods, were entered into the model through the HEC-HMS time series manager. The rest of the preparation includes double check on the simulation methods and the integrity of all input parameters, defining the simulation run for first trial, calibration and validation of the model.

#### 4.4.4. Model Calibration and Optimization

Calibration is defined as “a test of the model with known input and output information that is used to adjust or estimate factors for which data are not available”, while validation is defined as “comparison of model results with numerical data independently derived from experiments or observations of the environment” (ASTM, 1984). Model calibration and validation are very important steps to be carried out in any model development. As commonly implemented in the watershed modeling, calibration begins with comparison of simulated and observed discharge, and then followed by refinement of parameters as the model is generally able to estimate such parameters given the availability of calibration dataset (*e.g.* observed discharge) to compare with the result of the simulation. Model validation basically extends the calibration process by comparing the output of calibrated models with completely separated observed dataset. The purpose of validation processes is to ensure the model capability to handle largest range of inputs and variations of model parameters. In this study, upon the completion of the validation process, the model simulates the whole meteorological input’s time window to produce final simulation for the whole period of study (2002–2010).

In this study, the outputs from HEC-HMS simulation runs are confronted with observed discharge during periods of calibration (October 2008 – July 2009) and

validation (March – July 2008). The gaged discharge in the calibration and validation periods were actually computed based on the results of a velocity measurements using Horizontal Acoustic Doppler Current Profiler (H-ADCP), which took place at the outlet of Upper Mahakam Sub-watershed at Melak Town (Hidayat *et al*, 2011a).

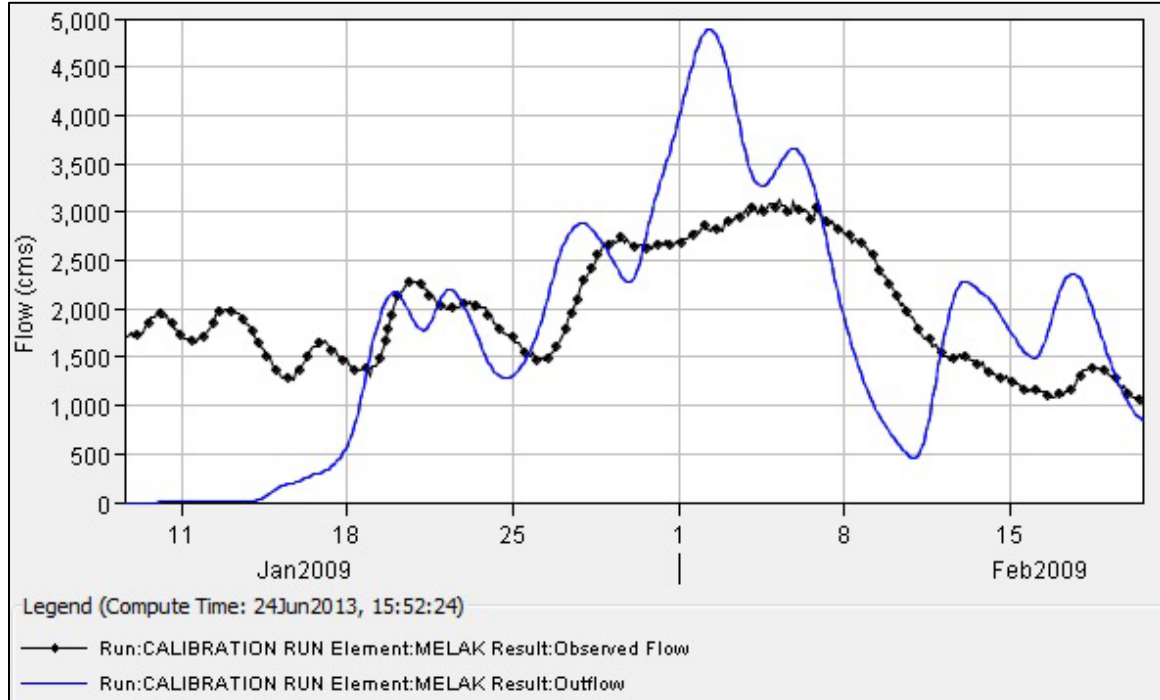


**Figure 4.16** HEC-HMS estimated and in-situ observed discharges at the main outlet of Upper Mahakam Sub-watershed as resulted from first calibration run

From the graph of the result of first trial run above, it is obvious that the Upper Mahakam Sub-watershed carries a significant baseflow rate, and the flow rate estimated by the model seems exaggerated to some extent. Therefore, the calibration process was focusing on tuning up the comprehensive flow ratio and baseflow parameters of the recession method, *i.e.* recession initial flow and constant, as well as the recession ratio. The initial baseflow was estimated as 20% of the peak flow for each sub-basin. This estimate was based on the constant discharge of the main outlet (Melak) when there was no precipitation for at least 14 days, as shown in the calibration period. The final recession constant is defined as 0.7, following the value range described in HEC (2000) and considering extent of the watershed and that the model deals mostly with surface runoff. The modified parameters during calibration period are listed as follow.

**Table 4.9** Summary of parameters modified during the calibration process

Run Name	Flow Ratio	Recession Initial Flow	Recession Constant	Recession Ratio
Calibration Run01	1	0.1	0.85	0.35
Calibration Run02	1	Monthly (1, 0.7, 0.4)	N/A	N/A
Calibration Run03	0.85	0.1	0.85	0.35
Calibration Run04	0.85	0.1	0.7	0.35
Calibration Run05	0.75	0.2	0.7	0.35
Calibration Run06*	0.80	0.1	0.7	0.35

\* Final parameters used for baseflow method and comprehensive flow ratio

Figure 4.17 shows that during the calibration period, the HEC-HMS model ran and produced the discharge, which was then compared with the measured discharge to adjust the parameters to produce the discharge that best match the observed discharge.

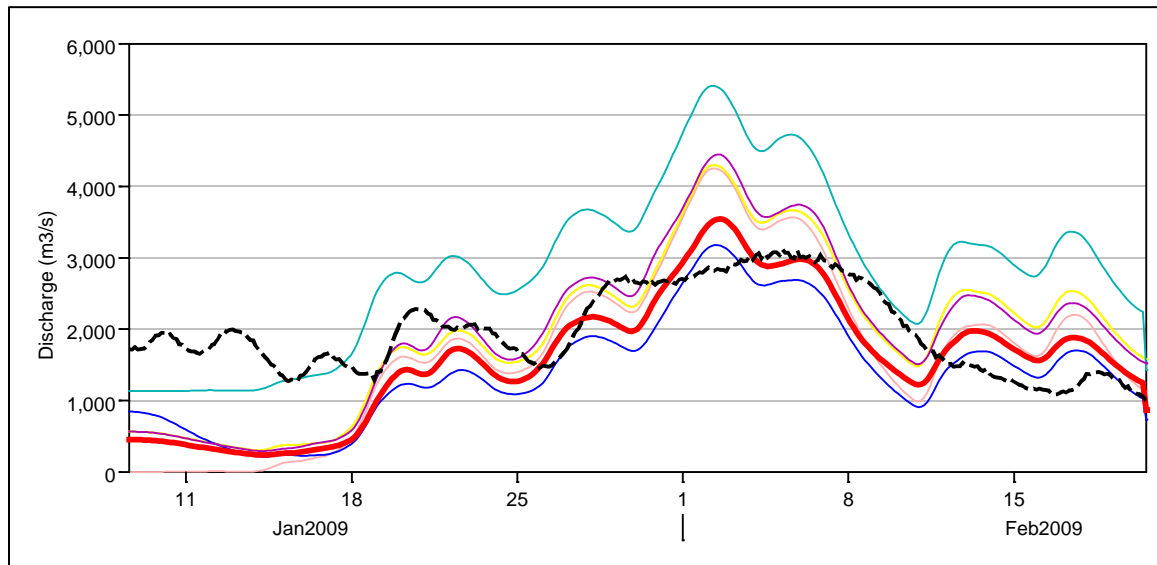


**Figure 4.17** Comparison of simulated and observed discharge at Melak during calibration period. Black dashed: observed discharge, the red bold: estimated discharge from the best fit model (Run 06), other lines: estimated discharge from other calibration runs.



**Table 4.10** Optimization for Clark Unit Hydrograph method's storage coefficient

Sub-basin	Initial Value	Optim. Value	Diff (%)	Objective Function Sensitivity	Sub-basin	Initial Value	Optim. Value	Diff (%)	Objective Function Sensitivity
Belenuang	139.73	140.38	0.47	-0.03	MahakamM25	8.62	8.62	0.00	-0.02
Belenuang	41.77	139.73	234.52	-0.05	MahakamM26	18.13	18.13	0.00	-0.00
Benaan	24.72	56.44	128.32	-0.03	MahakamM27	3.34	3.34	0.00	0.00
BohDS	55.03	81.91	48.84	-0.02	MahakamM28	25.99	59.35	128.34	-0.01
BohUS01	41.85	61.99	48.11	-0.01	MahakamT01	25.70	38.88	51.27	0.01
BohUS02	75.95	130.21	71.44	0.01	MahakamT03	6.49	1.28	-80.25	0.00
BohUS03	47.09	47.09	0.00	-0.02	MahakamT04	0.78	0.78	0.00	0.00
Bubuh	7.97	40.55	408.78	-0.00	MahakamT06	1.17	1.17	0.00	0.00
Buluh	12.61	12.61	0.00	-0.00	MahakamT10	7.34	7.34	0.00	-0.02
Dason	16.55	56.33	240.39	-0.01	MahakamT11	19.91	19.92	0.07	0.02
Halunge	12.98	29.53	127.51	-0.00	MahakamT12	6.42	6.42	0.00	-0.02
Jarumai	11.32	11.32	0.00	-0.00	MahakamT15	1.67	1.60	-3.96	0.00
Kasso	20.12	45.73	127.30	-0.01	MahakamT16	12.82	12.82	0.00	-0.02
Ketangui	14.31	46.25	223.20	-0.03	MahakamT17	7.67	7.67	0.00	0.00
Langsa	40.06	40.15	0.23	0.01	MahakamT18	9.73	6.41	-34.14	-0.02
MahakamM01	1.83	2.11	15.00	-0.00	MahakamT21	2.86	1.27	-55.56	0.00
MahakamM02	3.55	12.10	240.82	-0.00	Makko Hoti	18.32	139.12	659.39	-0.00
MahakamM03	34.78	118.54	240.83	-0.01	Malingan	2.15	1.43	-33.33	0.00
MahakamM04	17.39	26.34	51.47	0.01	Mau	23.49	34.01	44.76	-0.01
MahakamM05	8.18	18.22	122.70	-0.00	Merah	13.66	68.81	403.70	-0.01
MahakamM08	0.47	0.470	0.00	0.00	Meribu	22.00	74.47	238.49	0.02
MahakamM09	7.78	26.52	240.85	-0.00	Mubung	1.82	1.78	-2.00	0.00
MahakamM10	61.69	92.54	50.00	-0.01	Muyub	37.21	56.37	51.49	0.02
MahakamM11	5.48	2.11	-61.58	0.00	Nyerubungan	34.65	118.06	240.72	-0.01
MahakamM12	14.32	48.81	240.85	-0.00	OgaDS	7.18	7.18	0.00	-0.00
MahakamM14	16.10	24.34	51.20	-0.00	OgaUS	61.72	135.97	120.30	-0.05
MahakamM15	7.58	16.65	119.59	-0.00	Pahangai	13.00	44.31	240.82	-0.01
MahakamM16	3.09	1.373	-55.56	0.00	Pari	29.47	44.31	50.37	0.02
MahakamM17	20.35	30.53	50.00	-0.00	Parii	11.01	11.01	0.00	-0.00
MahakamM18	1.22	1.22	0.00	0.00	RatahDS	41.98	141.68	237.49	-0.05
MahakamM19	2.36	2.36	0.00	-0.02	RatahMS	20.98	70.30	235.10	-0.01
MahakamM21	8.39	8.39	0.00	-0.01	RatahUS	9.70	9.94	2.52	-0.00
MahakamM22	0.08	0.08	0.00	0.00	Sikke	14.12	32.08	127.16	0.03
MahakamM23	1.26	1.26	0.00	0.00	Topai	48.95	48.95	0.00	0.02
MahakamM24	2.43	2.43	0.00	-0.02	Trengu	26.46	90.12	240.58	0.03
					Usok	22.58	76.87	240.45	-0.01

Considering that HEC-HMS has the capability to conduct model optimization given the availability of output discharge, the storage coefficient value for each sub-basin was optimized in this study, since the first guess of this parameter was generated through the duplication of similar studies in the humid tropic region, *i.e.* Sarawak, Malaysia, instead of adopting the value from secondary data originated in the same region.

Optimization begins from initial parameter estimates and adjusts them so that the simulated results match the observed discharge as closely as possible. Considering that there was only one parameter to be optimized, the univariate gradient method was used as the search method, which evaluates and adjusts the storage coefficient parameter while holding other parameters constant. The objective function measures the goodness-of-fit

between the computed and observed discharge at the selected sub-basin. Out of seven different functions offered in HEC-HMS, this study uses the peak-weighted RMS error function to measure the objective function resulted by the optimization process, considering that the initial simulation shows significant discharge overestimates. This method is a modification of the standard root mean square error that gives greatly increased weight to above average discharge and less weight to below average discharge.

## 4.5. Results and Discussion

### 4.5.1. Validation of the Model

To evaluate the performance of the model after all measures (*i.e.* calibration, and optimization), the estimated discharge is evaluated using common statistical measures in hydrologic modeling. The Nash-Sutcliffe Efficiency Index (NS) is used to compare the estimated and observed variable and measure the reliability of the model to represent the response of the studied watershed to the variability of precipitation. The Nash-Sutcliffe Efficiency Index is calculated as follows (Nash and Sutcliffe, 1970).

$$E = 1 - \frac{\sum(Q_s - Q_o)^2}{\sum(Q_o - \bar{Q}_o)^2} \quad (4.2)$$

Where  $Q_s$  = Simulated discharge and  $Q_o$  = Observed discharge both in (m<sup>3</sup>/s). Nash-Sutcliffe efficiencies can range from  $-\infty$  to 1. An efficiency of 1 ( $E = 1$ ) corresponds to a perfect match of modeled discharge to the observed data. An efficiency of 0 ( $E = 0$ ) indicates that the model predictions are as accurate as the mean of the observed data, whereas an efficiency less than zero ( $E < 0$ ) occurs when the observed mean is a better predictor than the model.

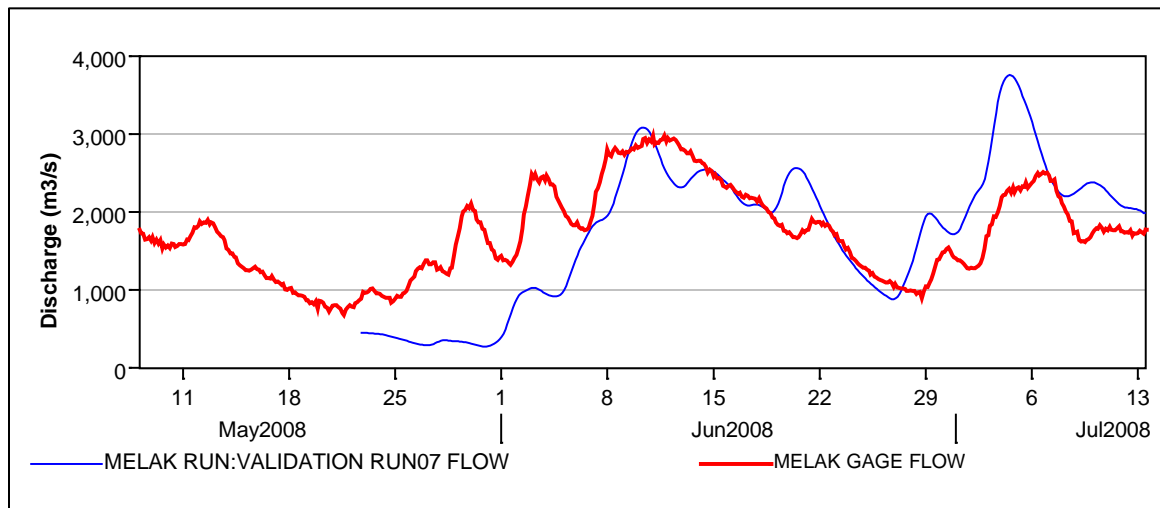


**Figure 4.18** Estimated and observed discharge during validation period at Melak

From Figure 4.18, it can be seen that the estimated discharge sufficiently match the observed discharge, with the exception of the first couple weeks of model execution, which is the model initiation phase. Calculated statistical measures, which include Root



Mean Square (RMS) Error, Coefficient of Correlation and the Nash-Sutcliffe Efficiency Index, are summarized in the following table.

**Table 4.11** Statistics for validation of HEC-HMS simulated discharge at Melak

Station	RMS Error (m <sup>3</sup> /s)	Coefficient of Correlation	NS Efficiency Index (E)
Melak	626.21	0.51	0.51

The RMS error and the correlation coefficient as resulted from the statistical analysis are both not good enough. RMS error in the magnitude of 626 m<sup>3</sup>/s or ~20% of the peak discharge of 3000 m<sup>3</sup>/s is significant considering size of the catchment.

The Nash-Sutcliffe Efficiency Index of the simulated discharge is just about the average compared to other studies and it could be seen that the simulated discharge somehow follows the pattern of the measured discharge. It is worth noting however, that the statistics above are calculated by excluding the simulated discharge during the initialization period. This couple week period is known to estimate much lower discharge, since the model assumes no saturation on the soil from the previous infiltration, so this may lead to greater differences that impact the RMS Error.

The performance of the HEC-HMS hydrologic model developed in this study is slightly lower than another study completed for the same sub-watershed. Hidayat *et al.* (2011b) developed the Hydrologiska Byrans Vattenbal-ansavdelning (HBV) light version with lumped input and the Variable Infiltration Capacity (VIC) models with distributed input forcing with a grid size of 0.25° x 0.25°. With the same TRMM Multi-mission Precipitation Analysis as the input forcing, the HBV produced better estimation than the VIC with Nash-Sutcliffe Efficiency Index (E) = 0.64 after the validation, compare to VIC that produced E = 0.29 after the validation. The HEC-HMS model developed in this study performs at about the average of other studies with HEC-HMS as main rainfall-runoff model, in terms of their assessed accuracy and/or efficiency, as listed in the following table.

**Table 4.12** Summary of studies applying HEC-HMS for rainfall-runoff model

References	Location	Precipitation Input	Model / Runoff Module	NS Efficiency Index (E)
Hidayat <i>et al</i> (2011b)	Upper Mahakam Sub-watershed, Indonesia	TRMM 3B42 TRMM 3B43	HBV & VIC	0.64
Zhang <i>et al</i> (2013)	Clear Creek Watershed, Iowa	NEXRAD Hourly	HEC-HMS SCS-CN	0.58
Yusop <i>et al</i> (2007)	Johor, Malaysia	Gauge (Tipping Bucket)	HEC-HMS SCS-CN	0.81
Verma <i>et al</i> (2010)	Baitarani River Basin, India	Gauge Daily	HEC-HMS SCS-CN	0.73
Gyawali and Watkins (2013)	Kalamazoo, Maumee and St Louis Watersheds, US	Gauge Daily	HEC-HMS SCS-CN	0.49
Fleming and Neary (2004)	Dale Hollow Watershed, TN, KY	Gauge Daily	HEC-HMS Soil Moisture Acc.	0.40
Chu and Steinman (2009)	Mona Lake Watershed, MI	Gauge Daily	HEC-HMS SCS-CN	0.69
Sulistioadi (2013)	Upper Mahakam Sub-watershed, Indonesia	TRMM 3B42 v7 Daily	HEC-HMS SCS-CN	0.51

#### 4.5.2. Final Simulation and the Flood Events

With this result, the input parameters are then finalized and used in the simulation of the whole period of study, *i.e.* 2002 – 2010 with the “water year” starts from August and ends at July each year. Some results of these simulations and its association with the recorded flood events are presented and discussed in the following series of figures.

To better understand the inter-relationship between the time of concentration, sub-basin inter-connection and resulting discharge, the Upper Mahakam Sub-watershed is further subdivided into the main contributing catchments and the main channels. In addition, HEC-HMS plots the discharge based on the element name, which is not identifiable, so Figure 4.19 above and Table 4.13 below refer those elements to the real sub-basin or channel name. The four contributing sub-basins and main channels of interests are listed in the following table and shown in the map.

**Table 4.13** HEC-HMS element name for the four contributing sub-basins and main channels of interest

Sub-basin	HEC Element Name	Channel	HEC Element Name
Boh Catchment	Reach-18	Tiongohang	Reach-2
Uppermost Catchment	Reach-9	Ujohbilang	Junction-4970
Pari-Meribu Catchment	PariDS	Longpahangai	Junction-5033
Ratah Catchment	Reach-24	Melak	Melak

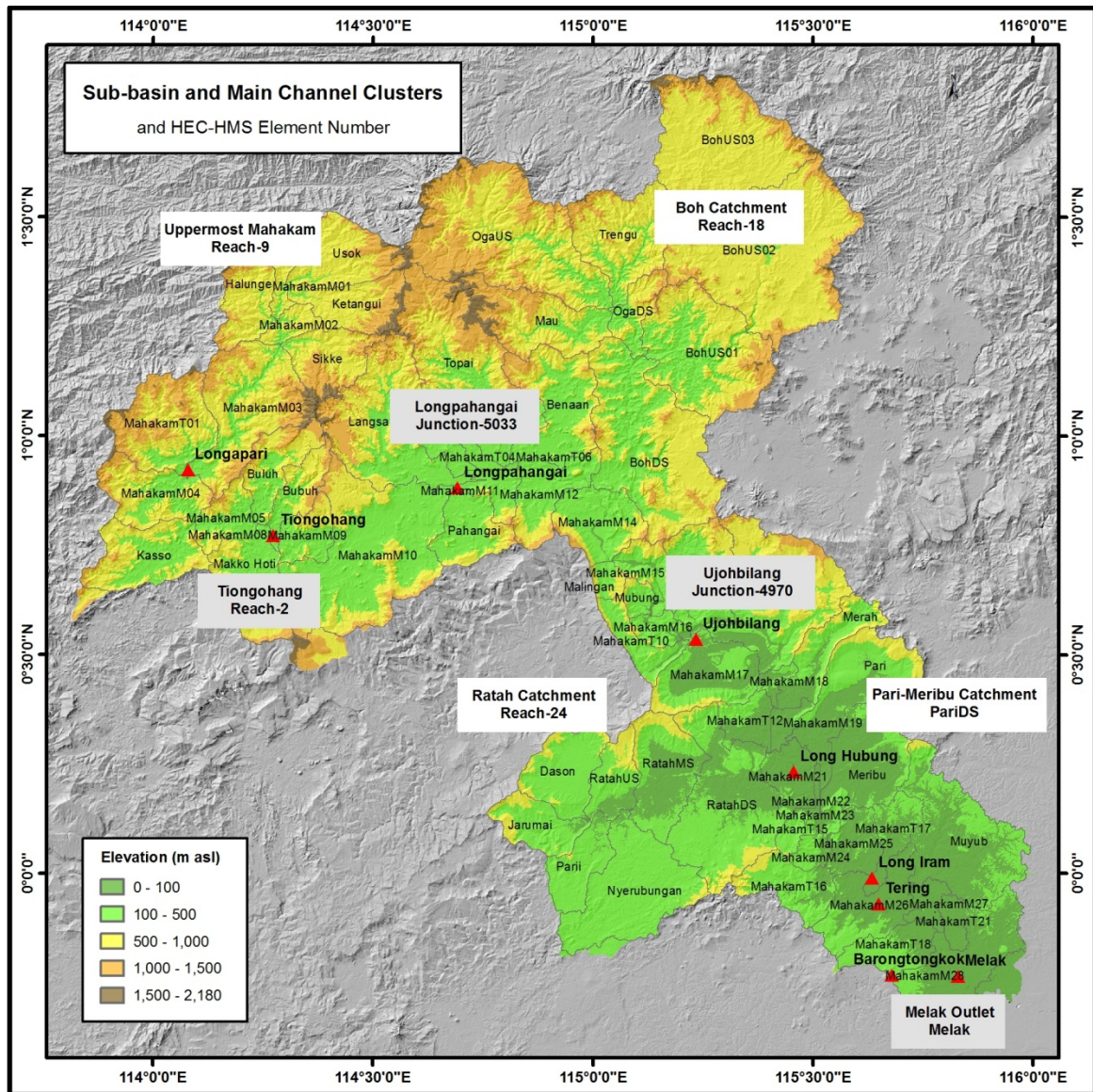


**Figure 4.19** Sub-division of Upper Mahakam Sub-watershed into clusters of contributing sub-basins (white) and main channels (grey)

(1) Flood event of May 2005

Little is known about the flood event in May 2005, except that the flood lasted for a couple of weeks and caused about 3,500 houses to be damaged due to the inundation during high water levels. From the graph of simulated discharge, it could be seen that the highest discharge occurred around April 2005, which slowly decreased until a couple of weeks before May, and rose again during the whole month of May. Keeping in mind that this model solely models discharge, the spread of the inundated area, along with its temporal progression remain unknown. It may be worth to note that during water year 2004-2005, there were two periods with sharp discharge rises, *i.e.* February and April

2005. The one in April 2005, has a very high discharge rate (beyond 5000 m<sup>3</sup>/s), which even exceeds the maximum discharge during all other water years.

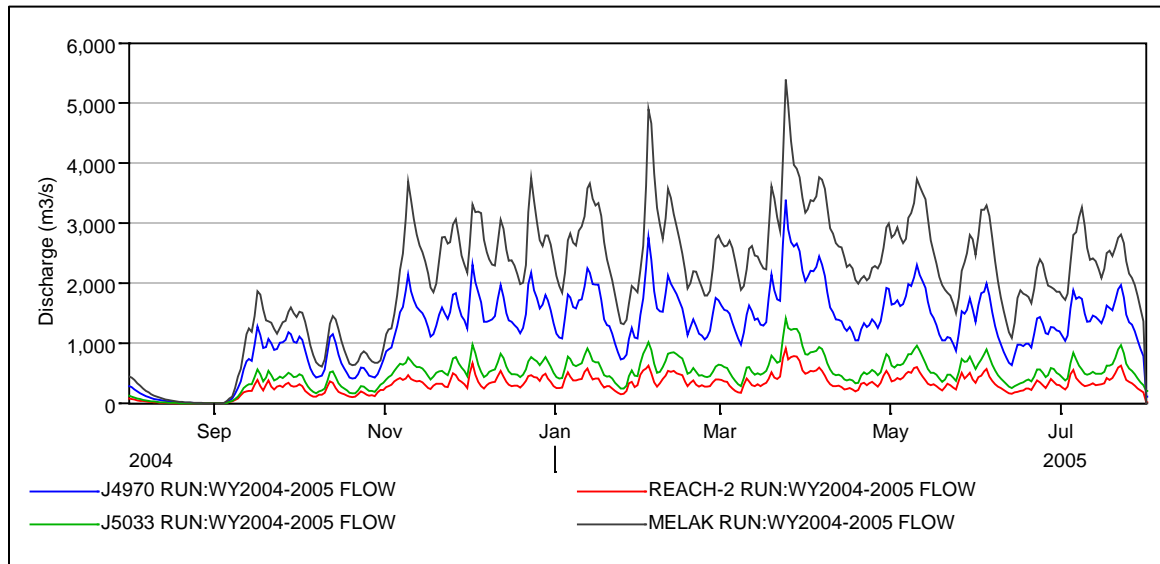


**Figure 4.20** HEC-HMS element name for the four contributing sub-basins and main channels of interest

## (2) Flood event of July 2006

This flood inundated 17 sub-districts out of 21 sub-districts in this area and forced about 40,000 people to be evacuated. The simulated discharge of the main channels indicates a long period of high discharge, but not the peak.

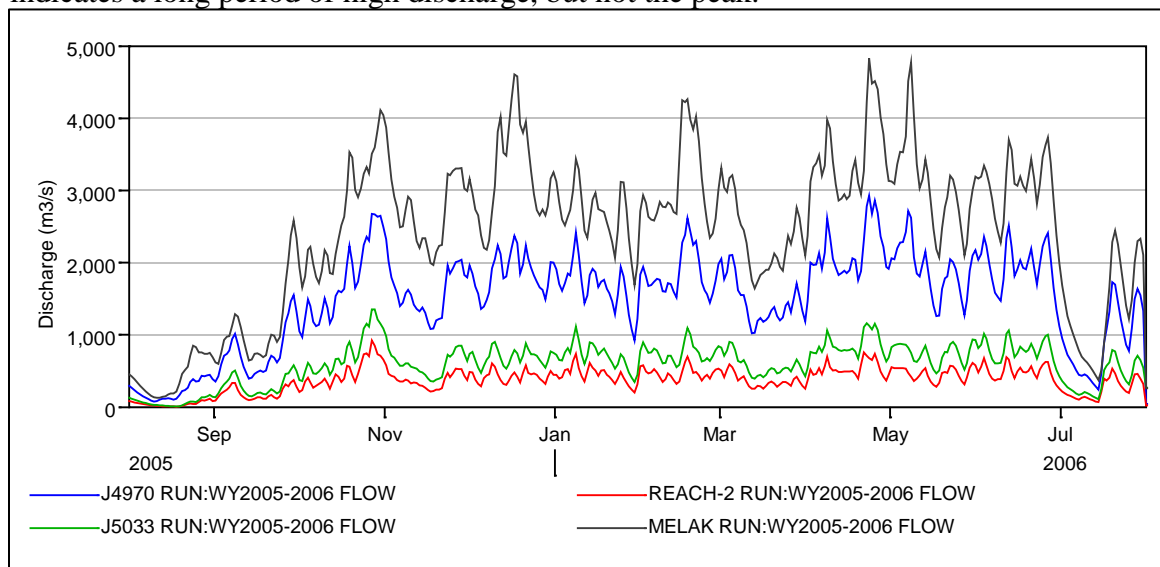


**Figure 4.21** Simulated discharge at the main channels during water year 2005-2006

### (3) Flood event of May 2007

This was the most disastrous flood that happened in this area in the last decade. 19 out of 21 sub-districts were inundated since April 26, 2007 and the water profile remained at about the same level for 6 weeks. From the graph of simulated discharge, it is obvious that the period of inundation exactly matches the highest discharge period of the Melak main channel. Even the discharge went down drastically for about a week; then it went back up and stayed high until the next month.

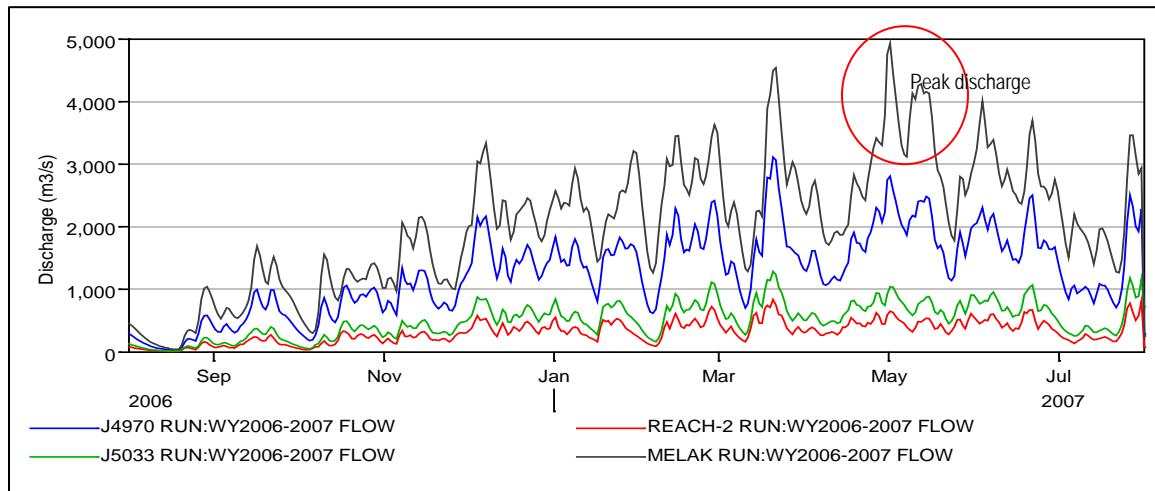


**Figure 4.22** Simulated discharge at the main channels during water year 2006-2007

### (4) Flood event of February 2008 at Boh Catchment

This special case occurred only at Boh Catchment. The precipitation estimate from TRMM shows a rainfall of 68 mm on 7 February 2008 right in the middle of 8-day period of about 10 mm/day. The following plot shows the response of each major sub-basin for the whole water year, which clearly shows the specific period of February 3-11, 2008. Note that precipitation remains high in November 2007 and April-May 2008. Also note the highest peak of BohUS02 sub-basin during June 2008 despite low precipitation.

From Figure 4.23, the discharge downstream of the Boh Catchment can be seen to reach its peak on 8 February 2008; however, this day was not the peak period most of the sub-basins. Therefore, it was assumed that a relatively high discharge on all sub-basins accumulatively increased the total discharge during this period.

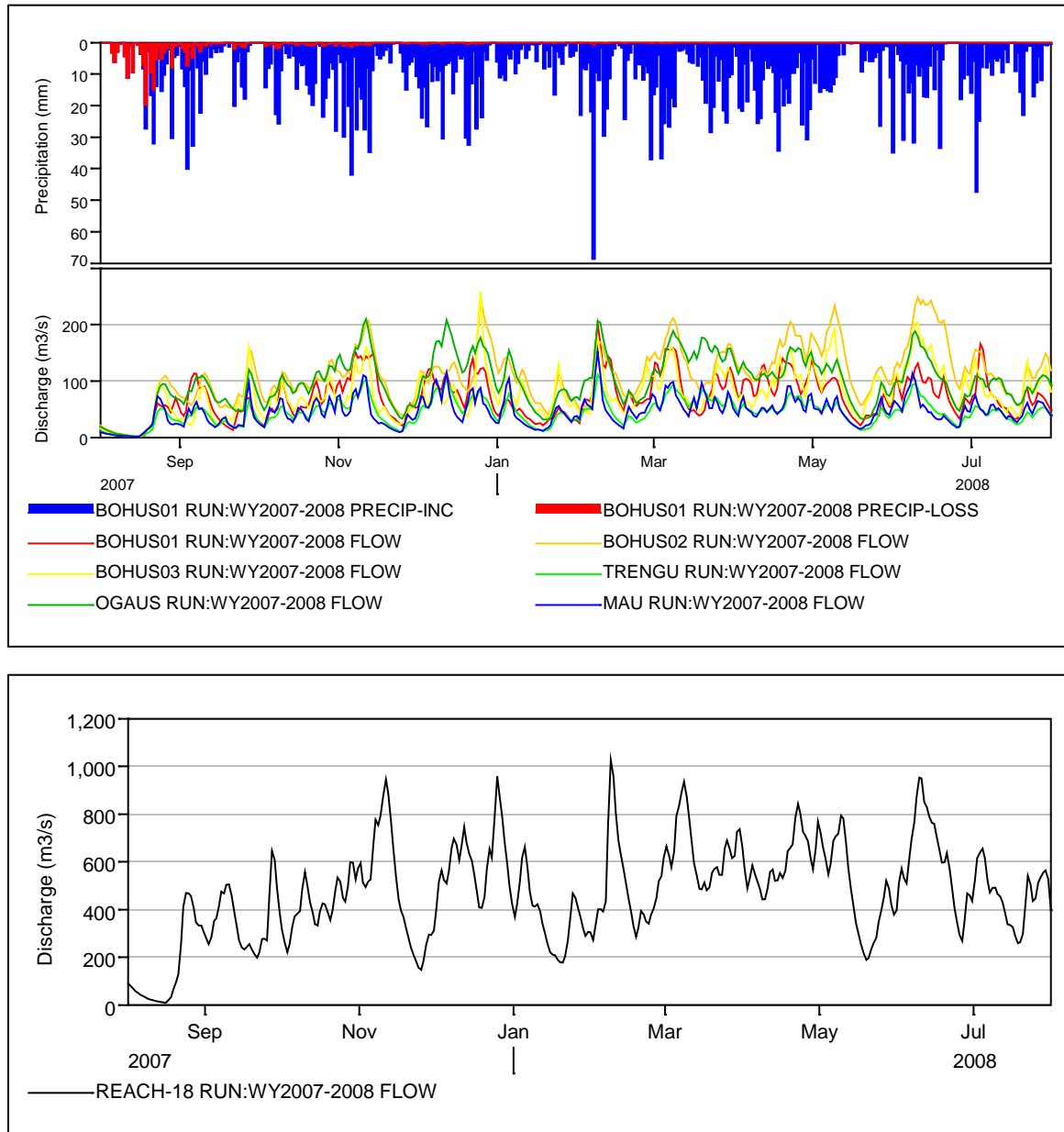


**Figure 4.23** Precipitation and simulated discharge at various sub-basins within Boh Catchment during the water year of 2007-2008 (top panel) and the accumulated discharge on the main channel (Boh River) (bottom panel)

(5) Flood event of September 2008 at Longhubung Town (Ratah Catchment)

This special case was occurred in Ratah Catchment, where 4 sub-districts were inundated up to 2 m. From Figure 4.24 it is hard to see this event, since the model was in the initialization period before running at full capability.



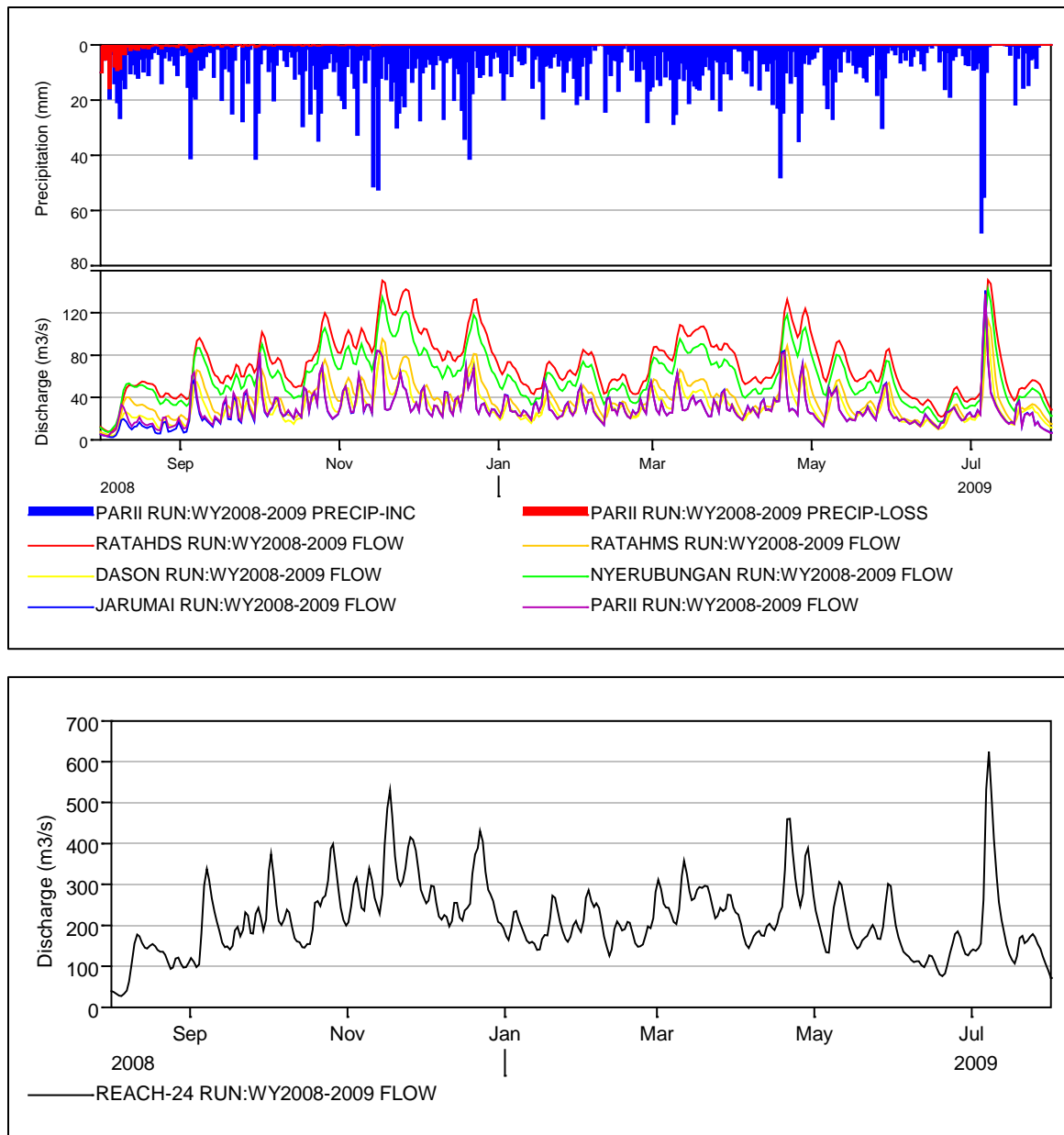


**Figure 4.24** Precipitation and estimated discharge at sub-basins within Ratah Catchment during the water year of 2008-2009 (top panel) and the accumulated discharge on the main channel (Ratah River) (bottom panel)

The precipitation panel shows a sharp precipitation increase at the beginning of September 2008 and followed by a significant increase of discharge. However, the magnitude as estimated by this model is arguably true, which makes this event look not as severe compared to other periods of peak (*e.g.* December 2008, May and July 2009).

(6) Flood event of April 2010

This flood event affected 10 sub-districts, which are mostly downstream of the Upper Mahakam Sub-watershed. Figure 4.25 shows the highest discharge rate during April 2010 with a slow falling rate followed by steady discharge at a relatively high rate.

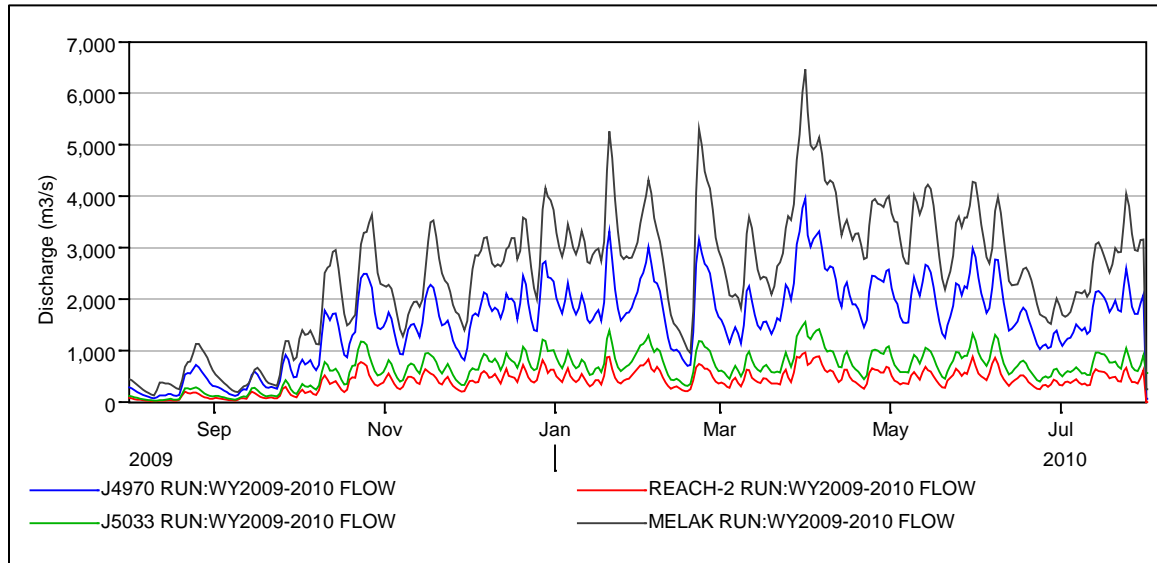


**Figure 4.25** Simulated discharge at the main channels during water year 2009-2010

It is interesting to see that the model seems not really stable until mid-September 2009, which is indicated by very low baseflow until the beginning of October 2009. In addition, it is also worth noting that the discharge dropped drastically just before the end of February 2010 and sharply rose during March 2010. This irregular fluctuation confirms there is no distinctive period of flooding at Upper Mahakam Sub-watershed.

#### 4.6. Conclusions and Recommendations

The response of the Upper Mahakam Sub-watershed to the variability of precipitation has been appropriately modeled through HEC-HMS event-based rainfall-runoff simulation. To summarize this chapter, the following conclusions are drawn based on the series of experiments carried out in this study.

- (1) The TRMM Multi-satellite Precipitation Analysis (TMPA) is considerably good to use in the absence of reliable-short-interval precipitation records in building a hydrologic model. Critical care should be taken however, due to the unpredictable offset between the estimated and observed precipitation as measured by meteorological station. In addition, the Thiessen polygon and area average hybrid method is proposed to virtually represent the spatial distribution of the meteorological stations, especially when those stations are separated by considerable distance and there is no daily precipitation data available from the closest meteorological station.
- (2) The preparation of geospatial data and input parameters, along with the calibration of the hydrologic model, besides being potentially tedious, needs the



most attention and careful execution. In addition, these critical steps define the quality and reliability of the model being built.

- (3) The performance evaluation of HEC-HMS discharge estimation confirms a reasonable match between the simulated discharges with the observed ones, as expressed by the Nash-Sutcliffe Efficiency Index of 0.51, which is about the average of other implementations of HEC-HMS based hydrologic model. In addition, the RMS Error and the correlation coefficient did not indicate close relationship between the simulated and observed discharges. This provides a room for improvement of the performance of the hydrologic model.
- (4) Regarding its reliability in detecting the flood events, most flood events as reported by the news agencies were successfully confirmed by this model, with various degrees of fit.

Further, by considering the findings and problems encountered during the execution of this research, the following measures are noted for future studies:

- (1) The use of TRMM Multi-satellite Precipitation Analysis (TMPA) in case of no better long-term precipitation data available is possible. However, it is highly recommended to perform a robust calibration based on good precipitation dataset with matching interval to those of the TRMM and to build an evident relationship between the two before incorporating the TRMM precipitation estimation as the main forcing in a hydrologic model.
- (2) An important note on the application of event-based models to monitor sub-watershed response to precipitation is that HEC-HMS could not simulate event-based methods for loss, direct runoff and hydrologic routing for long time windows (*e.g.* more than a year) due to the nature of its deterministic character. Hence, the use of continuous methods with more complete input parameters is desired for future studies that seek for continuous discharge estimation for the entire watershed.

## 5. Integrating Satellite Altimetry and Hydrologic Model

### 5.1. Introduction

The spatial and temporal resolution limits are well-known as the major impediments for the use of inland water level measurement from satellite altimetry as an operational substitute of *in-situ* measurement. However, the robustness of satellite altimetry range measurement, along with the comprehensive error corrections and its versatility to carry out measurement at any atmospheric condition convincingly encourage its use as a reliable measuring tool for inland water bodies.

The two preceding chapters explored the challenge of measuring narrow water bodies as well as developing a hydrologic model with insufficient input parameters and model forcing. From the first experiment, it was evident that satellite altimetry can provide reliable water level observations of rivers as narrow as 54 m with reasonable accuracy, while the second experiment pointed out the successful development of a hydrologic model based on satellite-inferred precipitation estimate as the model forcing. It is very important to note, however, that critical care should be taken prior to incorporating TRMM precipitation estimates into the hydrologic model, in order to keep the model reliable.

As it is desired to develop a complementary monitoring system through satellite altimetry and hydrologic model, this chapter explores the possibilities to link them up. First of all, the magnitude of discharge resulting from the HEC-HMS hydrologic model is transformed into “local” water height and water level anomaly, with the help of a local rating curve, as it has been developed for the Mahakam River by other researchers (Hidayat *et al.*, 2011a). The second step consists of relating these two measurements to a set of *in-situ* water level measurements within a validation period. The two measurements are then analyzed to see which measurement has a better relationship to the “true” measurement, *i.e.* presenting the most realistic water level anomaly estimation. Statistical measures used for the evaluation include the standard deviation, root-mean-square error and coefficient of correlation, as detailed in Page 82.

Various studies had been completed to integrate and complement satellite radar altimetry measurements and hydrologic models, to calibrate and validate one another. This effort is critical to improving continuous monitoring of un-gauged or poorly gauged watersheds through hydrologic modeling, considering the accuracy of range measurement provided by satellite altimetry and its repeated observation allows continuous monitoring of un-gauged or poorly gauged watersheds.

Efforts on developing a relationship between hydrologic models and satellite altimetry measurements include Getirana *et al.* (2009, 2010), which developed high accuracy relationships between satellite altimetry-measured water levels and discharge computed by hydrologic model for the northern Amazon basin based on a local rating curve that relates the observed water height and modeled discharge. In another study, it was found that the model that includes satellite altimetry data produced an estimated discharge of Mekong River with higher accuracy (Birkinshaw *et al.*, 2010). A contrasting result is shown by Siddique-E-Akbor *et al.* (2011), which compared the water level estimates from a one-dimensional hydraulic model with satellite altimetry observation,

and found that satellite altimetry shows disagreements with hydraulic models especially for small to medium-sized river basins that are mountainous and flashy.

In other studies, satellite altimetry was used to calibrate or validate hydrologic models developed with no in-situ data available. In Lake Turkana in Africa, a composite of TOPEX/Poseidon, Jason-1 and Envisat satellite altimetry data was used to calibrate and validate the water balance model based on digital elevation dataset, satellite-based rainfall estimates, runoff and evaporation. The study indicated a good agreement and the model capability for capturing patterns and seasonal variations of the lake (Velpuri *et al.*, 2012). In a large river in North America, Sun *et al.*, (2012) developed coupled hydrology and hydraulic models to describe the relation between streamflow and water stage of the Upper Mississippi Basin and calibrated them with TOPEX-Poseidon satellite radar altimetry. From that experiment, it is revealed that the contribution of remote sensing data uncertainty is minor.

These findings strongly encourage further measures in linking monitoring inland water bodies through satellite altimetry and hydrologic model as had been performed in the preceding chapters, through statistical analysis and measures of validation, which is shown in this chapter.

## 5.2. Simultaneous Validation of Satellite Altimetry and Hydrologic Model

The simultaneous validation between satellite altimetry and hydrologic model is conducted based on the *in-situ* discharge measurement conducted at the outlet of Upper Mahakam Sub-watershed at Melak Town. Both HEC-HMS simulated and *in-situ* gauged discharges ( $Q$ ) are transformed into local water depth ( $d$ ) through inverse of the rating curve for steady flow as developed by Hidayat *et al.*, (2011a) as follow.

$$Q = 125.98 \times (d + 1.5)^{1.256} \quad \text{with its inverse} \quad d = \left( \frac{Q}{125.98} \right)^{\frac{1}{1.256}} - 1.5 \quad (5.1)$$

Upon calculation of local water depth, the mean is then removed to infer the water level anomaly in meters. Statistical analyses (as detailed in Page 85) are then conducted to assess the relationship and reliability of both satellite altimetry and HEC-HMS model in estimating water level anomalies. As discussed in Section 4.5.1, the first weeks of a HEC-HMS simulation year could not be considered as valid estimations, since the model was still in the initiation phase. Therefore, the first 34 days of the water year (*i.e.* 31 July to 2 September each year) are excluded from the simultaneous validation.

Visually, the satellite altimetry measured water level anomaly matches closer than those inferred from HEC-HMS simulated discharge, as they are compared to *in-situ* data. While satellite altimetry measurement deviates considerably, HEC-HMS often provides significant underestimated and overestimated magnitudes of the water level anomaly. The following plots show the relationship between these three measurements.

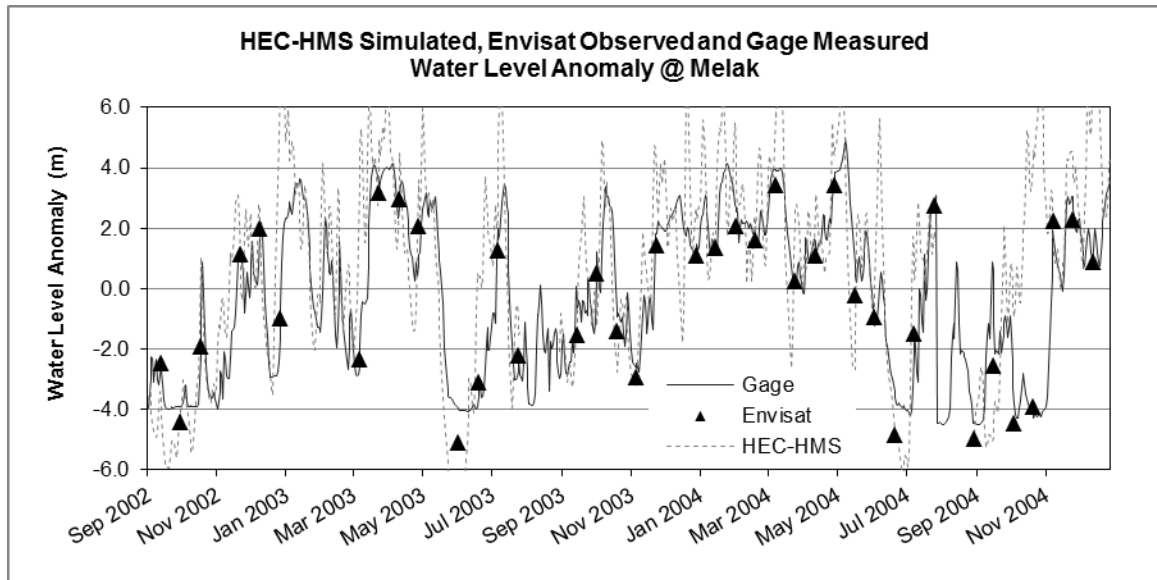


**Figure 5.1** HEC-HMS simulated, Envisat observed and gage measured water level anomaly at Melak 2002-2004

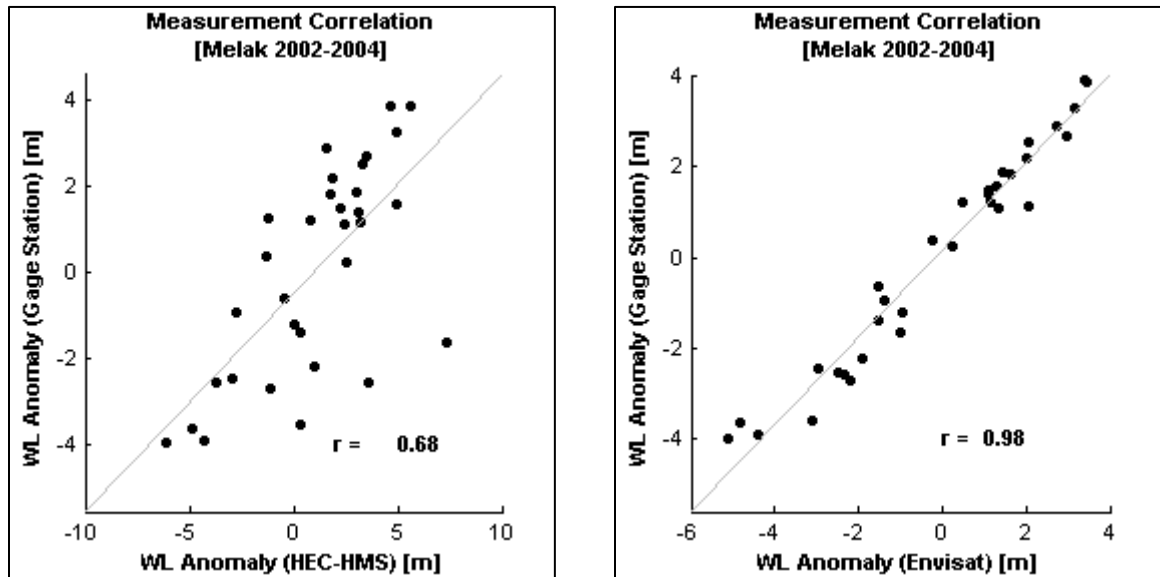


**Figure 5.2** Correlation between water level anomaly inferred from HEC-HMS simulated discharge (left) and Envisat RA-2 altimeter (right) with *in-situ* measurement

The results of quantitative analyses are presented in Table 5.1. Statistically, the satellite altimetry measurement confidently outperforms the HEC-HMS simulation in estimating water level anomaly as indicated by a higher correlation coefficient, a lower standard deviation, and lower RMS error.

**Table 5.1** Statistical measures of HEC-HMS simulated and Envisat RA-2 satellite altimetry measured water level anomaly relative to *in-situ* measurement

Approach	Standard Deviation (m)	RMS Error (m)	Coefficient of Correlation
HEC-HMS Model	2.39	2.56	0.68
Envisat RA-2 Satellite Altimetry	0.49	0.52	0.98

Based on the statistical measures described above, satellite altimetry obviously represents the behavior of water level anomaly better than HEC-HMS hydrologic model.

The capability of satellite altimetry to support the hydrologic model to estimate discharge agrees with similar studies as carried out in Mekong River (Birkinshaw *et al.*, 2010), the Amazon (Leon *et al.*, 2006, Getirana *et al.*, 2009, 2010), Ganga-Brahmaputra River (Papa *et al.*, 2010) and Upper Mississippi Basin (Sun *et al.*, 2012). It is then convincing to propose the use of water level anomaly measurements by satellite altimetry to validate the result of hydrologic model, in the absence of in-situ measurement on discharge or water level.

### 5.3. Conclusions and Recommendations

This chapter evaluated the relationship between HEC-HMS hydrologic model estimated and satellite altimetry measured water level anomaly through a simultaneous validation based on in-situ discharge measurement. From the results of the simultaneous validation, the following conclusions are presented.

- (1) The simultaneous validation over 32 measurements from all three approaches (*i.e.* HEC-HMS estimated, satellite altimetry and *in-situ* measured) to obtain water level anomaly indicates that satellite altimetry outperforms the HEC-HMS hydrologic model in terms of their correlation to the true discharge as well as their capability in representing the water level anomaly behavior.
- (2) Considering the high correlation between satellite altimetry measurements and in-situ measurements, it is worth exploring the use of satellite altimetry measurements as a source of validation of a hydrologic model, especially those developed in the Southeast Asia's humid tropic region

Considering the problems encountered in this evaluation process, the following recommendations are proposed to achieve better results in future studies.

- (1) The HEC-HMS hydrologic model developed in this study needs to be improved since the water level anomaly as inferred from the simulated discharge tends to be either be overestimated or underestimated with considerable offset
- (2) A complementary operational hydrology monitoring based on the rainfall-runoff model such as HEC-HMS and satellite altimetry may worth to explore, *e.g.* through exploration of data assimilation approach, which assumingly will improve the accuracy of simulated discharge from hydrologic model using satellite altimetry measurement, as it drastically reduces the errors generated during hydrologic model simulation (*e.g.* Clark 2006, Andreadis *et al.*, 2007, Durand *et al.*, 2008, Biancamaria *et al.*, 2011, Yoon *et al.*, 2012 and Getirana and Peters-Lidard, 2012, Michailovsky *et al.*, 2013 and Paiva *et al.*, 2013).

## 6. Conclusions and Future Studies

### 6.1. Conclusions

From the first experiments on the application of satellite altimetry to monitor small and medium-sized water bodies, it is evident that satellite altimetry has successfully revealed the dynamic of the water level profile of medium-sized river at Mahakam River and small lakes at Lake Semayang and Lake Matano. Even with the various correlation coefficient and RMS Error between the satellite-observed and *in-situ* water level measurements, this approach provides an alternative to hydrological monitoring of small and medium-sized river and lakes. In addition, this study successfully proved that medium-sized river as narrow as ~200 m can be monitored and validated appropriately through satellite altimetry. The waveform shapes selection procedure can be helpful in sorting out measurements with lower quality, which then improves the accuracy of satellite altimetry measurement and is therefore proposed to be applied for future studies involving small (40–200 m width) to medium rivers (200–800 m width), as well as small lakes (*e.g.* lakes with extent less than 1000 km<sup>2</sup>). As the last conclusion from the first study, water bodies narrower than 40 m should be excluded from the effort of satellite altimetry based water level measurement since the satellite sensor may not be able to infer the existence of water bodies on the Earth's surface.

Regarding the hydrologic modeling of a poorly-gauged watershed, it is evident that event-based rainfall-runoff modeling can provide reliable estimations of watershed response to the variability of precipitation. As presented in Chapter 4, the model was successfully validated and given a value of the Nash-Sutcliffe Efficiency Index that is close to the average of other studies. The HEC-HMS model also confirmed all flood events listed in the news report with various degrees of fit. In addition, the use of TRMM Multi-satellite Precipitation Analysis is possible, with the condition that there are enough field collected meteorology data to calibrate and calculate the relationship between the two. It is noteworthy that this study also proposes the Thiessen Polygon and area average hybrid approach to spatially process TRMM precipitation estimate to match the spatial distribution of the existing meteorological stations. From the practical view of the hydrologic model, the event-based rainfall-runoff model for loss, direct runoff and hydrologic routing used in this study has been successfully run for a simulation period of one year with 1-day calculation interval. For a longer simulation period, a continuous rainfall-runoff model such as the HEC-HMS soil moisture accounting model might perform better.

The simultaneous validation between the water level anomaly transformed from HEC-HMS simulated discharge, satellite altimetry and *in-situ* measurement shows that the satellite altimetry outperforms the HEC-HMS hydrologic model in terms of their correlation to the *in-situ* measured discharge. However, overall time series of the HEC-HMS simulated and satellite altimetry derived water level anomaly shows an agreement on their pattern.

### 6.2. Future Studies

To encompass the future on the studies related to satellite geodesy and its hydrological applications, broader studies on the use of satellite altimeter on other small

bodies of water might help scientists and government in the global effort of hydrological monitoring. To address technical issues in the altimetry data processing, waveform shape selection and categorization to strictly follow the standard waveform shape for inland water bodies as described in the previous studies (Koblinsky 1983, Birkett 1988, Berry *et al*, 2005, Dabo-Niang *et al*, 2007) is proposed to be applied for any future studies involving small to medium rivers (which characterized as 40-200 m width and 200-800 m width, respectively), as well as small lake (*e.g.* those with extent less than 1000 km<sup>2</sup>).

With regard to the hydrologic modeling, the HEC-HMS hydrologic model developed in this study needs to be improved since the discharge tends to either overestimate or underestimate with considerable offsets. In addition, a continuation of the hydrologic modeling, *i.e.* hydraulic model, is desired to specifically monitor the flood inundation area and dynamics, given the availability of topographical datasets.

As the final recommendation, to overcome the significant difference in terms of the number of observation between the hydrologic model (large number of observation, lower accuracy) and the satellite altimetry (small number of observation, higher accuracy), this study recommends exploration to data assimilation approach to improve the accuracy of the simulated discharge and water level anomaly to better estimate the true discharge and water level anomaly.

## Bibliography

- Alsdorf, D, C Birkett, T Dunne, J Melack, and L Hess. 2001. "Hydrology - Water Level Changes in a Large Amazon Lake Measured with Spaceborne Radar Interferometry and Altimetry (Paper 2001GL012962)". *Geophysical Research Letters*. 28 (14): 2671.
- Alsdorf, D.E., and D. P. Lettenmaier. 2003. "Tracking Fresh Water from Space". *Science*. 301 (5639): 1491-1494.
- Amarouche, L., P. Thibaut, O.Z. Zanife, J.-P. Dumont, P. Vincent & N. Steunou. 2004. Improving the Jason-1 Ground Retracking to Better Account for Attitude Effects, *Marine Geodesy*, 27:1-2, 171-197.
- Andreadis, K. M., E. A. Clark, D. P. Lettenmaier, and D. E. Alsdorf. 2007. "Prospects for river discharge and depth estimation through assimilation of swath-altimetry into a raster-based hydrodynamics model". *GEOPHYSICAL RESEARCH LETTERS*. 34 (10): L10403.
- ASTM, 1984. Standard Practice for Evaluating Environmental Fate Model of Chemicals Designation E978-84. American Society of Testing Materials. Philadelphia, PA. 8p.
- Bamber, J. L. 1994. Ice sheet altimeter processing scheme. *International Journal of Remote Sensing*. 15 (4): 925-938.
- Bao, L., Y. Lu, and Y. Wang. 2009. "Improved retracking algorithm for oceanic altimeter waveforms". *Progress in Natural Science*. 19 (2): 195-203.
- Bedient, P. B., and W. C. Huber. 2002. *Hydrology and floodplain analysis*. Upper Saddle River, N.J.: Prentice Hall.
- Benveniste J. 2011. Radar Altimetry: Past, Present and Future. A chapter of Vignudelli, S (Editor). 2011. *Coastal Altimetry*. Springer-Verlag Berlin Heidelberg 2011.
- Berry, P. A. M., J. D. Garlick, J. A. Freeman, and E. L. Mathers. 2005. "Global inland water monitoring from multi-mission altimetry". *Geophysical Research Letter*, 32, L16401.
- Berry, P.A.M. and J.L. Wheeler. 2009. Jason2-Envisat Exploitation: Development of Algorithms for the Exploitation of Jason2-Envisat Altimetry for the Generation of a River and Lake Product. ESA Product Handbook.
- Beven, K. J. 2004. "Robert E. Horton's perceptual model of infiltration processes". *Hydrological Processes*. 18 (17): 3447-3460.
- Beven, K. J. 2012. *Rainfall-runoff modelling the primer*. 2nd Edition. Chichester, West Sussex: Wiley-Blackwell.
- Biancamaria, S., K. M. Andreadis, M. Durand, E. A. Clark, E. Rodriguez, N. M. Mognard, D. E. Alsdorf, D. P. Lettenmaier, and Y. Oudin. 2010. "Preliminary Characterization of SWOT Hydrology Error Budget and Global Capabilities". *IEEE Journal of Selected Topics in Applied Earth Observations and Remote Sensing*. 3 (1): 6-19.
- Biancamaria, S., M. Durand, K.M. Andreadis, P.D. Bates, *et al.* 2011. "Assimilation of virtual wide swath altimetry to improve Arctic river modeling". *Remote Sensing of Environment*. 115 (2).



- Biondi, D., G. Freni, V. Iacobellis, G. Mascaro, and A. Montanari. 2012. "Validation of hydrological models: Conceptual basis, methodological approaches and a proposal for a code of practice". *Physics and Chemistry of the Earth*. 42-44: 70-76.
- Birkett, C. M., and I. M. Mason. 1995. "A New Global Lakes Database for a Remote Sensing Program Studying Climatically Sensitive Large Lakes". *Journal of Great Lakes Research*. 21 (3): 307-318.
- Birkett, C. M. 1998. Contribution of the TOPEX NASA radar altimeter to the global monitoring of large rivers and wetlands. *Water Resources Research*, Vol. 34, No. 5, Pages 1223-1239, May 1998.
- Birkett, C. M., L. A. K. Mertes, T. Dunne, M. H. Costa, and M. J. Jasinski. 2002. "Surface water dynamics in the Amazon Basin: Application of satellite radar altimetry". *Journal of Geophysical Research*. 107: LBA 26.
- Birkinshaw S.J., O'Donnell G.M., Moore P., Kilsby C.G., Fowler H.J., and Berry P.A.M. 2010. "Using satellite altimetry data to augment flow estimation techniques on the Mekong River". *Hydrological Processes*. 24 (26): 3811-3825.
- Blarel, F. and B. Legresy. 2012. Investigations on the Envisat RA2 Doppler Slope Corrections for Ice Sheets. *Proceedings of the ESA-CNES Symposium on Altimetry*. Venice, 2012.
- Brassel, K. E., and D. Reif. 1979. "A Procedure to Generate Thiessen Polygons". *Geographical Analysis*. 11 (3): 289-303.
- Brenner, A. C., H. V. Frey, and H. J. Zwally. 1990. "Comparisons between GEOSAT and SEASAT tracking over non-ocean surfaces". *Geophysical Research Letters*. 17 (10).
- Brown, G. 1977. "The average impulse response of a rough surface and its applications". *IEEE Transactions on Antennas and Propagation*. 25 (1): 67-74.
- Brown, O.B., and R.E. Cheney. 1983. Advances in satellite oceanography. *Reviews of Geophysics*. 21 (5).
- Cai X., and Ji W. 2009. "Wetland hydrologic application of satellite altimetry - A case study in the Poyang Lake watershed". *Progress in Natural Science*. 19 (12): 1781-1787.
- Calmant, S, F Seyler. 2006. Continental surface waters from satellite altimetry. *Internal Geophysics (Space Physics)*. C.R. Geoscience 338 (2006), pp 1113-1122.
- Cazenave, A., P. Bonnefond, K. Dominh, and P. Schaeffer. 1997. "Caspian sea level from Topex-Poseidon altimetry: Level now falling". *Geophysical Research Letters*. 24 (8): 881-884.
- Chang, J-H. 1993. Hydrology in Humid Tropical Asia. in Bonell M, MH Hufschmidt and JS Gladwell (eds.) (1993) *Hydrology and Water Resources in the Humid Tropics*. International Hydrology Series. Cambridge University Press. UNESCO.
- Chaudhry, M. H. 2008. *Open-channel flow*. New York: Springer.
- Chelton, D. B., E. J. Walsh, and J. L. MacArthur. 1989. "Pulse Compression and Sea Level Tracking in Satellite Altimetry". *Journal of Atmospheric and Oceanic Technology*. 6 (3): 407-438.

- Chelton, D.B, J.C. Ries, B.J. Haines, L-L Fu, P. S. Callahan. 2001. Satellite Altimetry. Fu, Lee-Lueng and A. Cazenave (Editors). 2001. Satellite Altimetry and Earth Sciences: A Handbook of Techniques and Applications. San Diego: Academic Press.
- Chow, V. T., D. R. Maidment, and L. W. Mays. 1988. Applied hydrology. New York: McGraw-Hill.
- Chu Y., Li J., Jiang W., Zou X., Fan C., Xu X., and Dadzie I. 2008. "Monitoring level fluctuations of the lakes in the Yangtze River basin from radar altimetry". *Terrestrial, Atmospheric and Oceanic Sciences*. 19 (1-2): 63-70.
- Chu, X., and A. Steinman. 2009. "Event and Continuous Hydrologic Modeling with HEC-HMS". *Journal of Irrigation and Drainage Engineering*. 135 (1): 119-124.
- Chang. X. 1993. Climate and Rainfall Variability in the Humid Tropics. in Bonell M, MH Hufhschmidt and JS Gladwell (eds.) (1993) *Hydrology and Water Resources in the Humid Tropics*. International Hydrology Series. Cambridge University Press. UNESCO.
- Clark, E. A. 2006. Prospects for river discharge estimation through assimilation of remotely-sensed altimetry into a raster-based hydraulics model. Thesis (M.S.E.)--University of Washington, 2006.
- CNES. 2013. SARAL/AltiKa: A French-Indian mission for the monitoring of the environment: Altimetry (AltiKa) and contribution to ARGOS system. <http://smc.cnes.fr/SARAL/>. Accessed on July 1, 2013.
- Coe, M. T., and C. M. Birkett. 2004. Calculation of river discharge and prediction of lake height from satellite radar altimetry: Example for the Lake Chad basin, *Water Resour. Res.*, 40, W10205, doi:10.1029/2003WR002543.
- Cretaux, J-F., and C. Birkett. 2006. "Lake studies from satellite radar altimetry". *Comptes Rendus - Geoscience*. 338 (14): 1098-1112.
- Cretaux, J-., A. V. Kouraev, F. Papa, M. Berge-Nguyen, A. Cazenave, N. Aladin, and I. S. Plotnikov. 2005. "Evolution of Sea Level of the Big Aral Sea from Satellite Altimetry and Its Implications for Water Balance". *Journal of Great Lakes Research*. 31 (4): 520-534.
- Cristescu M.E., S.J. Adamowicz, J.J. Vaillant, and D.G. Haffner. 2010. "Ancient lakes revisited: from the ecology to the genetics of speciation". *Molecular Ecology*. 19 (22): 4837-51.
- Cunge, J. A. 1969. "On The Subject Of A Flood Propagation Computation Method (Musklngum Method)". *Journal of Hydraulic Research*. 7 (2): 205-230.
- Dabo-Niang, S., F. Ferraty, and P. Vieu. 2007. "On the using of modal curves for radar waveforms classification". *Computational Statistics and Data Analysis*. 51 (10): 4878-4890.
- Davie, T. 2003. *Fundamentals of hydrology*. London: Routledge.
- Davis, C. H. 1993. A surface and volume scattering retracking algorithm for ice sheet satellite altimetry. *IEEE* 31, No.4.
- Davis, C.H. 1997. "A robust threshold retracking algorithm for measuring ice-sheet surface elevation change from satellite radar altimeters". *IEEE Transactions on Geoscience and Remote Sensing*. 35 (4): 974-979.

- Davis, C.H. 1997. "A robust threshold retracking algorithm for measuring ice-sheet surface elevation change from satellite radar altimeters". *IEEE Transactions on Geoscience and Remote Sensing*. 35 (4): 974-979.
- Deng, X. 2003. Improvement of Geodetic Parameter Estimation in Coastal Regions from Satellite Radar Altimetry, PhD thesis, Curtin University of Technology
- deSa, J. P. M. 2007. Applied Statistics using SPSS, Statistica, MATLAB and R. Springer-Verlag Berlin Heidelberg. ISBN 978-3-540-71971-7.
- Djokic, D.. 2008. Comprehensive Terrain Preprocessing Using Arc Hydro Tools. ESRI Technical Document. December 2008.
- Duan, Q. 2003. Calibration of watershed models. Washington, D.C.: American Geophysical Union.
- Durand M., D. E. Alsdorf, K. M. Andreadis, D. P. Lettenmaier, *et al.* 2008. "Estimation of bathymetric depth and slope from data assimilation of swath altimetry into a hydrodynamic model". *Geophysical Research Letters*. 35 (20).
- El-Swaify, S.A., E.W. Dangler and C.L. Armstrong. 1982. Soil erosion by water in the tropics. Coll. of Tropical Agric. and Human Resources, Univ. of Hawaii, Honolulu, USA
- Elliott, R. H., and L. K. Sherman. 1940. "Unit-hydrograph". *Transactions, American Geophysical Union*. 21 (3): 969.
- Estiaty, L. M., Y. Susilowati, E. Harsono, Tjptasamara. 2007. Pemodelan Spasial Fluks Polutan pada Sistem Daerah Aliran Sungai dan Angkutan Polutan pada Sistem Sungai. Studi Kasus: DAS Mahakam (In Indonesian). Pusat Penelitian Geoteknologi. Lembaga Ilmu Pengetahuan Indonesia. 2007.
- European Space Agency (ESA). 2006. Envisat RA-2/MWR Level 2 User Manual. Envisat Altimetry Quality Working Group. Ver. 1.2, 14 October 2006.
- European Space Agency (ESA). 2007. Envisat RA2/MWR Product Handbook. European Space Agency. 27 February 2007.
- European Space Agency (ESA). 2011. Envisat RA-2/MWR Level 2 User Manual. Envisat Altimetry Quality Working Group. Ver. 1.4, 08 September 2011.
- European Space Agency (ESA). 2012. Temporal Water Surface Height Variations in Enclosed Areas: the Amazon Basin. ESA Satellite Altimetry website. Accessed on October 1, 2012. [http://www.altimetry.info/html/use\\_cases/data\\_use\\_case\\_amazon1\\_en.html](http://www.altimetry.info/html/use_cases/data_use_case_amazon1_en.html)
- European Space Agency (ESA). 2013a. Geophysical Corrections. Radar Altimetry Tutorial. <http://www.altimetry.info/>. Accessed on July 21, 2013.
- European Space Agency (ESA). 2013b. Inverted Barometer. Radar Altimetry Tutorial. <http://www.altimetry.info/>. Accessed on July 29, 2013.
- European Space Agency (ESA). 2013c. RA-2 Auxilliary Data and Corrections. Earth Observation Product Control Service. <http://earth.eo.esa.int/pes/Envisat/ra2/auxdata/>. Accessed on August 13, 2013.
- Fenoglio-Marc L, Fehla M, Ferri L, Becker M, Gao Y, Vignudelli S (2009) Coastal sea surface heights from improved altimeter data in the Mediterranean Sea, Proceedings GGeo2008. Springer Verlag, IAG Symposia

- Fleming, M., and V. Neary. 2004. "Continuous Hydrologic Modeling Study with the Hydrologic Modeling System". *Journal of Hydrologic Engineering*. 9 (3): 175.
- Ford D.T. and D. Hamilton. 1996. *Computer Models for Water-Excess Management*. Larry W Mays (Ed.) *Water Resources Handbook*. McGraw-Hill, New York.
- Fosberg, F.B., B.J. Garnier and A.W. Kuchler. 1961. *Delimitation of the Humid Tropics*. *Geographical Review*, vol 51, pp. 333-347.
- Frappart, F., K. Do Minh, J. L'Hermitte, A. Cazenave, G. Ramillien, T. Le Toan, and N. Mognard-Campbell. 2006. "Water volume change in the lower Mekong from satellite altimetry and imagery data". *Geophysical Journal International*. 167 (2): 570-584.
- Frappart, F., F. Seyler, J-M. Martinez, J. G. Leon, and A. Cazenave. 2005. "Floodplain water storage in the Negro River basin estimated from microwave remote sensing of inundation area and water levels". *Remote Sensing of Environment*. 99 (4): 387-399.
- Fu, L-L, and A. Cazenave. 2001. *Satellite altimetry and Earth sciences: a handbook of techniques and applications*. San Diego: Academic Press.
- Fu, L-L, D Alsdorf, R Morrow, E Rodriguez. 2012. *SWOT: The Surface Water and Ocean Topography Mission. Wide-Swath Altimetric Measurement of Water Elevation on Earth*. JPL Publication 12-05. NASA Jet Propulsion Laboratory. February 2012.
- Gao H., D. P. Lettenmaier, and C. M. Birkett. 2012. "Global monitoring of large reservoir storage from satellite remote sensing". *Water Resources Research*. 48 (9).
- Gaspar, P., and J.-P. Florens. 1998. "Estimation of the sea state bias in radar altimeter measurements of sea level: Results from a new nonparametric method". *Journal of Geophysical Research*. 103 (C8): 15.
- Gentle, J. E. 2009. *Computational statistics*. Dordrecht: Springer.
- Getirana, A.C.V. 2010. "Integrating spatial altimetry data into the automatic calibration of hydrological models". *Journal of Hydrology*. 387 (3): 244-255.
- Getirana, A.C.V., M-P. Bonnet, S. Calmant, E. Roux, O.C.R. Filho, and W.J. Mansur. 2009. "Hydrological monitoring of poorly gauged basins based on rainfall-runoff modeling and spatial altimetry". *Journal of Hydrology*. 379 (3): 205-219.
- Guo, J., X. Chang, Y. Gao, J. Sun, and C. Hwang. 2009. "Lake Level Variations Monitored With Satellite Altimetry Waveform Retracking". *IEEE Journal of Selected Topics in Applied Earth Observations and Remote Sensing*. 2 (2): 80-86.
- Gyawali R., and Watkins D.W. 2013. "Continuous hydrologic modeling of snow-affected watersheds in the great lakes basin using HEC-HMS". *Journal of Hydrologic Engineering*. 18 (1): 29-39.
- Haryani, G.S., P.E. Hehanussa. 1999. *Pendekatan Ekohidrologi, Paradigma Baru Implementasi Penataan Ruang untuk Pengelolaan Danau dan Waduk (In Indonesian)*. Semiloka Nasional Pengelolaan dan Pemanfaatan Danau dan Waduk. Bogor. 1999
- Hausman, J., V. Zlotnicki. 2010. *Sea State Bias in Radar Altimetry Revisited*, *Marine Geodesy*, 33:S1, 336-347, DOI: 10.1080/01490419.2010.487804

- Hayne, G. 1980. "Radar altimeter mean return waveforms from near-normal-incidence ocean surface scattering". *IEEE Transactions on Antennas and Propagation*. 28 (5): 687-692.
- Hayne, G. S., and D. W. Hancock. 1990. "Corections for the effects of significant wave height and attitude on Geosat radar altimeter measurements". *Journal of Geophysical Research*. 95 (C3): 2837.
- Hayne, G. S., D. W. Hancock, C. L. Purdy, and P. S. Callahan. 1994. "The corrections for significant wave height and attitude effects in the TOPEX radar altimeter". *Journal of Geophysical Research*. 99 (C12): 24941.
- HEC. 2000. Hydrologic Modeling System HEC-HMS. Technical Reference Manual CPD-74B. US Army Corps of Engineers. Hydrologic Engineering Center. Davis, CA. March 2000.
- HEC. 2010. HEC-GeoHMS. Geospatial Hydrologic Modeling Extension Version 5.0. User Manual. US Army Corps of Engineers, Hydrologic Engineering Center. October 2010
- Hehanussa P.E. 2006. Land-inland Water Interactions of The Malili Lakes, Their Characteristics and Anthropogenic Effects. Article published in the Proceeding of The Ecology and Limnology of The Malili Lakes: International Symposium. Indonesian Institute of Sciences (LIPI). 2006.
- Hehanussa, P.E., Haryani, G.S. 1999. Morfologi cekungan dan profil suhu Danau Matano dan Danau Poso. *Limnotek : perairan darat tropis di Indonesia* (In Indonesian). Lembaga Ilmu Pengetahuan Indonesia - Pusat Penelitian Limnologi. Vol 6 No 1 PP 13-23.
- Herdendorf, C.E. 1982. Large Lakes of the World. *Journal of Great Lakes Research* 8(3):379-412. International Association of Great Lakes Research, 1982.
- Hersch, R.W. 2009. Streamflow Measurement 3rd edition. London. Routledge, Taylor and Francis group. ISBN 978-0-415-4132-8
- Hevizi, L.G.; Walsh, E.J.; McIntosh, R.E.; Vandemark, D.; Hines, D.E.; Swift, Robert N.; Scott, J. 1993. "Electromagnetic bias in sea surface range measurements at frequencies of the TOPEX/Poseidon satellite," *IEEE Transactions on Geoscience and Remote Sensing*, vol.31, no.2, pp.376,388, Mar 1993. doi: 10.1109/36.214914
- Hidayat H., Vermeulen B., Sassi M.G., F. Torfs P.J.J., and Hoitink A.J.F. 2011a. "Discharge estimation in a backwater affected meandering river". *Hydrology and Earth System Sciences*. 15 (8): 2717-2728.
- Hidayat H., A.J.F. Hoitink, M.G. Sassi, B. Vermeulen, R.T.W.L. Hurkmans, P.J.J.F. Torfs, R. Uiljenhoet. 2011b. Added Value of H-ADCP Data in Rainfall-Runoff Models Driven by Satellite Rainfall Input in a Tropical Basin. Poster Presented at European Geophysical Union Annual Conference. 2011.
- Hidayat H., Hoitink A.J.F., Hoekman D.H., and Vissers M.A.M. 2012. "Flood occurrence mapping of the middle Mahakam lowland area using satellite radar". *Hydrology and Earth System Sciences*. 16 (7): 1805-1816.
- Horritt, M.S., P.D. Bates. 2002. Evaluation of 1D and 2D Numerical Models for Predicting River Flood Inundation. *Journal of Hydrology* 268, 87 – 99.

- Huffman, George J., *et al*, 2007: The TRMM Multisatellite Precipitation Analysis (TMPA): Quasi-Global, Multiyear, Combined-Sensor Precipitation Estimates at Fine Scales. *J. Hydrometeor*, 8, 38–55.
- Hwang C., Guo J.Y., Deng X.L., Hsu H.Y., Liu Y.T. 2006. Coastal gravity anomalies from retracked Geosat/GM altimetry: improvement, limitation and the role of airborne gravity data. *J Geod* 80:204–216
- Hwang, C., M-F. Peng, J. Ning, J. Luo, and C-H. Sui. 2005. "Lake level variations in China from TOPEX/Poseidon altimetry: data quality assessment and links to precipitation and ENSO". *Geophysical Journal International*. 161 (1): 1-11.
- Jiang X., Lin M., Liu J., Zhang Y., Xie X., Peng H., and Zhou W. 2012. "The HY-2 satellite and its preliminary assessment". *International Journal of Digital Earth*. 5 (3): 266-281.
- Kaula WM. 1970. The terrestrial environment: solid Earth and ocean physics. NASA Contractor Report to Electronic Research Center. National Aeronautics and Space Administration. Washington DC. April 1970.
- Khan, M. Q. I., L. Venkataratnam, B. R. M. Rao, D. P. Rao, and C. Subrahmanyam. 2001. "International Classification and Codification of Watersheds and River Basins". *Journal of Water Resources Planning & Management*. 127 (5).
- Kilgus, C.C. 1988. "The Navy Geosat Radar Altimeter Satellite Mission". *Proceedings of IGARSS 88 Symposium, Edinburgh, Scotland 13-16 September 1988*. Published by ESA Publications Division, August 1988. doi: 10.1109/IGARSS.1988.570493
- Koblinsky C.J, R.T Clarke, A. C Brenner, H Frey, 1983. Measurement of River Water Levels with Satellite Altimetry. *Water Resources Research*, Vol. 29 No. 6, Pages 1839-1848, June 1993.
- Korotaev, G. K., O. A. Saenko, and C. J. Koblinsky. 2001. "Satellite altimetry observations of the Black Sea level". *Journal of Geophysical Research*. 106 (C1): 917.
- Kouraev, A.V., E.A. Zakharova, O. Samain, N.M. Mognard, and A. Cazenave. 2004. "Ob' river discharge from TOPEX/Poseidon satellite altimetry (1992-2002)". *Remote Sensing of Environment*. 93 (1): 238-245.
- Kuo, C-Y., and H-C. Kao. 2011. "Retracked Jason-2 Altimetry over Small Water Bodies: Case Study of Bajhang River, Taiwan". *Marine Geodesy*. 34 (3-4): 382-392.
- Kuok K.K., P.C. Chiu, C.M. Chung, T.H. Chuang. 2010 Relationship between Storage Coefficient and Catchment Area using HEC-HMS for Southern Region of Serawak. *The IUP Journal of Soil and Water Sciences*, Vol. III, No. 4, 2010
- Laxon, S. 1994. "Sea ice altimeter processing scheme at the EODC". *International Journal of Remote Sensing*. 15 (4): 915-924.
- Le Provost, C. *Ocean Tides*. Fu, Lee-Lueng and A. Cazenave (Editors). 2001. *Satellite Altimetry and Earth Sciences: A Handbook of Techniques and Applications*. San Diego: Academic Press.
- Lee, Hyongki. 2008. Radar altimetry methods for solid Earth geodynamics studies. PhD Dissertation. School of Earth Sciences. The Ohio State University. Columbus, Ohio

- Legresy, B., & F. Remy. 1997. Surface characteristics of the Antarctic ice sheet and altimetric observations. *Journal of Glaciology*, 43(144), 265 – 275.
- Li, Y. 2010. Root Mean Square Error. In Neil J. Salkind (Ed.), *Encyclopedia of Research Design*. (pp. 1288-1289). Thousand Oaks, CA: SAGE Publications, Inc.
- Lotspeich, F. B. 1980. "Watersheds as the Basic Ecosystem: This Conceptual Framework Provides a Basis for a Natural Classification System". *Journal of the American Water Resources Association*. 16 (4): 581-586.
- Lu, Z., J-W. Kim, H. Lee, C. K. Shum, J. Duan, M. Ibaraki, O. Akyilmaz, and C-H. Read. 2009. "Helmand River Hydrologic Studies Using ALOS PALSAR InSAR and Envisat Altimetry". *Marine Geodesy*. 32 (3): 320-333.
- Madsen, B. 2011. *Statistics for non-statisticians*. Berlin: Springer.
- Maheu, C., A. Cazenave, and C. R. Mechoso. 2003. "Water level fluctuations in the Plata Basin (South America) from Topex/Poseidon Satellite Altimetry Geophysical Research Letters. 30: 43.
- Martin, T.V., H.J. Zwally, A.C. Brenner, and R.A. Bindshadler. 1983. Analysis and retracking of continental ice sheet radar altimeter waveforms, *J. Geophys. Res.*, 88(C3), 1608–1616, doi:10.1029/JC088iC03p01608.
- Mays, L.W. 2012. *Ground and surface water hydrology*. Hoboken, N.J. John Wiley and Sons.
- McKinnon, K., G. Hatta, H. Halim, A. Mangalik. 1996. *The Ecology of Kalimantan: Indonesian Borneo. The Ecology of Indonesia Series. Volume 3*. Singapore: Periplus.
- McCarthy, Gerald T. 1939. *The unit hydrograph and flood routing*. Providence, R.I.: Army Engineer District, Providence.
- McCarthy, Dennis D. and Gérard Petit. 2003. *IERS Conventions (2003)*(IERS Technical Note No. 32) Frankfurt am Main: Verlag des Bundesamts für Kartographie und Geodäsie, 2004. 127 pp., paperback, ISBN 3-89888-884-3 (print version)
- McGoogan, J.T. 1975. "Satellite Altimetry Applications," *Microwave Symposium, 1975 IEEE-MTT-S International* , vol., no., pp.23,25, 12-14 May 1975. doi: 10.1109/MWSYM.1975.1123266
- Medina C.E., Gomez-Enri J., Alonso J.J., and Villares P. 2008. "Water level fluctuations derived from Envisat Radar Altimeter (RA-2) and in-situ measurements in a subtropical waterbody: Lake Izabal (Guatemala)". *Remote Sensing of Environment*. 112 (9): 3604-3617.
- Mercier, F., A. Cazenave, and C. Maheu. 2002. "Interannual lake level fluctuations (1993-1999) in Africa from Topex/Poseidon: connections with ocean-atmosphere interactions over the Indian Ocean". *Global and Planetary Change*. 32 (2): 141-163.
- Merwade V., F. Olivera, M. Arabi, and S. Edleman. 2008. "Uncertainty in flood inundation mapping: Current issues and future directions". *Journal of Hydrologic Engineering*. 13 (7): 608-620.

- Meybeck M., G. Friedrich, R. Thomas and D. Chapman. 1996. Rivers. Chapter in Water Quality Assessments - A Guide to Use of Biota, Sediments and Water in Environmental Monitoring - Second Edition. Deborah Chapman (Eds.) UNESCO/WHO/UNEP. 1992, 1996.
- Michailovsky C.I., McEnnis S., Bauer-Gottwein P., Berry P.A.M., and Smith R. 2012. "River monitoring from satellite radar altimetry in the Zambezi River basin". Hydrology and Earth System Sciences. 16 (7): 2181-2192.
- Michailovsky, C.I., C. Milzow, P. Bauer-Gottwein. 2013. Assimilation of radar altimetry to a routing model of the Brahmaputra River. Water Resources Research. Accepted Article. 10.1002/wrcr.20345. 1944-7973.
- Moore, R., and C. Williams. n.d. "Radar Terrain Return at Near-Vertical Incidence". Proceedings of the IRE. 45 (2): 228-238.
- Morris, C., S. Gill, 1994. Variation of Great Lakes water levels derived from Geosat altimetry. Water Resources Research, Vol. 30, No. 4, Pages 1009-1017, April 1994.
- Morris, C.S., and S.K. Gill. 1994. "Evaluation of the TOPEX/POSEIDON altimeter system over the Great Lakes". Journal of Geophysical Research. 99 (C12): 24527-24539
- Munyaneza O., U.G. Wali, S. Uhlenbrook, S. Maskey, and M. J. Mlotha. 2009. "Water level monitoring using radar remote sensing data: Application to Lake Kivu, central Africa". Physics and Chemistry of the Earth. 34 (13-16): 722-728.
- Nagler, J. 2004. Root Mean Square. In Michael S. Lewis-Beck, A. Bryman, & Tim Futing Liao (Eds.), The SAGE Encyclopedia of Social Science Research Methods. (pp. 978-979). Sage Publications, Inc.
- Nash, J. E. 1959. "A note on the Muskingum flood-routing method". Journal of Geophysical Research. 64 (8): 1053-1056.
- NWS. 2013. The Hydrologic Cycle. Jetstream - Online School for Weather. National Weather Service. National Oceanic and Atmospheric Administration. Accessed on June 4, 2013. <http://www.srh.noaa.gov/jetstream/>
- Paiva, R. C. D., Collischonn, W., Bonnet, M.-P., de Gonçalves, L. G. G., Calmant, S., Getirana, A., and Santos da Silva, J. 2013. Assimilating in situ and radar altimetry data into a large-scale hydrologic-hydrodynamic model for streamflow forecast in the Amazon, Hydrol. Earth Syst. Sci. Discuss., 10, 2879-2925
- Panik, M. J. 2012. Statistical Inference: A Short Course. Hoboken: John Wiley & Sons.
- Parke, M. E., R. H. Stewart, D. L. Farless, and D. E. Cartwright. 1987. "On the choice of orbits for an altimetric satellite to study ocean circulation and tides". Journal of Geophysical Research. 92 (C11): 11693.
- Ponce, V. M., and R. H. Hawkins. 1996. "Runoff Curve Number: Has It Reached Maturity?" Journal of Hydrologic Engineering. 1 (1): 11-19.
- Provost, C. Le. 2001. Ocean Tides. Fu, Lee-Lueng and A. Cazenave (Editors). 2001. Satellite Altimetry and Earth Sciences: A Handbook of Techniques and Applications. San Diego: Academic Press.



- Rabus, B., M. Eineder, A. Roth, and R. Bamler. 2003. "The shuttle radar topography mission—a new class of digital elevation models acquired by spaceborne radar". *ISPRS Journal of Photogrammetry and Remote Sensing*. 57 (4): 241-262.
- Rapley C.G., M.A.J. Guzkowska, W. Cudlip and I.M. Mason. 1987. "An Exploratory Study of Inland Water and Land Altimetry using SEASAT Data". ESA Contract Report 6483/85/NL/BI.
- Rapley, C.G., A.H.W. Rapley, W. Kersley, W. Cudlip, J.K. Ridley, and P. K. Chua. 1990. "The determination and use of orthometric heights derived from the Seasat radar altimeter over land". *Photogrammetric Engineering & Remote Sensing*. 57 (4).
- Rees, G. 1990. *Physical principles of remote sensing*. Cambridge [England]: Cambridge University Press
- Renggono, Findy. 2011. Pola Sebaran Hujan di DAS Larona. Rainfall Distribution Pattern of Larona Watershed. In Indonesian. *Jurnal Sains dan Teknologi Modifikasi Cuaca*. Vol 12 No 1, 2011. pp 17-24.
- Resti, A., J. Benveniste, M. Roca, G. Levrini, J. Johannessen. 1999. The Envisat Radar Altimeter System (RA-2). ESA Bulletin No 98. June 1999.
- Ridley, J.K., and K.C. Partington. 1988. "A model of satellite radar altimeter return from ice sheets". *International Journal of Remote Sensing*. 9 (4): 601-624.
- Roca, M.; Benveniste, J.; Levrini, G.; Resti, A.; Zelli, C.; Zanife, O-Z; Wingham, D.J.; Laxon, S.; Remy, F.; Vincent, P. 1999. "The Envisat RA-2/MWR instrument description, processing chain and data products," *Geoscience and Remote Sensing Symposium*, 1999. IGARSS '99 Proceedings. IEEE 1999 International , vol.3, no., pp.1689,1691 vol.3, 1999. doi: 10.1109/IGARSS.1999.772062
- Rodriguez, E., and B. Chapman. 1989. "Extracting ocean surface information from altimeter returns: The deconvolution method". *Journal of Geophysical Research*. 94 (C7): 9761.
- Rodriguez, E. 1988. "Altimetry for non-Gaussian oceans: Height biases and estimation of parameters". *Journal of Geophysical Research*. 93 (C11): 14107.
- Rodríguez E, and J. M. Martin. 1994a. "Estimation of the electromagnetic bias from retracked TOPEX data". *Journal of Geophysical Research*. 99 (C12): 24971.
- Rodríguez E., and J.M. Martin. 1994b. "Assessment of the TOPEX altimeter performance using waveform retracking". *Journal of Geophysical Research*. 99 (C12): 24957.
- Rodriguez, E, C.S. Morris, and J. E. Belz. 2006. "A Global Assessment of the SRTM Performance ". *Photogrammetric Engineering and Remote Sensing*. 72 (3): 249.
- Rosbjerg D. and H. Madsen. 2005. *Concepts of Hydrologic Modeling*. A section of the *Encyclopedia of Hydrological Sciences* by MG Anderson (ed.), John Wiley and Sons. 2005.
- Russel J, S. Bijaksana. 2012. The Towuti Drilling Project: Paleoenvironments, Biological Evolution, and Geomicrobiology of a Tropical Lake. *Scientific Drilling*, No. 14, September 2012. doi:10.2204/iodp.sd.14.11.2012
- Sabol, G. V. 1988. "Clark Unit Hydrograph and R-Parameter Estimation". *Journal of Hydraulic Engineering*. 114 (1): 103-111.

- Scott, R. F., S. G. Baker, C. M. Birkett, W. Cudlip, S. W. Laxon, D. R. Mantripp, J. A. Mansley, *et al.* 1994. "A comparison of the performance of the ice and ocean tracking modes of the ERS-1 radar altimeter over non-ocean surfaces". *Geophysical Research Letters*. 21 (7).
- Seeber, G. 2003. *Satellite Geodesy*. 2nd completely revised and extended edition. Walter de Gruyter. Berlin, New York. 2003.
- Shiklomanov, I.A. 1998. *World Water Resources: A New Appraisal and Assessment for the 21st Century*. A summary of the monograph of World Water Resources. UNESCO. 1998.
- Shum, C.K., B.D. Tapley, and J.C. Ries. 1993. "Satellite altimetry: Its applications and accuracy assessment". *Advances in Space Research*. 13 (11): 315-324.
- Shum, C. K., J. C. Ries, and B. D. Tapley. 1995. "The accuracy and applications of satellite altimetry". *Geophysical Journal International*. 121 (2): 321-336.
- Siddique-E-Akbor, A.H.M., F. Hossain, H. Lee, and C.K. Shum. 2011. "Inter-comparison study of water level estimates derived from hydrodynamic-hydrologic model and satellite altimetry for a complex deltaic environment". *Remote Sensing of Environment*. 115 (6): 1522-1531.
- Stewart, R.H. 1985. *Methods of satellite oceanography*. Berkeley: University of California Press.
- Straub, Timothy D., Charles S. Melching, and Kyle E. Kocher. 2000. *Equations for estimating Clark unit-hydrograph parameters for small rural watersheds in Illinois*. Urbana, Ill: U.S. Dept. of the Interior, U.S. Geological Survey.
- Sulistioadi, YB. 2013. *An inventory on the flood occurrence in Upper Mahakam Sub-watershed*. Unpublished report.
- Sun, W., H. Ishidaira, and S. Bastola. 2012. "Calibration of hydrological models in ungauged basins based on satellite radar altimetry observations of river water level". *Hydrological Processes*. 26 (23): 3524-3537.
- Tang, Q., H. Gao, H. Lu, and D. Lettenmaier. 2009. "Remote sensing: hydrology". *Progress in Physical Geography*. 33 (4): 490-509
- Townsend, W. 1980. "An initial assessment of the performance achieved by the Seasat-1 radar altimeter," *Oceanic Engineering, IEEE Journal of* , vol.5, no.2, pp.80,92, April 1980. doi: 10.1109/JOE.1980.1145459
- Troitskaya, Y. I., G. V. Rybushkina, I. A. Soustova, G. N. Balandina, S. A. Lebedev, A. G. Kostyanoi, A. A. Panyutin, and L. V. Filina. 2012. "Satellite altimetry of inland water bodies". *Water Resources*. 39 (2): 184-199.
- Tseng, K. H., C. K. Shum, Y. Yi, H. S. Fok, C. Y. Kuo, H. Lee, X. Cheng, and X. Wang, 2013: *Envisat altimetry radar waveform retracking of quasispecular echoes over the ice-covered Qinghai Lake*. *Terr. Atmos. Ocean. Sci.*, 24, 615-627
- Tseng, K-H. 2012. *Satellite Altimetry and Radiometry for Inland Hydrology, Coastal Sea-Level and Environmental Studies*. School of Earth Sciences. The Ohio State University. Columbus, Ohio
- Twomey, S. 1963. "On the Numerical Solution of Fredholm Integral Equations of the First Kind by the Inversion of the Linear System Produced by Quadrature". *Journal of the ACM (JACM)*. 10 (1): 97-101.

- Ulaby, F. T., R. K. Moore, and A. K. Fung. 1981. Microwave remote sensing: active and passive. Reading, Mass: Addison-Wesley Pub. Co., Advanced Book Program/World Science Division.
- USDA NRCS. 2004. Simulation of Direct Runoff from Storm Rainfall. Part 630 Hydrology, Chapter 10. National Engineering Handbook. United States Department of Agriculture. Natural Resources Conservation Services. 2004. Revised version of the same document released by Soil Conservation Services. 1972.
- USDA-NRCS. 1993. Storm Rainfall Depth. Part 630 Hydrology, Chapter 4. National Engineering Handbook. United States Department of Agriculture. Natural Resources Conservation Service. September 1993.
- USDA NRCS. 1986. Urban Hydrology for Small Watersheds (TR-55). Technical Release 55. US Department of Agriculture. Natural Resources Conservation Service. Conservation Engineering Division. June 1986.
- Vaillant, J.J., G.D. Haffner, and M.E. Cristescu. 2011. "The Ancient Lakes of Indonesia: Towards Integrated Research on Speciation". Integrative and Comparative Biology. 51 (4): 634-643.
- Vandemark, D, N Tran, B D Beckley, B Chapron, and P Gaspar. 2002. "Direct estimation of sea state impacts on radar altimeter sea level measurements". Geophysical Research Letters. 29 (24): 1-4.
- van Zyl, J. 2001. "The Shuttle Radar Topography Mission (SRTM): a breakthrough in remote sensing of topography". Acta Astronautica. 48 (5-12): 559-565.
- Velpuri N.M., Senay G.B., and Asante K.O. 2012. "A multi-source satellite data approach for modelling Lake Turkana water level: Calibration and validation using satellite altimetry data". Hydrology and Earth System Sciences. 16 (1): 1-18.
- Verma, A.K., M.K. Jha, and R.K. Mahana. 2010. "Evaluation of HEC-HMS and WEPP for simulating watershed runoff using remote sensing and geographical information system". Paddy and Water Environment. 8 (2): 131-144.
- Vincent, P.; Verron, J.; Bahurel, P.; Le Traon, P.Y.; Eymard, L.; Remy, F.; Cretaux, J.-F.; Tournadre, J.; Chapron, B., "The AltiKa altimetry mission: science objectives and system definition," Geoscience and Remote Sensing Symposium, 2000. Proceedings. IGARSS 2000. IEEE 2000 International , vol.7, no., pp.3036,3038 vol.7, 2000. doi: 10.1109/IGARSS.2000.860327
- Wahr, J. M. 1985. "Deformation induced by polar motion". Journal of Geophysical Research. 90 (B11): 9363.
- Wingham, D.J, C.G. Rapley, and H.G. Griffiths. 1986. New techniques in satellite altimeter tracking systems. III IGARRS 1986 Symposium. Zurich. Proceedings. Noordwijk, ESTEC. Scientific and Technical Publications Branch, 1339-1344. (ESA SP-254.)
- Wingham, D.J., and C.G. Rapley. 1987. Saturation effects in the Seasat altimeter receiver. International Journal of Remote Sensing. 8 (8): 1163-1173

- Wingham, D.J. 1988. "Onboard correction of mispointing errors in satellite altimeter returns [oceanographic measurement]," *Oceanic Engineering, IEEE Journal of* , vol.13, no.2, pp.77,81, Apr 1988. doi: 10.1109/48.557
- Witter, D. L., and D. B. Chelton. 1991. "A Geosat altimeter wind speed algorithm and a method for altimeter wind speed algorithm development". *Journal of Geophysical Research*. 96 (C5): 8853.
- Wunsch, C and D Stammer. 1997. "Atmospheric loading and the oceanic "inverted barometer" effect". *Reviews of Geophysics*. 35 (1): 79.
- Xu X-Y, H-G. Liu. 2007. "An innovative algorithm for radar altimeter acceleration bias compensation," *Geoscience and Remote Sensing Symposium, 2007. IGARSS 2007. IEEE International* , vol., no., pp.3829,3831, 23-28 July 2007. doi: 10.1109/IGARSS.2007.4423678
- Yoon, Y., M. Durand, C.J. Merry, E.A. Clark, K.M. Andreadis, and D.E. Alsdorf. 2012. "Estimating river bathymetry from data assimilation of synthetic SWOT measurements". *Journal of Hydrology*. 464-465: 363-375.
- Yusop, Z., C.H. Chan, and A. Katimon. 2007. "Runoff characteristics and application of HEC-HMS for modelling stormflow hydrograph in an oil palm catchment". *Water Science and Technology : a Journal of the International Association on Water Pollution Research*. 56 (8): 41-48.
- Zakharova, E.A, A.V. Kouraev, J-F. Crétau, F. Al-Yamani, I. Polikarpov. 2007. *Radar Altimetry for Studies of Large River Basins: Hydrological Regime of the Euphrates-Tigris Rivers. Proc. 'Envisat Symposium 2007', Montreux, Switzerland. 3-27 April 2007 (ESA SP-636, July 2007).*
- Zhang, H. L., Y. J. Wang, Y. Q. Wang, D. X. Li, and X. K. Wang. 2013. "The effect of watershed scale on HEC-HMS calibrated parameters: a case study in the Clear Creek watershed in Iowa, US". *Hydrology and Earth System Sciences*. 17 (7): 2735-2745.
- Zhang, J., K. Xu, Y. Yang, L. Qi, S. Hayashi, and M. Watanabe. 2006. "Measuring Water Storage Fluctuations in Lake Dongting, China, by Topex/Poseidon Satellite Altimetry". *Environmental Monitoring and Assessment*. 115 (1-3): 1-3.
- Zwally H.J., A.C. Brenner. 2001. *Ice Sheet Dynamics and Mass Balance. A chapter in Fu, L-L., A. Cazenave. 2001. Satellite Altimetry for Earth Sciences: A Handbook of Techniques and Applications. San Diego: Academic Press.*
- Zwally, J.H. 1996. *GSFC Retracking Algorithms. Technical document published in NASA GSFC website. Accessed on July 5, 2013. [http://icesat4.gsfc.nasa.gov/radar\\_data/data\\_processing/gsfcretrackdoc.960725.php](http://icesat4.gsfc.nasa.gov/radar_data/data_processing/gsfcretrackdoc.960725.php).*